

AD-A124 722

A MIND TUNNEL STUDY OF THE EFFECTS OF A CLOSE-COUPLED
CANARD ON THE AEROD. (U) AIR FORCE INST OF TECH

1/3

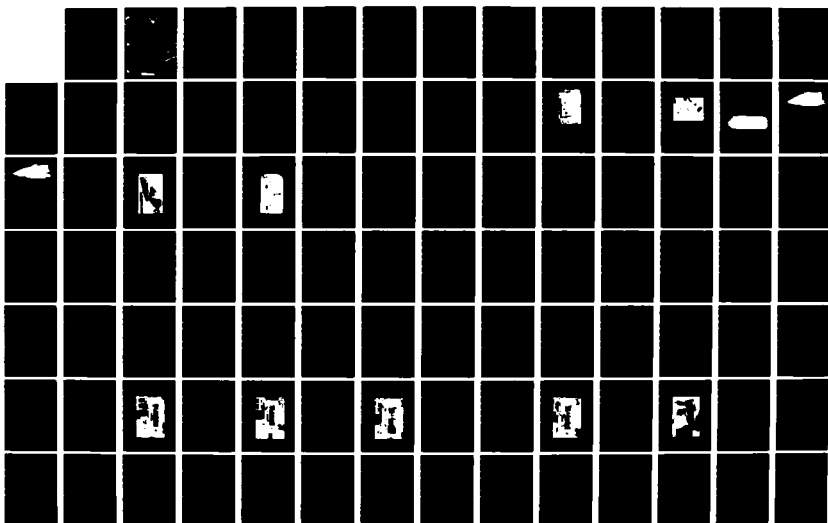
WRIGHT-PATTERSON AFB OH SCHOOL OF ENGI. P M WEAVER

UNCLASSIFIED

DEC 82 AFIT/GAE/AA/82D-38

F/G 1/3

NL





MICROCOPY RESOLUTION TEST CHART
NATIONAL BUREAU OF STANDARDS-1963-A

AD A124722



A WIND TUNNEL STUDY OF THE EFFECTS
OF A CLOSE-COUPLED CANARD ON THE
AERODYNAMIC CHARACTERISTICS OF A
FORWARD-SWEPT WING IN
INCOMPRESSIBLE FLOW

THESIS

AFIT/GAE/AA/82D-30 Paul M. Weaver
Capt USAF

DTIC
FEB 23 1983
H
DISTRIBUTION STATEMENT A
Approved for public release
Distribution Unlimited

UNITED STATES AIR FORCE
AIR UNIVERSITY

AIR FORCE INSTITUTE OF TECHNOLOGY

Wright-Patterson Air Force Base, Ohio

FILE COPY

[REDACTED]

83

02

022 090

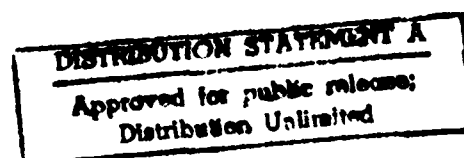


A WIND TUNNEL STUDY OF THE EFFECTS
OF A CLOSE-COUPLED CANARD ON THE
AERODYNAMIC CHARACTERISTICS OF A
FORWARD-SWEPT WING IN
INCOMPRESSIBLE FLOW

THESIS

AFIT/GAE/AA/82D-30 Paul M. Weaver
Capt USAF

Approved for public release; distribution unlimited



A WIND TUNNEL STUDY OF THE EFFECTS OF A
CLOSE-COUPLED CANARD ON THE AERODYNAMIC
CHARACTERISTICS OF A FORWARD-SWEPT
WING IN INCOMPRESSIBLE FLOW

THESIS

Presented to the Faculty of the School of Engineering
of the Air Force Institute of Technology

Air University

in Partial Fulfillment of the
Requirements for the Degree of
Master of Science

by

Paul M. Weaver, B.S.A.E
Capt USAF

Graduate Aeronautical Engineering

December 1982

Approved for public release; distribution unlimited



1000	1000
NEIS	1000
DTIC	1000
Unavail	1000
Just	1000
By	1000
8.1	1000
As	1000
Dist	1000

A

Preface

This thesis provides incompressible flow data on the differences among the aerodynamic characteristics of a forward-swept wing and the aerodynamic characteristics of several close-coupled canard/forward-swept wing configurations. Wind tunnel tests of a variable-configuration wing/canard model were conducted in the Air Force Institute of Technology fourteen inch wind tunnel. The experimental results not only increased the data base in this area, but also provided a more thorough understanding of canard/forward-swept wing interaction. Also, a basis was established for further investigation of the phenomena observed.

I would like to express my thanks to Jack Tiffany, John Brohas, Russell Murry, Dave Paine, and Carl Shortt of the Model Fabrication Division for a superb job in constructing the models and equipment needed for this thesis. Also, my thanks go to Whales Whitt and Nick Yardich for their competent instruction in correct wind tunnel procedure.

I would like to express special appreciation to Professor Harold C. Larsen, Maj Eric Jumper, Capt Wesley Cox, and my advisor Maj Michael Smith for their guidance and support throughout this effort. Finally, my thanks to Phyllis Reynolds for her assistance in the typing of this report.

Contents

	Page
Preface	ii
List of Figures	v
List of Tables	viii
List of Symbols	ix
Abstract	xii
I. Introduction	1
Objective	1
Background	1
Scope	2
Approach	4
II. Wind Tunnel Test Program	6
Wind Tunnel	6
Test Models	9
Model Installation	13
Test Conditions	14
Test Procedures	14
III. Experimental Results and Analysis, Model #3	24
Wing/Canard Configuration Results, C_L	24
Wing/Canard Configuration Analysis, C_L	29
Wing/Canard Configuration Results, C_D	36
Wing/Canard Configuration Analysis, C_D	39
Wing/Canard Configuration Results, C_M	40
Wing/Canard Configuration Analysis, C_M	42
General Comments, Swept Wings	44
IV. Experimental Results and Analysis, Model #4	45
Model Analysis	45
V. Conclusions and Recommendations	47
Conclusions	47
Recommendations	47
Bibliography	49

	Page
Appendix A: Model Geometry	51
Appendix B: Wind Tunnel Calibration	54
Appendix C: Data Reduction	70
Appendix D: Force and Moment Data	77
Appendix E: Flow Visualization Data	179
Vita	221

List of Figures

Figure	Page
1. Schematic, AFIT Fourteen Inch Wind Tunnel . . .	7
2. Wind Tunnel Balance	8
3. Wind Tunnel Console/Control Panel	10
4. Model #1 With Inclinator Platform Mounted	11
5. Model #2	12
6. Model #3	13
7. Typical Installation for Models #1-#3 (Model #3 Shown)	15
8. Calibration Rig and Associated Equipment . . .	17
9. Lift Curve Change, Test Positions 1-3	25
10. $C_{L\alpha}$ Change for $\beta > 6$ Deg	26
11. Change in $C_{L\alpha}$ for Change in β , Test Positions 6-8	27
12. C_L vs α Shift for Horizontal Δ Change, Test Positions 1-5	27
13. $C_{L\alpha}$ Change for Horizontal Δ Change, Test Positions 6-8	28
14. $C_{L\alpha}$ Change for Vertical Δ Change	28
15. Velocity Changes in a Wake	30
16. Canard/Wing Vortex Interaction	32
17. Effect of Canard Tip Vortices on Wing Airflow	32
18. Effect of Canard Wake on Wing Airflow	33
19. C_D Curve Change Due to a Change in β	37

Figure	Page
20. C_D Change for a Horizontal Change in Δ , Test Positions 1-5	37
21. C_D Change for a Horizontal Change in Δ	38
22. C_D Change for a Vertical Change in Δ From a High to a Low Canard Test Position	39
23. C_M Curve Shift with Increasing β	40
24. Data Spike on Wing/Canard C_M Curve	41
25. C_M Curve Shift for a Change in Δ From a High to a Low Test Position	41
26. Model #3 Schematic Side View	52
27. Model #3 Schematic Plan View	53
28. Dynamic Pressure Calibration Curve	55
29. Lift Calibration	57
30. Lift Calibration Curve	58
31. Drag Calibration	59
32. Drag Calibration Curve	60
33. Pitching-Moment Calibration	61
34. Pitching-Moment Calibration Curve	62
35. Component Interaction Calibration	64
36. Inclinator Position for Calibration	66
37. Angle of Attack Calibration Curve	67
38. Test Position Location With Respect to Wing Root 1/4 Chord	78

Figure		Page
39.	Figures 39A1L to 39A40L-- Lift Coefficient vs Alpha	79-118
	Figures 39A1D to 39A40D-- Drag Coefficient vs Alpha	119-158
	Figures 39A1M to 39A40M-- Moment Coefficient vs Alpha	159-178
40.	Figures 40A0 to 40A40-- Boundary Layer Flow Patterns	180-220

Note: Each plot in Fig 39 can be matched with a set of photographs in Fig 40 by matching the respective figure subscripts. For example, the plots in Figs 39A1L, 39A1D, and 39A1M would match the photographs in Fig 40A1.

List of Tables

Table	Page
I. Proposed Canard Geometries and Locations	3
II. Wind Tunnel Models	4
III. Wind Tunnel Balance Capacities and Accuracies .	9
IV. Location of Canard $.5c_r$	19
V. Model #3 Data and Dimensions	51

List of Symbols

A	Tunnel test section cross-sectional area, in ²
AFIT	Air Force Institute of Technology
AFWAL	Air Force Wright Aeronautical Laboratories
a_{wb}	Wing/body lift curve slope
a_t	Tail lift curve slope
AR	Aspect ratio
b	Airfoil span, in
b_e	Effective span, in
c	Chord, in
\bar{c}	Mean aerodynamic chord, in
C_D	Drag coefficient
C_{D0}	Zero lift drag coefficient
C_L	Lift coefficient
$C_{L\alpha}$	Lift curve slope
C_{Law}	Wing lift curve slope
C_{Lawc}	Wing/canard lift curve slope
C_{Lu}	Uncorrected lift coefficient
C_M	Moment coefficient
$C_{M\alpha}$	Moment curve slope
C_{Mtr}	Moment coefficient about mounting trunion
C_{Mu}	Uncorrected moment coefficient
c_r	Root chord, in
c_t	Tip chord, in

d	Vertical distance of model from tunnel test section centerline, ft
D _u	Uncorrected drag, lbs
D _o	Drag calibration curve abscissa intercept
FIMB	Office Symbol, Vehicle Synthesis Branch, AFWAL
FIMM	Office Symbol, Aerodynamics/Airframe Branch, AFWAL
L	Length of model in front of forward mounting trunion, in
L _c	Console lift, lbs
L _u	Uncorrected lift, lbs
L _o	Lift calibration curve abscissa intercept
M	Mach number
M _c	Console moment, in lbs
M _{ac}	Moment about aerodynamic center, in lbs
M _{TR}	Moment about trunion, in lbs
P _M	Pitching-moment, in lbs
P _{Mc}	Console pitching-moment, in lbs
P _{Mo}	Pitching-moment calibration curve abscissa intercept
P _{Mu}	Uncorrected pitching-moment, in lbs
q	Dynamic pressure, lbf/ft ²
q _c	Corrected dynamic pressure, lbf/ft ²
q _u	Uncorrected dynamic pressure, lbf/ft ²
R	Radius of wind tunnel, ft
S	Wing area, in ²
S _a	Model strut frontal area, in ²
S _c	Canard area, in ²
S _t	Tail area, in ²

T	Temp, deg Kelvin
t/c	Airfoil thickness ratio
V	Velocity, ft/sec
V_H	Tail volume
α	Model angle of attack, deg
α_i	Induced angle of attack, deg
α_{oL}	Zero lift angle of attack, deg
α_u	Uncorrected angle of attack, deg
α_{wb}	Wing/body angle of attack, deg
β	Canard incidence, deg
Δ	Canard location
ϵ_{tb}	Total blockage correction factor
ϵ_∞	Zero angle of attack downwash
Λ	Wing sweep
Λ_c	Canard sweep
λ	Taper ratio
T_2	Tail length
μ	Viscosity, slug/ft sec

Abstract

Low speed wind tunnel tests and a boundary layer flow visualization study were conducted in the Air Force Institute of Technology fourteen inch wind tunnel to determine the differences in the aerodynamic characteristics among a forward-swept wing and several forward-swept wing/canard configurations. Both the wing and canard were constructed with an NACA 0006 airfoil section and had quarter chord sweeps of -30 and $+40$ deg, respectively. All tests were conducted at a constant dynamic pressure of 25.6 lbf/ft^2 and a Reynolds number of 1.9×10^5 based on the wing mean aerodynamic chord.

The results show that the changes in the aerodynamic characteristics are dependent upon canard location relative to the wing, canard incidence, and model angle of attack. The largest increases in C_L were observed for the two canard positions above and closest to the wing. A decrease in C_M was noted as the canard location changed vertically from the upper to the lower test positions. An increase in C_D occurred as the canard location approached the wing horizontally.

Comparison of the force and moment data with the flow study photographs suggests that the manner in which the canard wake/vortex system interacts with the airflow over the wing is responsible for the changes in the aerodynamic characteristics of the wing/canard configuration.

A WIND TUNNEL STUDY OF THE EFFECTS OF A
CLOSE-COUPLED CANARD ON THE AERODYNAMIC
CHARACTERISTICS OF A FORWARD-SWEPT WING
IN INCOMPRESSIBLE FLOW

I. Introduction

Objective

The objective of this thesis was to improve the understanding of how a close-coupled canard interacts with a forward-swept wing in the incompressible flow regime.

Background

Until recently, structural limitations have prevented any extensive exploitation of forward-swept wings. Design advantages such as increased fuselage volume and better maneuvering characteristics were offset by the extra structural weight needed to prevent wing failure due to low divergence speed (Refs 6; 12:1). However, recent advances in the field of composite materials have again made forward-swept wings practical as a design concept.

Due to the lack of interest in the development of forward-swept wings, there is a dearth of aerodynamic data on them. In particular, data on thin forward-swept wings ($t/c < .1$) are extremely rare. Such wings were tested by the NACA in the late 1940s. However, much more attention

was given to the then more structurally feasible aft-swept wings (Ref 12:1).

The Vehicle Synthesis Branch (FIMB) of the Air Force Wright Aeronautical Laboratories (AFWAL) expressed an interest in adding to the forward-swept wing data base. Specifically, FIMB was interested in how the aerodynamic characteristics of a forward-swept wing differed from those generated by a close-coupled canard/forward-swept wing configuration.

Canards are lift to trim surfaces. They have been employed as trim devices or as an integral part of the total lifting surface area of a particular configuration. In forward-swept wing design, the canard is usually close-coupled in order to augment aircraft maneuverability in high angle of attack situations (Ref 8:74). A complete knowledge of how a close-coupled canard interacts with a forward-swept wing would permit FIMB to correctly evaluate the performance of any aircraft employing this design concept.

Scope

The items that FIMB is interested in include the variation of C_{LMAX} , $C_{L\alpha}$, $C_{M\alpha}$, C_{Do} , C_L vs C_D , the span-wise lift distribution, and the center of pressure location as a function of canard geometry and location with respect to the forward-swept wing. Table I lists the specific canard geometries and locations of interest. All canard

Table I
Proposed Canard Geometries and Locations

Parameter	Wing	Canard
Sweep Angle	0 to -70 deg	40 to 60 deg
Taper Ratio	0 to .5	.2 to .6
Aspect Ratio	3.0 to 5.5	1.5 to 4.0
Thickness Ratio	.04 to .06	.03 to .045
Relation of Canard to Wing:		
Exposed Canard Area/Total Wing Area		.15 to .30
Exposed Canard Span/Total Wing Span		.15 to .50
Canard Vertical Position/ \bar{c}		0 to ± 1.5
Canard $1/4 c_r$ Horizontal Position from Wing $1/4 c_r/\bar{c}$.8 to ± 1.5

specifications are given in relation to the forward-swept wing.

For this thesis, the problem was confined to the variation of wing/canard lift, drag, and pitching-moment with changes in canard incidence and location. The test models were designed so that a study of how these parameters vary with canard geometry could also be accomplished.

The aerodynamic characteristics were determined for eight forward-swept wing/canard configurations in incompressible flow. In addition, a boundary layer flow visualization study was conducted in order to aid in the analysis of the changes in the aerodynamic characteristics of the wing/canard configurations.

Approach

Wind tunnel tests were conducted with four models. The models and their distinguishing characteristics are listed in Table II.

Table II
Wind Tunnel Models

Model Number	Model Type	Model Configuration	Distinguishing Characteristics
1	Plate Body	Body only	1/8 in steel plate, all mounting holes drilled
2	Wing/body	Wing + body	Model #1 with wings attached
3	Wing/body	Wing + body + canard	Model #2 with canards mounted on same body plate
4	Wing/body	Wing + body + canard	Model #3, except canards mounted on separate body plate

All tests were conducted in the Air Force Institute of Technology (AFIT) fourteen inch wind tunnel. Lift, drag, and pitching-moment were measured with a three-degree-of-freedom, pyramidal balance. Data on all wing/canard configurations were gathered at 2 deg increments in model angle of attack. The angle of attack test range extended from -2 deg to 24 deg or the angle of attack corresponding to the pitching-moment balance limit, whichever occurred first. All data were corrected

for balance inaccuracies and wind tunnel effects, and were reduced to coefficient form. All coefficients were plotted vs corrected model angle of attack in order to show the effect of changes in canard position and incidence on the wing/canard aerodynamic characteristics. After all force and moment runs were completed, the boundary layer flow visualization study was conducted.

II. Wind Tunnel Test Program

Wind Tunnel (Ref 3:16-18)

The AFIT fourteen inch wind tunnel is a closed circuit, single return tunnel powered by a three hundred horsepower electric motor (Fig 1). The wind tunnel has a cylindrical test section 32.5 inches long. The entrance diameter is 13.9 inches and the exit diameter is 14.0 inches. The slight divergence allows for boundary layer growth along the test section walls. The test section is clear plexiglass. The upper half (canopy) is removable in order to provide access to the model and its mounting system.

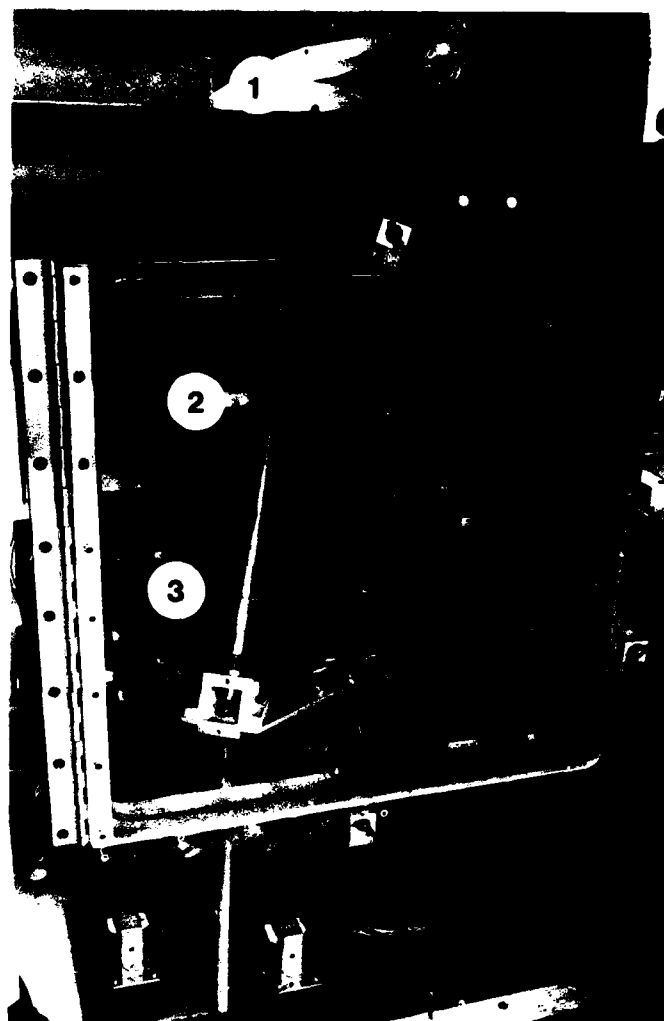
The model mounting system consists of two struts which project through aluminum inserts in the tunnel floor, and attach to the force and moment balance located below.

The tunnel is equipped with a three-degree-of-freedom, null-type, pyramidal balance having automatic beam balance scales (Fig 2). The balance registers lift, drag, dynamic pressure, and pitching-moment. The load capacities and guaranteed accuracies of the balance are shown in Table III.

①



Figure 1. Schematic, AFIT Fourteen Inch Wind Tunnel



1. Model
2. Balance pitching-arm
3. Balance beam assembly

Figure 2. Wind Tunnel Balance

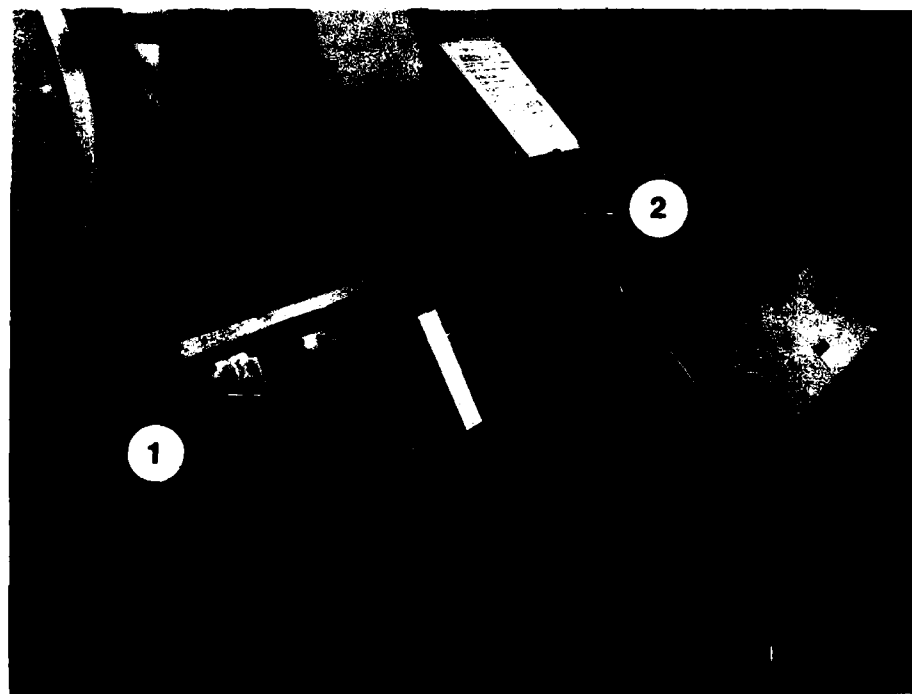
Table III
Wind Tunnel Balance Capacities and Accuracies

Component	Capacity	Guaranteed Accuracy
Lift	+50/-25 lbs	±0.05 lbs
Drag	±10 lbs	±.01 lbs
Pitching-Moment	±17 in lbs	±0.05 in lbs
Dynamic Pressure	500 lbs/ft ²	±.5 lbs/ft ²

All forces and moments are displayed on a console located next to the test section (Fig 3). From the console, the operator can set model angles of attack up to ±45 deg.

Test Models

Three models were built by the AFIT Model Fabrication Division. The first is a body only with all appropriate mounting holes drilled. The second is a wing/body model with the movable canard mounted on the same body plate as the wing. The third is similar to the second with the exception that the canard and wing are mounted on separate body plates. Table II lists four models. These are the configurations tested. All of the different configurations are combinations of the components of the three models actually built. For the remainder of this thesis, however, all references to the test models will be by the model number as listed in Table II.



1. Tunnel Console
2. Tunnel Control Panel

Figure 3. Wind Tunnel Console/Control Panel

Model #1 is a body only configuration (Fig 4). This body type was selected as one that would generate the least amount of airflow interference and still hold the airfoils in the desired position relative to each other. The body width was chosen in order to avoid exposing the canard mounting plates to the tunnel free stream when the canard was mounted in either the upper or lower test positions. The body length was determined by the model mounting system, the placement of the wing, and the locations desired for the canard. Additional mounting holes were provided so that the model could be mounted inverted.



Figure 4. Model #1 with Inclinometer Platform Mounted

Model #2 is composed of a body identical to Model #1 and a forward-swept wing (Fig 5). The wing was cast in epoxy resin, shaped, and glued in place on the model body. Ease of construction and the canard geometric relationships specified by FIMB dictated the wing

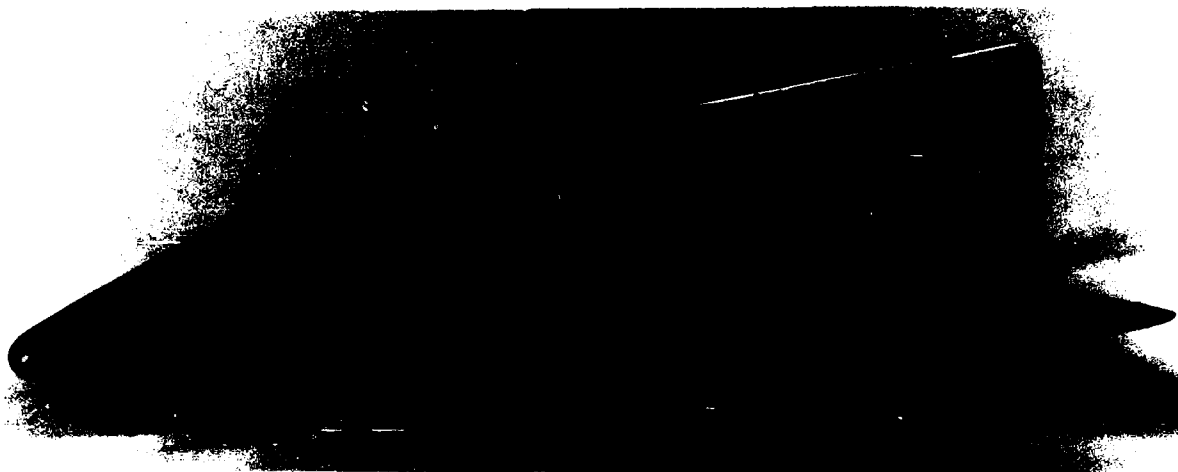


Figure 5. Model #2

geometry. An NACA 0006 airfoil section was selected for the wing for the following reasons: one, it was easy to construct; two, data for it were readily available; and three, inverted testing could be easily accomplished. A wing-span of 10 inches was chosen because this was the largest span that would both fit in the tunnel and avoid direct interaction with the tunnel boundary layer. The -30 deg wing sweep was selected in order to prohibit the canard tips from striking the wing leading edge when the canard was mounted directly in front of the wing. The wing location on the model body was dictated by a desire to generate pitching-moments larger than the noise inherent in the pitching-moment balance.

Model #3 is composed of a forward-swept wing and a canard mounted to a model #1 body plate (Fig 6). Like the wing, the canard was cast in epoxy resin, shaped, and



Figure 6. Model #3

glued in place on its circular brass mounting plates. An NACA 0006 airfoil section was selected for the canard also because a thinner section would have been too difficult to fabricate. The canard mounting plates were designed to facilitate canard installation and enable the adjustment of the canard to any even incidence from -20 deg to $+20$ deg. Located by a small pin at the canard $.5c_r$ point, the brass plates were held in place by four screws which passed through the model body. These screws were secured with four nuts on the opposite side of the model body.

Model #4 is identical to model #3 except that the canard was not attached to the same body plate as the wing.

See Appendix A for more detail on the respective model geometries and planforms.

Model Installation

The mounting system used for all models consisted of two support struts which extended through the tunnel floor and connected to the tunnel balance. The forward

strut (trunion) was rigidly attached to the balance while the rear strut was connected to the balance pitching-arm. This strut was used to alter the model angle of attack (Fig 7).

Models #1, #2, and #3 were mounted to the struts with set screws which were adjusted to avoid unnecessary friction between the struts and the model body. Model #4, however, required the addition of a wind screen in order to properly secure the separate canard body plate. The wind screen also served to maintain the correct canard orientation with respect to the wing. With this mounting system, the wing was effectively isolated from the canard so that the balance measured forces generated only by the wing instead of the wing/canard system.

Test Conditions

All tests were conducted at a constant dynamic pressure of 25.6 lbf/ft^2 . This yielded an average air-speed of 146.67 ft/sec ($M=.135$). This speed was selected not only because it is well within the incompressible range, but also because it permitted running the tunnel motor for long periods of time without undue noise or wear on the equipment. The test Reynolds number based on c_r was 1.9×10^5 .

Test Procedures

Calibration of Equipment. No usable apparatus was available at the start of this experiment to calibrate



Figure 7. Typical Installation for Models #1-#3 (Model #3 Shown)

the lift, drag, and pitching-moment scales of the tunnel balance. Nor was there any standard calibration procedure or record of any previous calibration. A calibration rig was designed and built so that the balance could be calibrated accurately (Fig 8). Also, a general calibration procedure was developed and used to insure a systematic, thorough, and repeatable calibration. Additional equipment required for the calibration included a Meriam Inst Co. 20 inch micro manometer, an inclinometer, a carpenter's square, a plumb bob, and a set of standard laboratory weights.

The tunnel was calibrated by comparing known forces to the console readings for all of the scales. A calibration curve for each balance component was drawn. From these curves, a correction equation for each balance component was derived. The console readings could then be corrected for balance errors and component interactions. For the complete force and moment calibration process and the derivation of the balance correction equations, see Appendix B.

Calibration for Tare and Interference Effects.

Once the tunnel balance had been calibrated, the model tare and interference effects were determined by mounting model #1 in the tunnel and running a complete test cycle. The data from this run were corrected for balance errors and component interactions and were used in the reduction



Figure 8. Calibration Rig and Associated Equipment

of all airfoil data. It was assumed that the interference effects between the body and the airfoils were minimal.

Test Procedures. The original aerodynamic coefficient test program employed four different model configurations. However, only three were actually tested. Model #1 provided the tare and interference data. Model #2 provided the aerodynamic characteristics of the wing alone. Model #3 provided the aerodynamic characteristics of the wing/canard configurations. Model #4 was to provide the effects of the canard on the wing aerodynamic characteristics with the canard not connected to the balance. This model was not tested, however, due to problems that developed in the mechanism designed to change the model angle of attack.

At each of the eight canard test positions, the canard incidence was set to plus and minus 12 deg, plus and minus 6 deg and 0 deg. A complete test run was made for each canard incidence. The location of the test positions relative to the wing root $1/4c$ is listed in Table IV. The positive sense for both the x and y coordinates denotes a position ahead of and above the wing root $1/4c$ point as viewed from the wing trailing edge toward the canard.

After a model was mounted, tape was applied around the balance struts at the tunnel wall and on all other openings to the test section with the exception of the tight fitting canopy. This was done in order to seal the test section as tightly as possible. Then, the

Table IV
Location of Canard $.5c_r$

Position	x location in	y location in
1	3.970	0
2	3.970	.4
3	3.354	.4
4	2.736	.4
5	3.354	0
6	3.970	-.4
7	3.354	-.4
8	2.738	-.4

particular canard incidence for that run was set and tape was applied over the plate mounting screws in order to avoid any flow disturbance over the canard.

Once everything was secure, the canopy was installed and a set of pre-run static readings (wind-off) of all forces and moments was taken for each angle of attack in the test range. Then, the tunnel was started and the dynamic pressure was set at 25.6 lbf/ft^2 . After the tunnel airflow had stabilized, the model angle of attack was checked at 0 deg and the barometric pressure, tunnel temperature, and all forces and moments were recorded. Then, the model angle of attack was varied in two degree increments from -2 to either 24 deg or the angle of attack corresponding to the pitching-moment

balance limit, whichever occurred first. The flow was allowed to stabilize at each test point and all forces and moments were recorded. All test angles were approached from the same direction in order to eliminate hysteresis effects.

Once all forces and moments for all test positions had been recorded, the model angle of attack was reset to 0 deg and repeat points were taken at 4 deg increments.

After all repeat point forces and moments had been recorded, the model angle of attack was reset to 0 deg, the tunnel airflow was stopped, and a set of post-run static readings (wind-off) was taken. These were averaged with the pre-run static readings to provide a zero wind balance reference for the data reduction. Then, the balance was turned off, all necessary changes to the model configuration were made, and the above procedure was repeated for the new configuration.

In order to check the repeatability of the balance, a previous configuration was re-set and re-run after every five configuration changes (five different canard incidences). These data were compared with the original run for that configuration. Also, the inclinometer was used to check a set angle of attack at random intervals. This was done in order to confirm the capability to duplicate any given angle of attack within 3 min of arc.

Boundary Layer Flow Visualization Tests. To avoid undue delay, possible interference with the force and

moment data, and difficulty with photographic coordination, the flow visualization tests were conducted after the force and moment runs were completed.

Mineral oil containing titanium dioxide was used as the fluid medium for the flow study. This liquid was selected because it provided good contrast and clarity when used with an available light source. Also, it was relatively easy to apply. All airfoils were sprayed with a thin coat of non-reflective black paint in order to improve the photographic contrast. All photographs were taken with a 35mm camera located directly above the tunnel test section. Kodak Tri-X black and white film was used.

Prior to the actual flow study, several different wing/canard configurations were painted with the oil mixture and were run at different angles of attack in order to ascertain the best method of fluid application and those angles of attack which best displayed canard/wing interaction phenomena.

By this trial and error method, the model angles of attack of 4 deg and 12 deg were selected and the oil mixture was applied with an artist's camel hair brush. Stripes of the mixture were painted along the .5c of the canard, .75c of the wing directly behind the canard on the wing, and on the .25c of the wing near the tip. These areas were determined to be the best for observing the boundary layer flow characteristics.

During the flow study, the canard incidences set at each test position were identical to those used for the force and moment tests, i.e., at plus and minus 6 and 12 deg and 0 deg. After a particular configuration had been set and painted with the oil mixture, the tunnel canopy was installed, the airflow was started and the proper q was set.

Once the flow pattern had developed fully, the tunnel airflow was stopped, the canopy was removed, proper photographic equipment was set in place, and all necessary photographs were taken.

Data Reduction. All tunnel force and moment measurements were made relative to the balance axis (model wind axis). Upon completion of all the tests, the data were reduced to coefficient form in the following manner. After the average of the pre- and post-run static values had been subtracted from the wind-on data, the forces and moments for model #1 for each angle of attack were subtracted from the data to correct for tare and interference effects. This gave the true airfoil forces and moments uncorrected for either balance irregularities or wind tunnel boundary effects.

The equations developed from the balance calibration were used to determine the values for lift, drag, and pitching-moment about the trunion uncorrected for wind tunnel boundary effects. See Appendix B for the complete listing and development of these equations.

The corrections for wind tunnel boundary effects such as solid and wake blockage, streamline curvature, and downwash were made by using the equations for three-dimensional flow in a circular jet found in Pope and Harper (Ref 12). These equations gave the final values for lift coefficient, drag coefficient, and moment coefficient about the aerodynamic center. The wing area was used as the reference area for all coefficients. The wing mean aerodynamic chord was used for the moment arm in the moment coefficient. See Appendix C for the complete listing of the wind tunnel correction equations and the development of the reduction program.

Once all data had been corrected and reduced to coefficient form, they were plotted vs corrected model angle of attack along with the values for the wing alone. This permitted comparison of the wing/canard configuration data with that obtained for the wing alone. These plots can be found in Appendix D.

After all runs had been plotted, they were reviewed for consistency. All questionable data were identified, checked, re-run in the tunnel, and were reduced in the manner already described. The boundary layer flow visualization study photographs were also reviewed and any questionable results were verified by re-running that particular configuration in the tunnel. The photographs from the flow study can be found in Appendix E.

III. Experimental Results and Analysis,

Model #3

After all the force and moment data had been reduced and plotted, different runs were compared by overlapping two plots and noting changes in curve maxima, minima, slope, and general shape. All curves were compared in two different ways. First, the curves for any given test position were compared to one another in order to identify differences due to change in canard incidence. Second, the curves generated by the same canard incidence at each of the eight canard test positions were compared in order to identify differences due to change in canard location.

Refer to Fig 38 in Appendix D for the location of all canard test positions relative to the wing root quarter chord point. In the following sections, the results for a coefficient are presented first and the analysis for that coefficient follows immediately.

Wing/Canard Configuration Results, C_L

On the C_L vs α curve for the wing alone, a small mound-shaped anomaly appears at the top of the linear range (Fig 39A1L). This anomaly is due to the thin

airfoil, but is absent from the C_L vs α curves obtained from the wing/canard configurations.

The wing/canard configurations generated lift curves that differ from the lift curve for the wing alone in three ways. The first is the shift of an entire wing/canard curve left from the wing alone curve by a specific amount. The second is a wing/canard lift curve slope ($C_{L\alpha wc}$) that is different from the lift curve slope for the wing alone ($C_{L\alpha w}$). The third is the greater C_L generated by the wing/canard configurations than by the wing alone. All these effects are a function of canard location (Δ), canard incidence (β), and model angle of attack (α).

For all the curves at test position 1, the $C_{L\alpha wc}$ is slightly steeper than the $C_{L\alpha w}$. The main effect, however, is a shift of the entire wing/canard lift curve a specific distance to the left of the lift curve for the wing alone. This is true for each value of β (Fig 9).

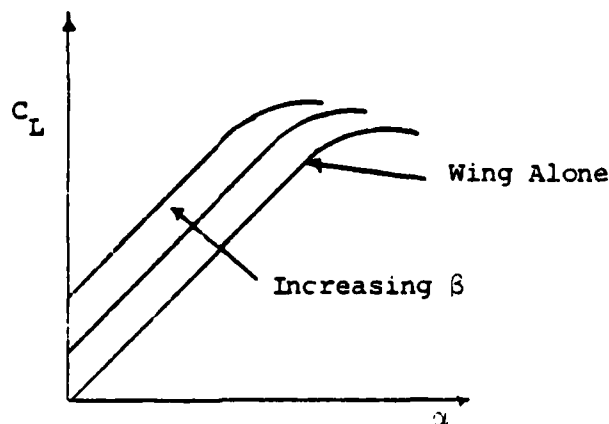


Figure 9. Lift Curve Change, Test Positions 1-3

The larger the β , the larger the left shift. This trend does not hold for $\beta=12$ deg, however. The curve shifts left for this incidence also, but not quite as much as the curve for $\beta=6$ deg. The same phenomena occurs at test positions 2 and 3.

Test positions 4 and 5 present a combination of all observed phenomena. For $\beta \leq 6$ deg, the effect on the wing/canard lift curve is the same as that observed for the first three test positions. However, for $\beta > 6$ deg at position 4, $C_{L\alpha wc}$ decreases to a value between $C_{L\alpha wc}$ for $\beta=0$ deg and $C_{L\alpha w}$ (Fig 10).

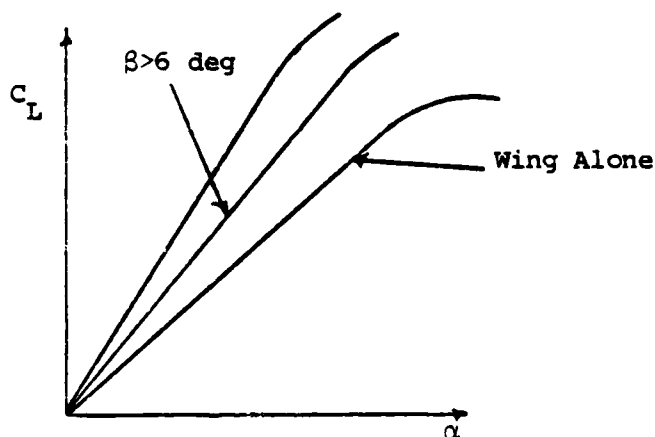


Figure 10. $C_{L\alpha}$ Change for $\beta > 6$ Deg

The same effect occurs at position 5, except that $C_{L\alpha wc}$ continues to decrease as β increases above 6 deg.

For test positions 6, 7, and 8, the main effect of a change in β is a change in $C_{L\alpha wc}$. For $\beta \leq -6$ deg, $C_{L\alpha wc}$ increases. For $\beta > -6$ deg, $C_{L\alpha wc}$ decreases (Fig 11).

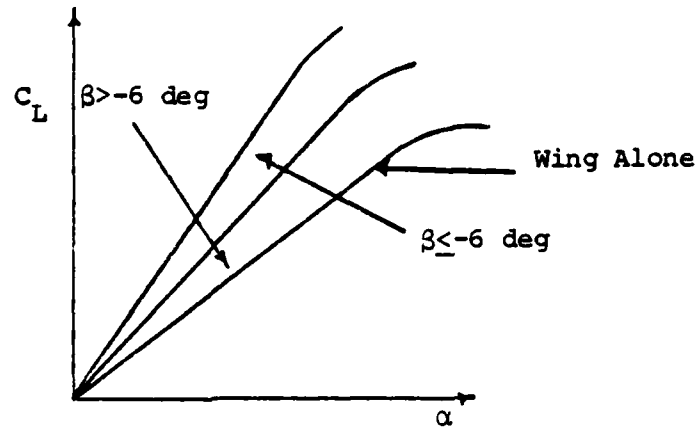


Figure 11. Change in $C_{L\alpha wc}$ for Change in β ,
Test Positions 6-8

Both the left shift of the C_L curve and the change in $C_{L\alpha}$ are also observed with a change in Δ . For a constant β , a horizontal change in Δ causes a shift of the wing/canard lift curve to the left of the lift curve for the wing alone (Fig 12).

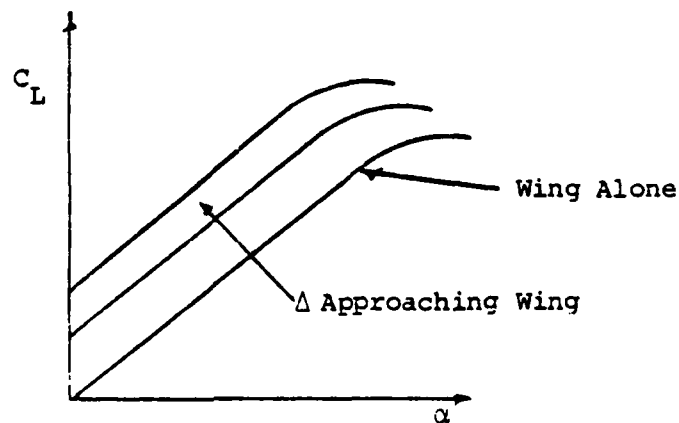


Figure 12. C_L vs α Shift for Horizontal Δ Change,
Test Positions 1-5

This is true for all test positions except 6, 7, and 8. For these three positions, the general trend is a decrease in $C_{L\alpha wc}$ for a horizontal change in Δ (Fig 13).

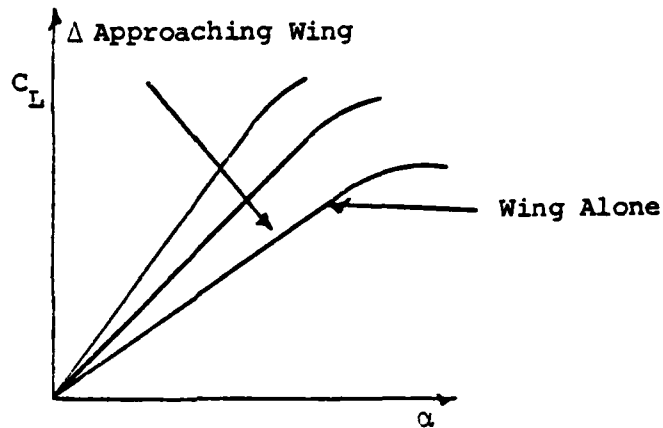


Figure 13. $C_{L\alpha}$ Change for Horizontal Δ Change, Test Positions 6-8

There is one exception to this last trend. For $\beta=12$ deg, $C_{L\alpha}$ increases as Δ changes from test position 7 to test position 8.

For a constant β , a vertical change in Δ from an upper test position toward a lower test position produces a decrease in $C_{L\alpha}$ (Fig 14).

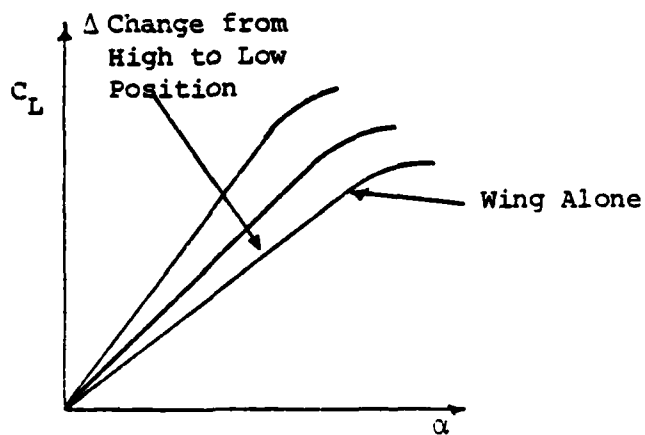


Figure 14. $C_{L\alpha}$ Change for Vertical Δ Change

The configuration with the largest $C_{L\alpha}$ has the canard in test position 3 with $\beta=6$ deg. The configuration

with the smallest $C_{L\alpha}$ has the canard in test position 7 with $\beta=12$ deg. The maximum C_L generated by the wing/canard combination is always greater than that generated by the wing alone.

Wing/Canard Configuration Analysis, C_L

The results obtained from model #3 give evidence of several phenomena all interacting at the same time. Since the data taken were of the entire wing/canard system together, it is difficult to ascribe any particular curve change to a specific physical phenomena associated with a lifting surface. The best that can be done here is to identify the phenomena which are most likely to be responsible for causing a particular result. Further investigation is required to determine if the following are indeed responsible for the results seen in the force and moment data and flow study photographs.

The anomaly seen near the top of the linear region of the data curve for the wing alone can be explained by a detachment of the airflow at the wing leading edge and a subsequent re-attachment of the flow to the wing at a point not too far downstream. This phenomena, common to thin airfoils with sharp leading edges at low Reynolds numbers, changes the potential flow around the airfoil in a manner equivalent to increasing the airfoil leading edge radius (Ref 11). This induced change in airfoil camber appears in a lift coefficient greater than that

expected for the particular airfoil. As α increases, the flow completely detaches from the wing and the lift coefficient obtained reflects the flow about the airfoil.

When present, the canard changes the airflow over the wing to such an extent that the flow doesn't detach over a large part of the leading edge. As a result, the anomaly doesn't appear on the C_L vs α curves for the wing/canard configurations.

The airflow coming from the canard is made up of two parts. One part is the wake that is formed behind any solid body placed in a stream of fluid. The velocities in the wake are smaller than those in the main stream. The losses in velocity in the wake amount to a loss of momentum which is due to the drag on the body. The spread of the wake increases as the distance from the body is increased. As this happens, the differences between the velocity in the wake and that outside become smaller (Ref 14:730) (Fig 15).

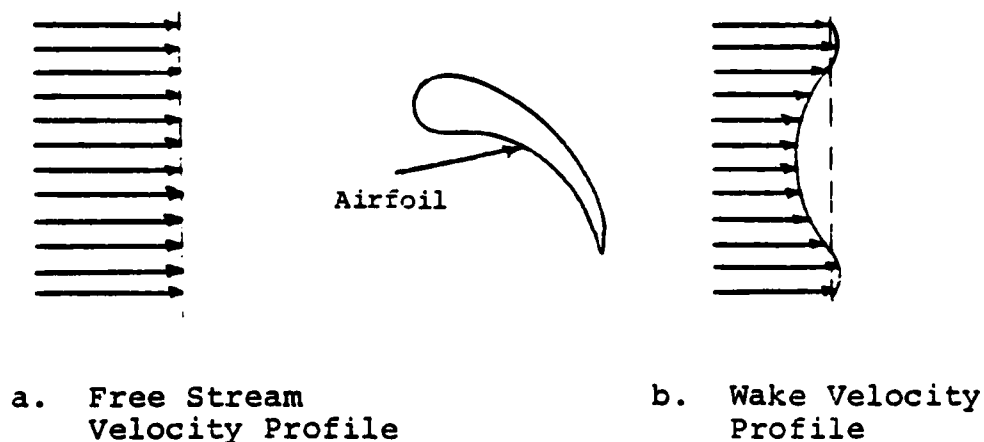


Figure 15. Velocity Changes in a Wake

The other part of the canard airflow is a vortex system. Every lifting body has a vortex pattern which exists as a vortex sheet behind it. This sheet rolls up into two concentrated vortices commonly called tip vortices. These vortices follow the general streamline pattern about the airfoil and their strength is determined by how much lift is being generated (Refs 9:Chap 6; 11).

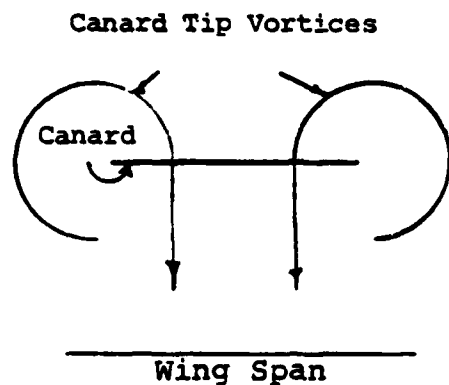
For the close-coupled canard configuration, the changes observed in the configuration lift curves can be explained by the interaction of the canard wake/vortex system with the flow over the forward-swept wing.

The changes in $C_{L\alpha}$ noted in the C_L results section can be explained by how much the flow over the wing is altered by the canard tip vortices. Etkin states (Ref 6:23-24)

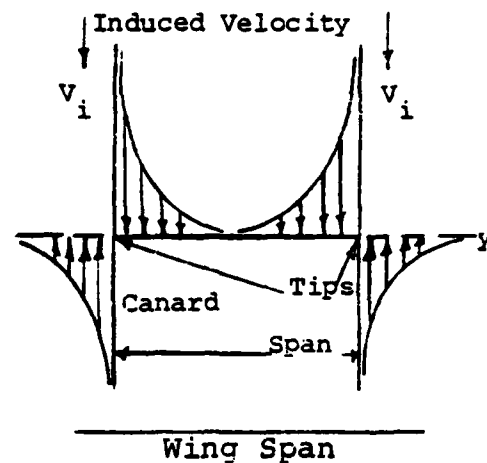
$$C_{L\alpha} = \frac{\partial C_L}{\partial \alpha} = a_{wb} \left[1 + \frac{a_t}{a_{wb}} \frac{S_t}{S} \left(1 - \frac{\partial \epsilon}{\partial \alpha} \right) \right] \quad (1)$$

This equation expresses the slope of the lift curve as a function of the wing downwash $\left(\frac{\partial \epsilon}{\partial \alpha} \right)$. The canard tip vortices can change the value of the wing downwash by changing the wing induced angle of attack (α_i) .

As Fig 16 shows, the velocities induced on the wing can change from mid-span to tip as a function of the spanwise location of the canard tip vortices. The strength of the tip vortices is a function of how much lift is being developed by the canard. Also, the vortices will



a. Canard Tip Vortices
Viewed From Wing
Trailing Edge



b. Velocities Induced
by Canard Tip
Vortices

Figure 16. Canard/Wing Vortex Interaction

follow the streamlines about the body. Therefore, the most change in $C_{L\alpha}$ occurs when the canard develops a large lift and the canard tips position the canard tip vortices so that they follow streamlines close to the wing upper surface (Fig 17).

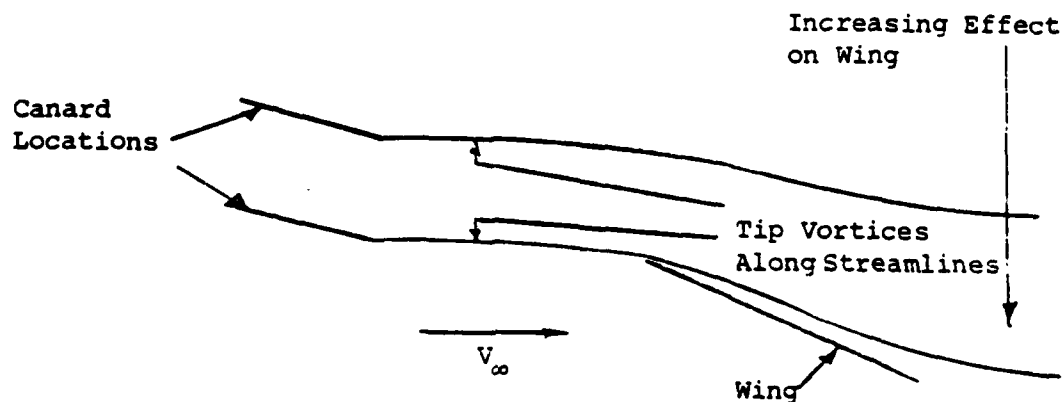


Figure 17. Effect of Canard Tip Vortices
on Wing Airflow

The shift of an entire lift curve to the left relative to the lift curve for the wing alone can be explained as follows. Etkin states (Ref 6:23-24)

$$\alpha_{OL} = \alpha_{wb} - \frac{a_t}{a} \frac{S_t}{S} (\epsilon_o + i_t) \quad (2)$$

This equation expresses the angle of zero lift as a function of the incidence angle of the tail (i_t). Since the tail in this case is the canard, an increase in β would decrease the α_{OL} ($\beta = i_t$). As α_{OL} decreases, the entire lift curve would shift to the left. As noted, this trend continues for $\beta \leq 6$ deg. That the same trend did not extend to $\beta = 12$ deg can be explained as follows. The canard wake for this β would be nearly as wide as the canard frontal area. If the wing is situated somewhere in this area of reduced velocity, less lift would be developed due to the decrease in q . Such three-dimensional effects are not allowed for in Etkin's equation (Fig 18).

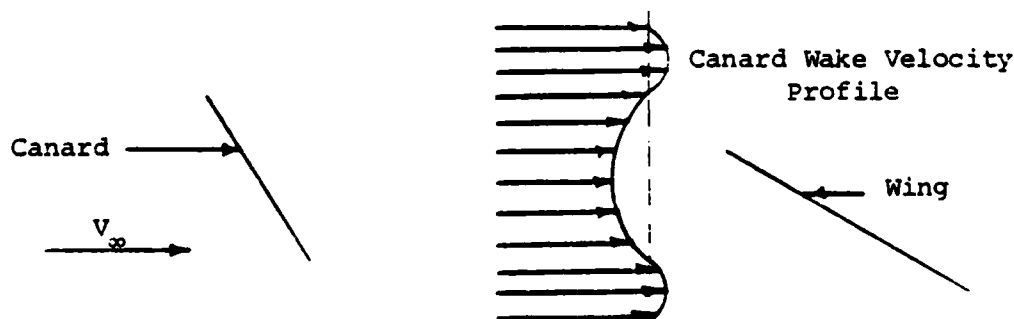


Figure 18. Effect of Canard Wake on Wing Airflow

This entire analysis is supported by the boundary layer flow visualization study. The photographs in Figs 40A9a, 40A10a, 40A14a, 40A15a, 40A18a through 40A20a, and 40A23a through 40A25a show the progressive development of symmetric indentations behind the canard tips. Each indentation can be interpreted as the increasing influence of a tip vortex core on the upper surface of the wing. That this core exists was verified by Oseen in 1911 (Ref 14:89-90). That it influences the flow over the upper surface of the wing has been verified in water tunnel studies conducted at the Wright Aeronautical Laboratories (Ref 2). A computer simulation of the wake/vortex system behind the canard of a similar wing/canard configuration done at the Air Force Academy Frank J. Seiler Laboratory also verifies the influence of the tip vortex core (Ref 7). In all these experiments, the canard tips were in a position close to and above the surface of the wing.

These symmetric indentations are absent from the photographs in which the canard tips are farther away from the wing upper surface (Figs 40A6b through 40A8b for example). If β is held constant and the photographs for a vertical change in Δ are examined, the indentations disappear as the Δ changes from above to below the wing. These two trends indicate that the influence of the vortices on the wing upper surface is a function of the proximity of the canard tips to that surface.

At higher α , the effects of the velocities induced by the canard tip vortices are much more noticeable. All the photographs of the wing/canard configurations at $\alpha=12$ deg exhibit two distinct characteristics. First, different amounts of wing area near the root show flow patterns unlike those outboard of the canard tips. Second, the movement of flow spanwise and toward the wing leading edge occurs at a point closer to the wing tip than on the wing alone (Figs 40A1b through 40A25b).

The flow patterns in the affected wing root areas resemble the patterns generated by the wing alone at $\alpha=4$ deg (Fig 40A0a). This indicates that the wing root is at a lower effective α and is still flying. If the canard tip vortices are inducing a downwash in this area, then the induced angle of attack (α_i) for the wing root would be greater than that of the rest of the wing. As a result, the wing root sees the free stream velocity at a lower effective α . This would explain the formation of flow patterns similar to those formed by the wing alone at a lower α . Outboard of the canard tips, the vortices would produce an upwash. The α_i would be smaller than that for the rest of the wing. As a result, this area of the wing stalls prematurely. This explains the appearance in these areas of patterns that resemble those of the wing alone at high α (Fig 40A0b).

Taken together, these phenomena indicate that an aerodynamic twist has been induced in the wing by the presence of the canard in the flow (Ref 11).

The increase in C_{LMAX} can also be explained by the interaction of the canard wake/vortex system. The particular α , β , and Δ involved for a given configuration dictate how much lift is being produced by the canard, how close the tip vortices will be to the wing upper surface, and the location of the wing in the canard wake. All of these factors could combine to increase the wing downwash and as a result, the total lift. Other work has indicated that the C_L would increase due to the presence of the canard in all flight regimes dependent upon α , β , and Δ (Refs 4; 5; 10).

Wing/Canard Configuration Results, C_D

The C_D curves for the wing/canard configurations differ from the C_D curve for the wing alone in two ways. First, the wing/canard C_D either increases or decreases relative to the C_D for the wing alone. Second, the wing/canard C_D curve shifts to the left relative to the C_D curve for the wing alone.

For any canard test position, as β increases, the wing/canard C_D increases at both extremes of α (Fig 19).

The exception to this trend at all test positions is a decrease in wing/canard C_D in the low α range from the value of $\beta = -12$ deg to that for $\beta = -6$ deg.

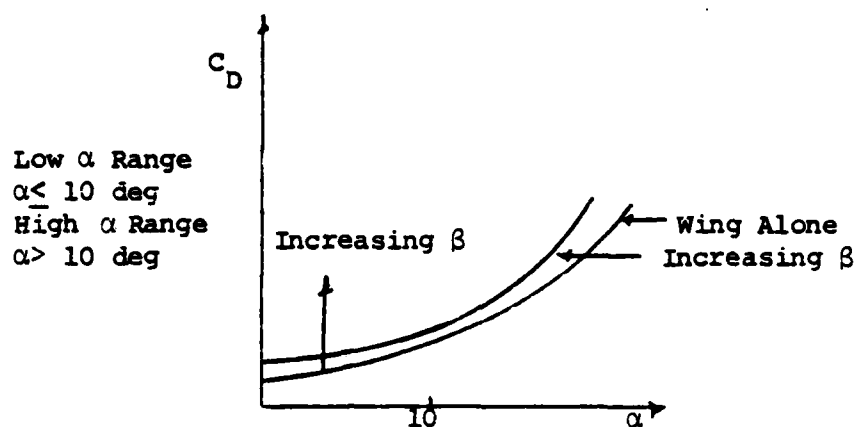


Figure 19. C_D Curve Change Due to a Change in β

As the Δ approaches the wing horizontally on or above the model centerline, the wing/canard C_D either doesn't change or decreases slightly in the low α range. In the high α range, the wing/canard C_D either doesn't change or increases slightly (Fig 20).

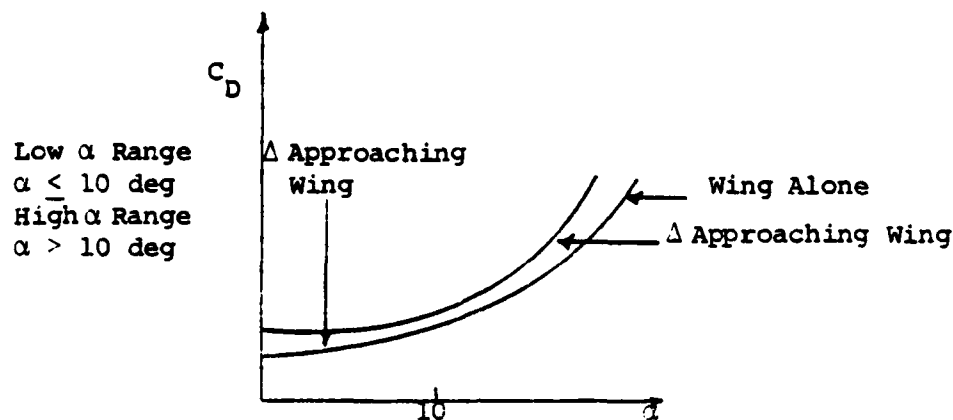
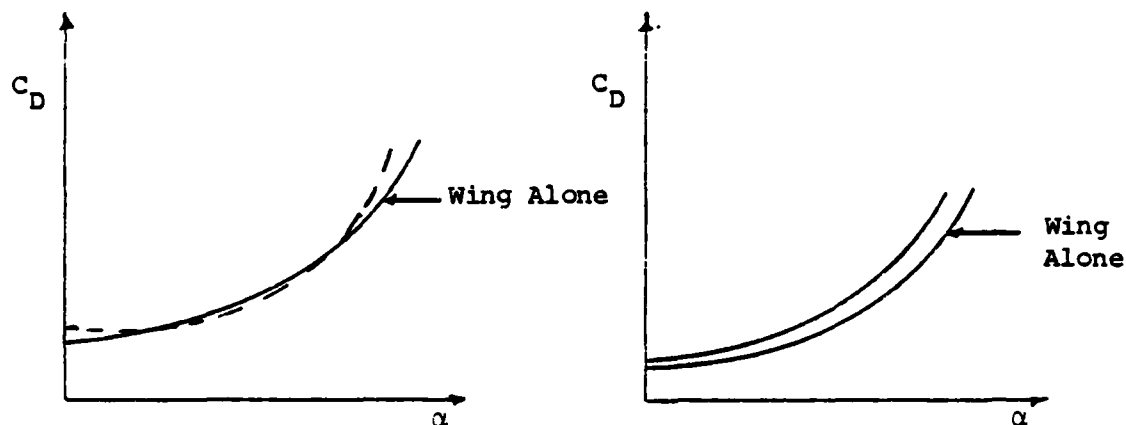


Figure 20. C_D Change for a Horizontal Change in Δ , Test Positions 1-5

Two trends in the wing/canard C_D curve movement result from a horizontal change in Δ toward the wing in test positions 6, 7, and 8. The first is a decrease in

the wing/canard C_D to a value equal to or less than that for the wing alone in the low α range. This occurs when $\beta \leq 0$ deg. The second is a shift of the wing/canard C_D curve a constant distance to the left of the C_D curve for the wing alone. This occurs when $\beta = 12$ deg (Fig 21).



a. C_D Decrease $\beta \leq 0$ deg

b. C_D Shift $\beta = 12$ deg

Figure 21. C_D Change for a Horizontal Change in Δ

The only exceptions to these last trends occur at test positions 7 and 8. At both of these positions, a constant left shift occurs when $\beta = 6$ deg also.

As the Δ changes vertically from the higher to the lower test positions, the general trend is a decrease in C_D toward the wing only data in the high α range, and a slight increase in C_D relative to the wing only data in the low α range (Fig 22).

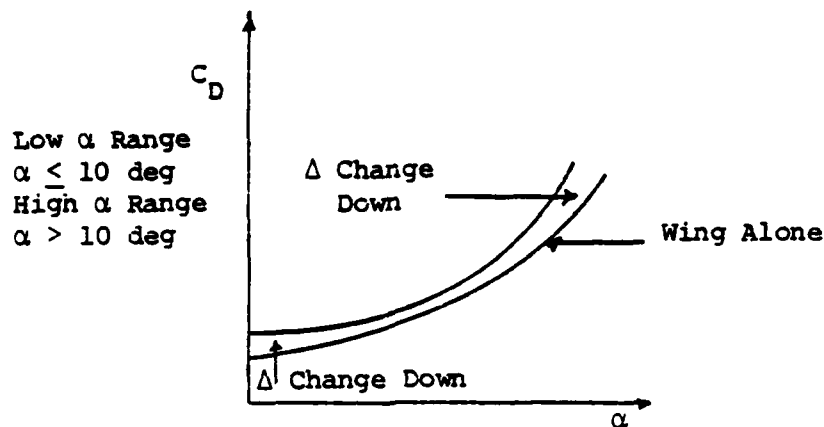


Figure 22. C_D Change with Vertical Change in Δ From a High to a Low Canard Test Position

Wing/Canard Configuration Analysis, C_D

The changes in the wing/canard C_D curves relative to the C_D curve for the wing alone can be explained by the phenomena discussed in the C_L analysis. The shifts in the C_D curves are dependent upon α , β , and Δ . As already discussed, these variables can directly affect how much the canard wake/vortex system interacts with the airflow over the wing. If more lift is produced by this interaction, the induced drag produced by the wing increases. Any increase in wing induced drag plus any induced drag produced by the canard would be responsible for the changes in the wing/canard C_D curves.

The photographs in Appendix E support this. They clearly show different amounts of the wing root area being affected by the canard airflow as α , β , and Δ change. As discussed, this induces various amounts of aerodynamic twist into the configuration. A consequence of this is a

change in the wing span-wise load distribution. This would result in a change in the wing induced drag. Similar effects have been noted in the study of canard interaction with aft-swept wings (Ref 10).

Wing/Canard Configuration Results, C_M

The C_M curves for the wing/canard configurations differ from the C_M curve for the wing alone in two ways. The first is a shift of the wing/canard C_M curve up relative to the C_M curve for the wing alone. This occurs as β increases (Fig 23).

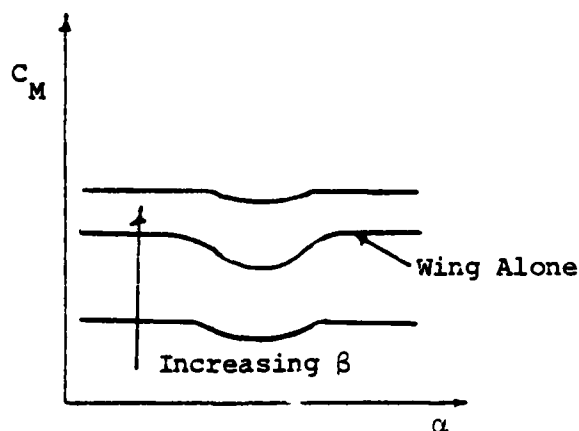


Figure 23. C_M Curve Shift with Increasing β

The second is the appearance of either a positive or negative data spike somewhere along the C_M curve for some of the wing/canard configurations (Fig 24).

The main effect of an increase in β at any test position is the wing/canard curve shift already discussed. As the Δ changes toward the wing horizontally from test position 2 to test position 4, no C_M curve shift occurs

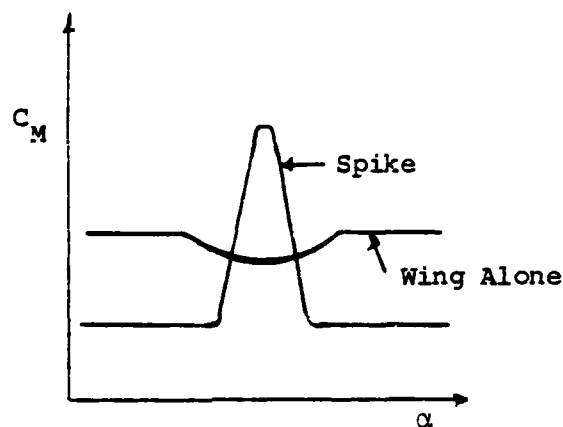


Figure 24. Data Spike on Wing/Canard C_M Curve

if $\beta < 6$ deg. If $\beta \geq 6$ deg, the wing/canard C_M curve shifts up relative to the C_M curve for the wing alone. This upward shift occurs as the Δ changes toward the wing horizontally for all β in all the other test positions.

As the Δ changes position vertically from a high to a low test position, the general trend is a downward shift of the wing/canard C_M curve relative to the C_M curve for the wing alone (Fig 25).

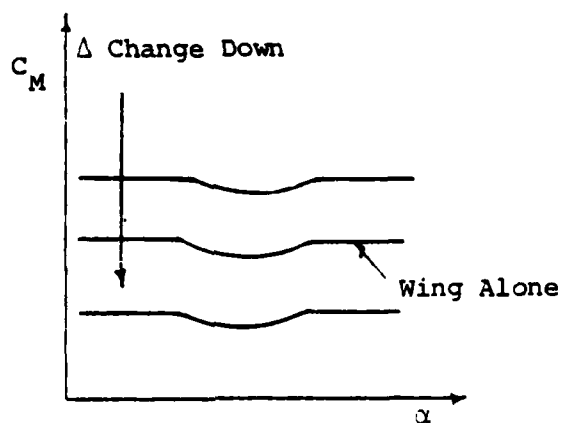


Figure 25. C_M Curve Shift for a Change in Δ From a High to a Low Test Position

Wing/Canard Configuration Analysis, C_M

The changes in the wing/canard C_M curves relative to the C_M curve for the wing alone can be explained by two different phenomena. The first is a characteristic inherent in the wind tunnel balance. The second is the same canard wake/vortex system responsible for the changes in the other coefficients.

The spikes noted in some of the wing/canard data can be explained by the characteristic inherent in the tunnel balance. Being a null-type balance, a small carriage is moved back and forth along the balance beam by a screw mechanism until the beam is positioned properly for a reading. The proper position is determined by a photo-cell which is activated by a light shining through a slot in one end of the beam. There is no colimator on the balance so once the light trips the photo-cell, the balance beam stops moving. Friction in the screw mechanism can cause the balance beam to stop with the light beam located either at the top, bottom, or middle of the slot. In any case, the balance still gives a reading. As the moment changes algebraic sign, this effect is most frequently observed and likely to occur (Ref 11). The random nature of the spikes seems to support this as their cause.

The shifts in the moment curves can be explained by the interaction of the canard wake/vortex system with the airflow over the wing. Etkin states (Ref 6:24)

$$C_{MAC} = C_{MACwb} + a_t V_H (\epsilon_o + i_t) \left[1 - \frac{a_t}{a} \frac{S_t}{S} \left(1 - \frac{\partial \epsilon}{\partial \alpha} \right) \right] \quad (3)$$

This equation expresses the C_{MAC} for a configuration as a function of the incidence angle of the tail (i_t) and the wing downwash ($\frac{\partial \epsilon}{\partial \alpha}$). The upward shifts of the wing/canard C_M with increasing β can be explained by an increase in the term $(\epsilon_o + i_t)$. The magnitude of this term increases as β increases ($\beta = i_t$). The changes in the wing/canard C_M curves due to a change in Δ are readily explained when it is remembered that the downwash of the wing can be affected by the location of the canard. For example, if the canard tip vortices are close to the wing upper surface the downwash of the wing root area would increase and the C_M would increase as a result.

Also affecting the total moment generated by any wing/canard configuration is the amount of lift being produced by the canard. Since the canard is always in front of the configuration aerodynamic center, any lift produced by it would produce a moment opposite to that of the wing. This would decrease the total moment about the aerodynamic center. The C_M for that configuration would also decrease as a result. It is the sum of these effects caused by the canard wake/vortex system that determines the amount the wing/canard C_M curve changes relative to the C_M curve for the wing alone.

General Comments, Swept Wings

Aft-swept wings have been mentioned from time to time in the discussion so far. These wings have been extensively tested and their characteristics are well known. The difference between the two types, aft and forward-swept wings, under the influence of a canard or close-coupled canard is not as widely known. Basically, the difference lies in how the stalling mechanism for each type is affected by the canard wake/vortex system. For the aft-swept wing, a canard improves the stalling characteristics by delaying the progression of the stall inboard from the tips as α is increased. For the forward-swept wing, however, the stall is prevented by the wake/vortex system from the canard changing the flow characteristics and the span-wise load distribution of the wing (Ref 4).

IV. Experimental Results and Analysis,

Model #4

No data were obtained from model #4. Although constructed as specified and installed correctly with all working parts, the solenoids used to separate the canard from the wing were found to be too weak. To correct this problem will require an extensive re-design of the solenoid mechanism.

Model Analysis

The solenoid mechanism for model #4 was designed so that the tunnel operator could change the α of both the wing and canard mounting plates simultaneously from the tunnel console. The solenoid problem was discovered after the model was mounted on the tunnel balance. Since the solenoids are too weak to correctly position the canard plate lockout pins, larger solenoids may prove to be the answer. However, larger solenoids would further obstruct the airflow in the tunnel, present more difficult mounting and alignment problems than the present design, and would necessarily have to be custom made or procured.

A more practical approach may be to design a mechanism which would be mounted beneath the tunnel in the tunnel balance box. This mechanism would activate

the existing model linkage by a rod projecting through a convenient opening in the tunnel floor. The correct alignment of the canard plate with the rest of the model body could be determined by a micro-switch set to trip a light at the tunnel console.

V. Conclusions and Recommendations

Conclusions

1. The aerodynamic characteristics of the forward swept wing/canard configuration change with and are a function of the model angle of attack, the canard position and canard incidence.

2. The changes in the aerodynamic characteristics of the wing/canard configuration can be explained by considering the location of the canard wake/vortex system relative to the upper surface of the wing. The more this system interacts with the airflow over the wing upper surface, the greater the change in the aerodynamic characteristics will be.

Recommendations

1. Complete the re-design of model #4 and conduct a series of wind tunnel tests similar to those in this thesis in order to compare the aerodynamic coefficients of the wing influenced by the canard to those of the wing alone.

2. Perform a study employing either a rake survey, a vortex meter, a hot wire anemometer, or a combination of all three in order to determine the nature of the canard wake/vortex system and how it interacts with the flow over the forward-swept wing.

3. Conduct water tunnel studies with similar wing/canard configurations mounted to the tunnel wall in order to qualitatively determine how the canard wake/vortex system interacts with the flow over the forward-swept wing.

4. Conduct wind tunnel tests with different canard geometries in order to discover what kind of effect they would have on the aerodynamic characteristics of the wing/canard combination and the wing alone with the canard mounted on a separate plate.

Bibliography

1. Abbott, I. H. and A. E. Von Doenhoff. Theory of Wing Sections. New York: Dover Publications, Inc., 1959.
2. Andersen, David, Engineer, AFWAL/FIMM. Personal interview, Wright Patterson AFB, Ohio, September 27, 1982.
3. Bluford, Guion S. An Experimental Investigation of Aerodynamic Forces and Moments on Several Wing/Canard Configurations. MS Thesis, Wright-Patterson AFB, Ohio: Air Force Institute of Technology, December 1981.
4. Boucheron O. and Y. Brocard. Comparison of Aerodynamic Characteristics of Aircraft Models with Forward and After Swept Wings at Mach Number 0.5. 92320 Chatillon, France: Office National D'Etudes et de Recherches Aerospatiales (ONERA), March, 1982.
5. De Meis, Richard. "Forward Swept Wings Add Supersonic Zipp," High Technology, 2:33-40 (January/February, 1982).
6. Etkin, Bernard. Dynamics of Flight Stability and Control. New York: John Wiley & Sons, Inc., 1959.
7. Griffin, Kenneth E. "Experimental Documentation of the Lifting Surface Wakes of a Canard and Forward Swept Wing Configuration," Air Force Academy Aeronautics Digest, Fall/Winter, 1981, 8:2-31 (June, 1982).
8. Kocivar, Ben. "Wrong Way Wings and Maneuverability of Supersonic Planes," Popular Science, 72-75 (April, 1980).
9. Kuethe, Arnold M. and Chuen-Yen Chow. Foundations of Aerodynamics. New York: John Wiley & Sons, Inc., 1976.
10. Lacey, David W. Aerodynamic Characteristics of the Close-Coupled Canard as Applied to Low-to-Moderate Swept Wings Volume 1: General Trends. U.S. Navy Report on Canard Research, Bethesda, Maryland: David W. Taylor Naval Ship Research and Development Center, January 1979.

11. Larsen, Marold C., Head, Aero Design Center, AFIT/ENF. Personal interview, Wright-Patterson AFB, Ohio, 1982.
12. Pope, Alan and John J. Harper. Low Speed Wind Tunnel Testing. New York: John Wiley & Sons, Inc., 1966.
13. Savage, Paul W. Experimental Analysis of the Effects of Sweep and Aspect Ratio on Incompressible Flow About Forward Swept Wings. MS Thesis, Wright-Patterson AFB, Ohio: Air Force Institute of Technology, December, 1981.
14. Schlichting, Hermann. Boundary Layer Theory. 7th ed. New York: McGraw-Hill, 1979.

Appendix A
Model Geometry

All model bodies and wing sections have the same basic dimensions as model #3. The difference between the models is either the addition or deletion of particular assemblies as needed. For example, model #1 is just model #3 without the wings and canard assembly attached. So, the dimensions and geometry for that model are identical to those for model #3 without the airfoils. The same concept can be applied to the other models.

Table V
Model #3 Data and Dimensions

	Wing	Canard
c_t	1.454 in	.795 in
c_r	3.4914 in	2.088 in
\bar{c}	2.612 in	1.540 in
b	10 in	2.94 in
λ	.42	.38
S	24.727 in ²	4.230 in ²
AR	4.04	2.04
Λ	-30 deg	40 deg
Body Length	12.373 in	
Body Width	2.756 in	
Body Plate Thickness	.125 in	
Body Material	Steel	

Permits inverted testing and tare measurement

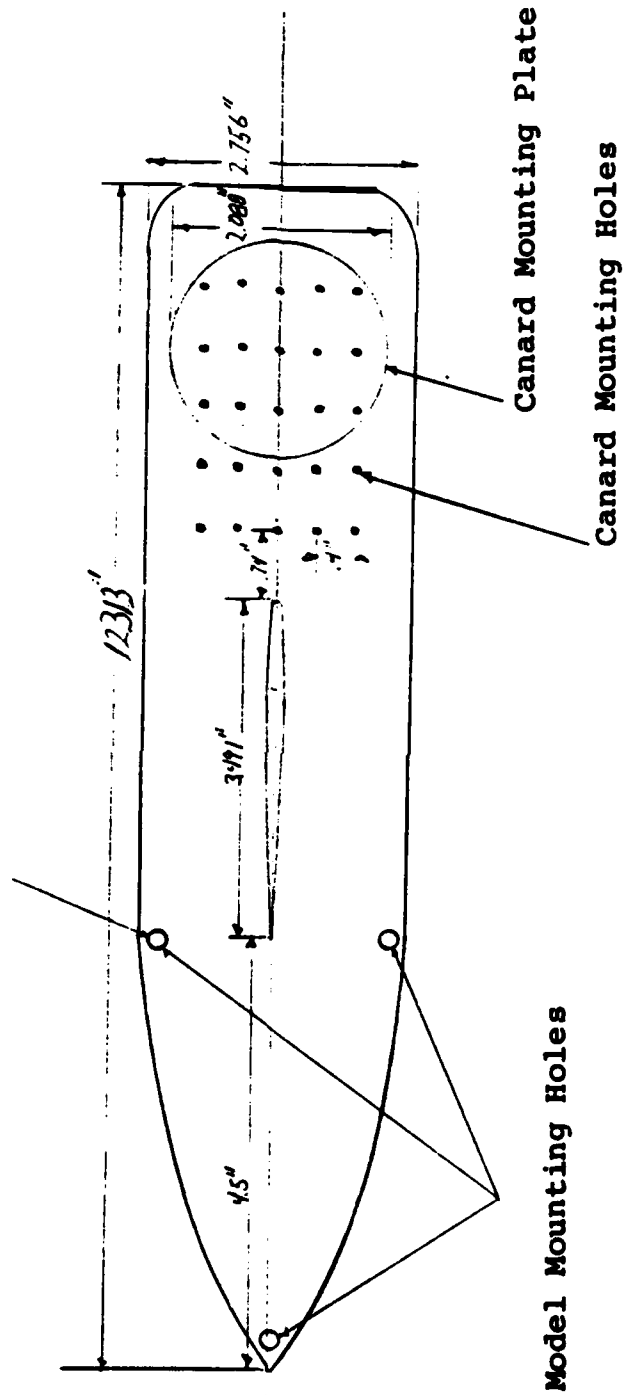


Figure 26. Model #3 Schematic Side View

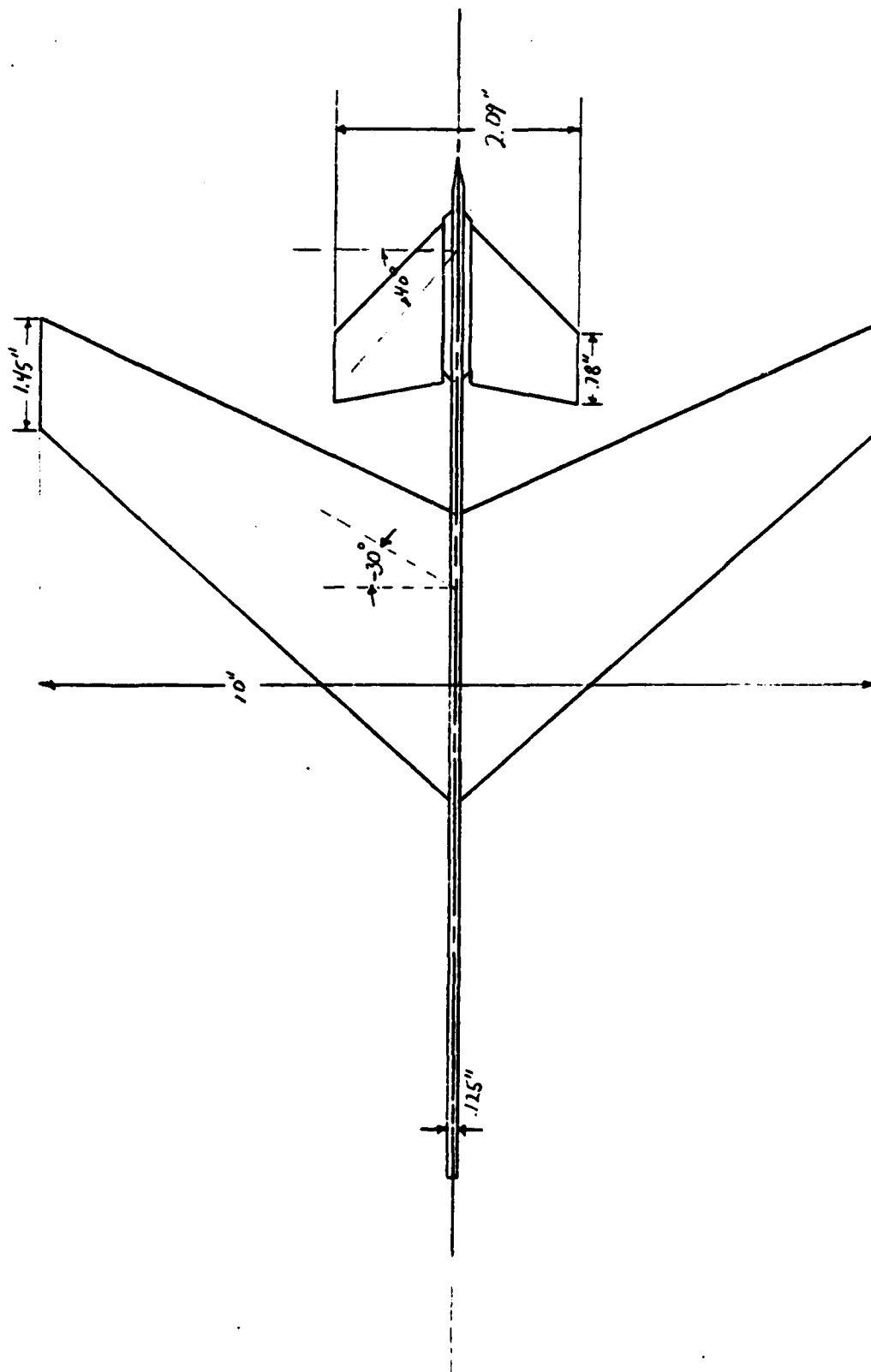


Figure 27. Model #3 Schematic Plan View

Appendix B
Wind Tunnel Calibration

Calibration Procedure

In order to obtain balance readings that were as close as possible to the actual forces applied, after each load was added to the calibration rig the entire assembly was vibrated with the motor mounted on top. This eliminated bearing friction effects. Two readings for each calibration point were taken, one when the force or moment being calibrated was increased and one when that force or moment was decreased. Once all forces, both known and indicated, had been recorded, the data was plotted and the equation for the resulting curve was derived from the plot.

The tunnel dynamic pressure was calibrated by comparing console readings with the dynamic pressure measured in the tunnel by a Meriam Inst Co. 20 in micro-manometer (tunnel total pressure minus static pressure). The tunnel was run over a dynamic pressure range from 0 to 64.43 lbf/ft². This range was at least double that expected in the experiment and provided a good calibration curve (Fig 28). The slope of this curve was used to set the console q guage as a backup for the 20 in micro manometer. The manometer was used to maintain a constant q of 25.6 lbf/ft² during all data and flow study runs.

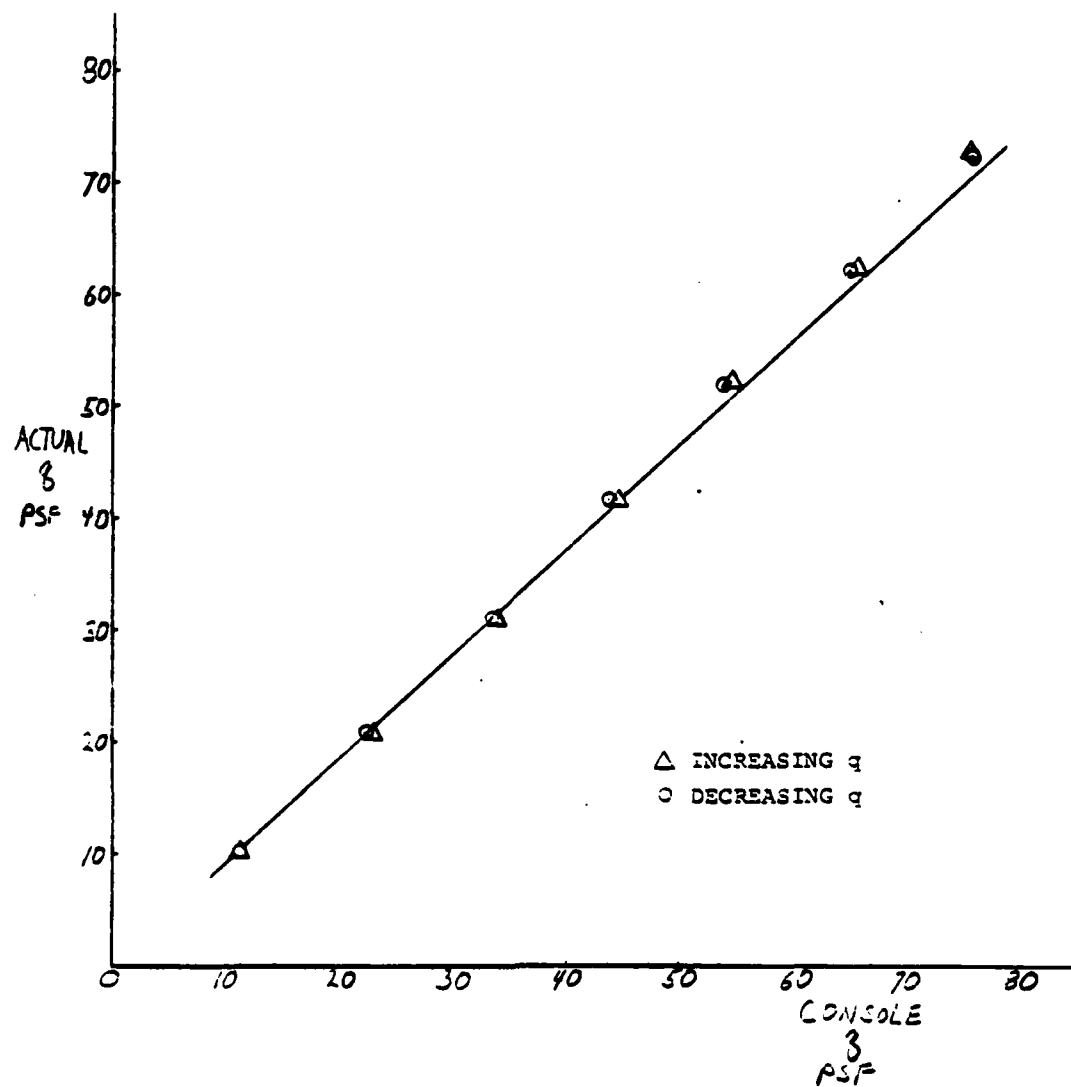


Figure 28. Dynamic Pressure Calibration Curve

For the lift calibration, a calibration rig vernier was adjusted with the aid of a plumb bob so that all forces were applied along a line through the trunion and perpendicular to the tunnel centerline. Known standard laboratory weights were then applied (Fig 29) and all forces recorded. The curve plotted from this calibration yielded part of the total lift correction for the balance (Fig 30). The remainder came from a contribution due to pitching-moment as determined by the interaction calibration.

The drag calibration was performed by adjusting a calibration rig vernier so that force was applied to the trunion parallel to the tunnel centerline (Fig 31). The curve plotted from this calibration yielded the total drag correction for the balance (Fig 32).

The pitching-moment calibration was performed with the calibration rig and model #1. The distance from the trunion to the first row of holes from the front of the model was determined from the model design plans. A calibration rig vernier was adjusted with a plumb bob so that all forces were applied at these holes perpendicular to the tunnel centerline (Fig 33). The curve plotted from this calibration yielded only part of the total pitching-moment correction (Fig 34). The rest came from contributions due to changes in lift, drag, and angle of attack as determined by the interaction calibration.

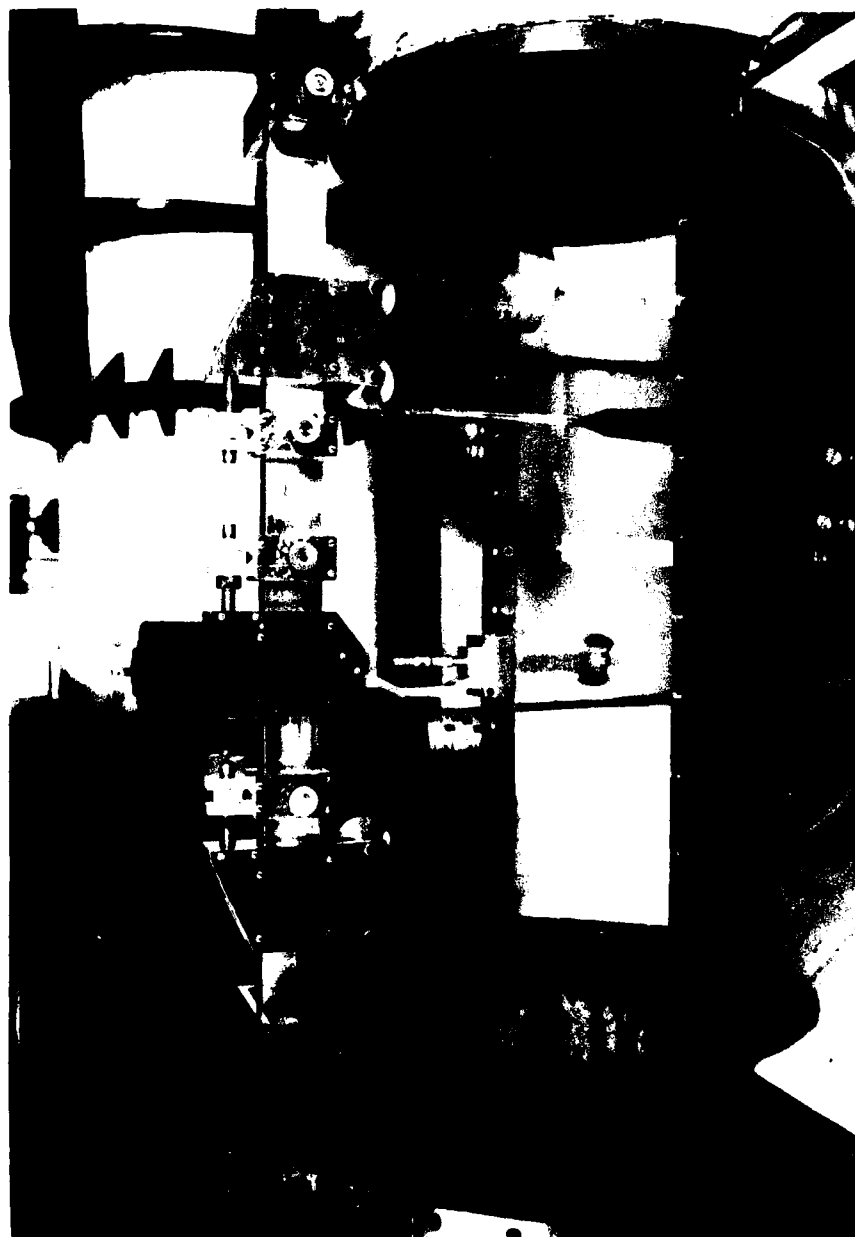


Figure 29. Lift Calibration

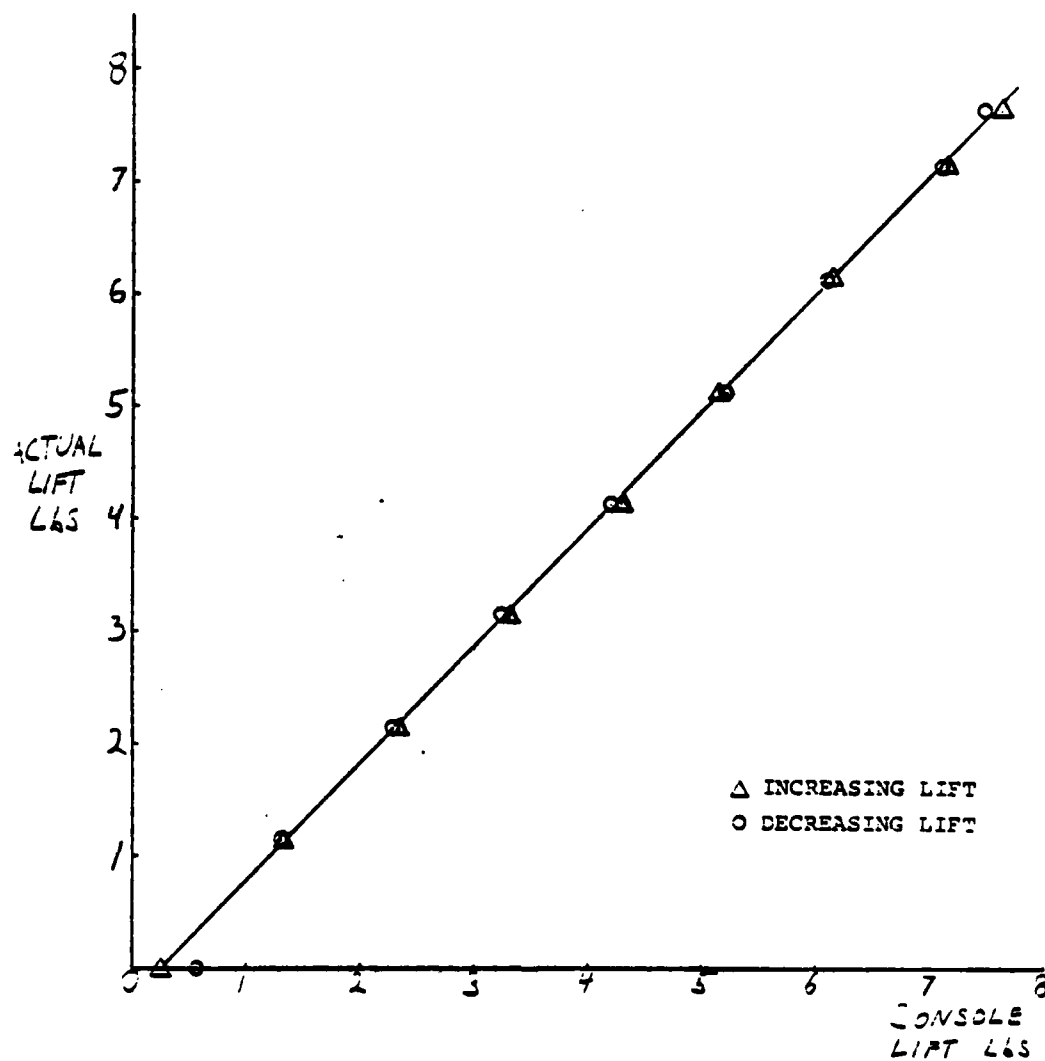


Figure 30. Lift Calibration Curve

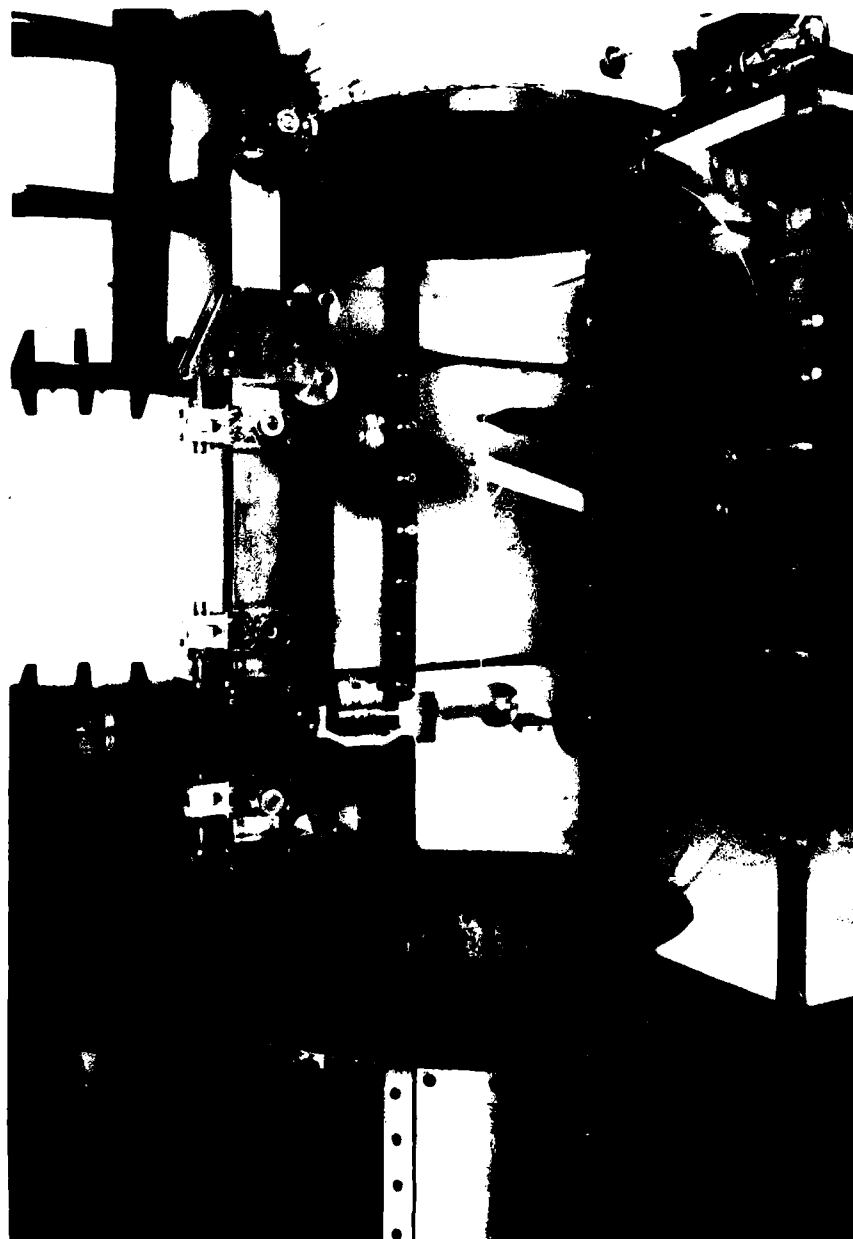


Figure 31. Drag Calibration

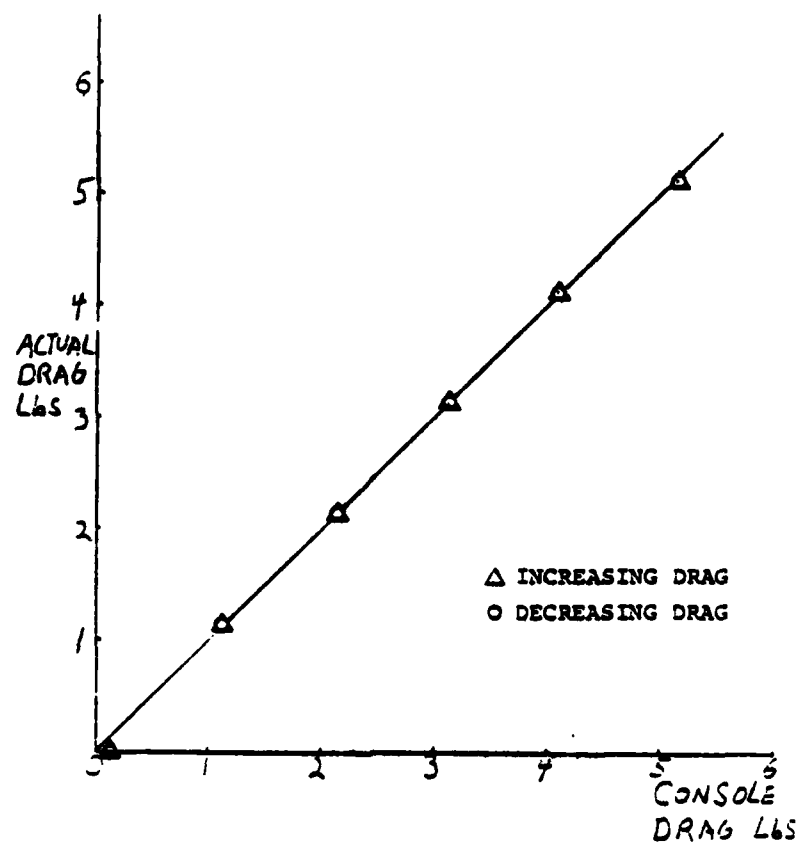


Figure 32. Drag Calibration Curve

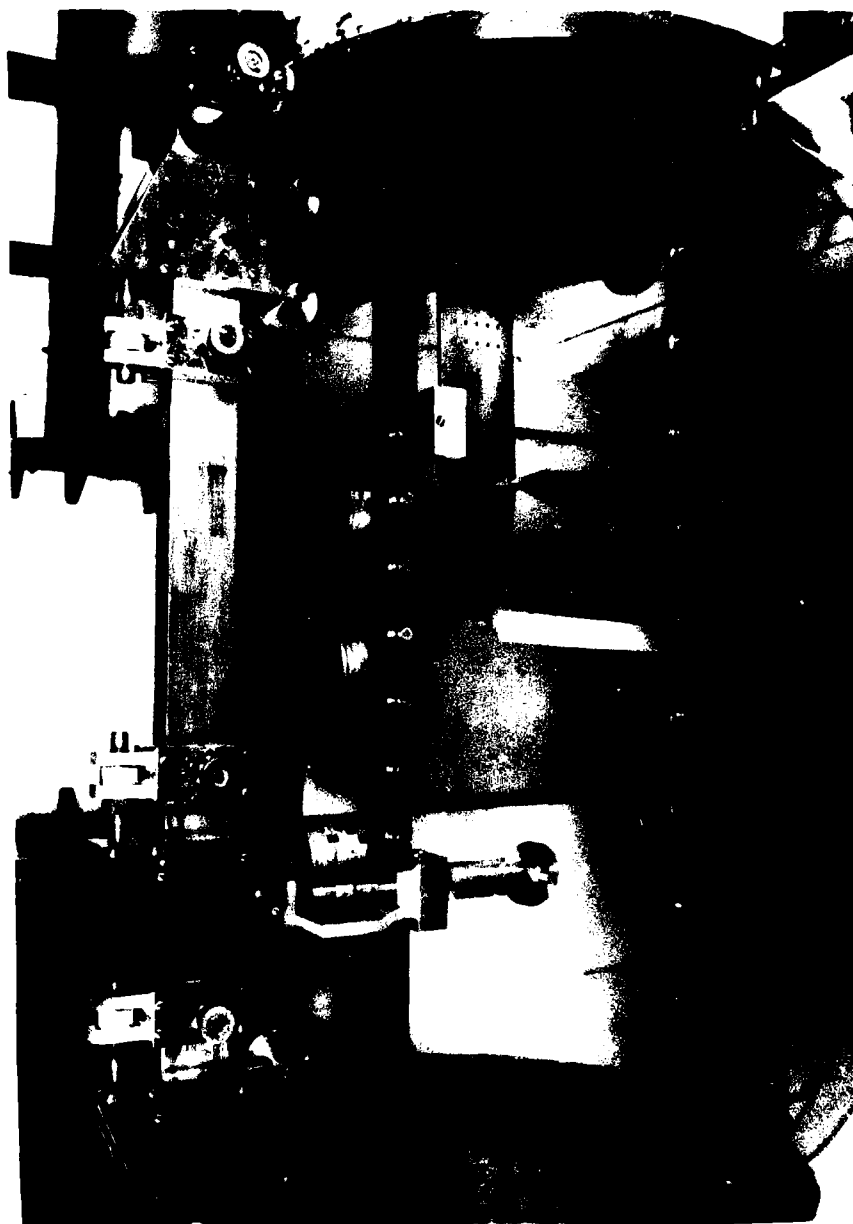


Figure 33. Pitching-Moment Calibration

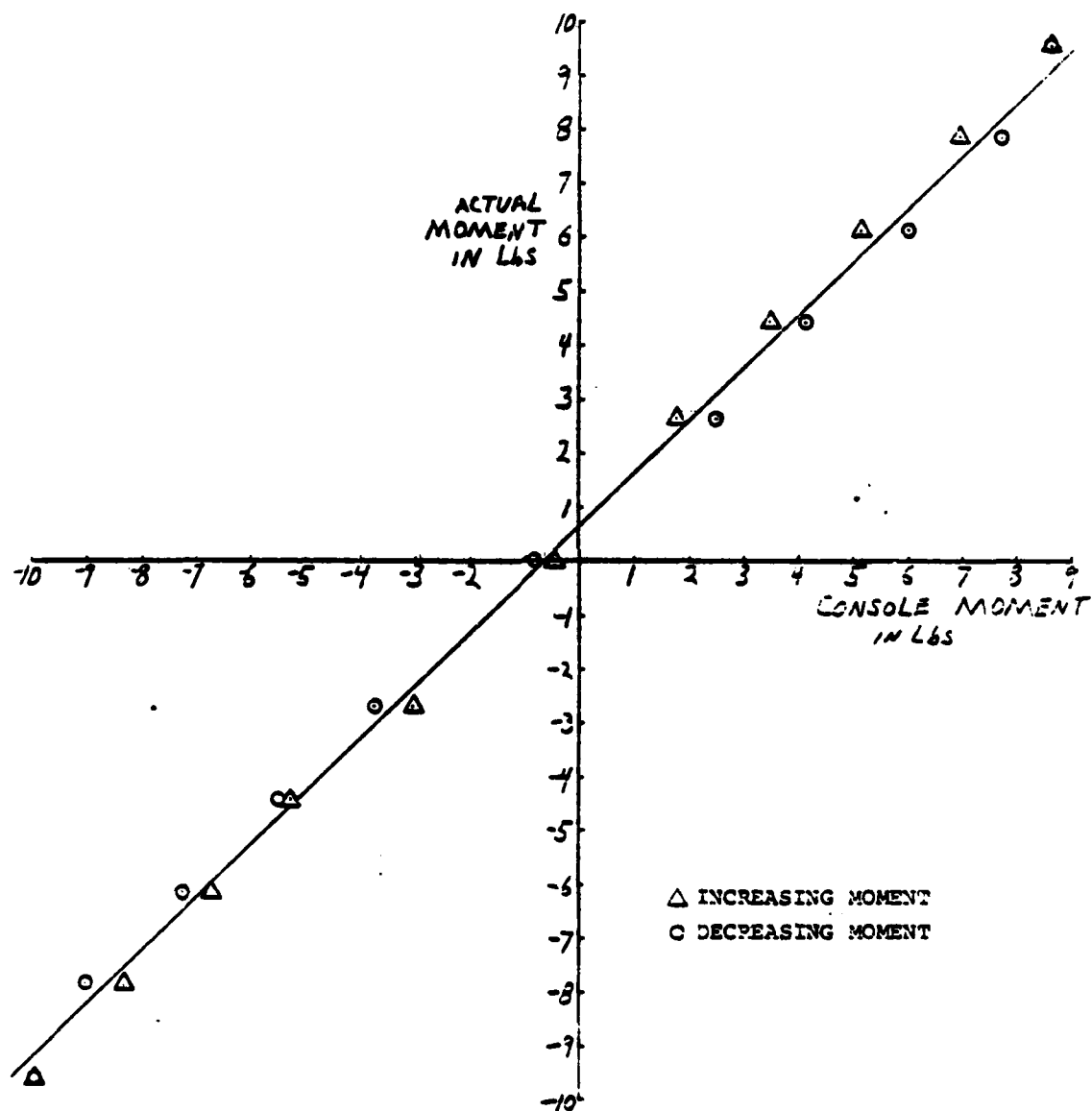


Figure 34. Pitching-Moment Calibration Curve

Since the trunion was not located exactly at the apex of the three-beam balance, a certain degree of interaction among the separate force and moment components was expected. The tunnel was calibrated for interaction of the following components: drag and pitching moment contributions due to a change in lift, lift and drag contributions due to a change in pitching-moment, and pitching-moment and lift contributions due to a change in drag. All these interaction calibrations were done in the following manner with the calibration rig and model #1.

To determine the influence on drag and pitching-moment due to an incremental change in lift, known constant drag forces and pitching-moments were applied and the lift varied throughout the lift calibration range (Fig 35). Each component was incremented in a specific order. First, zero drag and pitching-moment were set and the lift force was cycled through the lift calibration range. Then, a drag force expected to occur often in the experiment was applied with no pitching-moment and the lift force was cycled again. Finally, a drag force expected to be well out of the experimental range was applied with the pitching-moment still at zero and the lift force was cycled again. The drag was then re-set to zero and the pitching-moment was increased first to a value expected to occur in the experiment, then to a value expected to be out of the experimental range. For each incremental value of

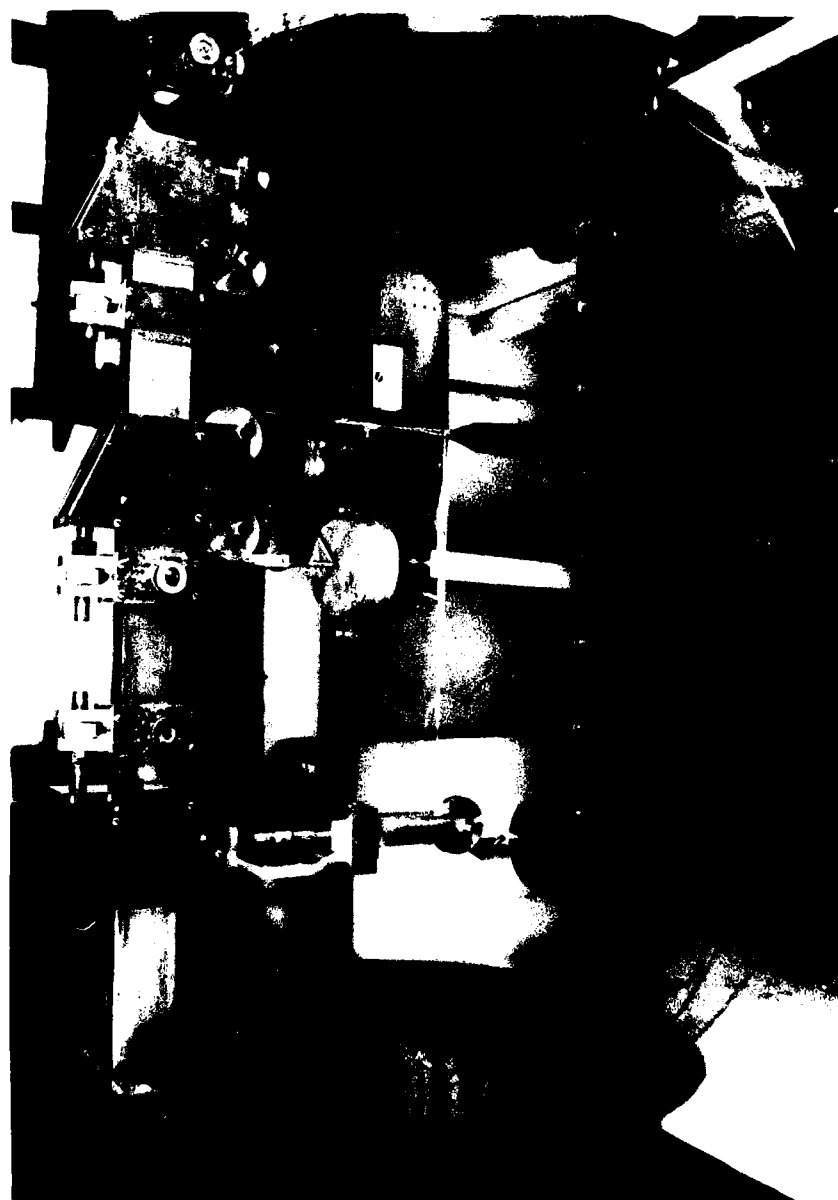


Figure 35. Component Interaction Calibration

pitching-moment, the entire lift/drag cycle as already described was repeated. The same type of cycle was accomplished for both the influence on lift and drag due to an incremental change in pitching-moment and for the influence on lift and pitching-moment due to an incremental change in drag. The entire procedure as described above was repeated for three different angles of attack, (0, 3, and 6 deg) in order to determine if any of the interactions varied with angle of attack.

The angle of attack was calibrated by mounting the inclinometer on model #1 (Fig 36). Each test angle of attack was then set to within plus or minus 1 min of arc and the console reading recorded. The curve from this calibration yields the actual model angle of attack for any given angle set on the tunnel console (Fig 37).

Calibration Equation Determination

The equations used to determine the actual lift, drag, and pitching-moment from the console readings are (Ref 11):

$$\begin{aligned}
 L_u = L_o + \frac{\partial L}{\partial L_c} \Delta L_c + \frac{\partial L}{\partial \alpha} \Delta \alpha + \frac{\partial L}{\partial D} \Delta D + \frac{\partial L}{\partial P_M} \Delta P_M + \frac{\partial^2 L}{\partial \alpha^2} \frac{\Delta \alpha^2}{2!} \\
 + \frac{\partial^2 L}{\partial \alpha \partial D} \frac{\Delta D \Delta \alpha}{2!} + \frac{\partial^2 L}{\partial \alpha \partial P_M} \frac{\Delta P_M \Delta \alpha}{2!} + \frac{\partial^2 L}{\partial D^2} \frac{\Delta D^2}{2!} + \frac{\partial^2 L}{\partial P_M^2} \frac{\Delta P_M^2}{2!} \quad (4)
 \end{aligned}$$

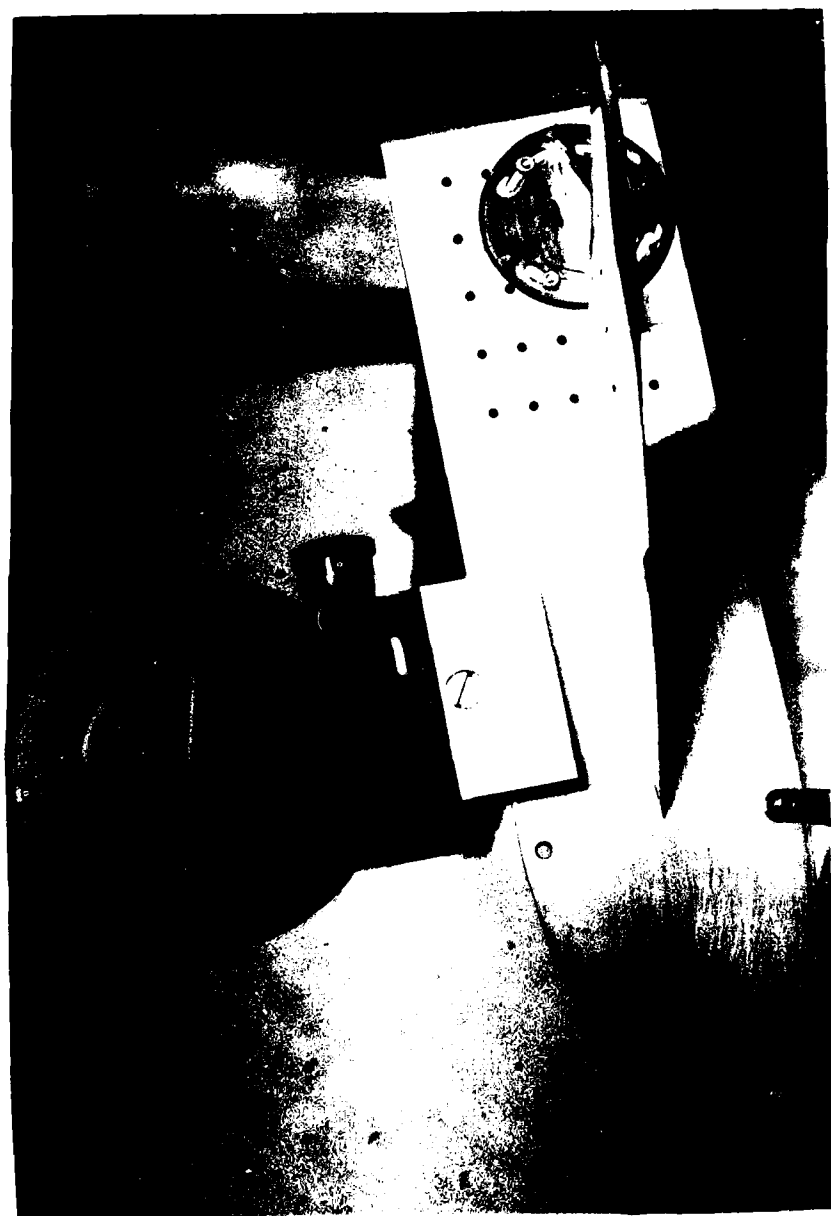


Figure 36. Inclinometer Position for Calibration

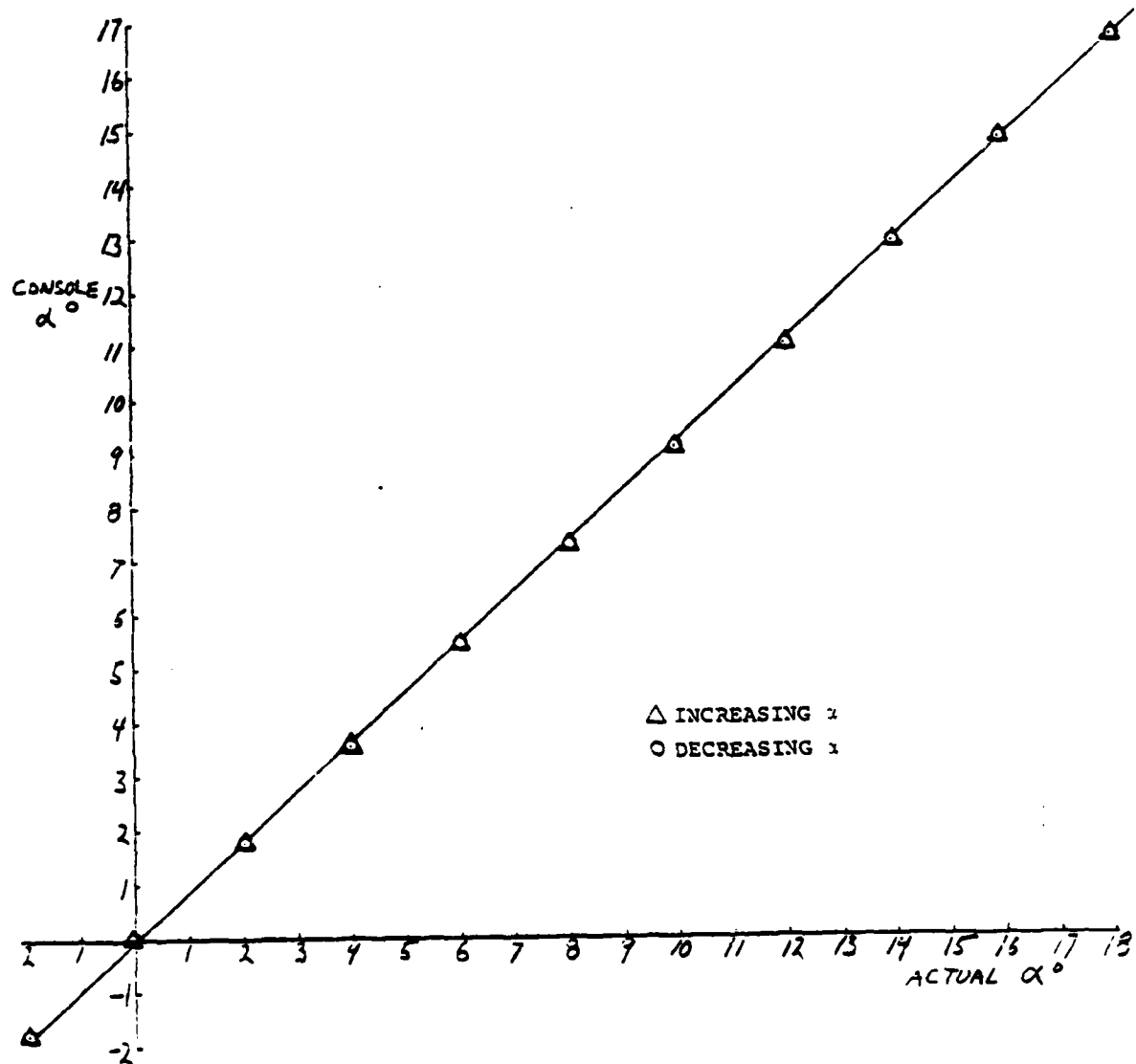


Figure 37. Angle of Attack Calibration Curve

$$\begin{aligned}
D_u = D_o + \frac{\partial D}{\partial D_c} \Delta D_c + \frac{\partial D}{\partial \alpha} \Delta \alpha + \frac{\partial D}{\partial L} \Delta L + \frac{\partial D}{\partial P_M} \Delta P_M + \frac{\partial^2 D}{\partial \alpha^2} \frac{\Delta \alpha^2}{2!} \\
+ \frac{\partial^2 D}{\partial \alpha \partial L} \frac{\Delta \alpha \Delta L}{2!} + \frac{\partial^2 D}{\partial \alpha \partial P_M} \frac{\Delta \alpha \Delta P_M}{2!} + \frac{\partial^2 D}{\partial L^2} \frac{\Delta L^2}{2!} + \frac{\partial^2 D}{\partial P_M^2} \frac{\Delta P_M^2}{2!} \quad (5)
\end{aligned}$$

$$\begin{aligned}
P_{Mu} = P_{Mo} + \frac{\partial P_M}{\partial P_{Mc}} \Delta P_{Mc} + \frac{\partial P_M}{\partial \alpha} \Delta \alpha + \frac{\partial P_M}{\partial D} \Delta D + \frac{\partial P_M}{\partial L} \Delta L \\
+ \frac{\partial^2 P_M}{\partial \alpha^2} \frac{\Delta \alpha^2}{2!} + \frac{\partial^2 P_M}{\partial \alpha \partial D} \frac{\Delta \alpha \Delta D}{2!} + \frac{\partial^2 P_M}{\partial \alpha \partial L} \frac{\Delta \alpha \Delta L}{2!} + \frac{\partial^2 P_M}{\partial D^2} \frac{\Delta D^2}{2!} \\
+ \frac{\partial^2 P_M}{\partial L^2} \frac{\Delta L^2}{2!} \quad (6)
\end{aligned}$$

By doing an order of magnitude analysis of the slopes of the calibration curves obtained, the only terms that were large enough to enter the error ranges of the respective balance scales were:

$$L_u = L_o + \frac{\partial L}{\partial L_c} \Delta L_c + \frac{\partial L}{\partial P_M} \Delta P_M$$

$$D_u = \frac{\partial D}{\partial D_c} \Delta D_c$$

$$\begin{aligned}
P_{Mu} = P_{Mo} + \frac{\partial P_M}{\partial P_{Mc}} \Delta P_{Mc} + \frac{\partial P_M}{\partial L} \Delta L + \frac{\partial P_M}{\partial D} \Delta D \\
+ \frac{\partial^2 P_M}{\partial \alpha \partial L} \frac{\Delta \alpha \Delta L}{2!}
\end{aligned}$$

All other terms were either zero or smaller than the respective balance guaranteed accuracy and were counted as zero.

From the lift, drag, pitching-moment, and interaction curve slopes, the following values for the remaining terms were obtained:

$$L_u = -.26 + 1.04\Delta L_c + .1496\Delta P_M$$

$$D_u = 1.01\Delta D_c$$

$$P_{Mu} = -.6413 + .9867\Delta P_{Mc} + .018\Delta D \\ + .0802\Delta L + .01 \frac{\Delta L \Delta \alpha}{2!}$$

These equations were programmed into a Hewlett Packard HP 41 CV calculator and used in the data reduction to obtain the true measured values for lift, drag, and pitching-moment about the trunion for all experimental tunnel runs.

Appendix C
Data Reduction

Once all data had been corrected for balance errors, it was then corrected for the following boundary layer phenomena. All correction equations and techniques can be found in Pope and Harper (Ref 12:213-370).

Solid and Wake Blockage (Ref 3:277)

Corrections for both solid and wake blockage were performed in one operation by using the following equation:

$$\epsilon_{tb} = \frac{1}{4} \frac{\text{Model Frontal Area}}{\text{Test Section Area}} \quad (7)$$

For the models used in this experiment, this equation was expanded to:

$$\epsilon_{tb} = \frac{S \sin \alpha + S_c \sin (\alpha + \beta) + S_A (L \sin \alpha + L \cos \alpha) .125 + 2.7313}{4\pi R^2}$$

Both solid and wake blockage are very similar. Solid blockage corrects for the greater velocity and dynamic pressure due to the presence of the model and wake blockage corrects for the increase in these quantities due to the reduction in tunnel cross-sectional area by the presence of the wake behind the model (Ref 3:227).

This term was used to correct the tunnel dynamic pressure as follows:

$$q_c = q_u (1 + 2 \epsilon_{tb}) \quad (8)$$

Streamline Curvature (Ref 3:278-279)

The streamline curvature correction accounts for the variation in fluid flow about the model. The presence of the tunnel ceiling and floor prevents normal curvature of the streamlines about the model. This causes a boundary-induced upwash along the chord which makes the airfoils seem to have more than their actual camber. Thus, the model has too much lift and pitching-moment about the aerodynamic center for a given angle of attack. This correction was applied to the angle of attack, lift and pitching-moment about the aerodynamic center.

For the angle of attack, the correction is

$$\Delta\alpha = T_2 \delta \left(\frac{S}{AR} \right) \quad (9)$$

where T_2 is a downwash correction factor. In the data reduction program, T_2 was set at .1 (Ref 12, Fig 6.54) based on an $\ell_t/2R = .0421$ where ℓ_t is $\bar{c}/4$ for the wing. Since the wings and canards were offset from the tunnel centerline, the boundary correction factor (δ) was determined from:

$$\delta = \frac{1}{32\sigma^2} \left\{ \log \frac{1+2 \left[\sigma^2 - \left(\frac{d}{R} \right)^2 \right] + \left[\sigma^2 + \left(\frac{d}{R} \right)^2 \right]}{1-2 \left[\sigma^2 + \left(\frac{d}{R} \right)^2 \right] + \left[\sigma^2 + \left(\frac{d}{R} \right)^2 \right]^2} \right\} \quad (10)$$

where

$$\sigma = \frac{b_e}{2R}$$

and

$$b_e = .9b$$

The final δ was calculated as 0.0644.

Downwash (Ref 3:279)

When a three-dimensional model is placed in a wind tunnel, the tunnel walls act as stream surfaces through which no fluid can pass. Since they are not present in actual flight, the effect is to decrease the downwash caused by the wing trailing vortices so that the airfoils have a smaller induced angle of attack and a reduced amount of induced drag.

The downwash correction applied to α is

$$\alpha = \alpha_u + \delta \frac{S}{A} C_L \quad (57.3) \quad (11)$$

The total α correction is found by combining the streamline curvature correction and downwash correction as follows:

$$\alpha = \alpha_u + \delta (1+T_2) \frac{S}{A} C_{L\alpha} \quad (57.3) \quad (12)$$

Coefficient Determination

Once q_c has been found, the uncorrected lift coefficient was calculated by

$$C_{Lu} = \frac{L_u}{q_c S} \quad (13)$$

and α was then computed using Eq (12).

The corrected lift coefficient was computed using

$$C_L = C_{Lu} [1 - T_2 \delta \frac{S}{A} (57.3) a] \quad (14)$$

where a is the slope of the C_{Lu} vs α_u curve plotted for that particular run.

Once C_L has been determined, the corrected drag coefficient was calculated from

$$C_D = \frac{D_u}{q_c S} + \delta \frac{S}{A} C_L^2 \quad (15)$$

An aerodynamic center was determined for each wing/canard configuration (each change in canard position relative to the wing). The aerodynamic center was found by plotting the uncorrected coefficients of lift, drag and pitching-moment about the trunion vs the uncorrected angle of attack. These plots were used to obtain the information required by the following equation:

$$\begin{aligned} \frac{dC_{MTR}}{d\alpha} = & \left[\left(\frac{dC_L}{d\alpha} + C_D \right) \cos \alpha + \left(\frac{dC_D}{d\alpha} - C_L \right) \sin \alpha \right] x_1 \\ & + \left[\left(\frac{dC_D}{d\alpha} - C_L \right) \cos \alpha - \left(\frac{dC_L}{d\alpha} + C_D \right) \sin \alpha \right] y_1 \quad (16) \end{aligned}$$

Two different angles in the linear area of the lift curve were chosen, the appropriate information was substituted in the equation and both resulting equations were solved simultaneously for x_1 and y_1 . These values express the location of the aerodynamic center as a fraction of \bar{c} relative to the trunion. These values were then used in

$$(y_{TR} - y_1) \bar{c} = y_p \quad (17)$$

and

$$\left(\frac{x_{TR}}{\bar{c}} - x_1 \right) \bar{c} = x_p \quad (18)$$

These equations express the position of the aerodynamic center relative to the wing vertex and model centerline. The positive sense for the above is toward the trailing edge from the vertex for x_p and above the model centerline for y_p .

The moment about the aerodynamic center was then calculated by

$$\begin{aligned} M_{AC} = & M_{TR} - x_1 \bar{c} (L_u \cos \alpha + D_u \sin \alpha) \\ & - y_1 \bar{c} (D_u \cos \alpha - L_u \sin \alpha) \quad (19) \end{aligned}$$

Once the moment about the aerodynamic center had been found, the following equation was used to determine C_M :

$$C_M = \frac{M_{AC}}{q_c S \bar{c}} - .25 (C_L T_2 \delta \frac{S}{A} (57.3)) \quad (20)$$

In addition to the aerodynamic coefficients, velocity, Reynolds number, and Mach number were also calculated using

$$V = \sqrt{\frac{2q_c}{\rho}} \quad (21)$$

$$R_e = \rho V \bar{c} \quad (22)$$

and

$$M = \frac{V}{\sqrt{\gamma R' T}} \quad (23)$$

respectively. The density ρ was determined from the ideal gas law and the recorded barometric pressure from each tunnel run. The temperature was expressed in degrees Kelvin and then used in Sutherlands formula:

$$\mu = \frac{3.059 \times 10^{-8} T^{3/2}}{T + 114} \quad (24)$$

in order to determine the viscosity used in the Reynolds number calculation. The value of 1.4 was used for γ and 3088.8 ft-lbf/slug deg Kelvin for the gas constant R' along

with the temperature in degrees Kelvin to determine the Mach number.

Appendix D

Force and Moment Data

This appendix contains the data plots of C_L , C_D , and C_M about the aerodynamic center for all model #3 test runs. The location of each test position relative to the wing root $1/4c$ point can be found in Fig 38. Each figure in this appendix has two sets of data plotted. The data denoted by the squares are for the wing only and the data denoted by the circles are for the wing/canard configuration. This is done to facilitate comparison of the wing only data with the data obtained from the wing/canard configuration. Also, the reference to canard AOA means canard incidence. This was included in the legends of the plots to facilitate matching a particular plot with the correct flow study photographs in Appendix E.

Each plot can be associated with a set of photographs in Appendix E by matching the respective figure subscripts. For example, Figs 39AlL, 39AlD, and 39AlM in Appendix D would go with Fig 40Al in Appendix E.

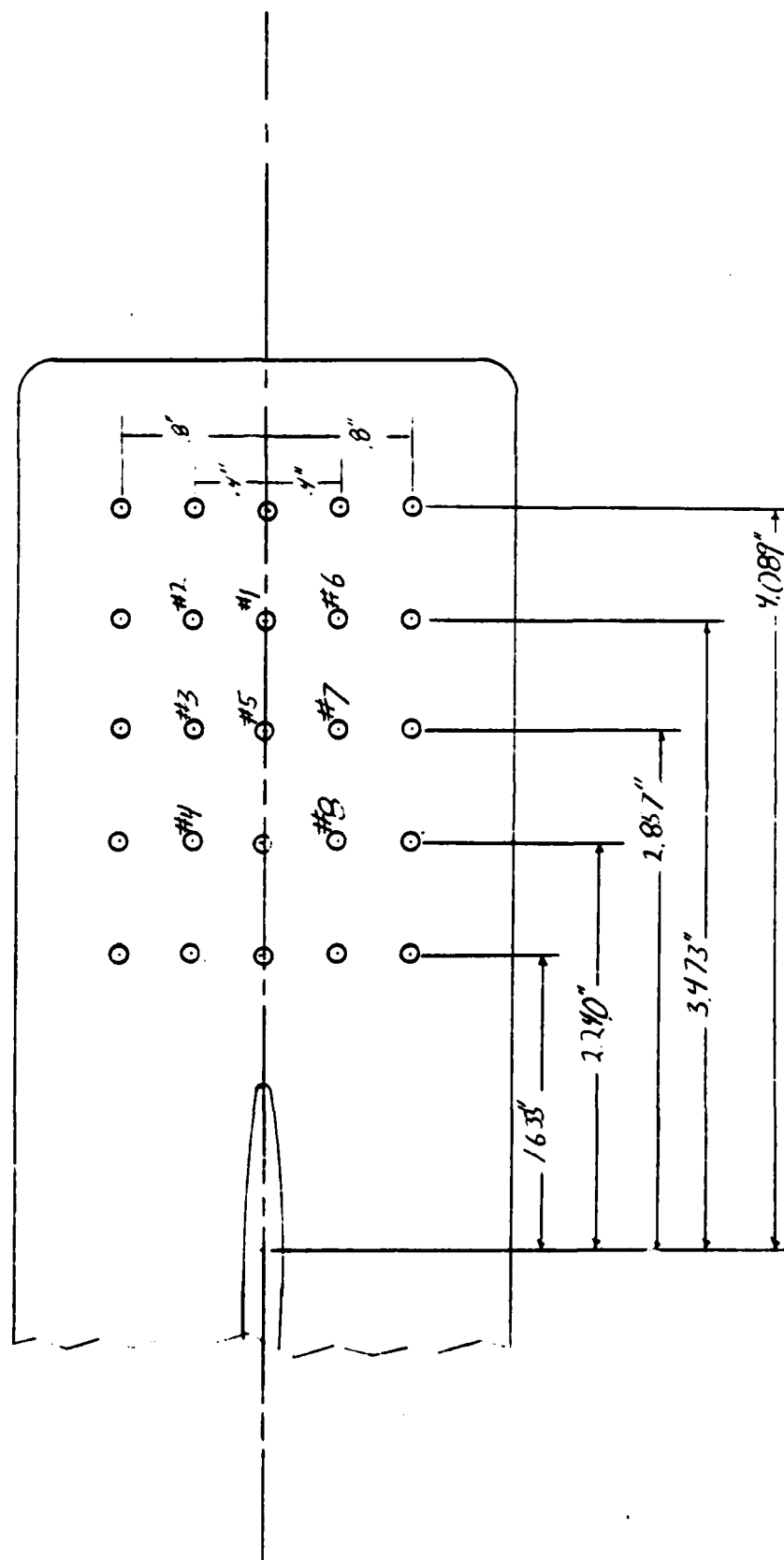


Figure 38. Test Position Location with Respect to Wing Root 1/4 Chord

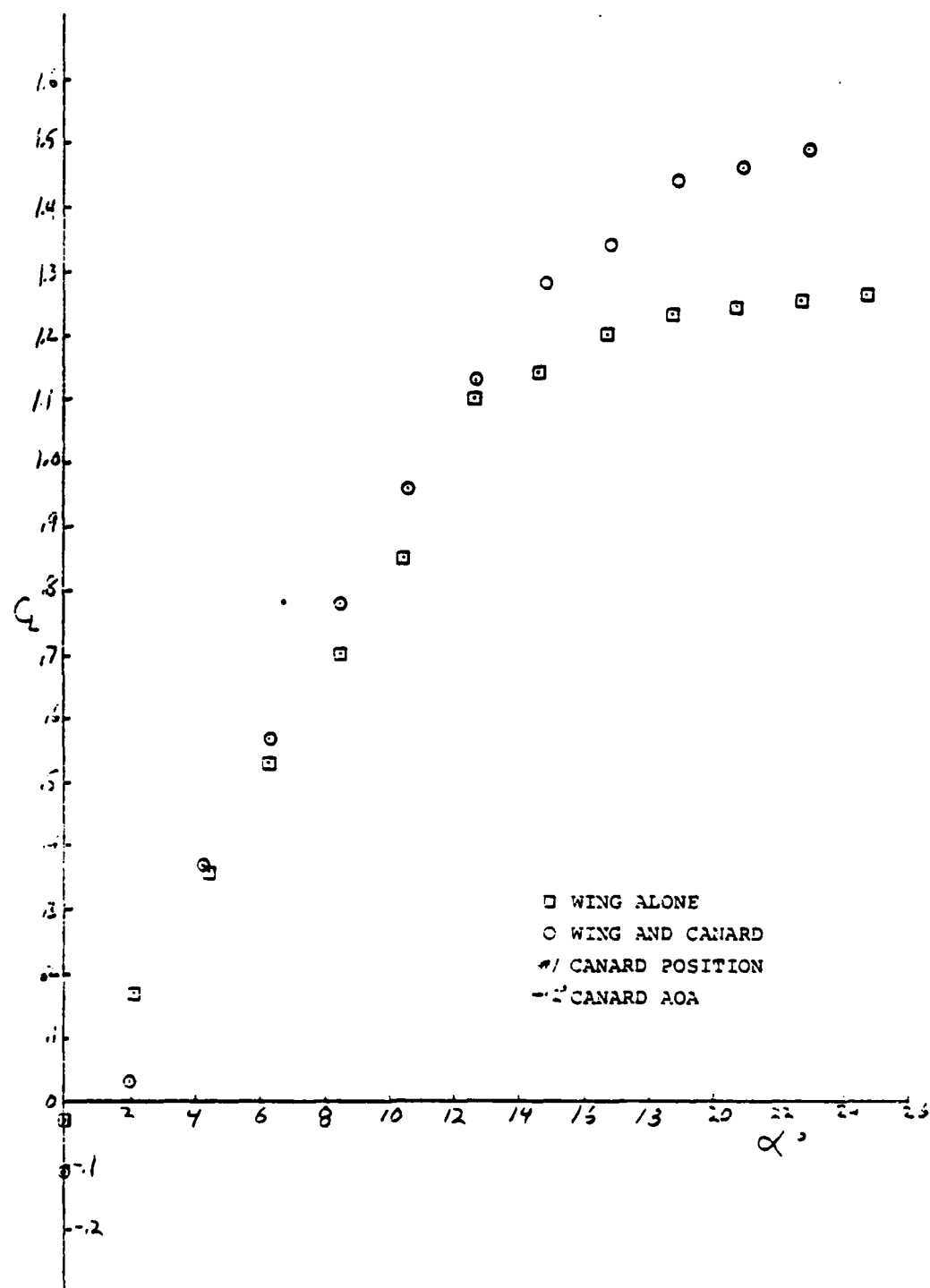


Figure 39All. Lift Coefficient vs Alpha

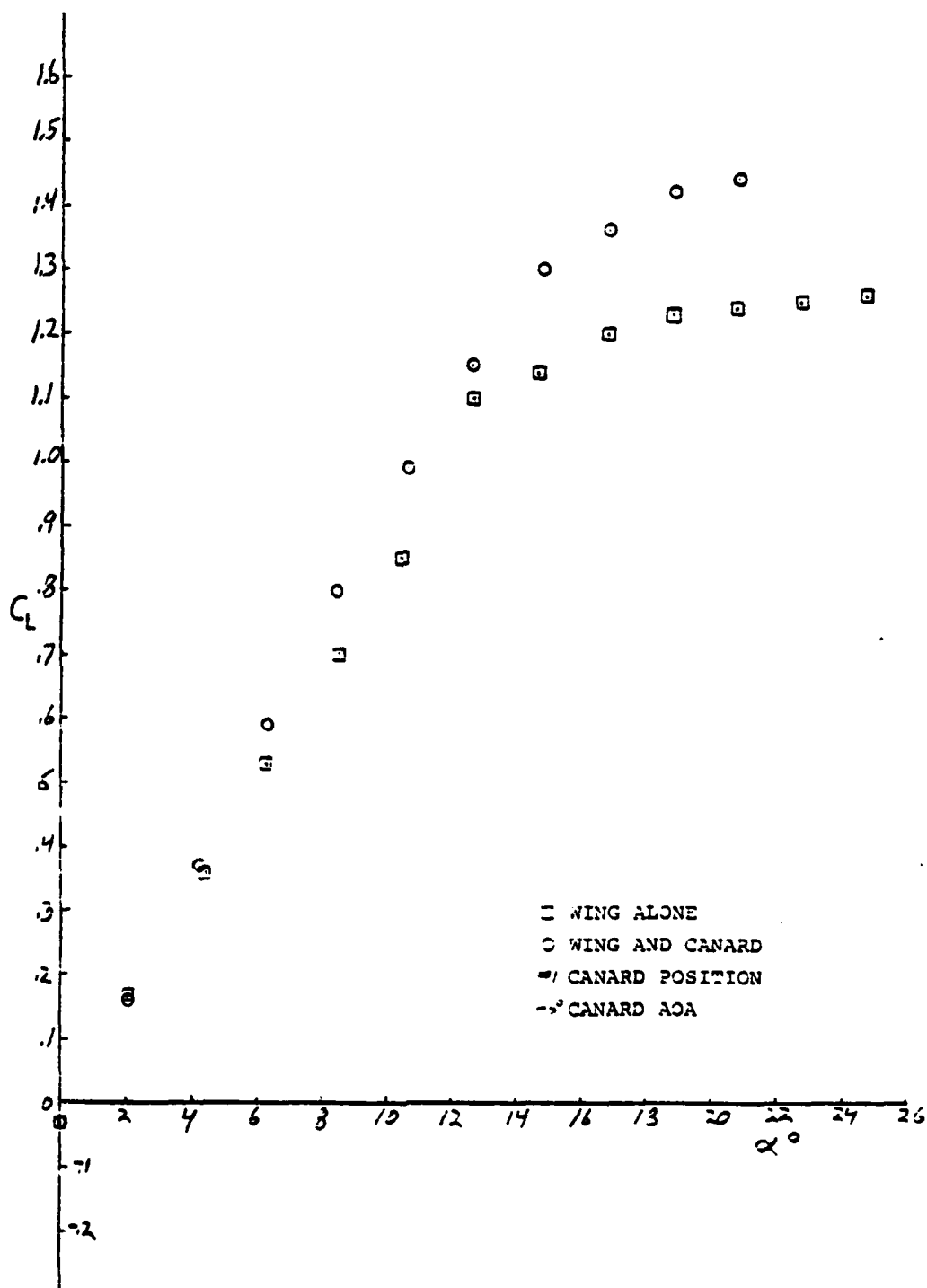


Figure 39A2L. Lift Coefficient vs Alpha

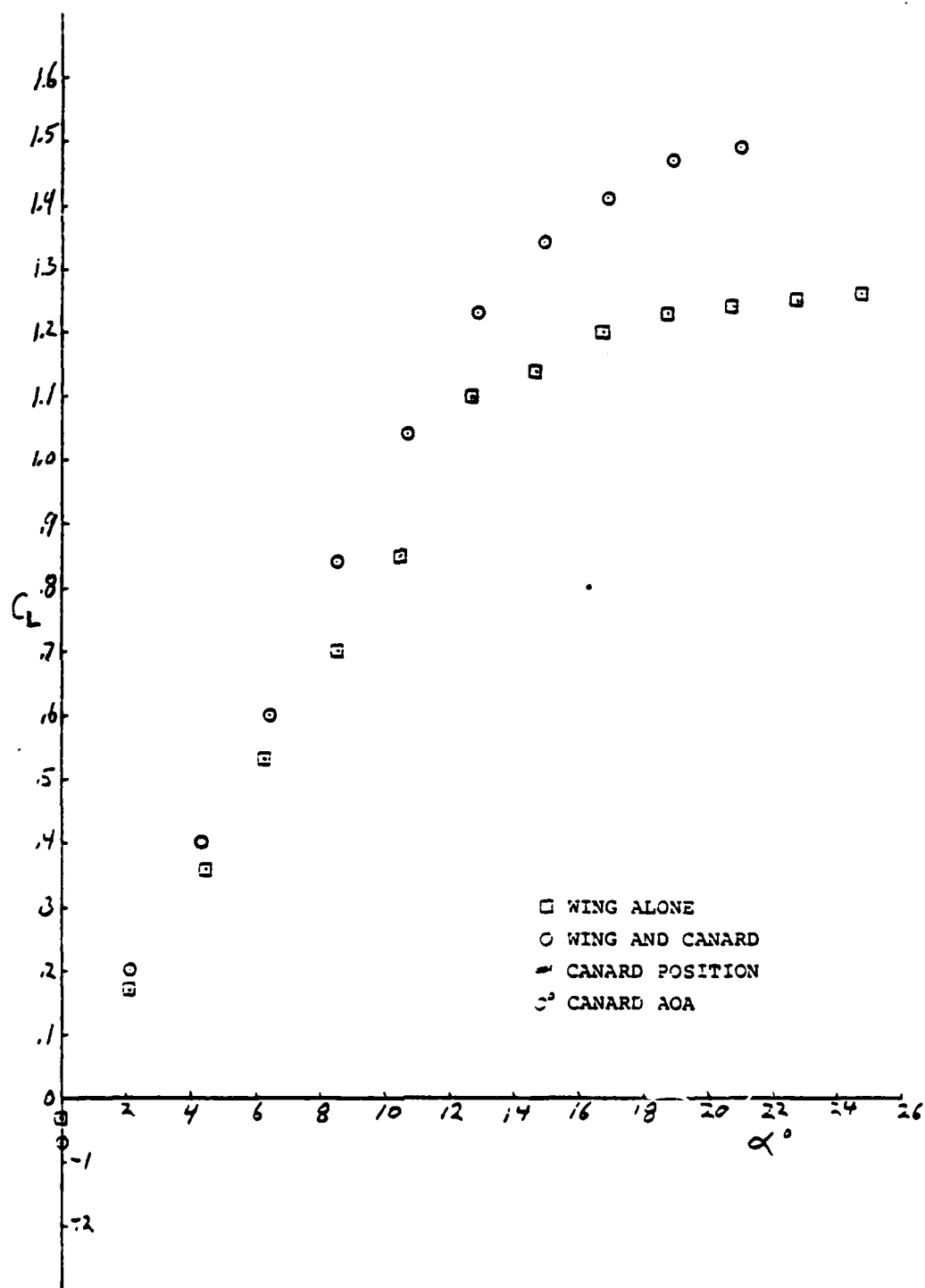


Figure 39A3L. Lift Coefficient vs Alpha

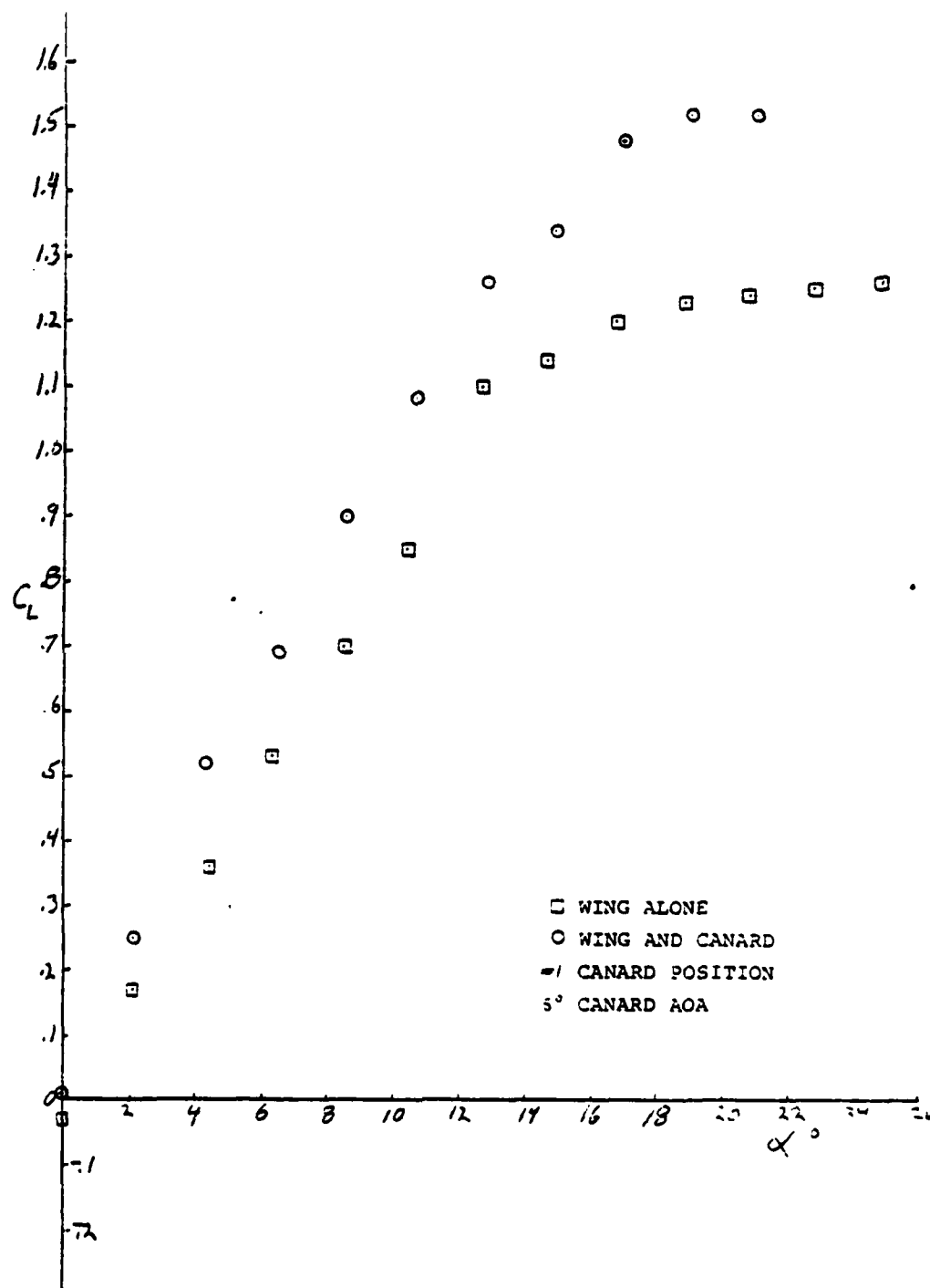


Figure 39A4L. Lift Coefficient vs Alpha

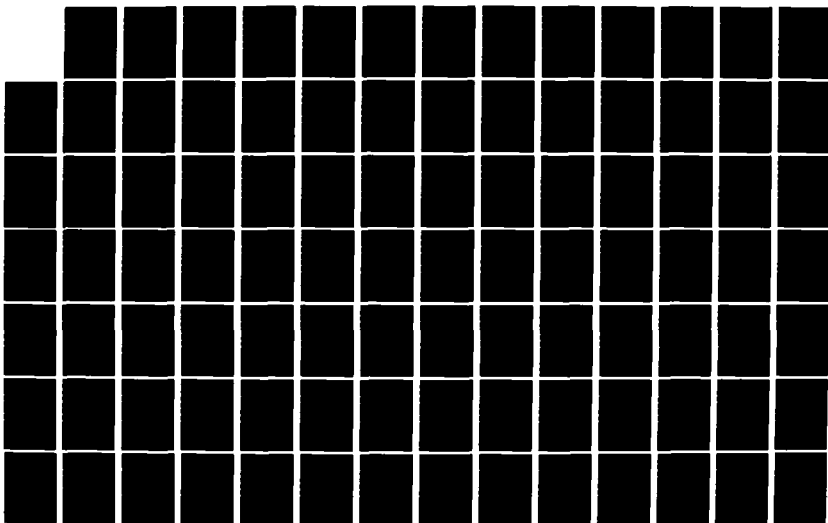
AD-A124 722

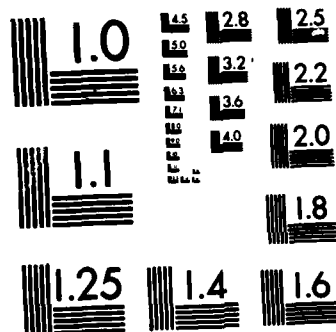
A WIND TUNNEL STUDY OF THE EFFECTS OF A CLOSE-COUPLED
CANARD ON THE AEROD. (U) AIR FORCE INST OF TECH
WRIGHT-PATTERSON AFB OH SCHOOL OF ENGI.. P M WEAVER
DEC 82 AFIT/GRE/AR/82D-30 F/G 1/3

2/3

UNCLASSIFIED

NL





MICROCOPY RESOLUTION TEST CHART
NATIONAL BUREAU OF STANDARDS-1963-A

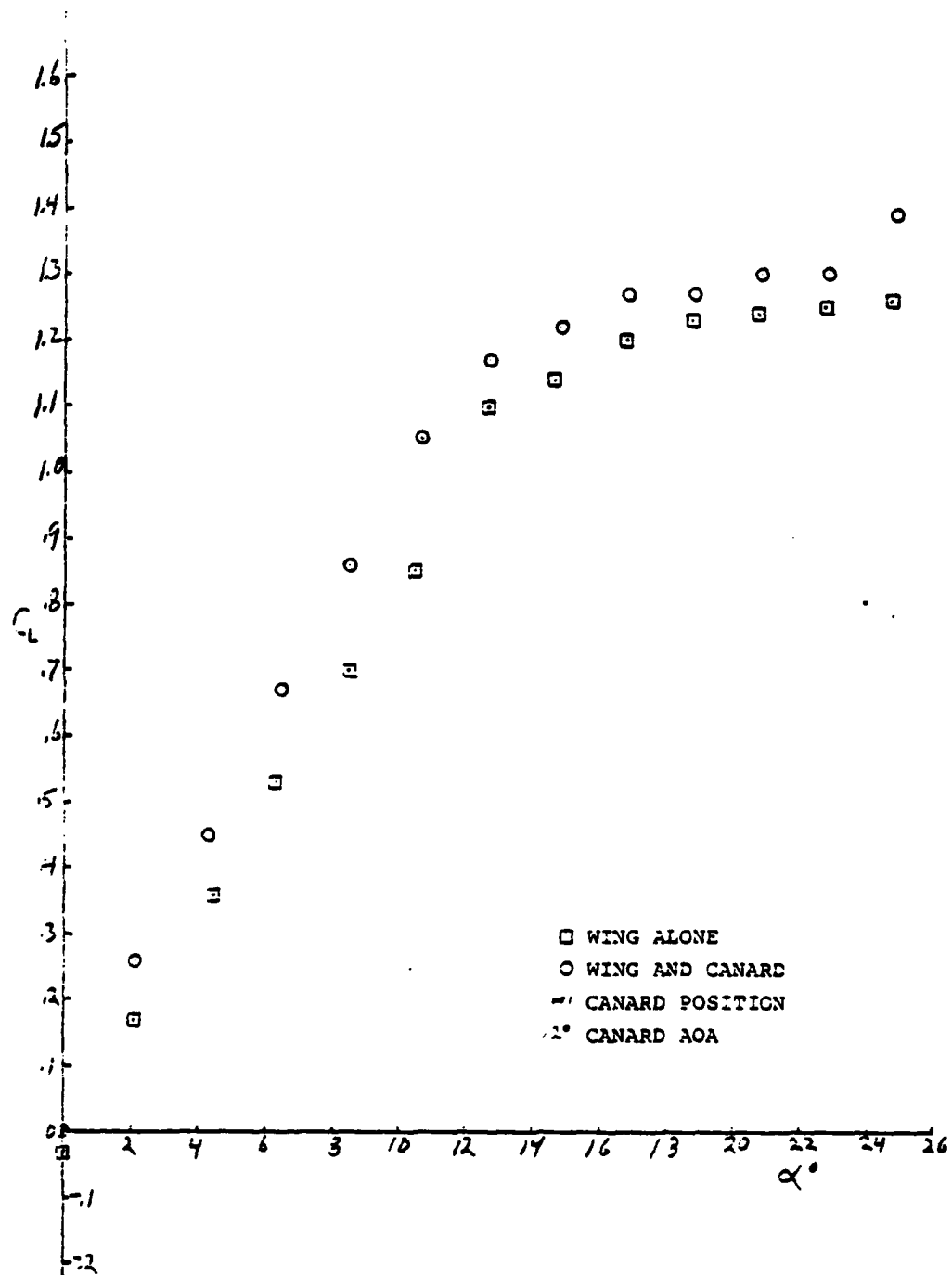


Figure 39A5L. Lift Coefficient vs Alpha

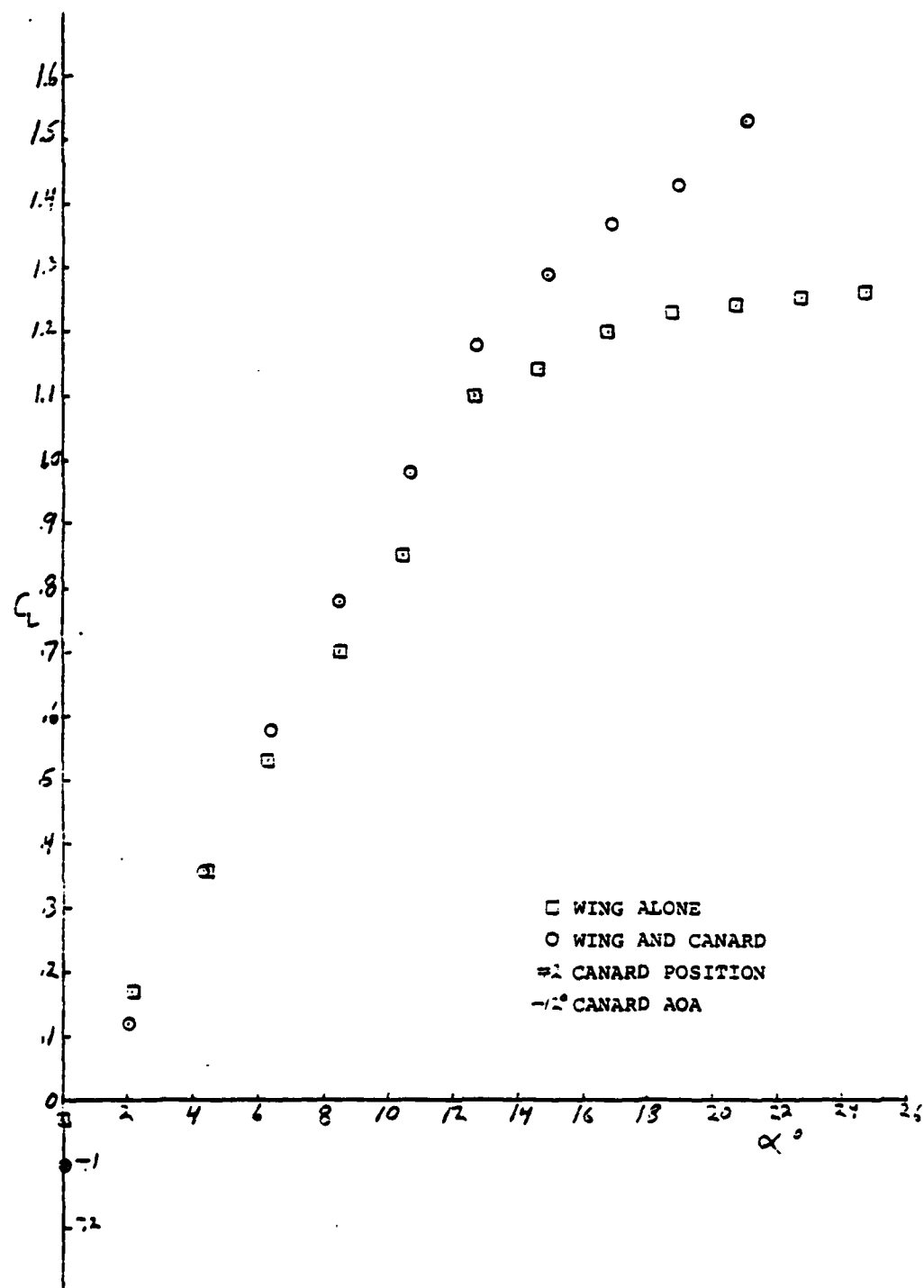


Figure 39A6L. Lift Coefficient vs Alpha

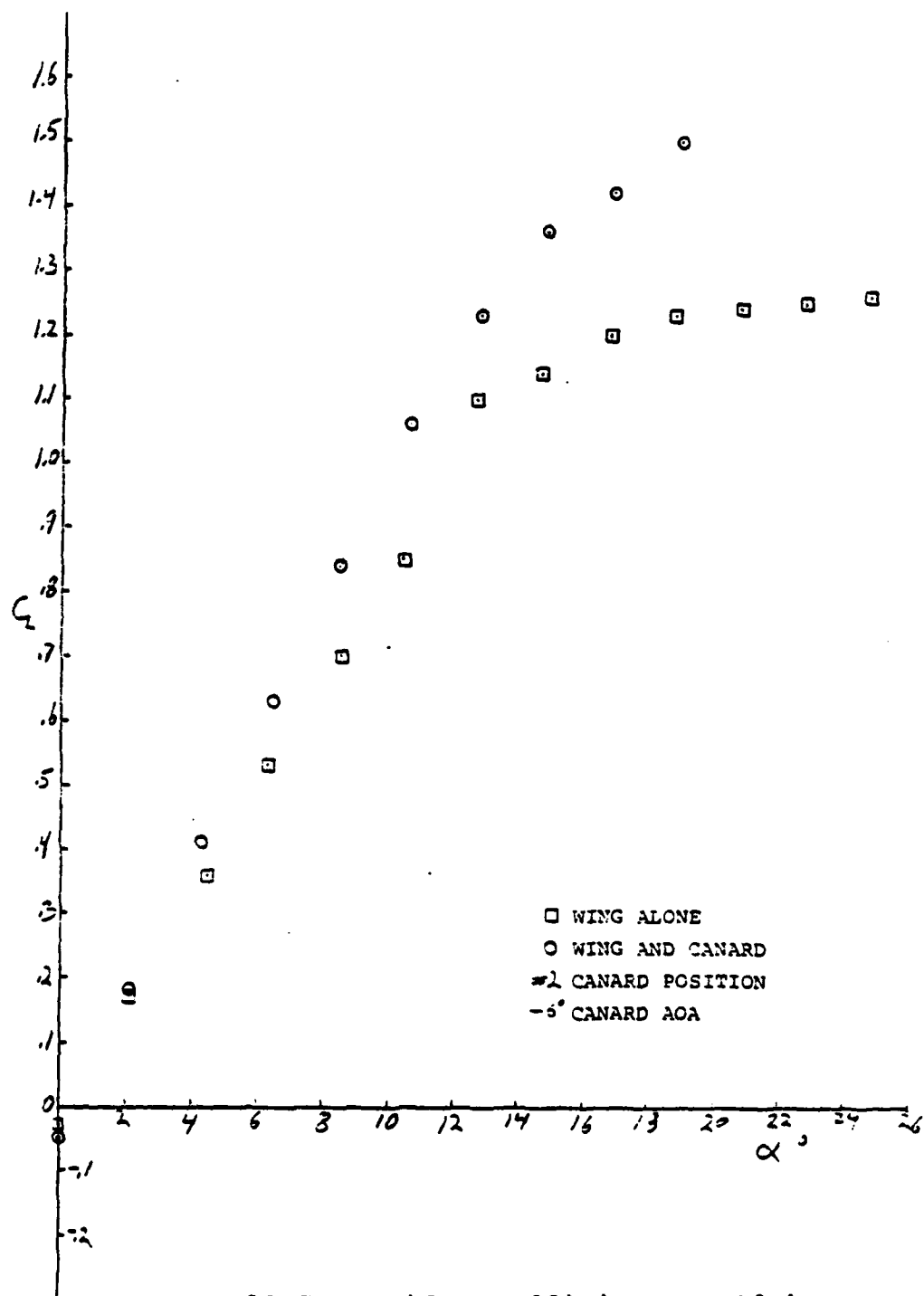


Figure 39A7L. Lift Coefficient vs Alpha

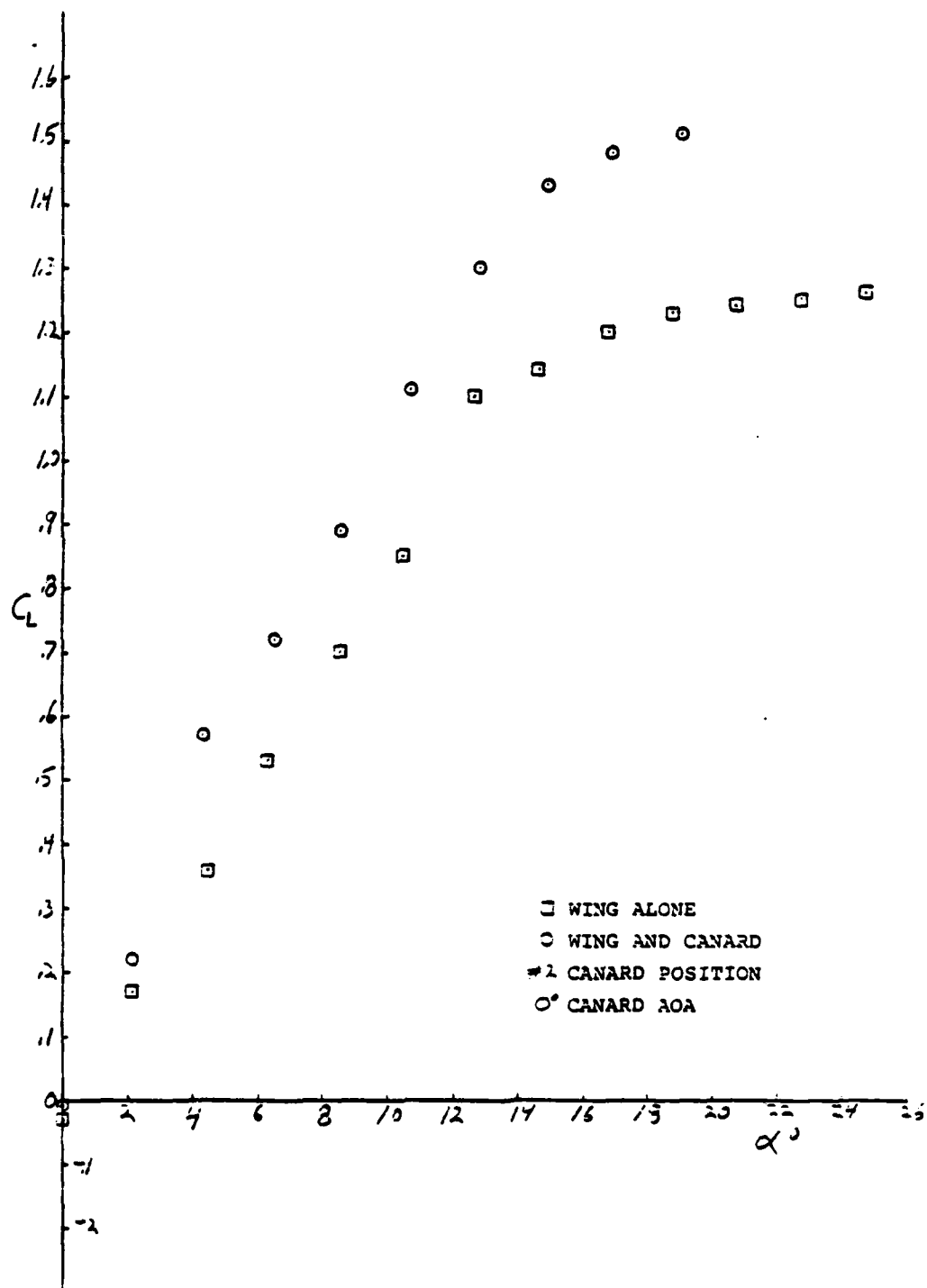


Figure 39A8L. Lift Coefficient vs Alpha

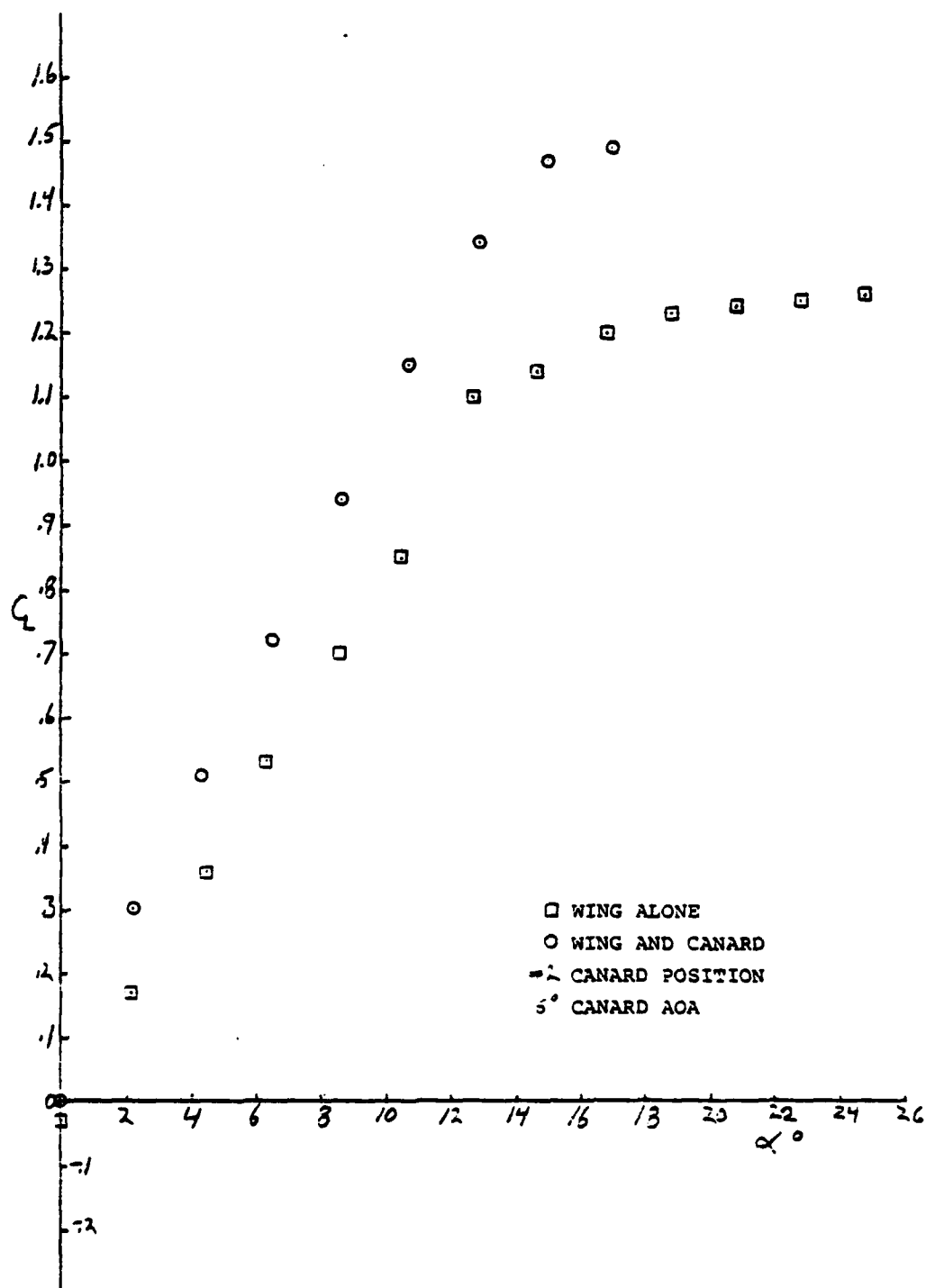


Figure 39A9L. Lift Coefficient vs Alpha

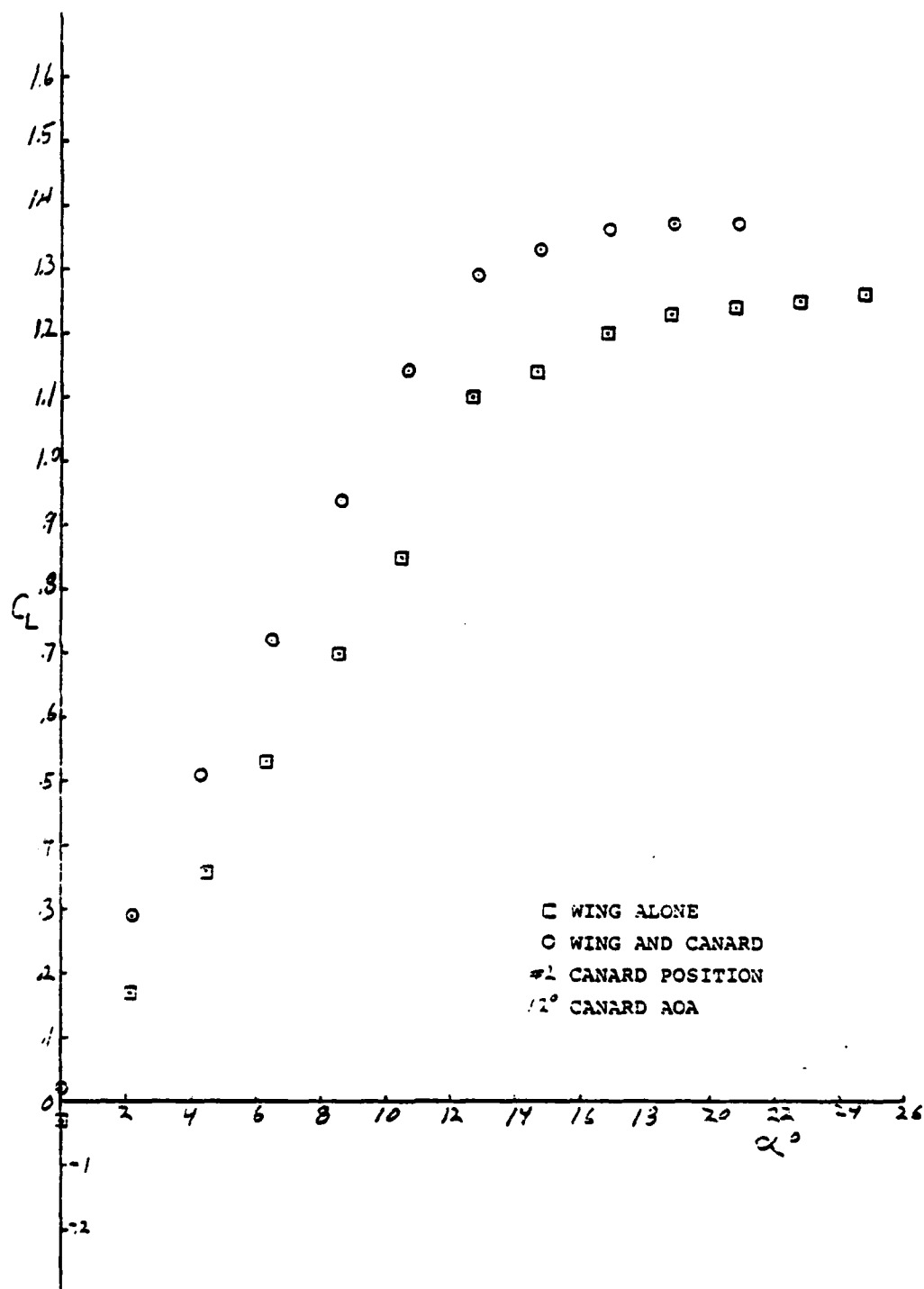


Figure 39A10L. Lift Coefficient vs Alpha

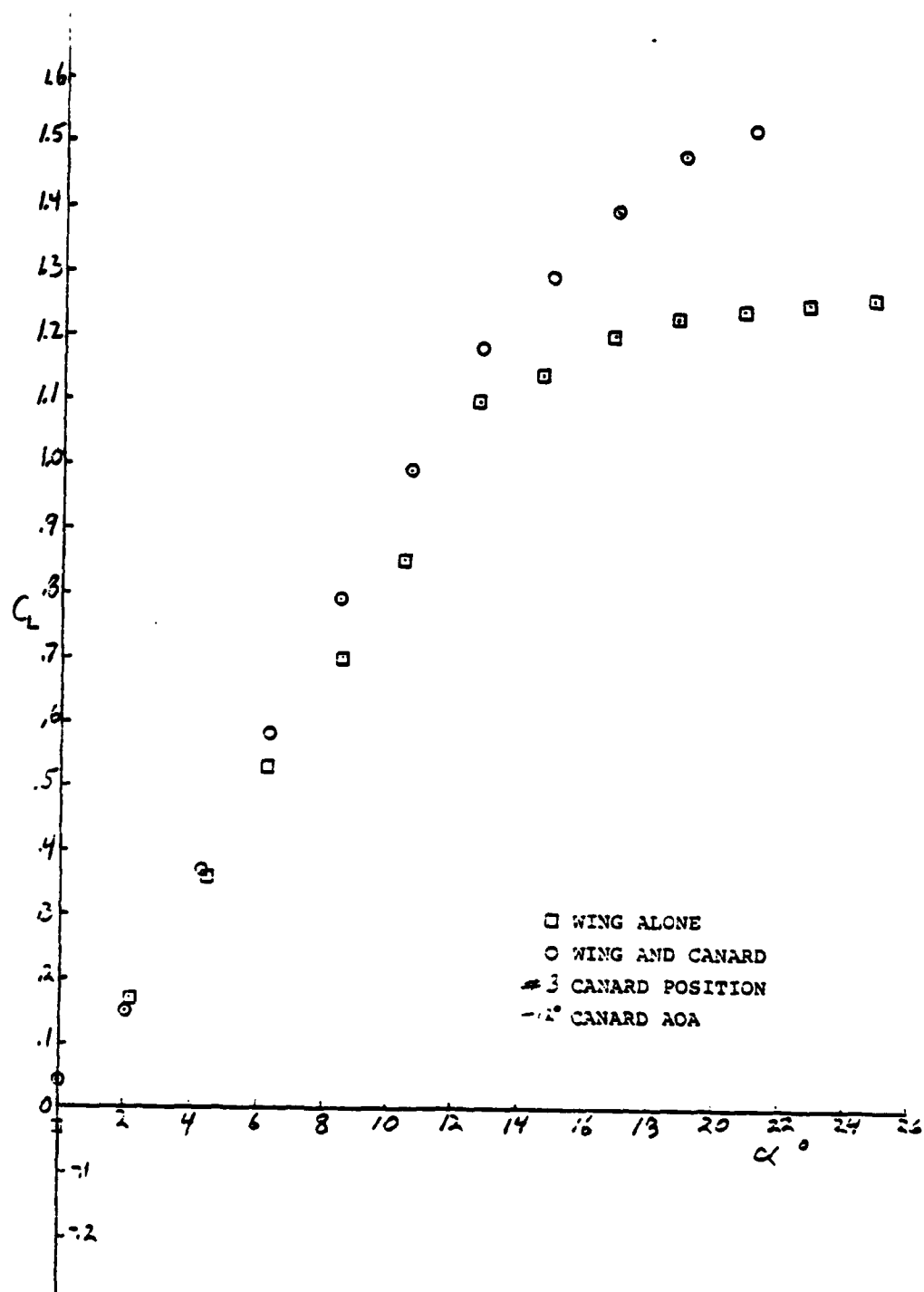


Figure 39A11L. Lift Coefficient vs Alpha

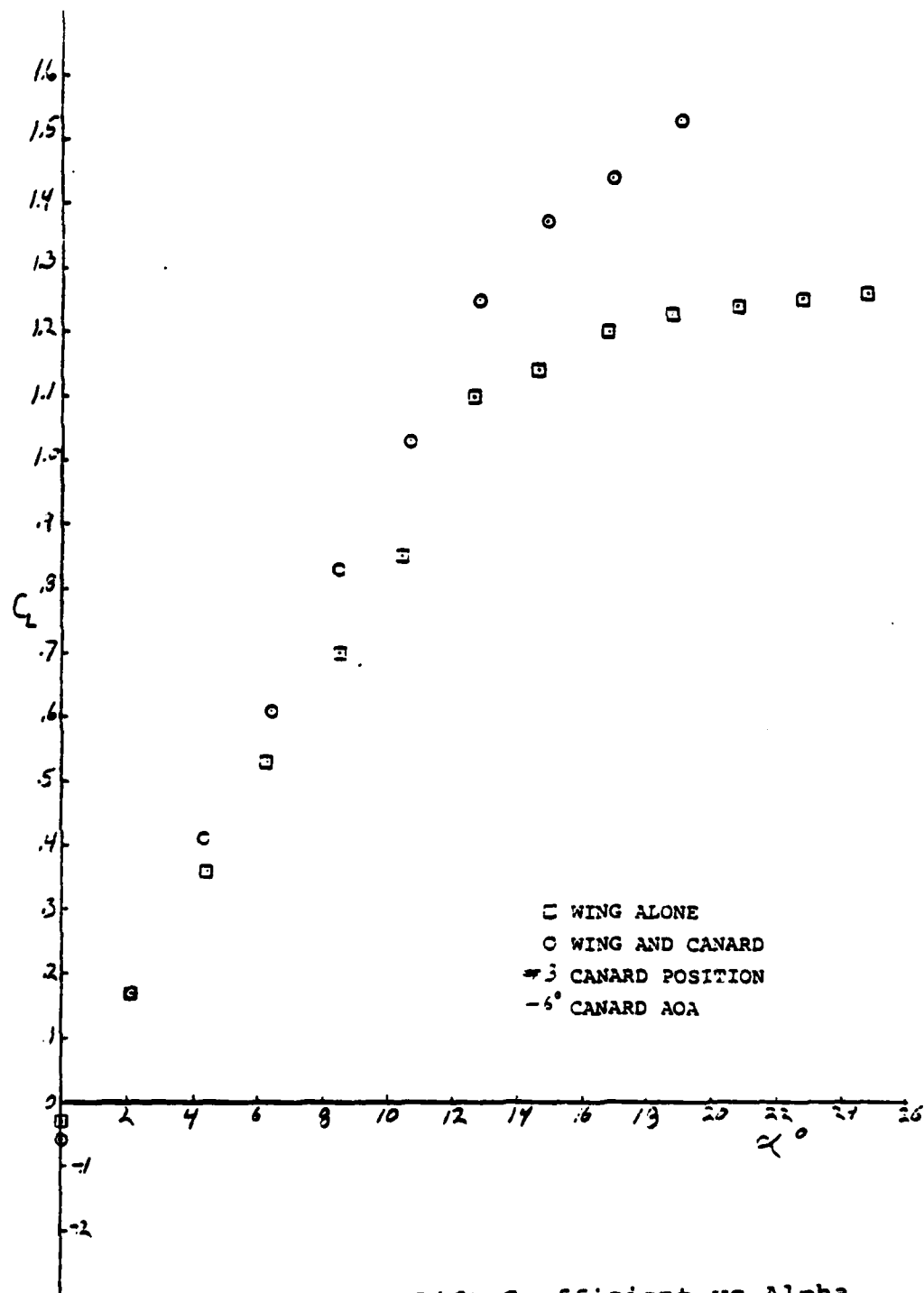


Figure 39A12L. Lift Coefficient vs Alpha

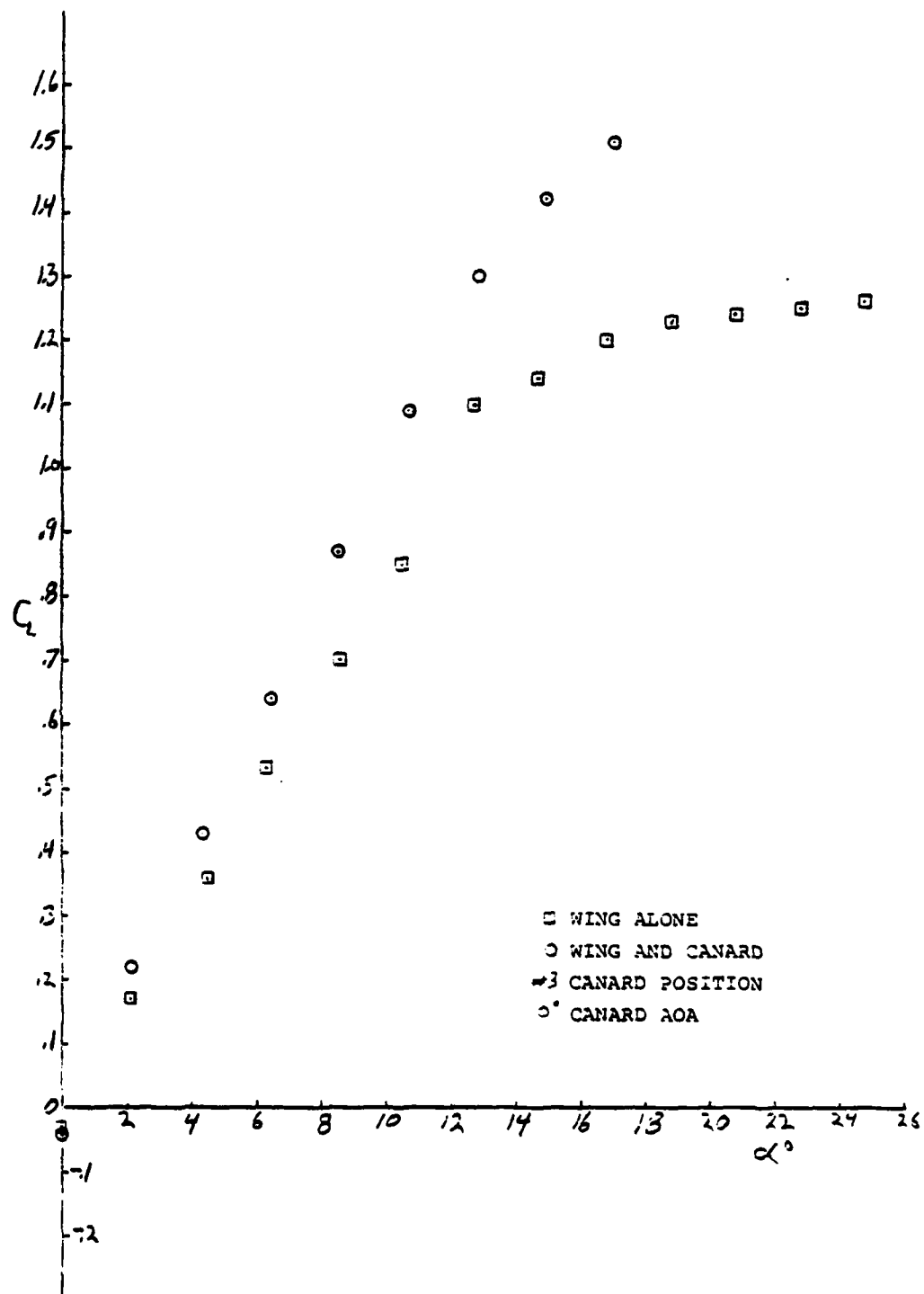


Figure 39A13L. Lift Coefficient vs Alpha

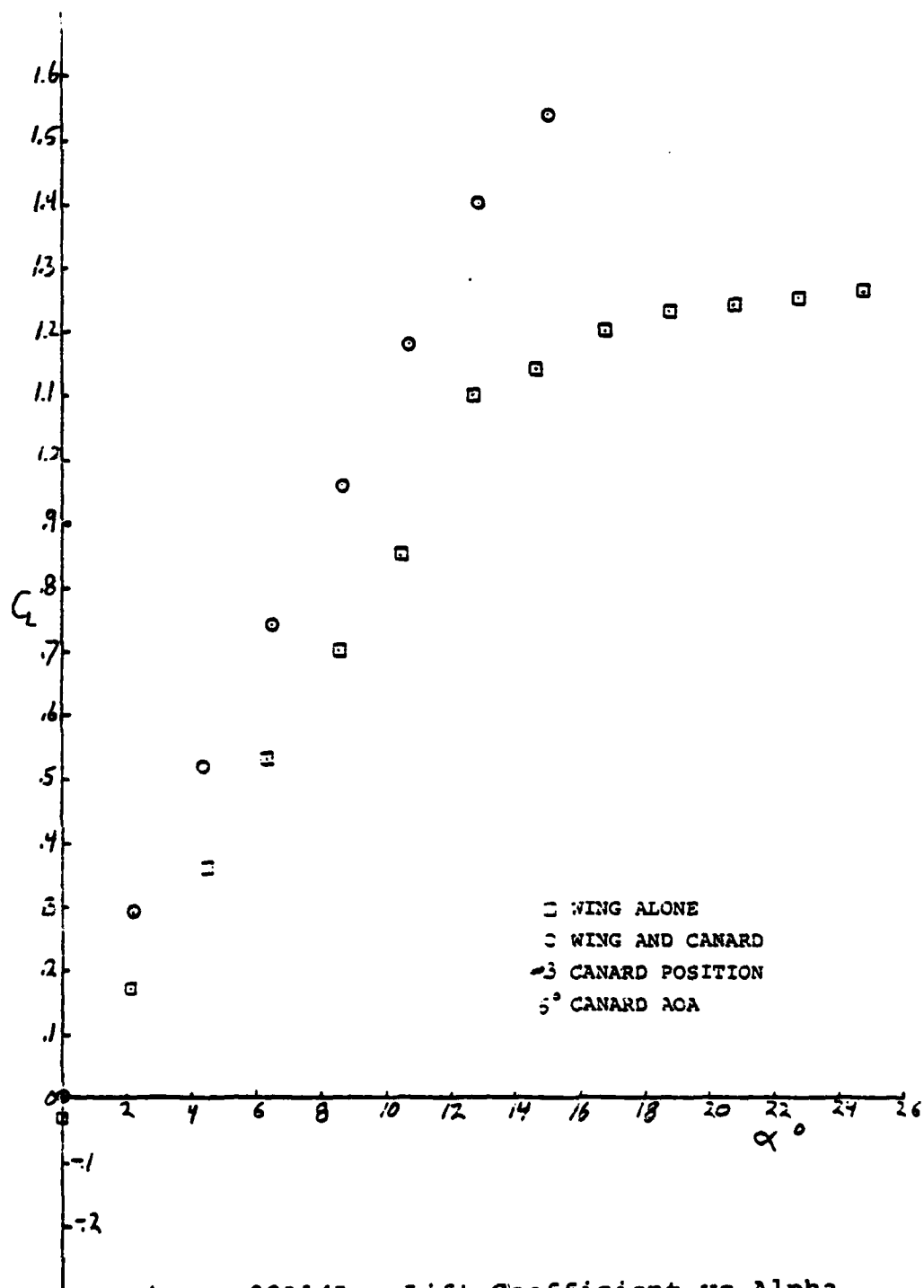


Figure 39A14L. Lift Coefficient vs Alpha

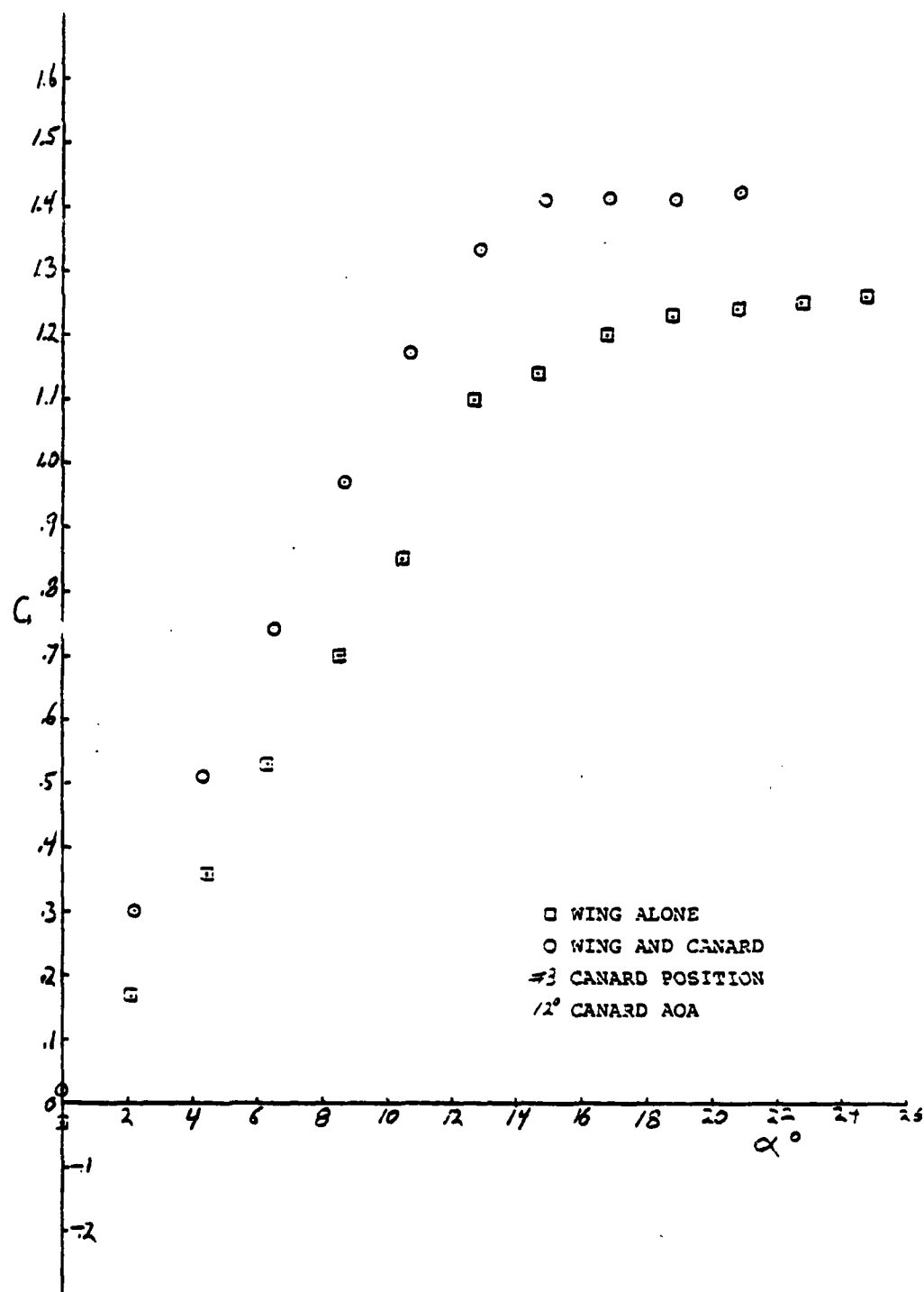


Figure 39A15L. Lift Coefficient vs Alpha

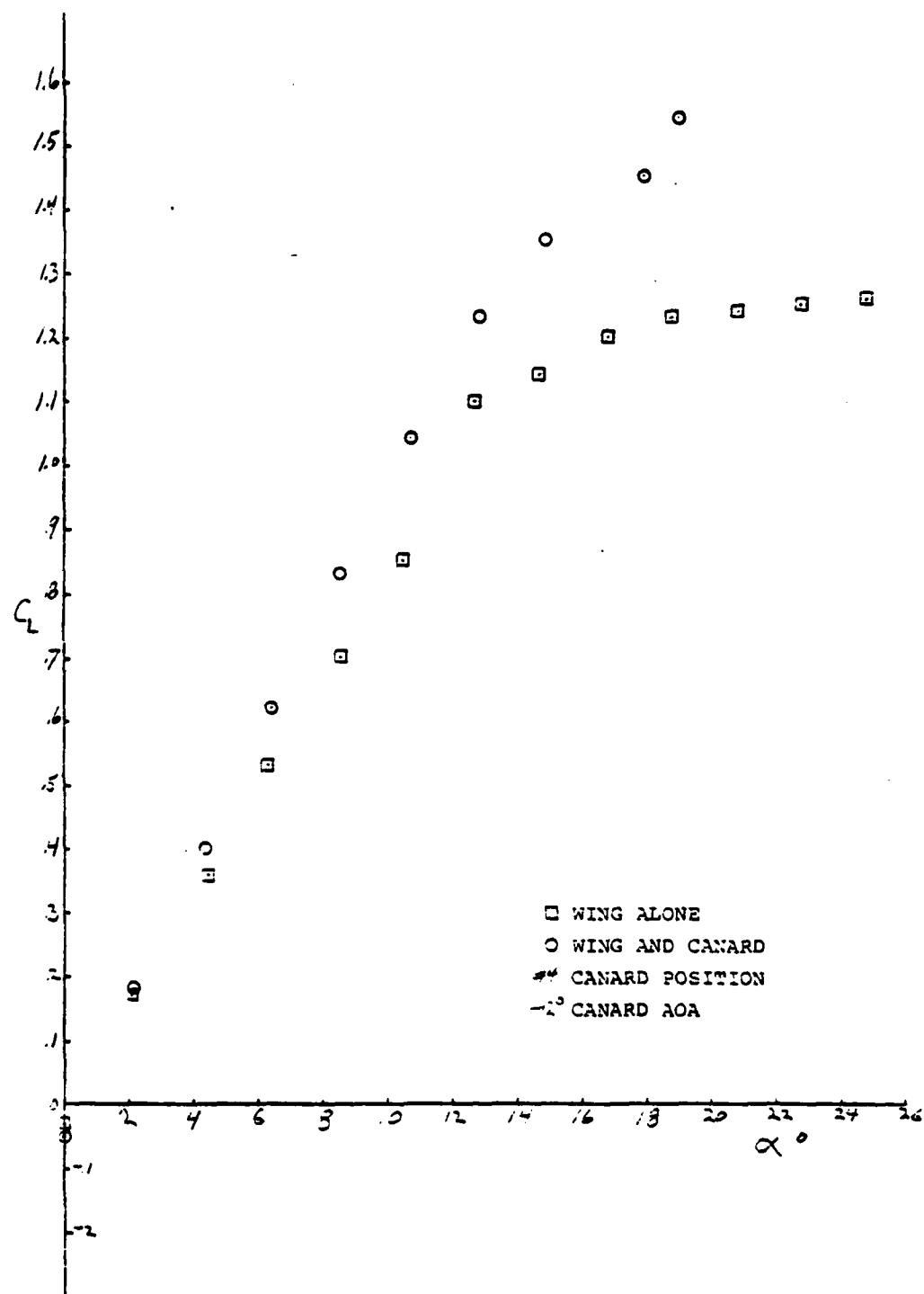


Figure 39A16L. Lift Coefficient vs Alpha

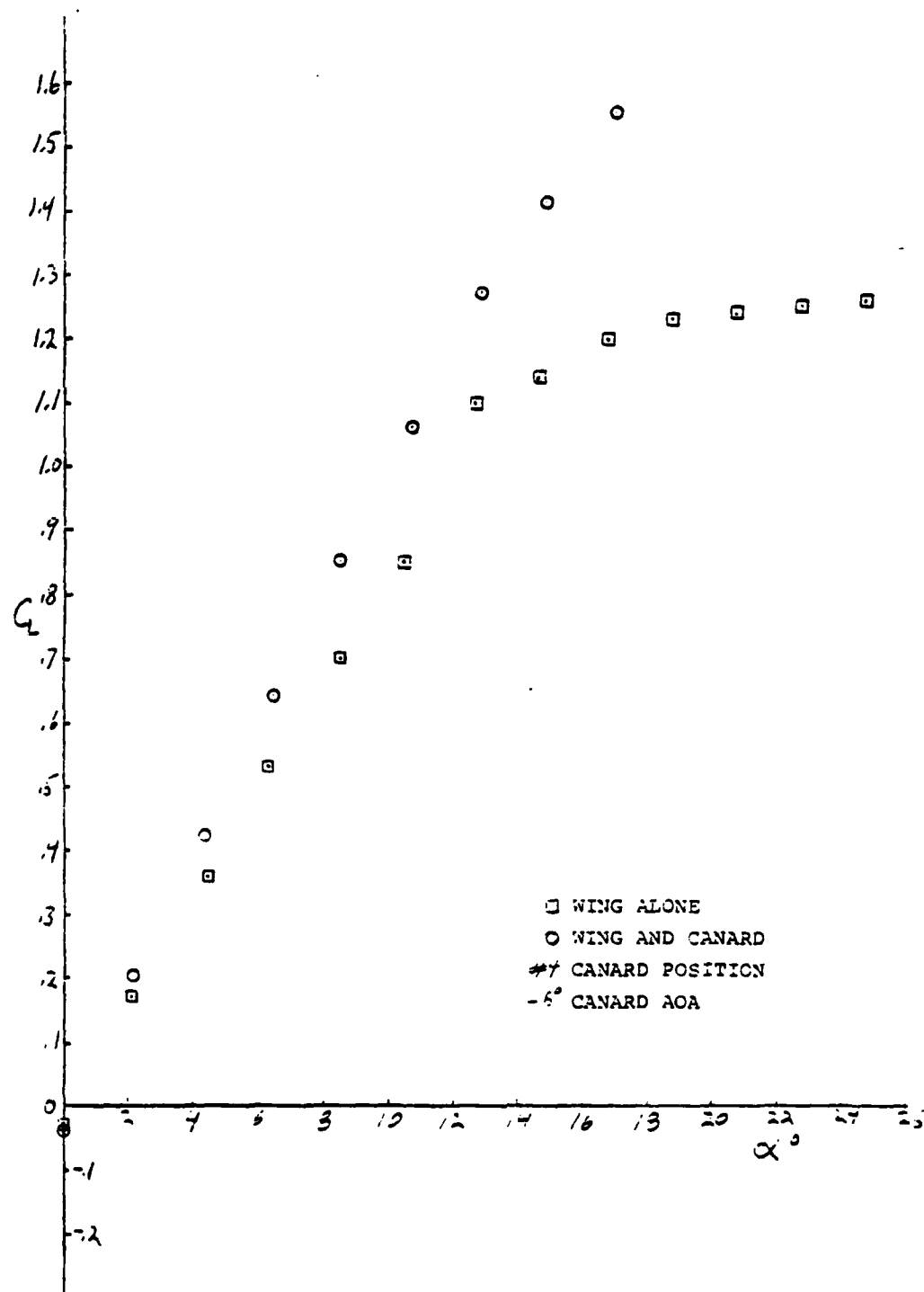


Figure 39A17L. Lift Coefficient vs Alpha

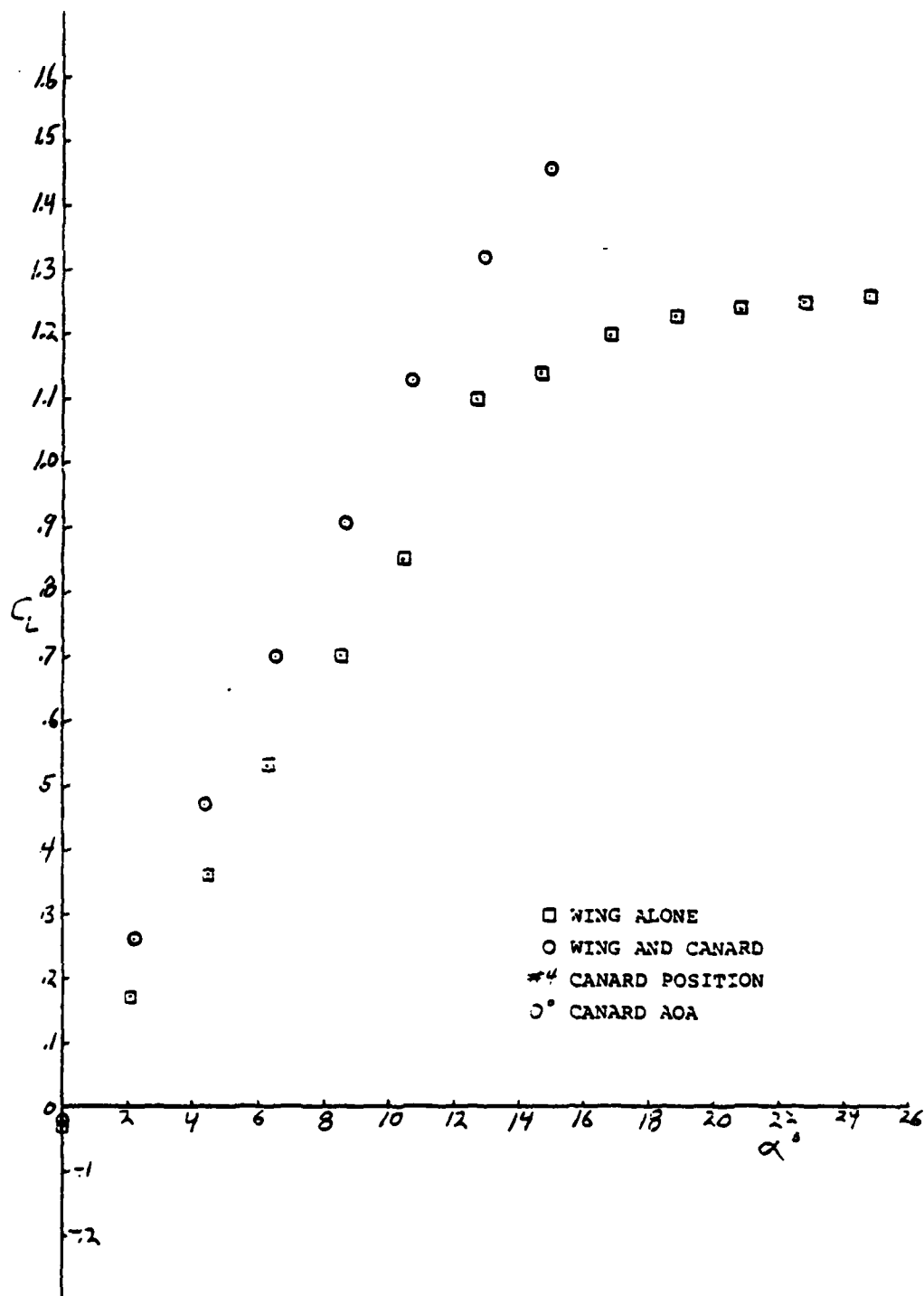


Figure 39A18L. Lift Coefficient vs Alpha

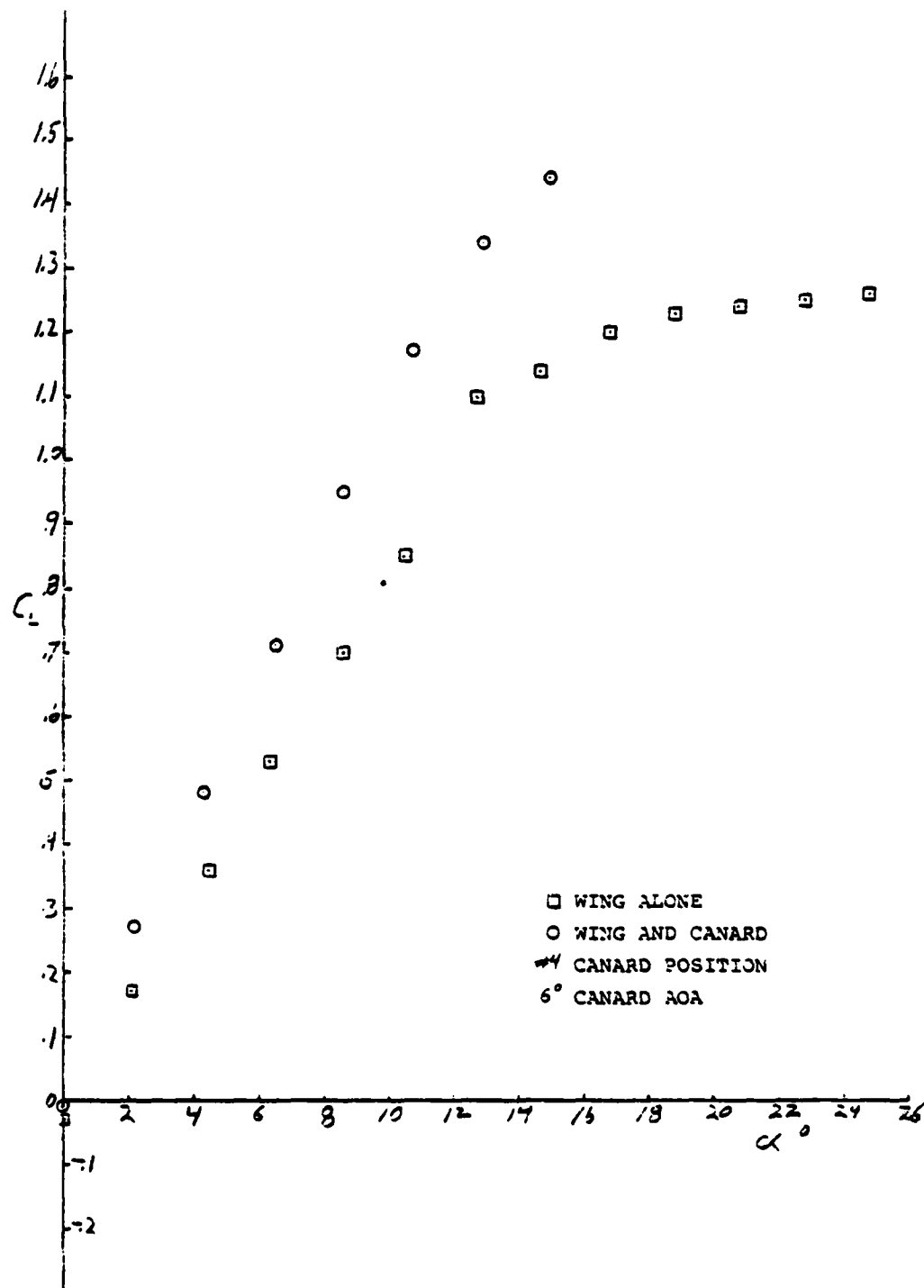


Figure 39A19L. Lift Coefficient vs Alpha

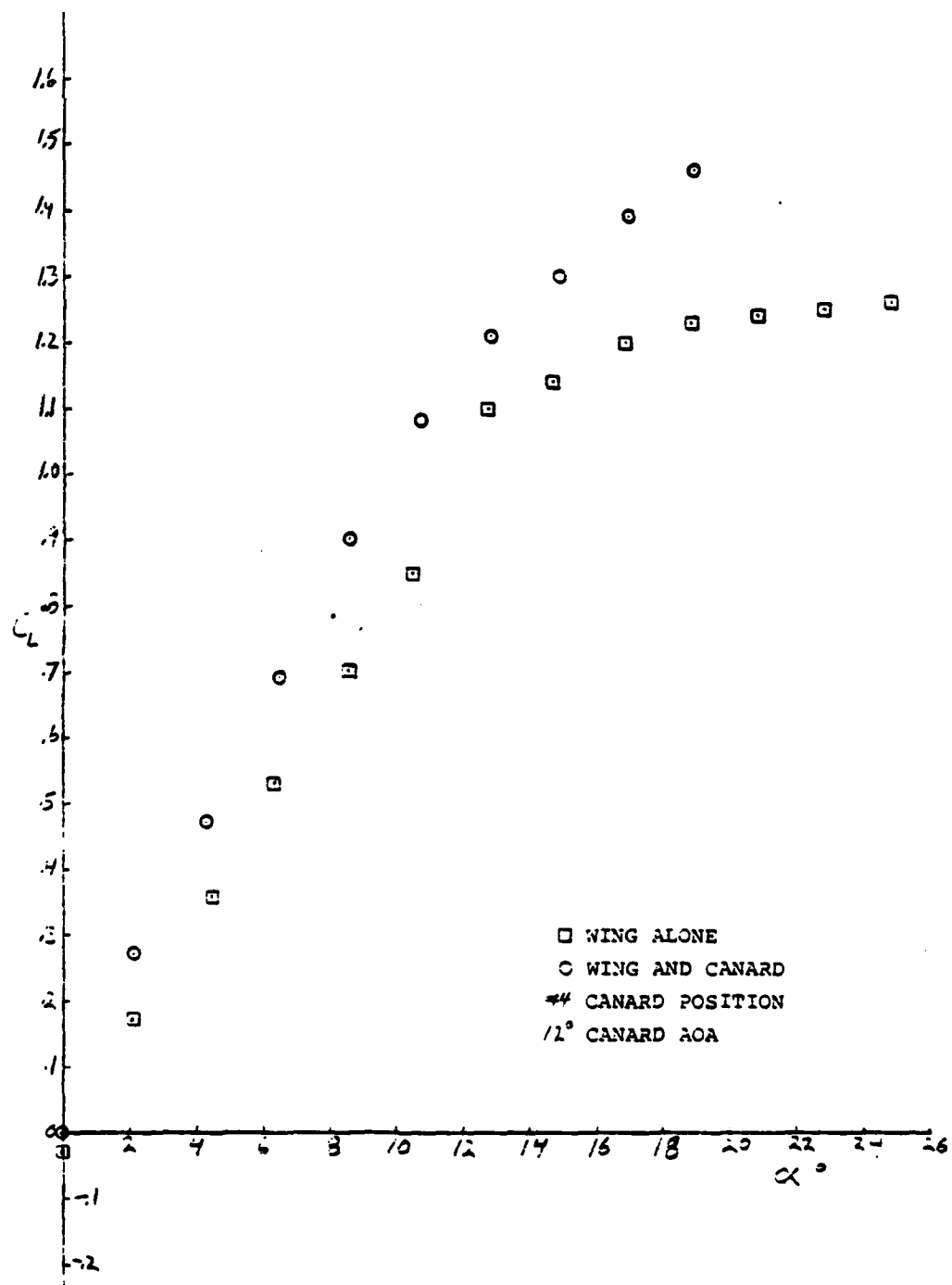


Figure 39A20L. Lift Coefficient vs Alpha

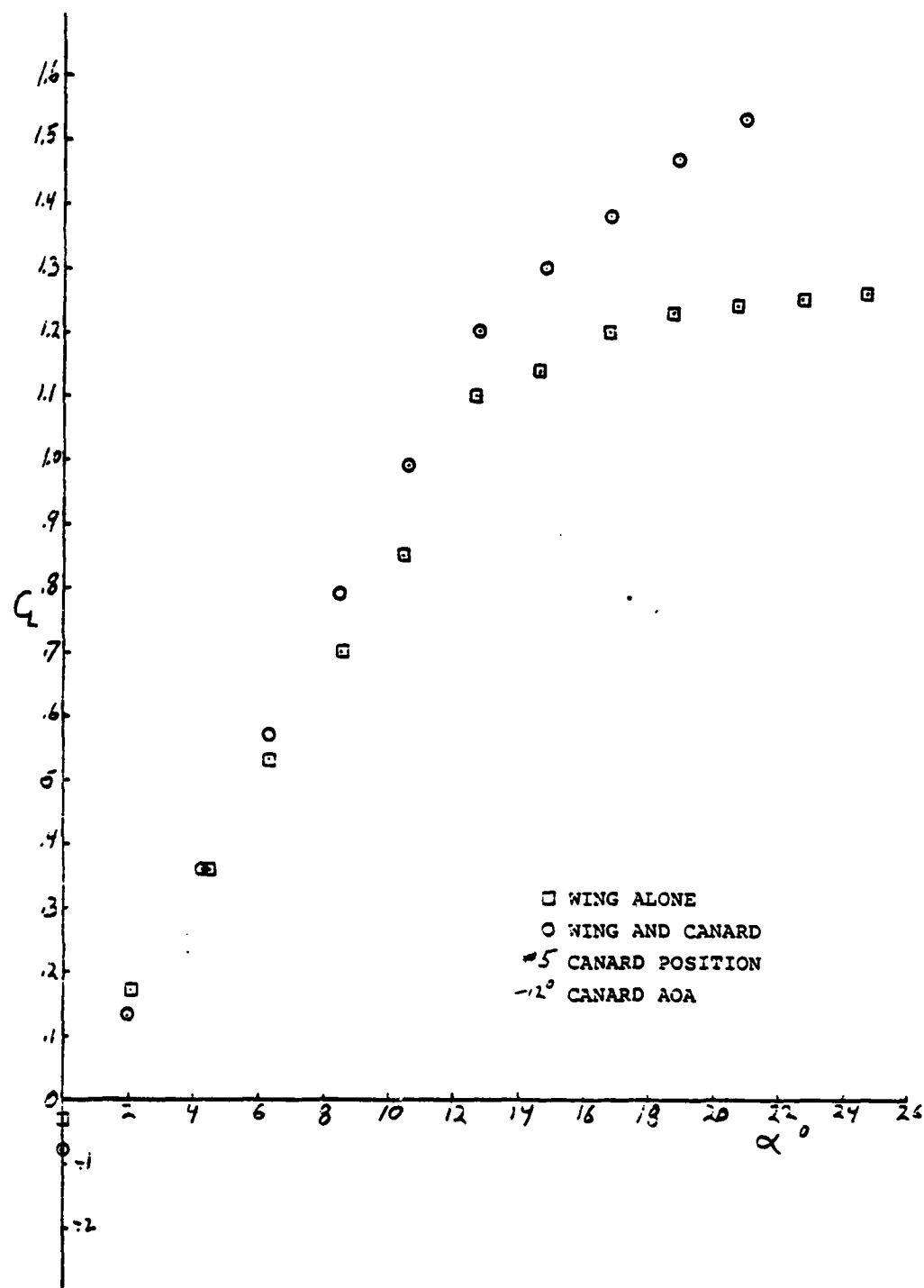


Figure 39A21L. Lift Coefficient vs Alpha

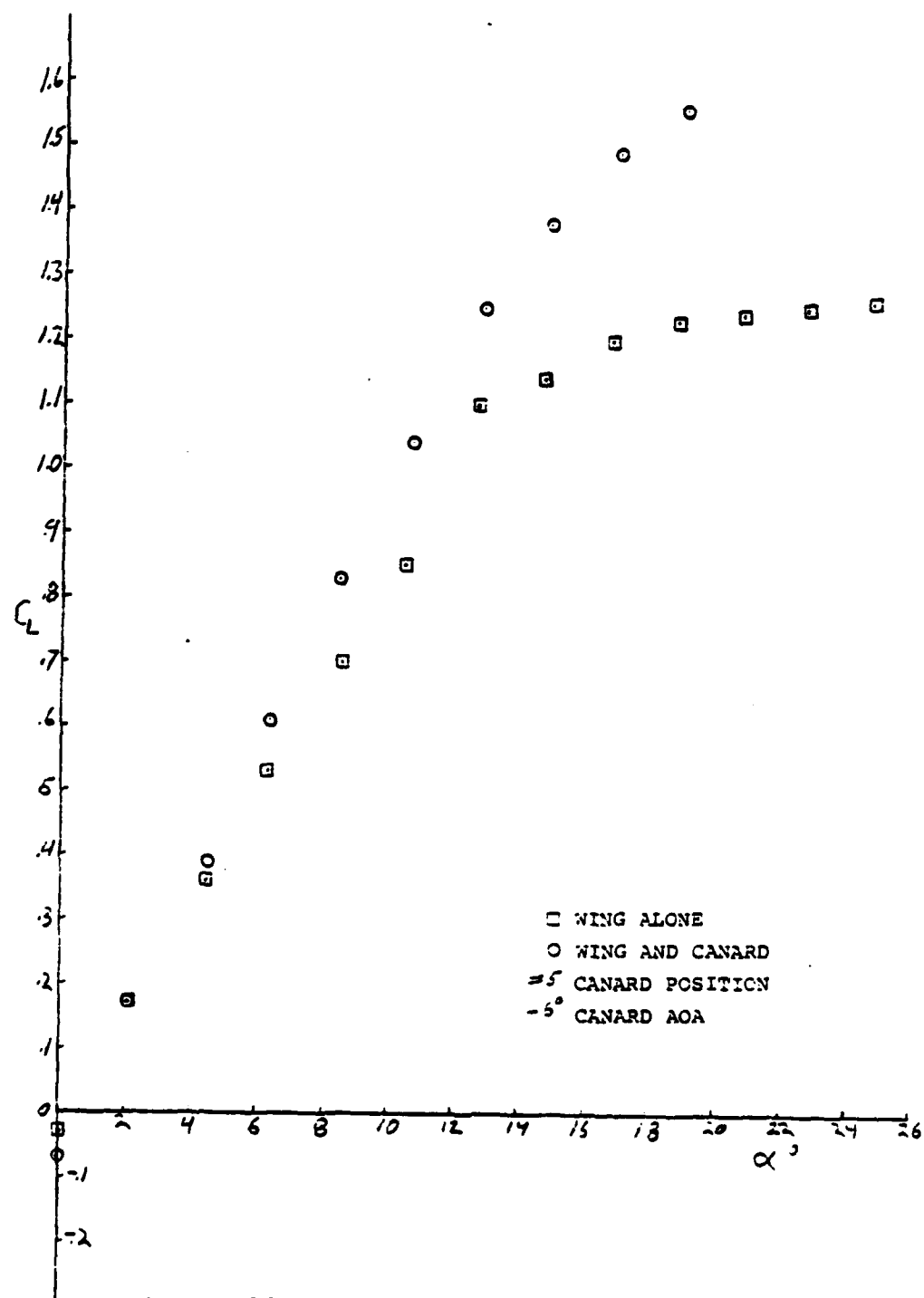


Figure 39A22L. Lift Coefficient vs Alpha

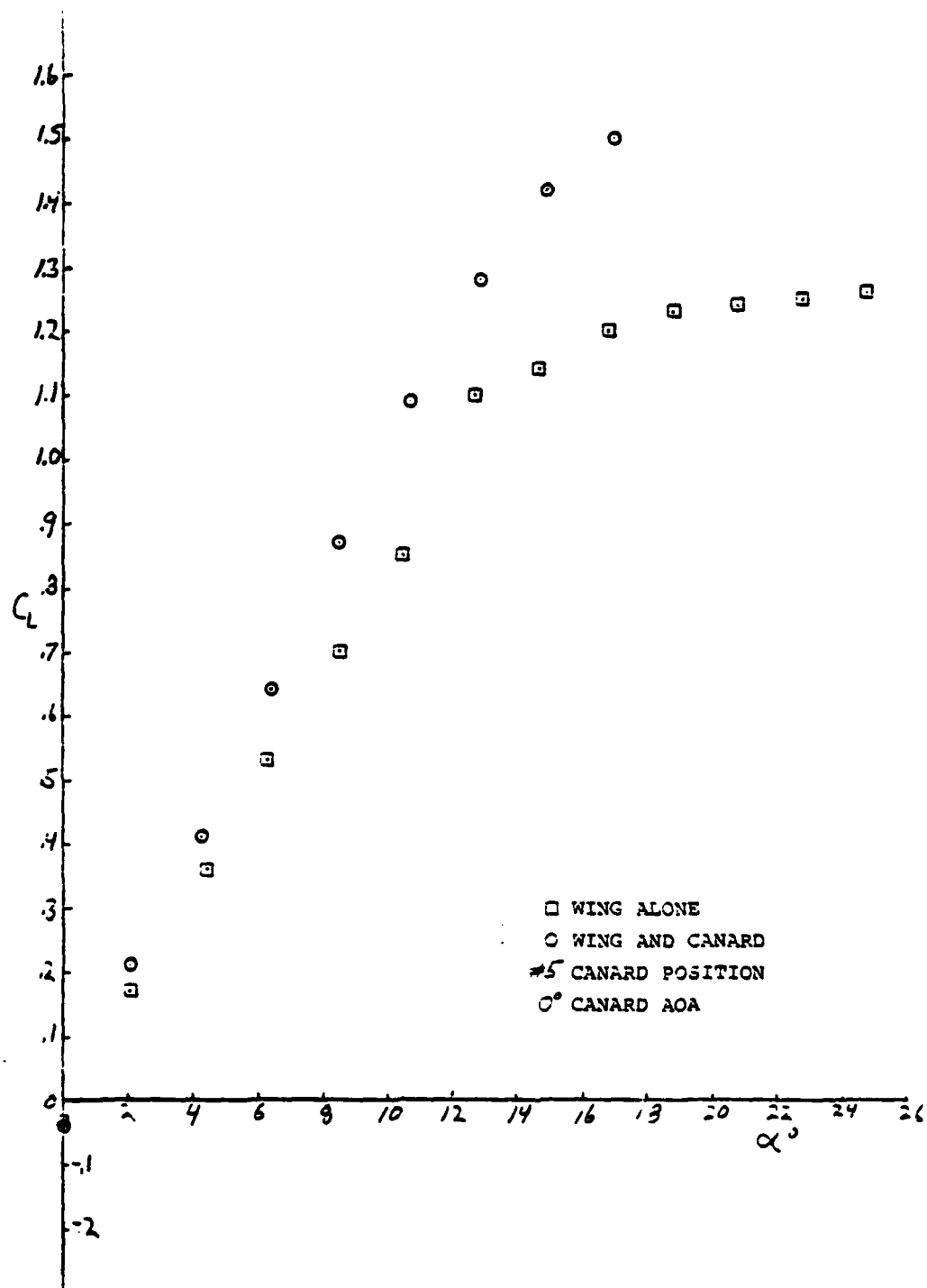


Figure 39A23L. Lift Coefficient vs Alpha

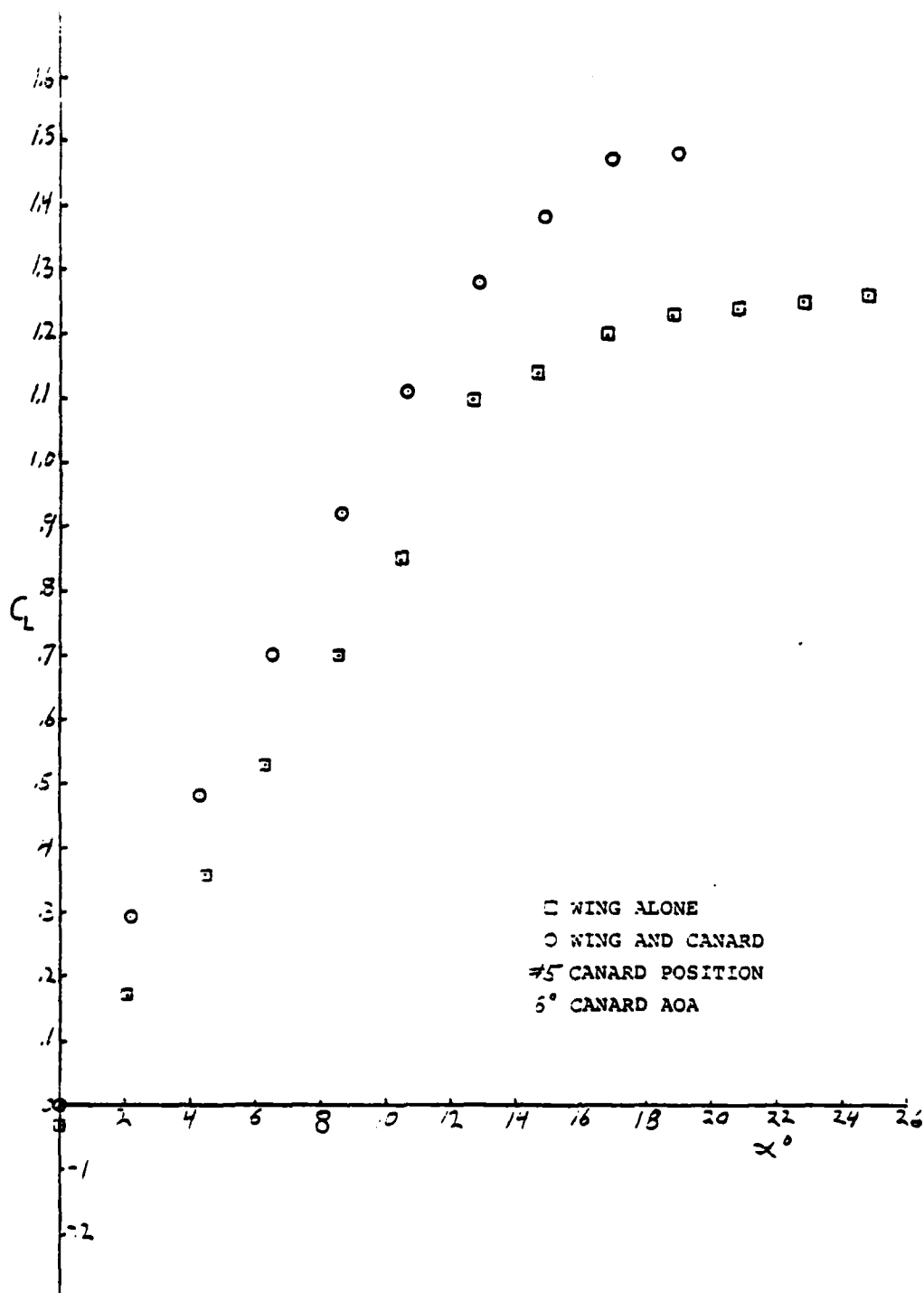


Figure 39A24L. Lift Coefficient vs Alpha

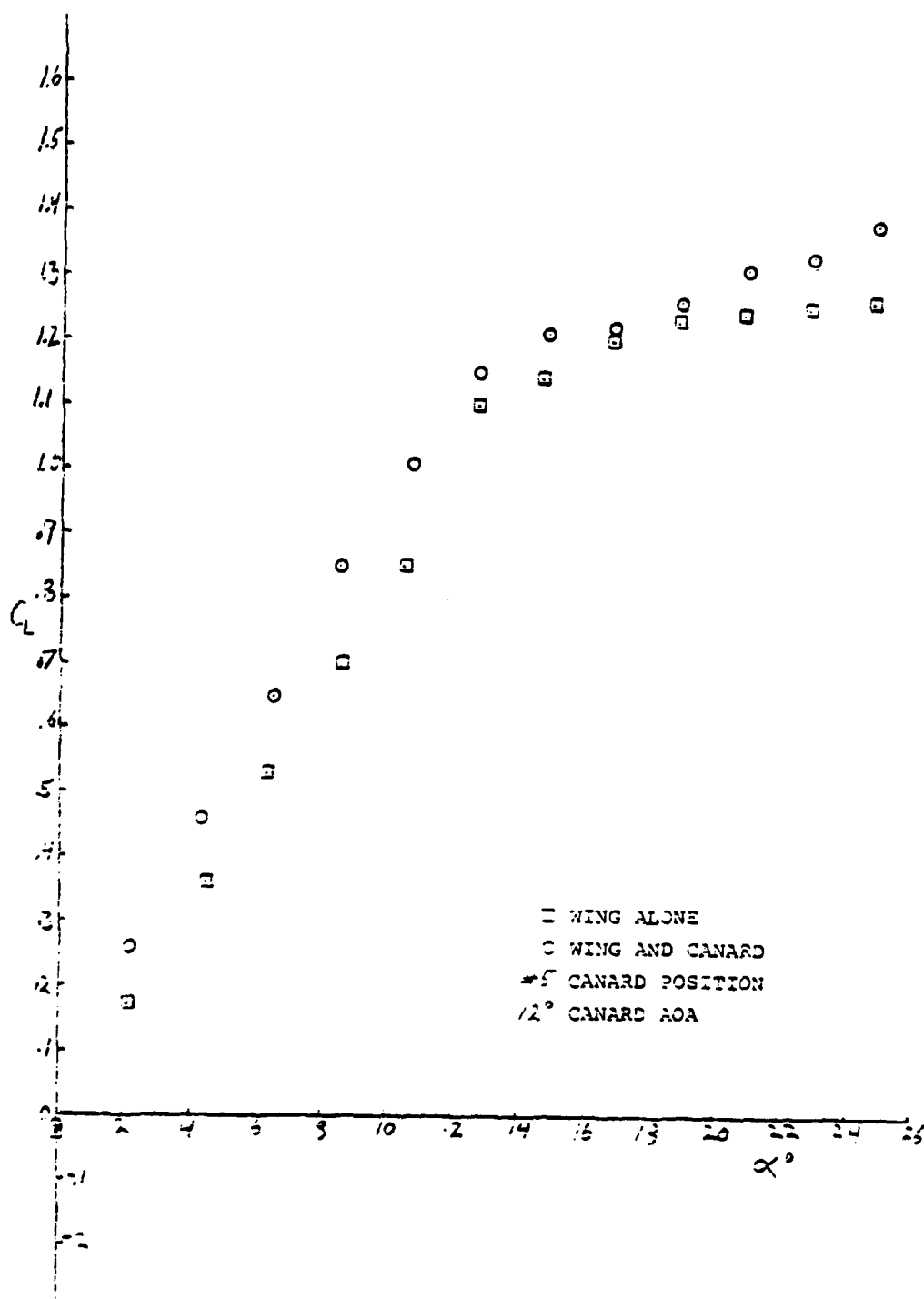


Figure 39A25L. Lift Coefficient vs Alpha

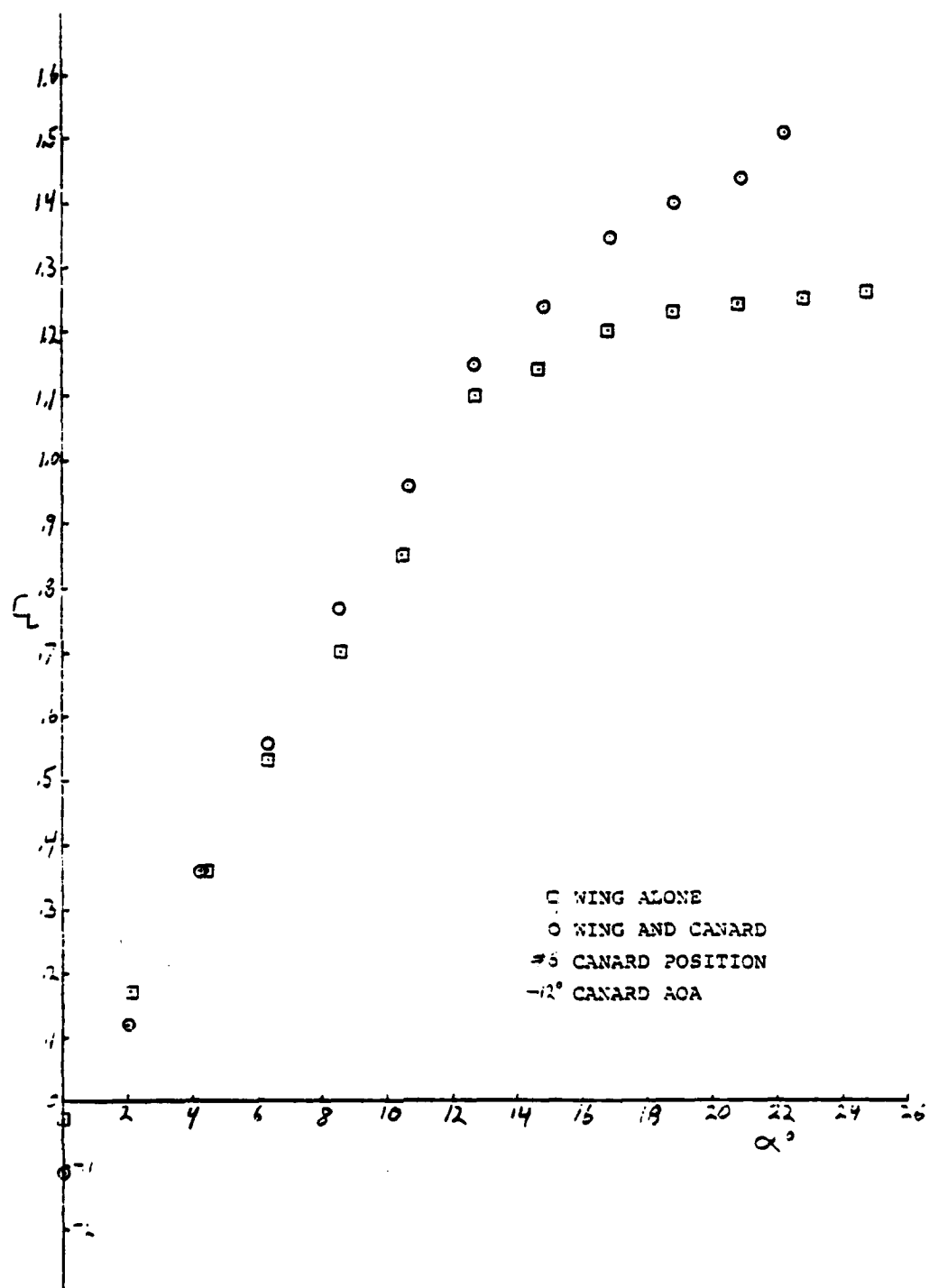


Figure 39A26L. Lift Coefficient vs Alpha

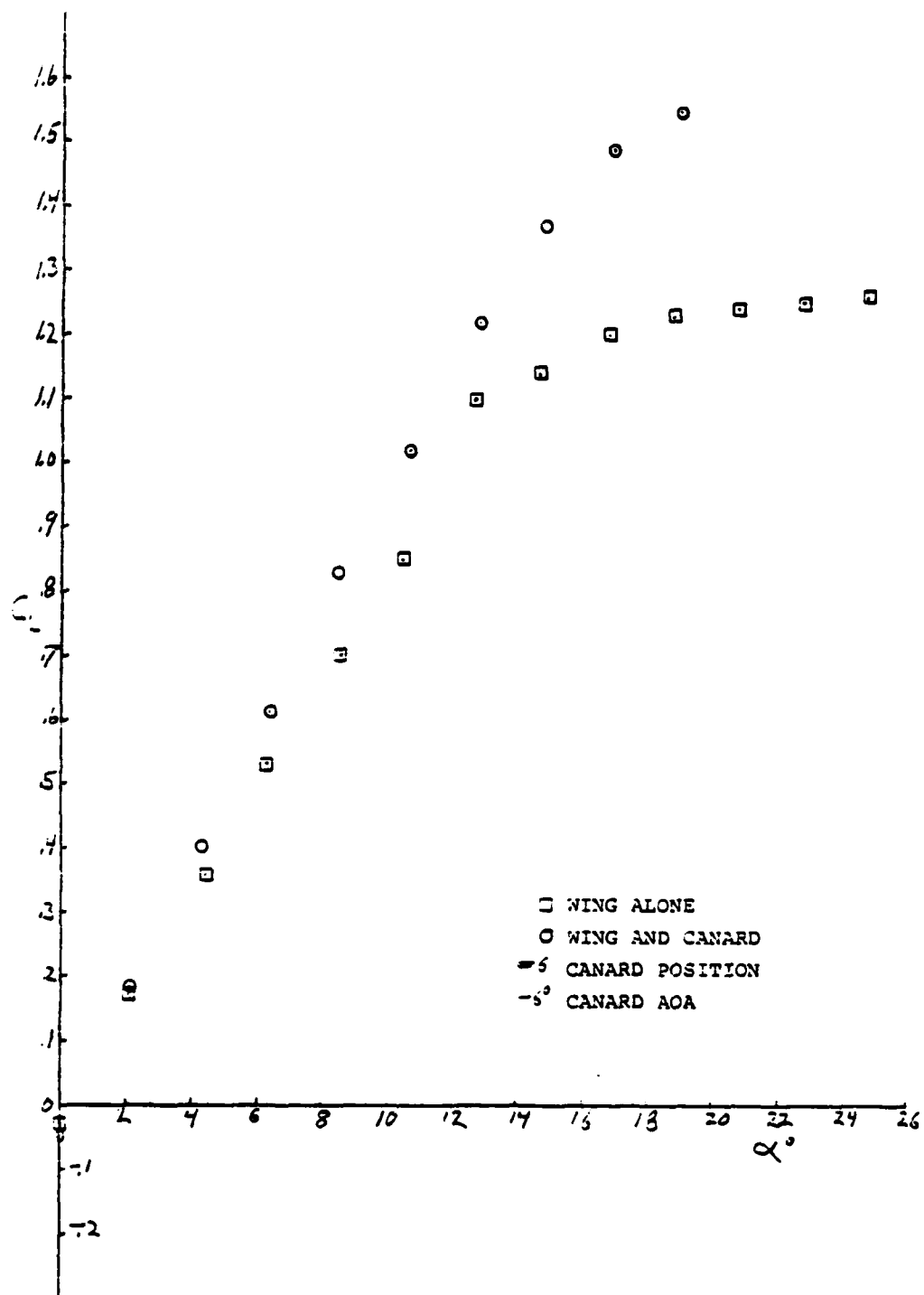


Figure 39A27L. Lift Coefficient vs Alpha

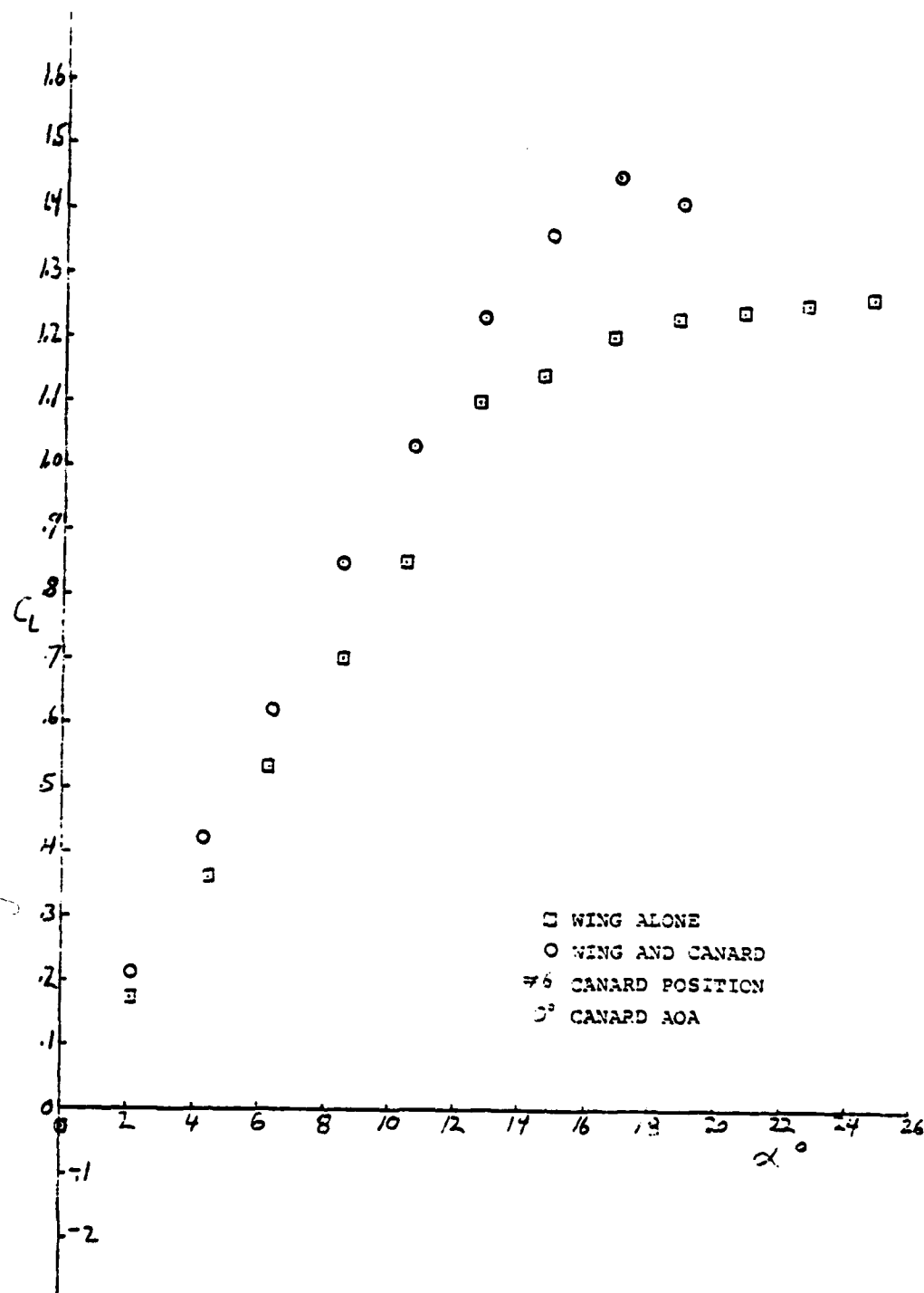


Figure 39A28L. Lift Coefficient vs Alpha

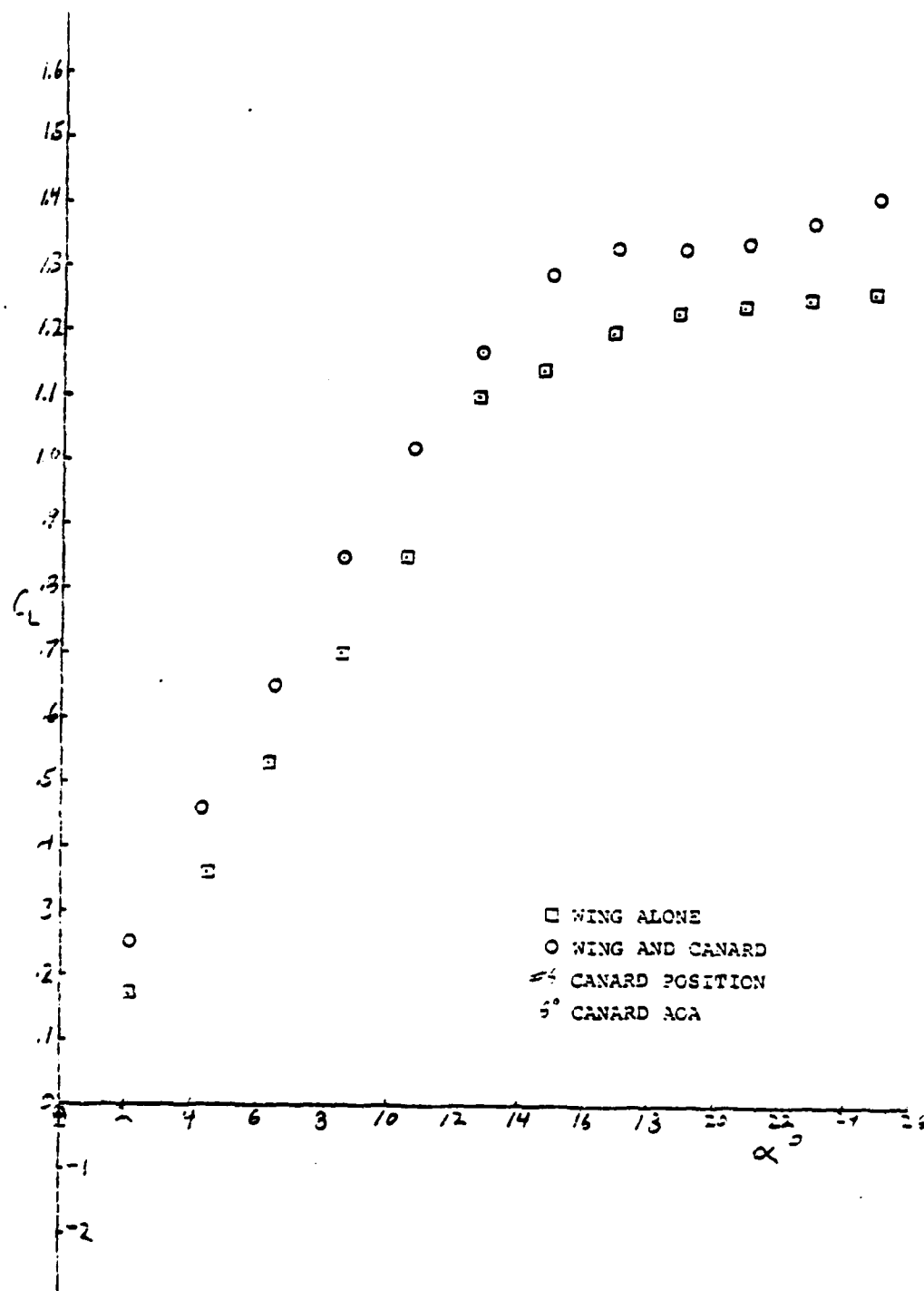


Figure 39A29L. Lift Coefficient vs Alpha

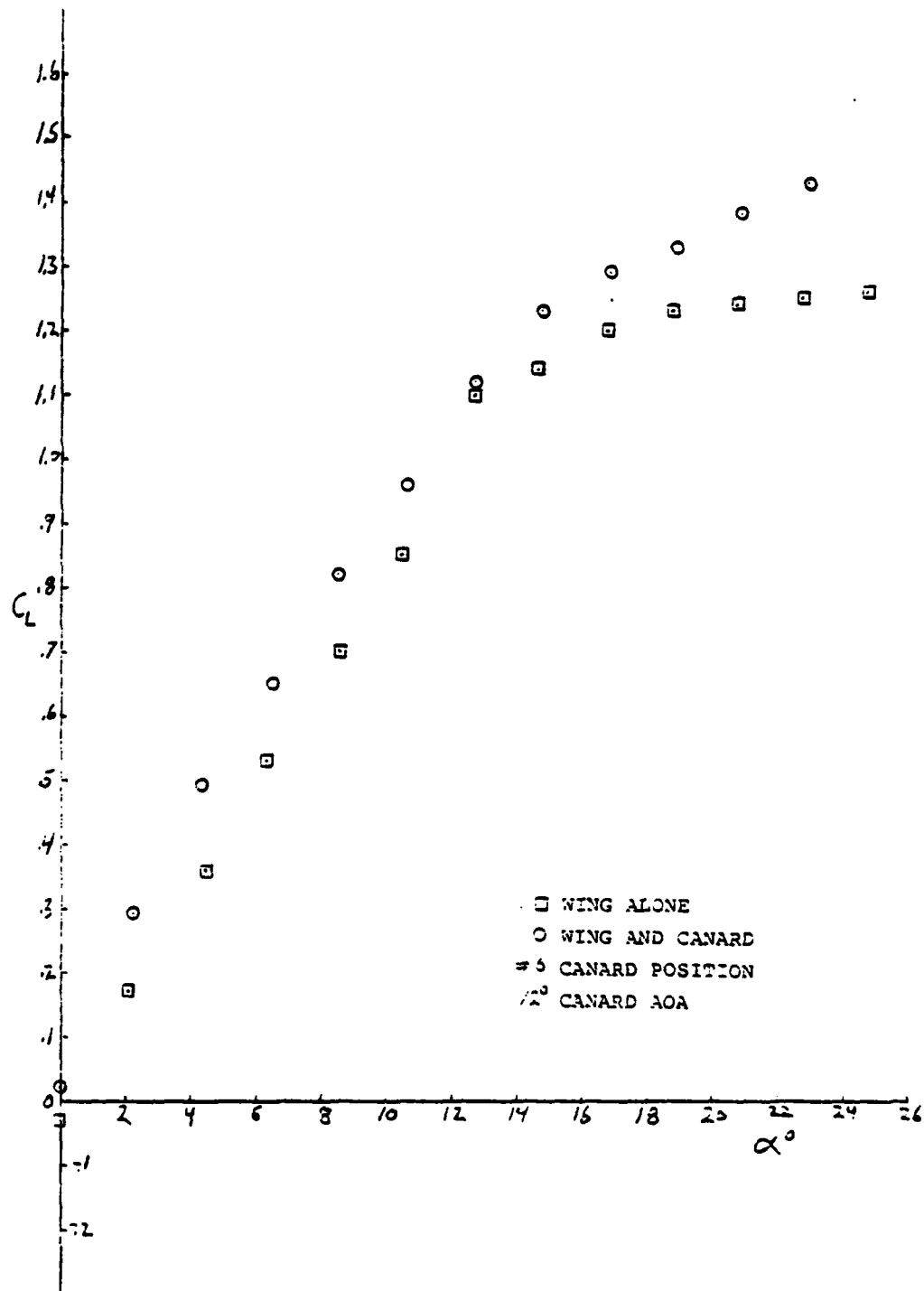


Figure 39A30L. Lift Coefficient vs Alpha

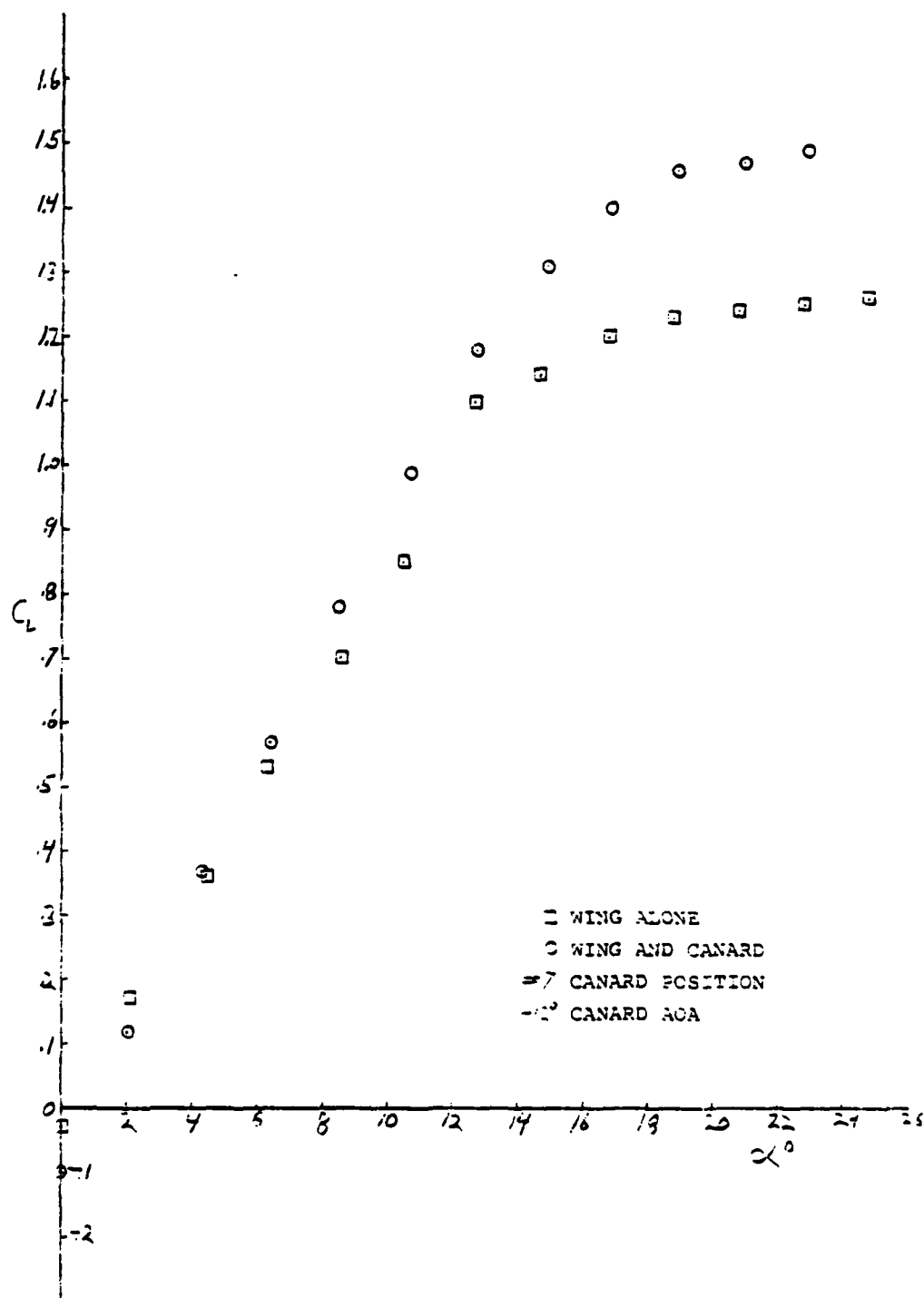


Figure 39A31L. Lift Coefficient vs Alpha

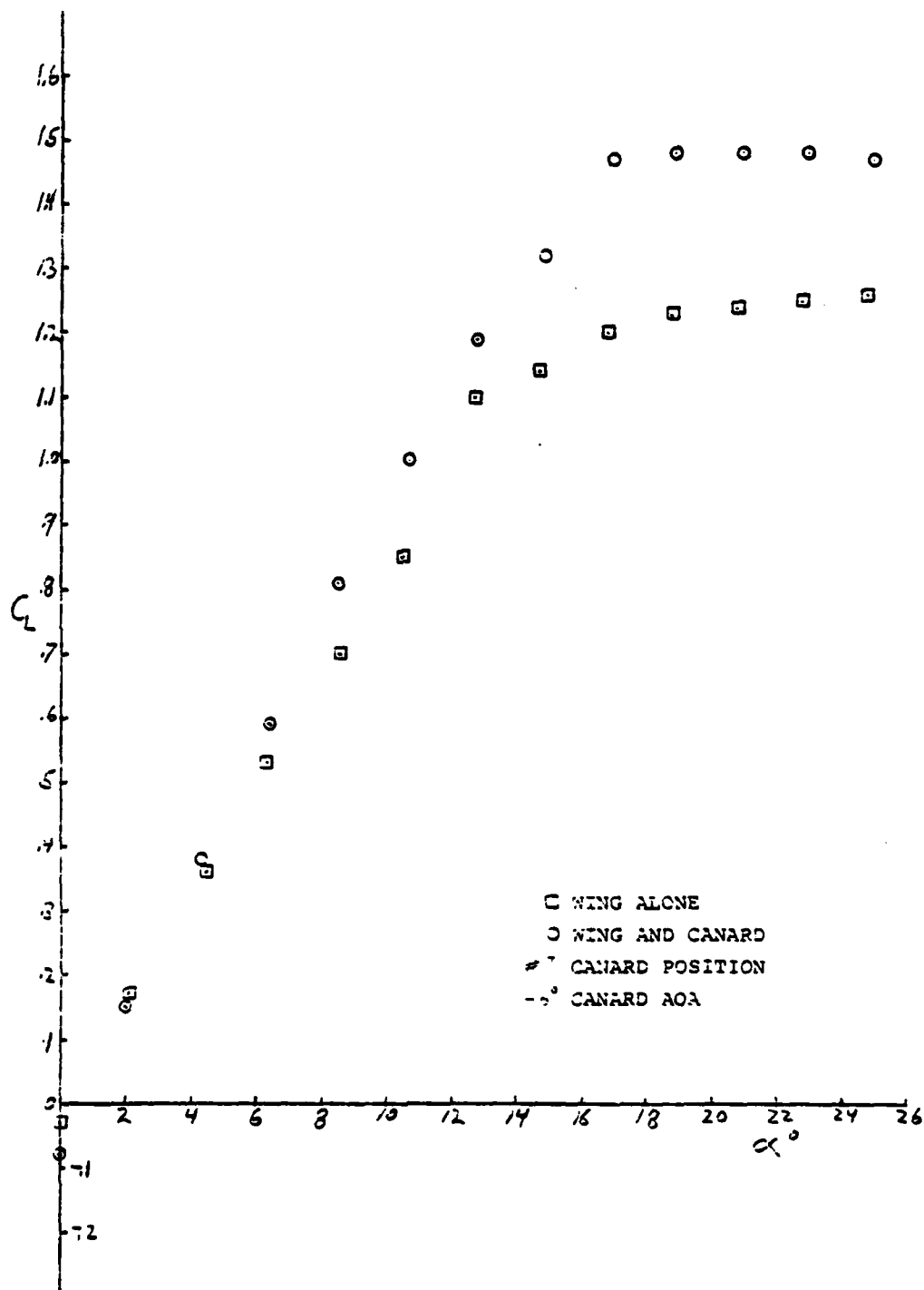


Figure 39A32L. Lift Coefficient vs Alpha

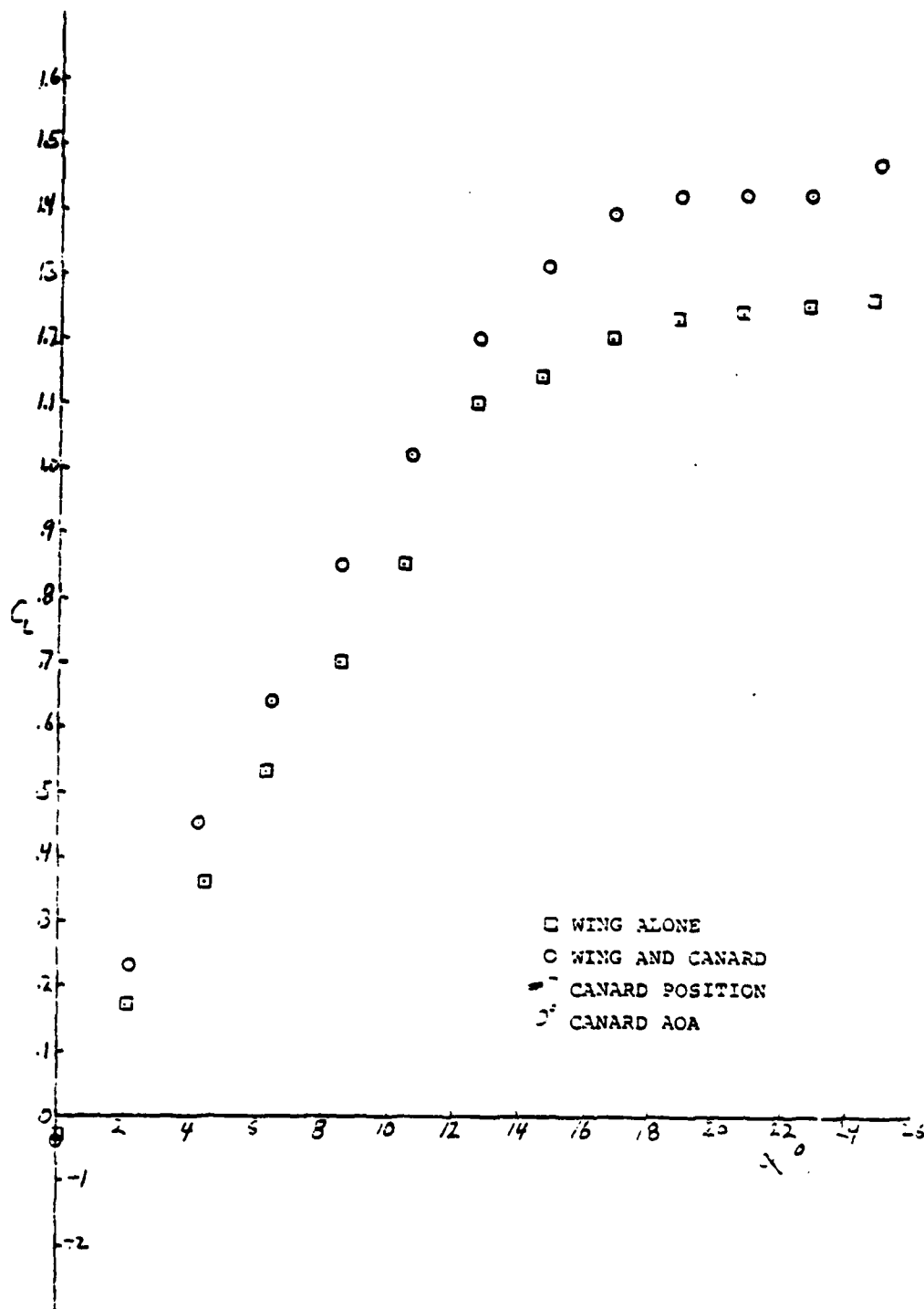


Figure 39A33L. Lift Coefficient vs Alpha

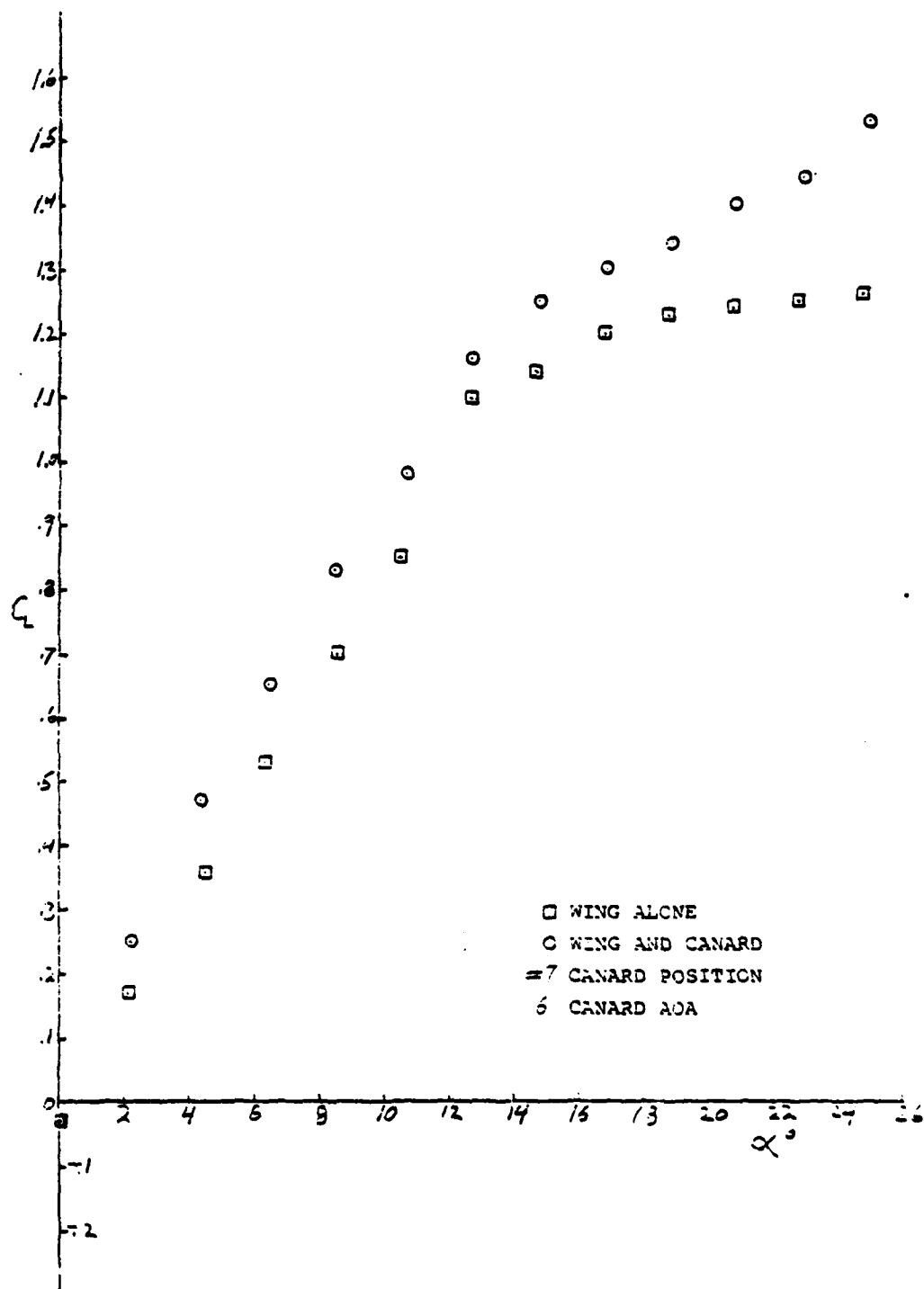


Figure 39A34L. Lift Coefficient vs Alpha

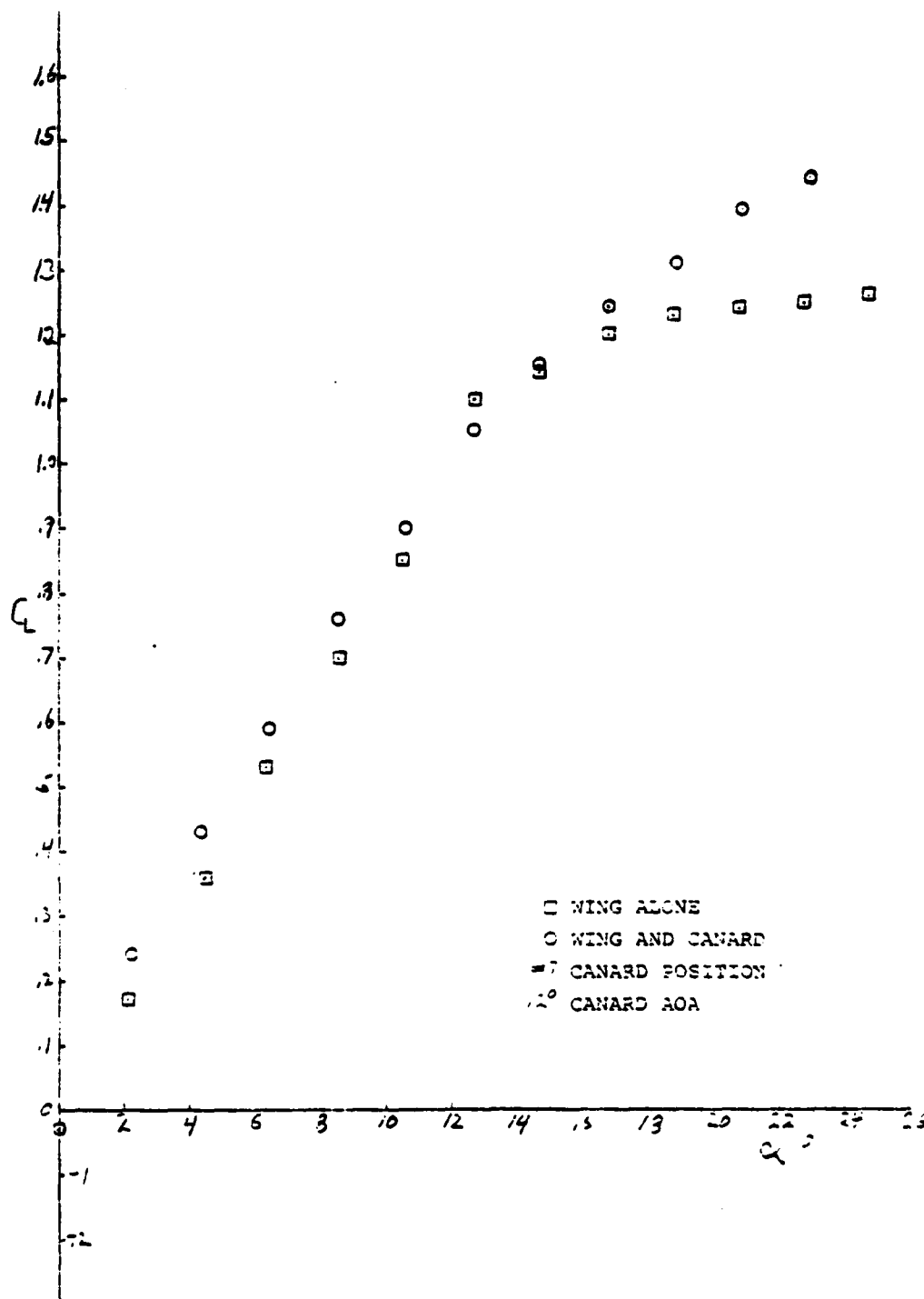


Figure 39A35L. Lift Coefficient vs Alpha

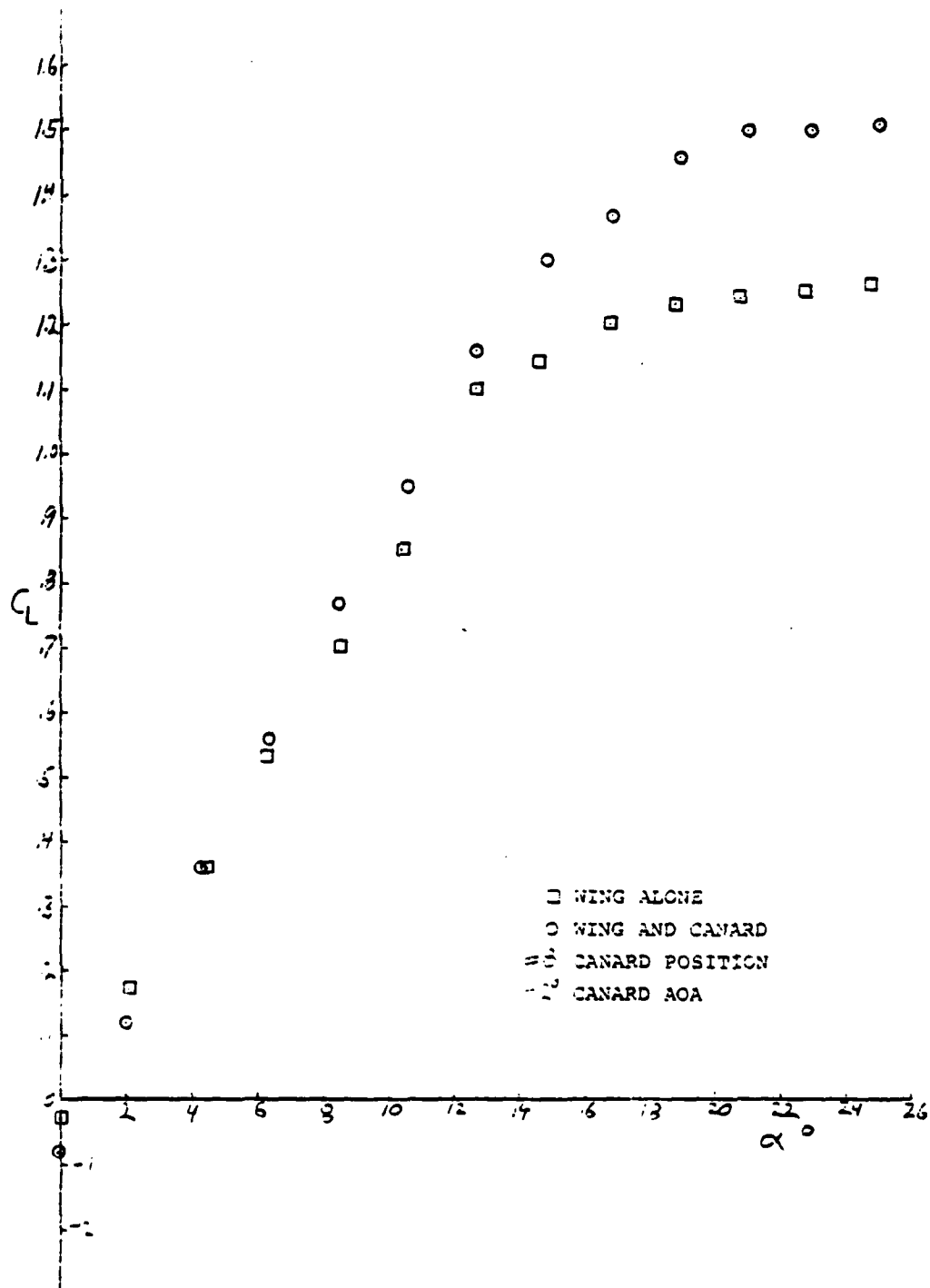


Figure 39A36L. Lift Coefficient vs Alpha

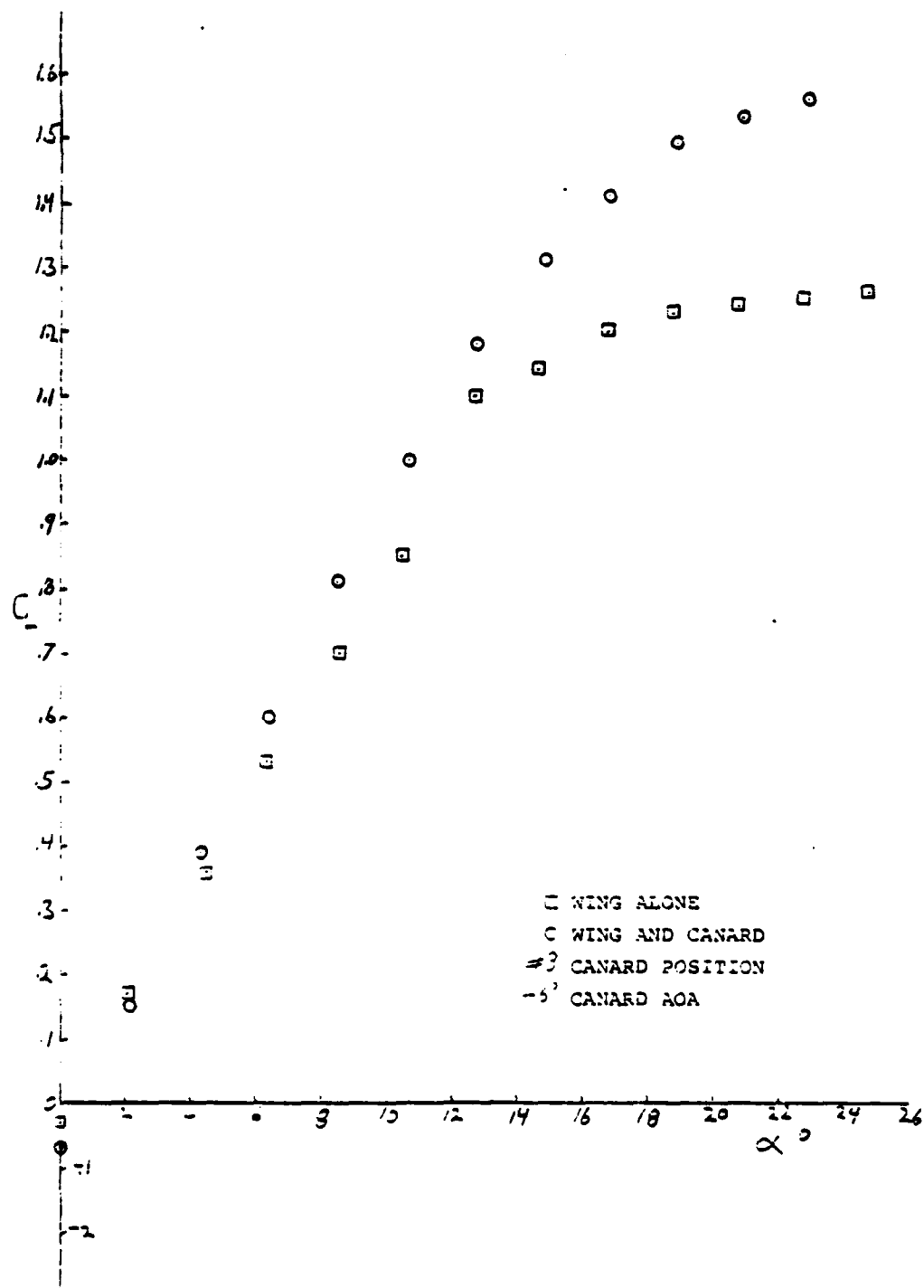


Figure 39A37L. Lift Coefficient vs Alpha

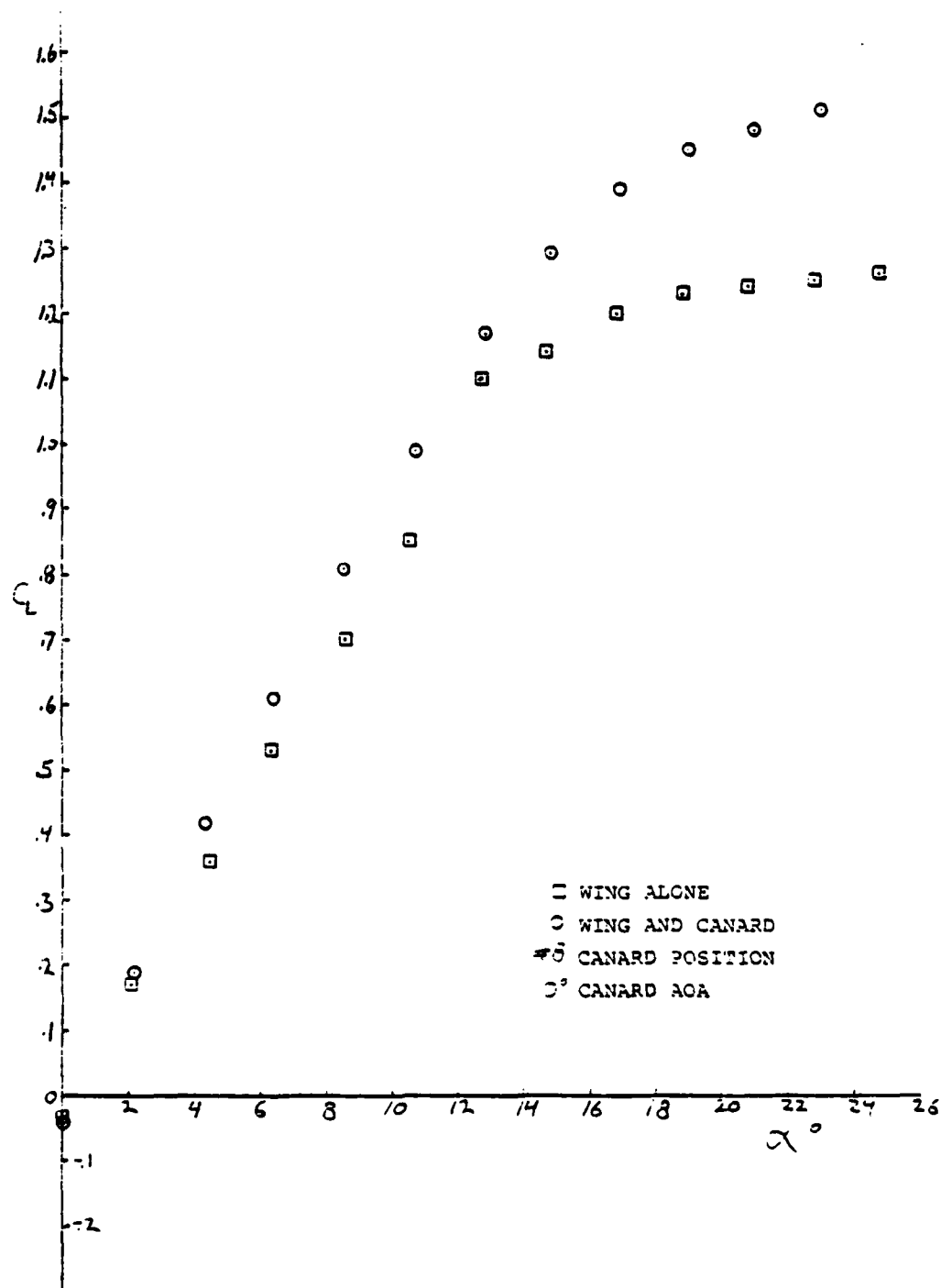


Figure 39A38L. Lift Coefficient vs Alpha

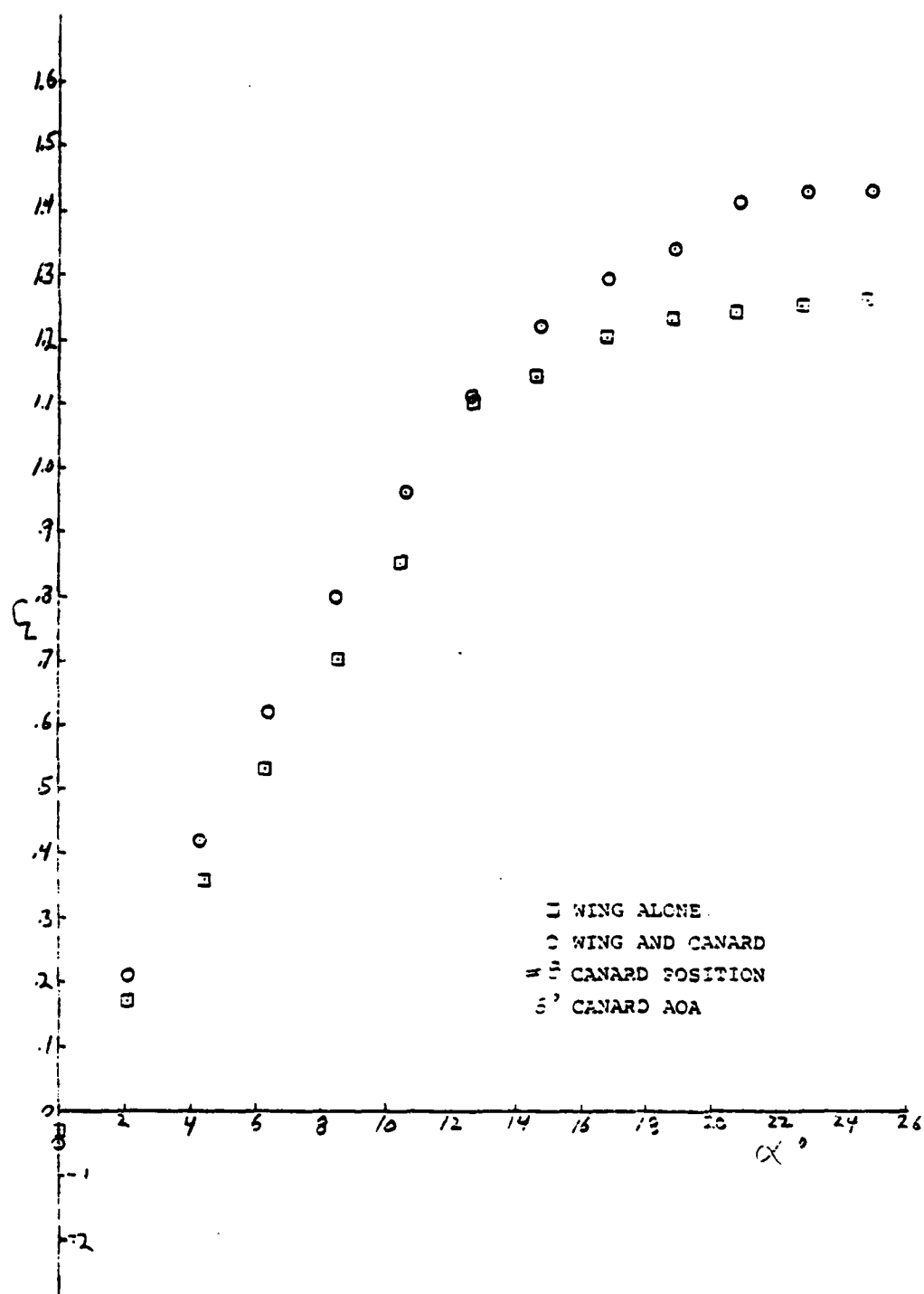


Figure 39A39L. Lift Coefficient vs Alpha

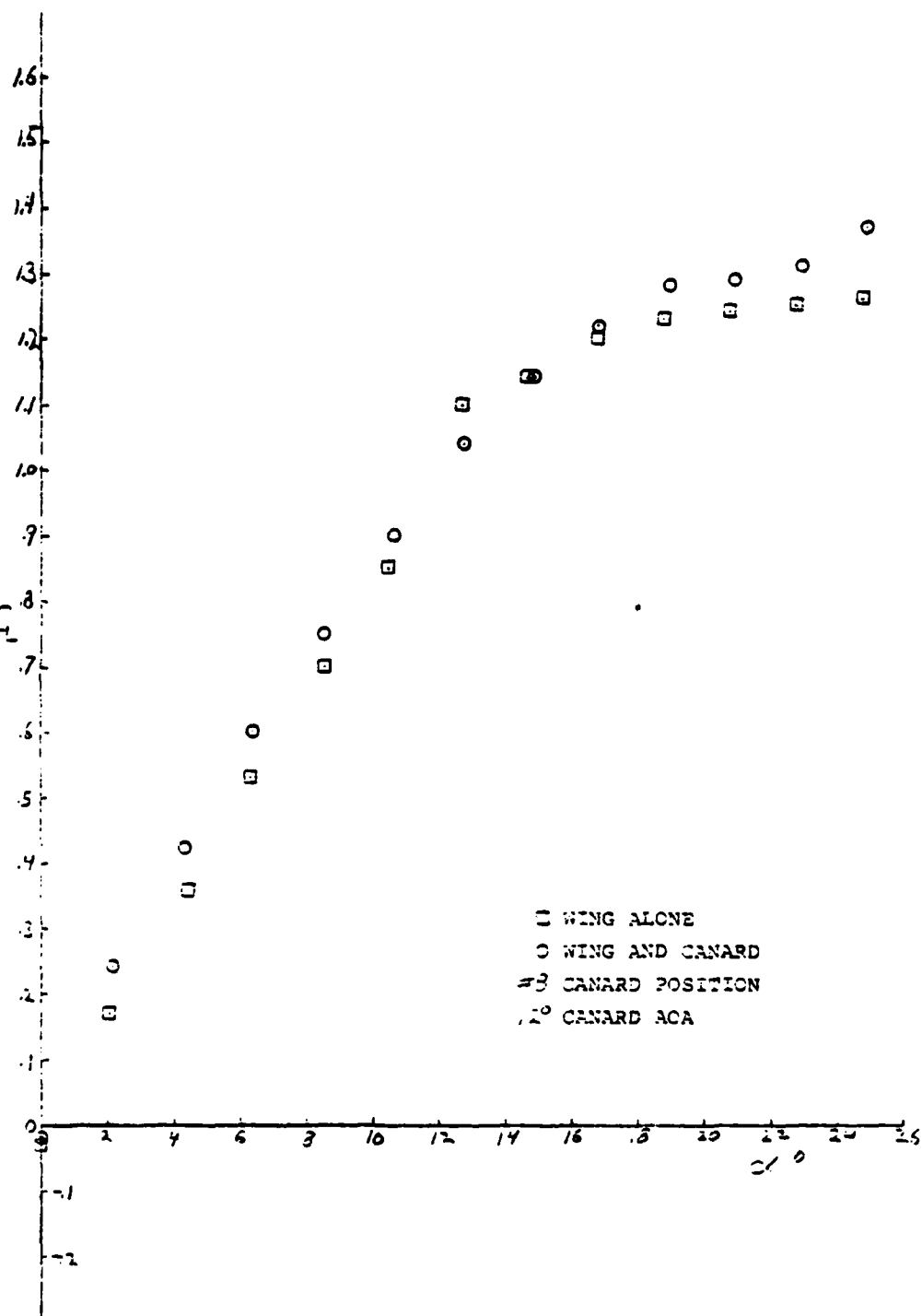


Figure 39A40L. Lift Coefficient vs Alpha

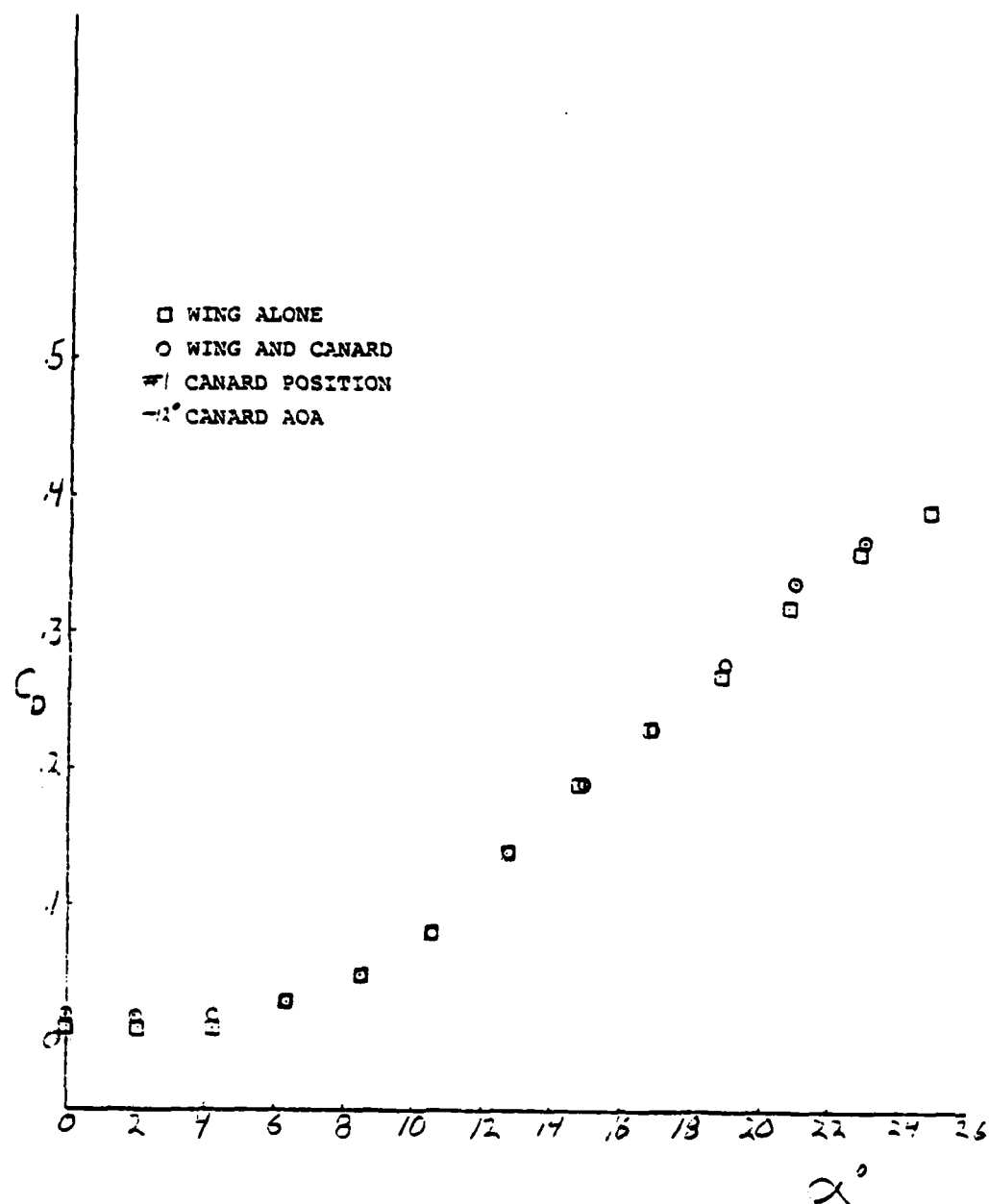


Figure 39A1D. Drag Coefficient vs Alpha

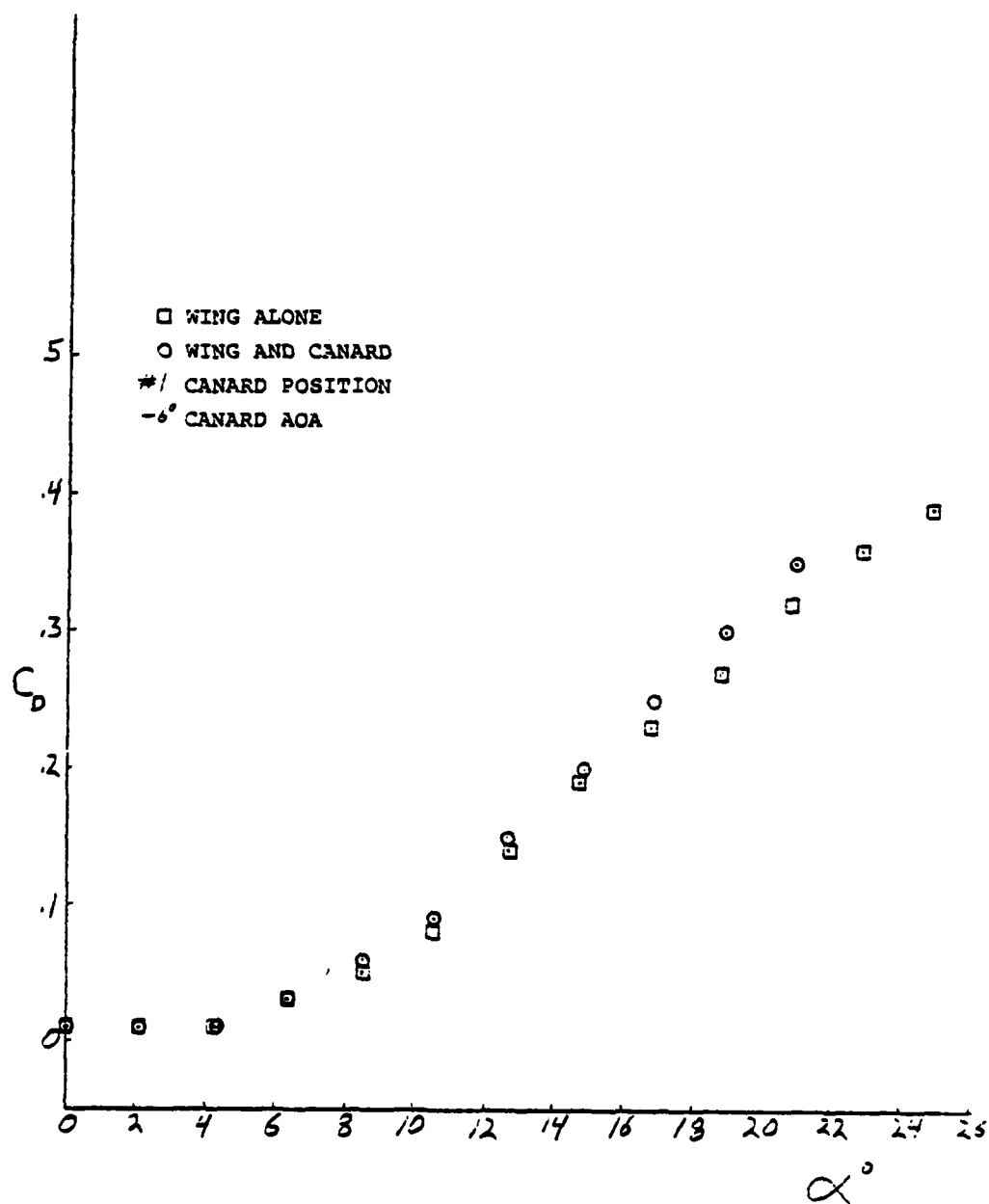


Figure 39A2D. Drag Coefficient vs Alpha

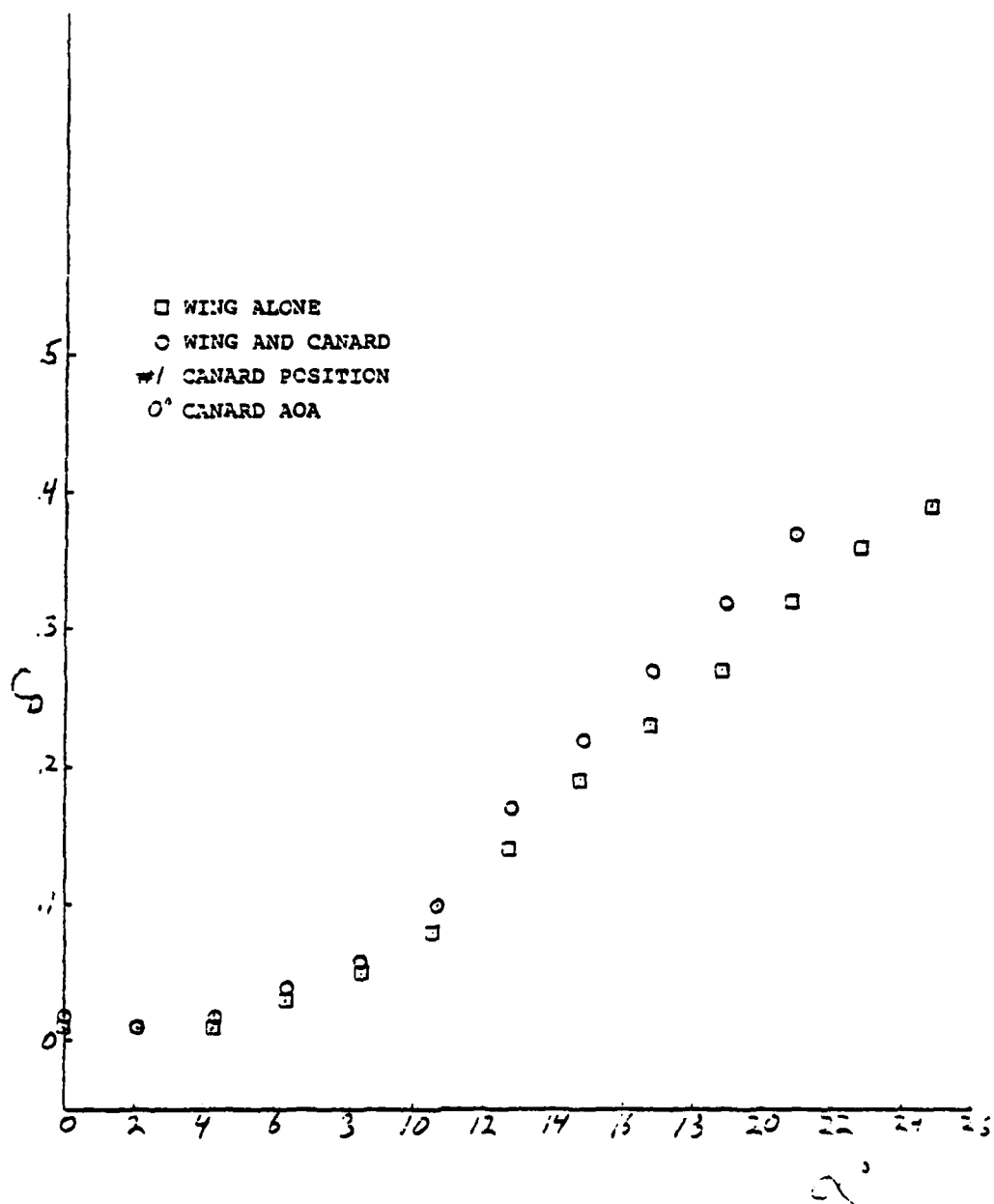


Figure 39A3D. Drag Coefficient vs Alpha

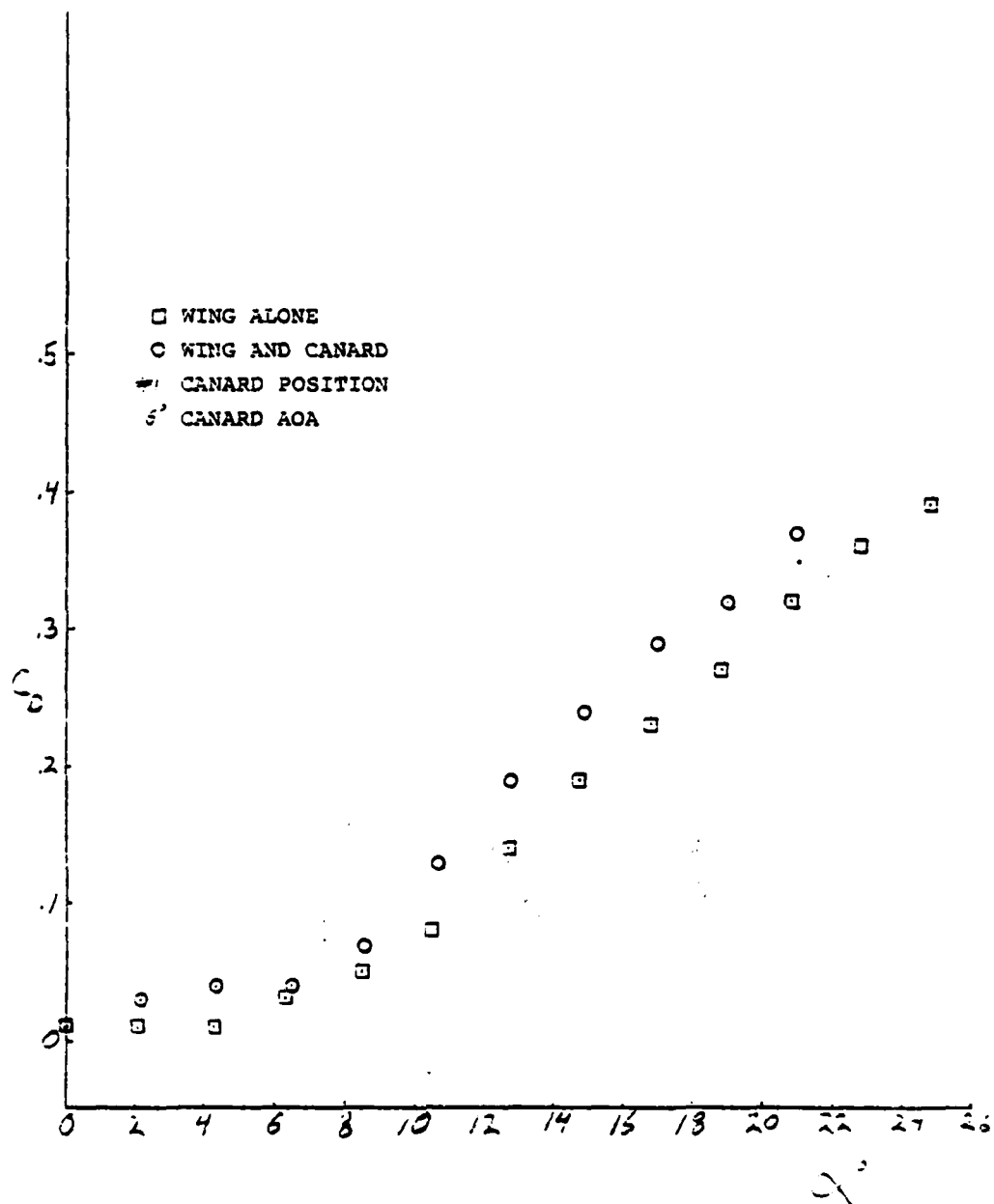


Figure 39A4D. Drag Coefficient vs Alpha

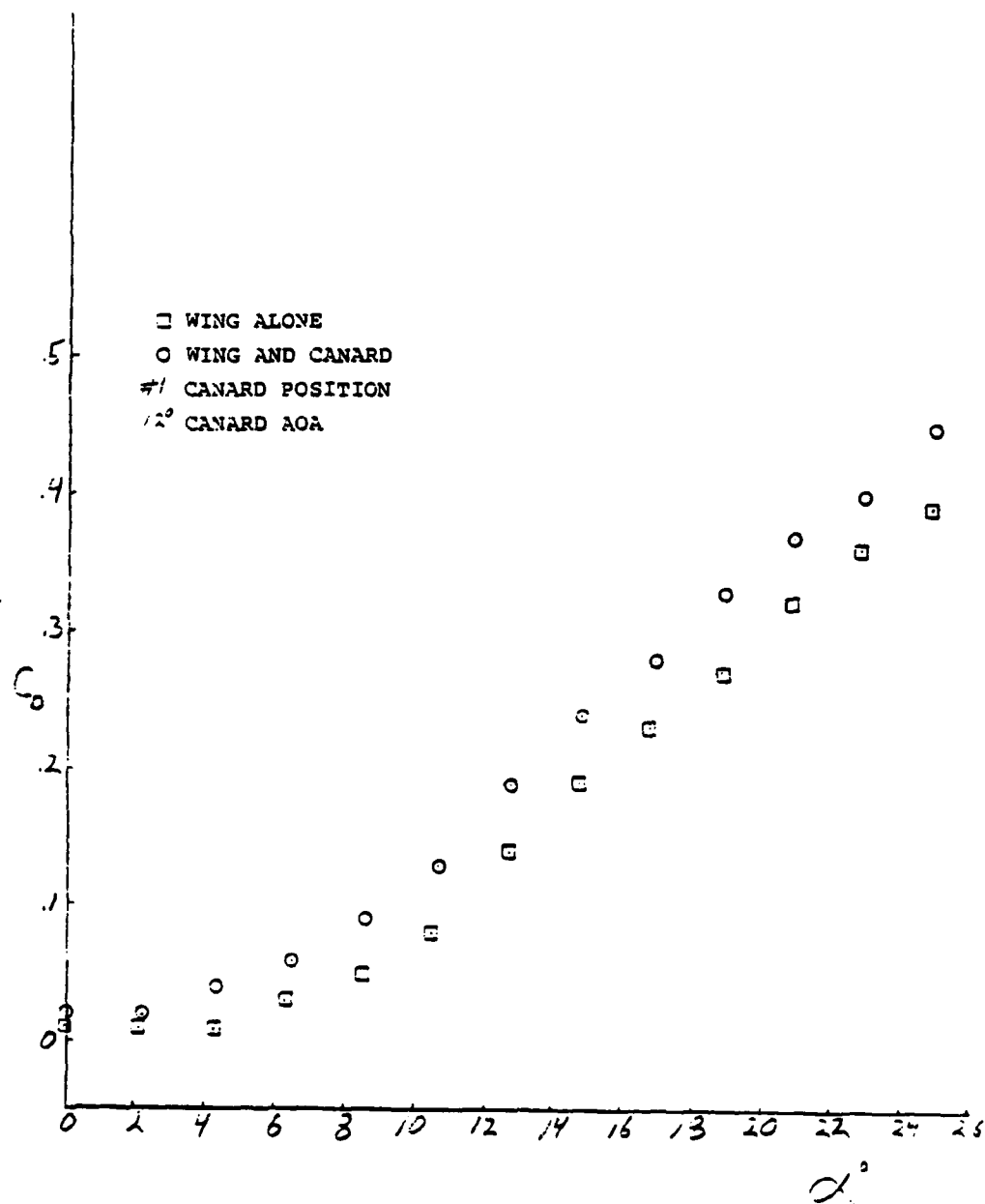


Figure 39A5D. Drag Coefficient vs Alpha

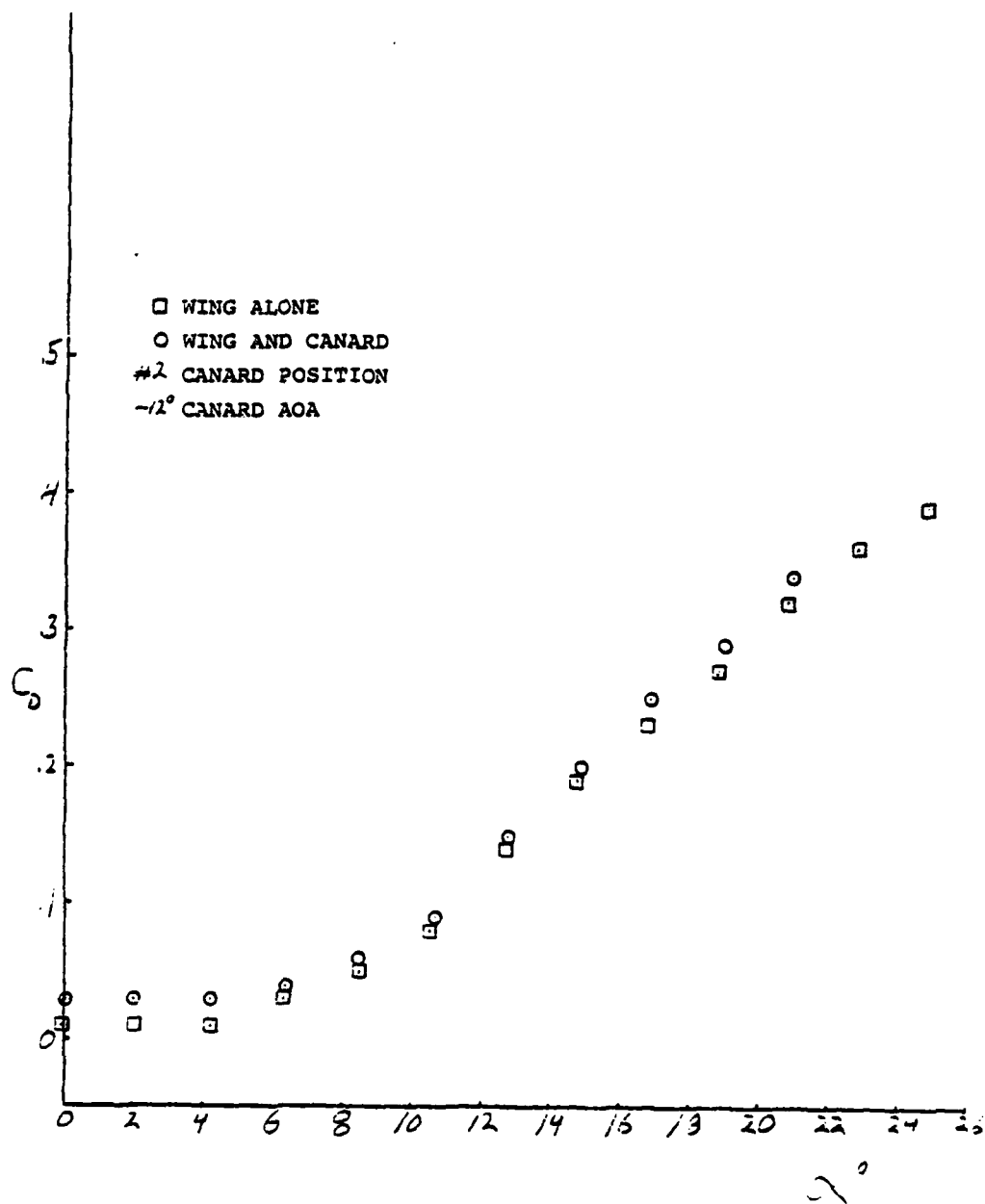


Figure 39A6D. Drag Coefficient vs Alpha

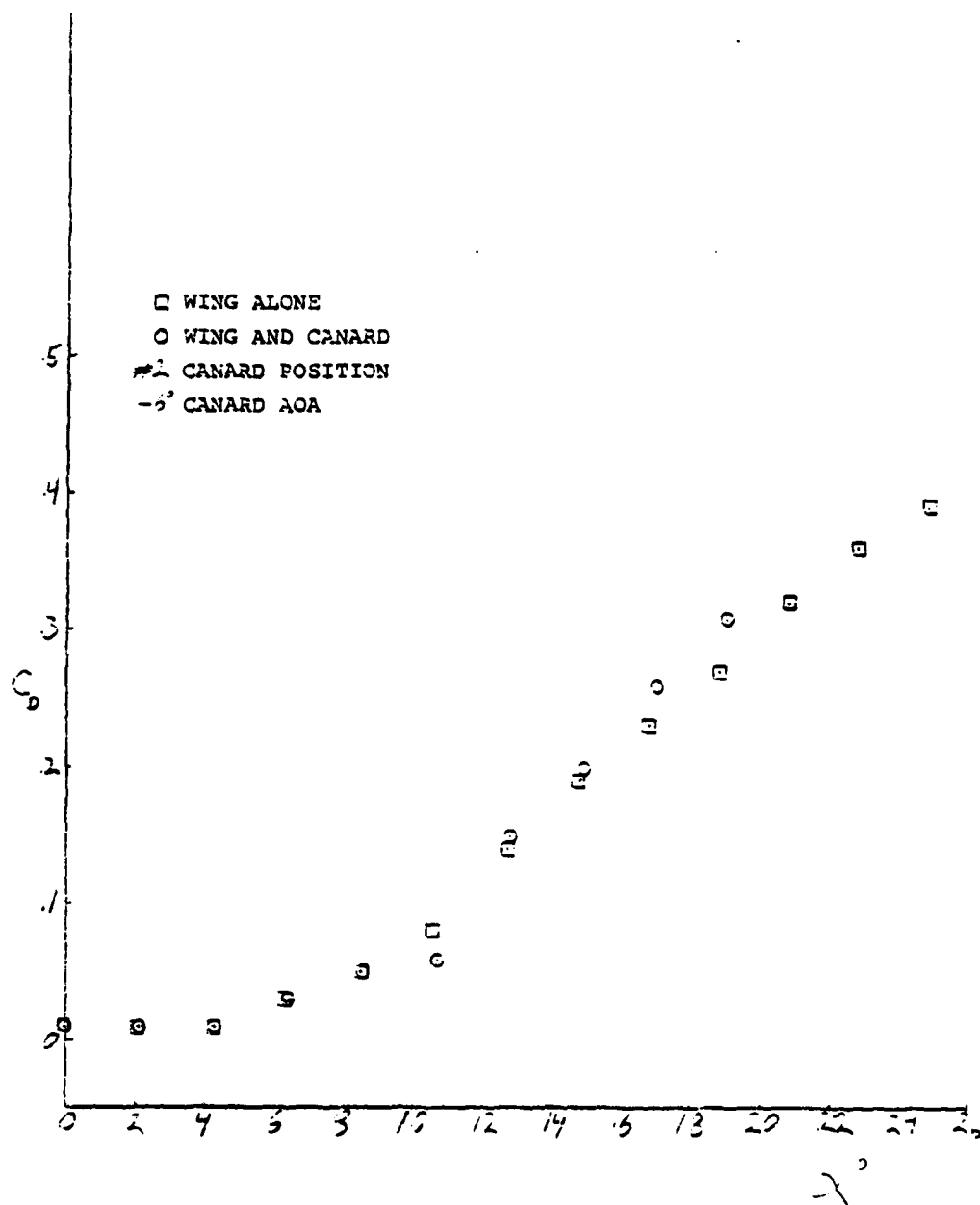


Figure 39A7D. Drag Coefficient vs Alpha

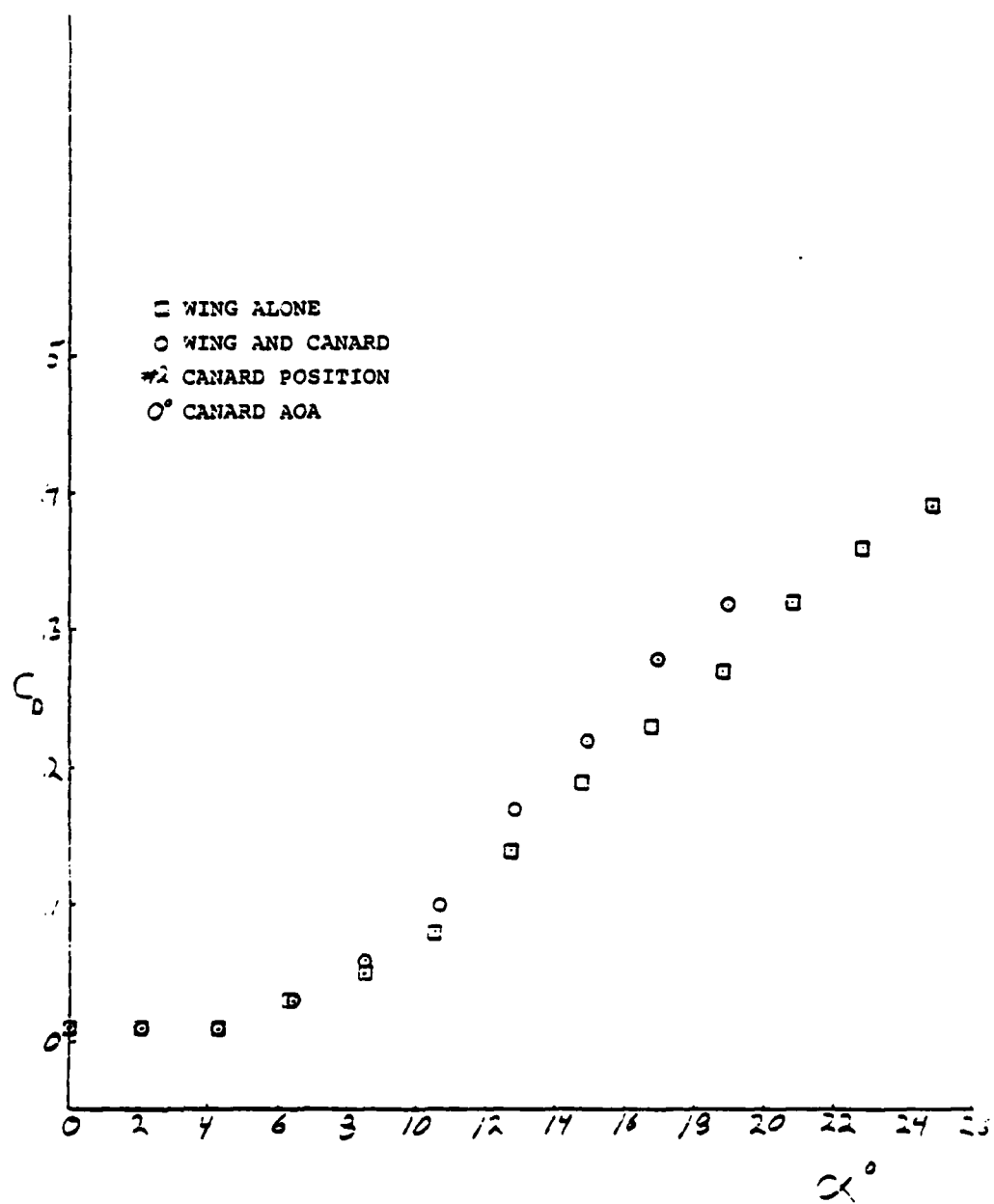


Figure 39A8D. Drag Coefficient vs Alpha

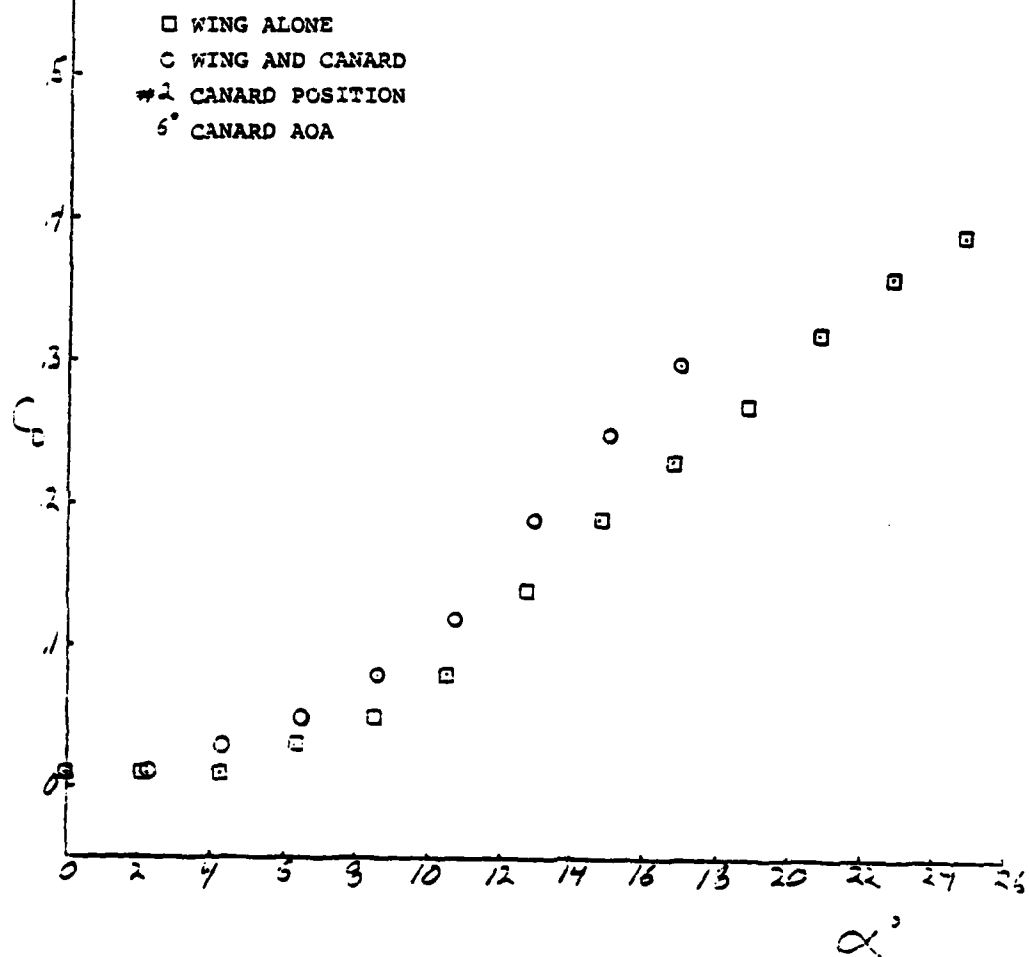


Figure 39A9D. Drag Coefficient vs Alpha

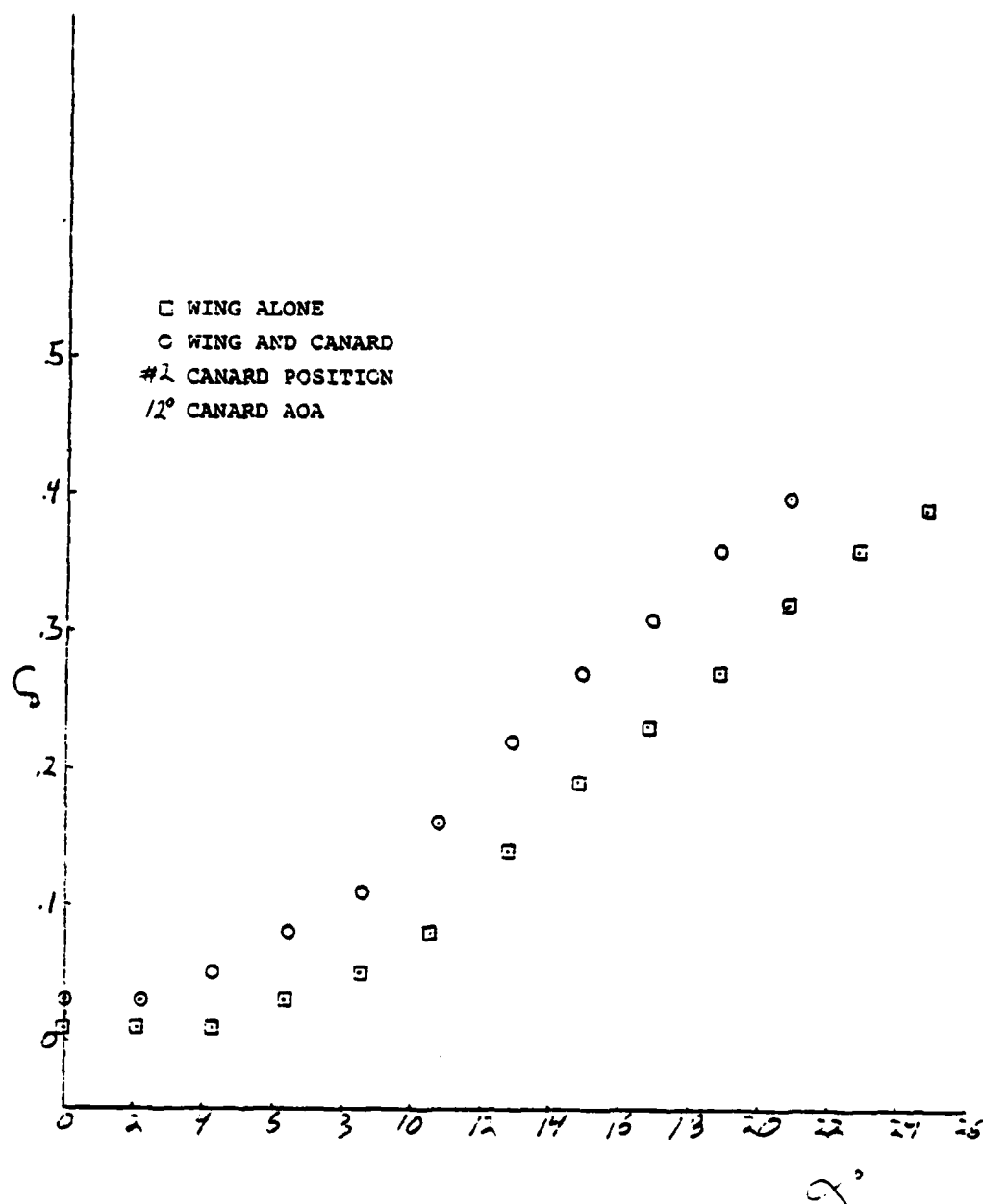


Figure 39A10D. Drag Coefficient vs Alpha

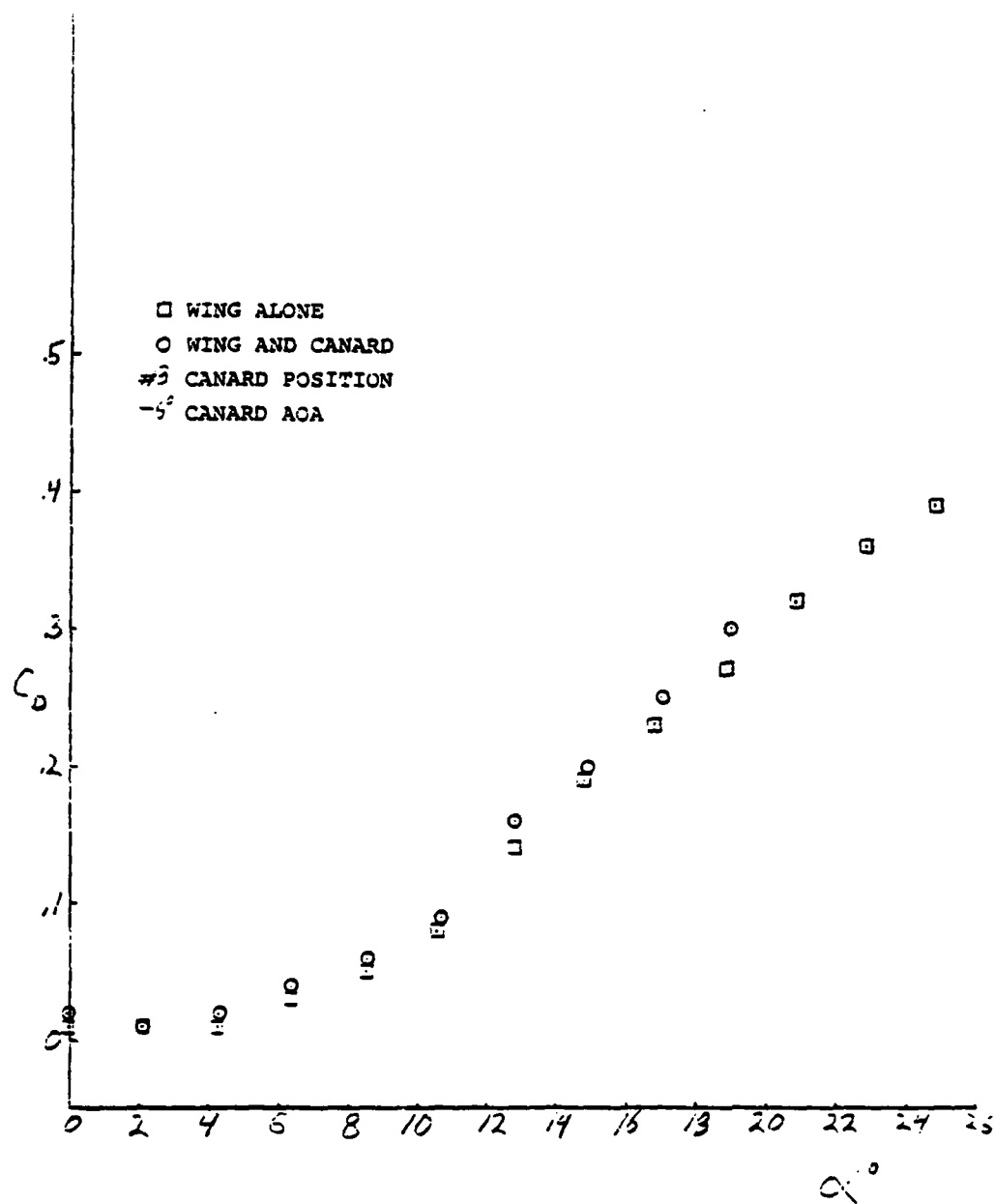


Figure 39A12D. Drag Coefficient vs Alpha

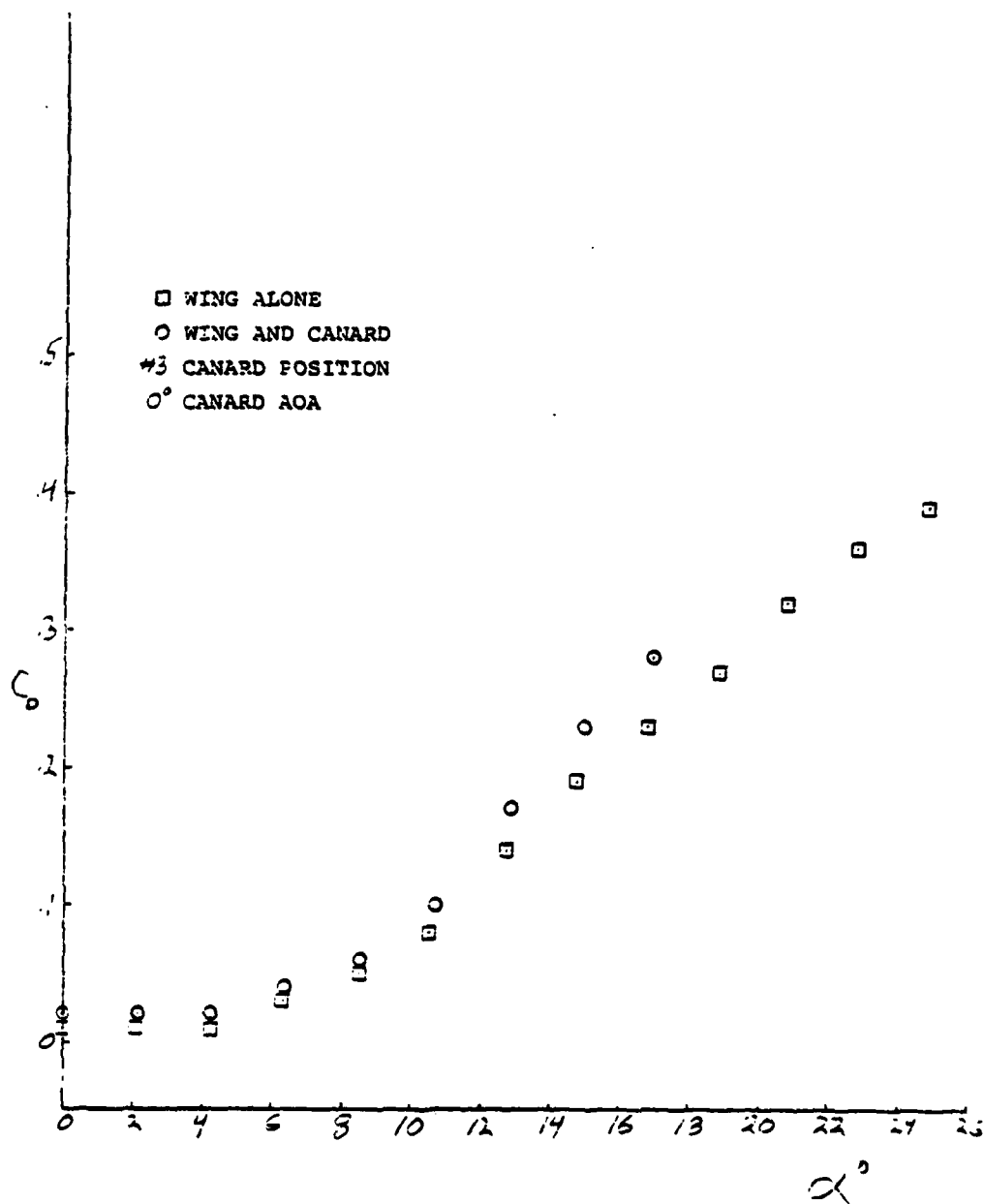


Figure 39A13D. Drag Coefficient vs Alpha

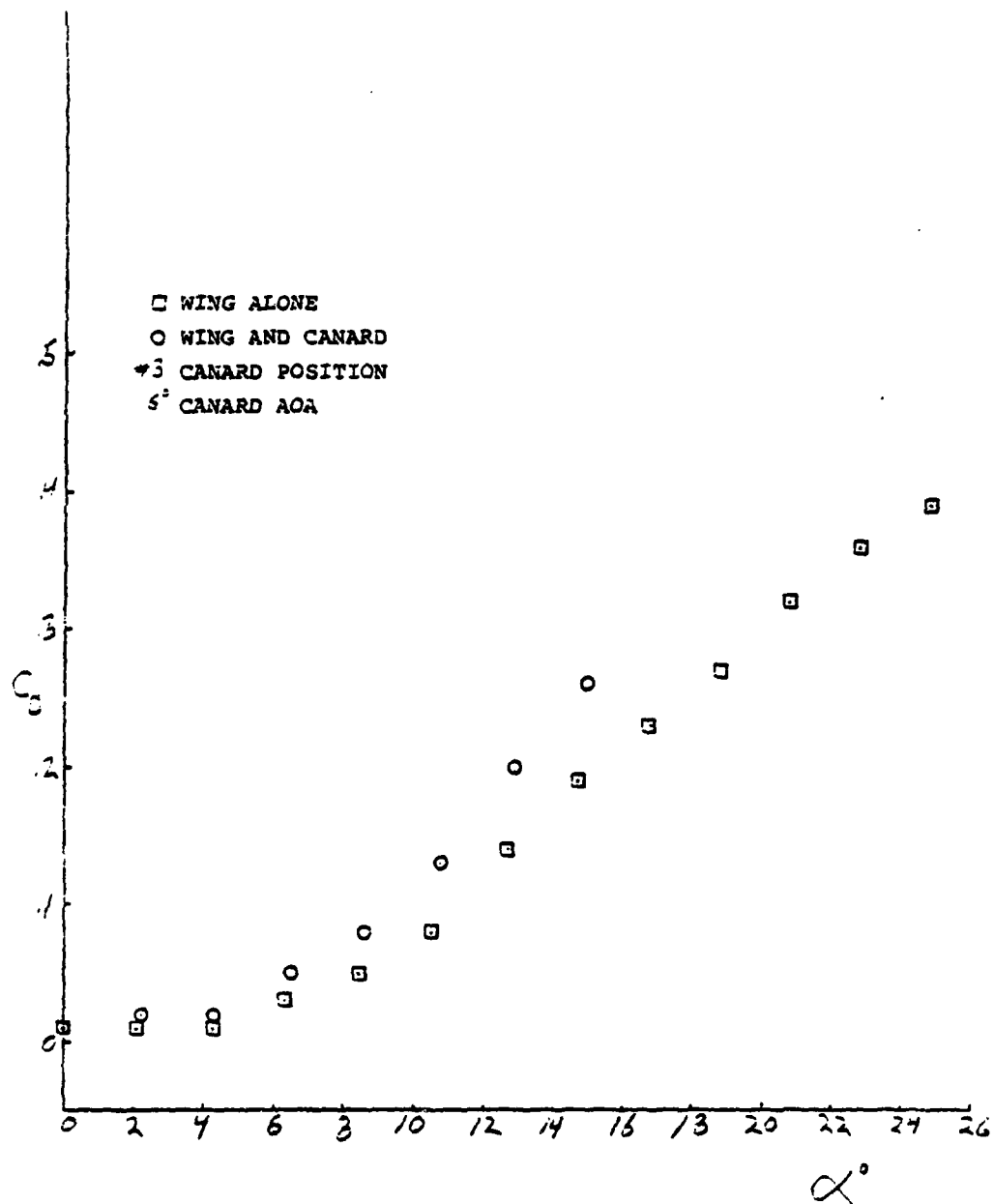


Figure 39A14D. Drag Coefficient vs Alpha

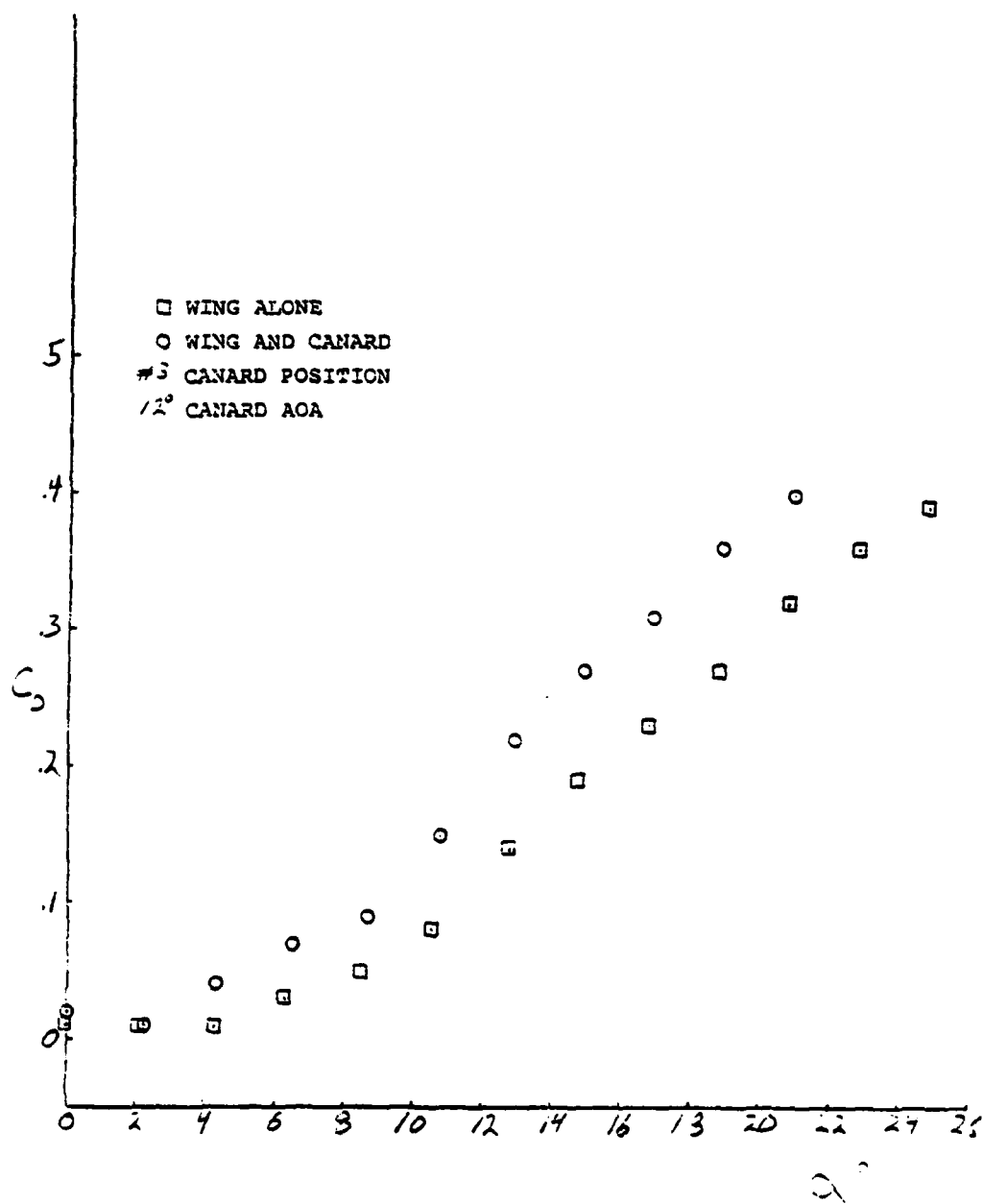


Figure 39A15D. Drag Coefficient vs Alpha

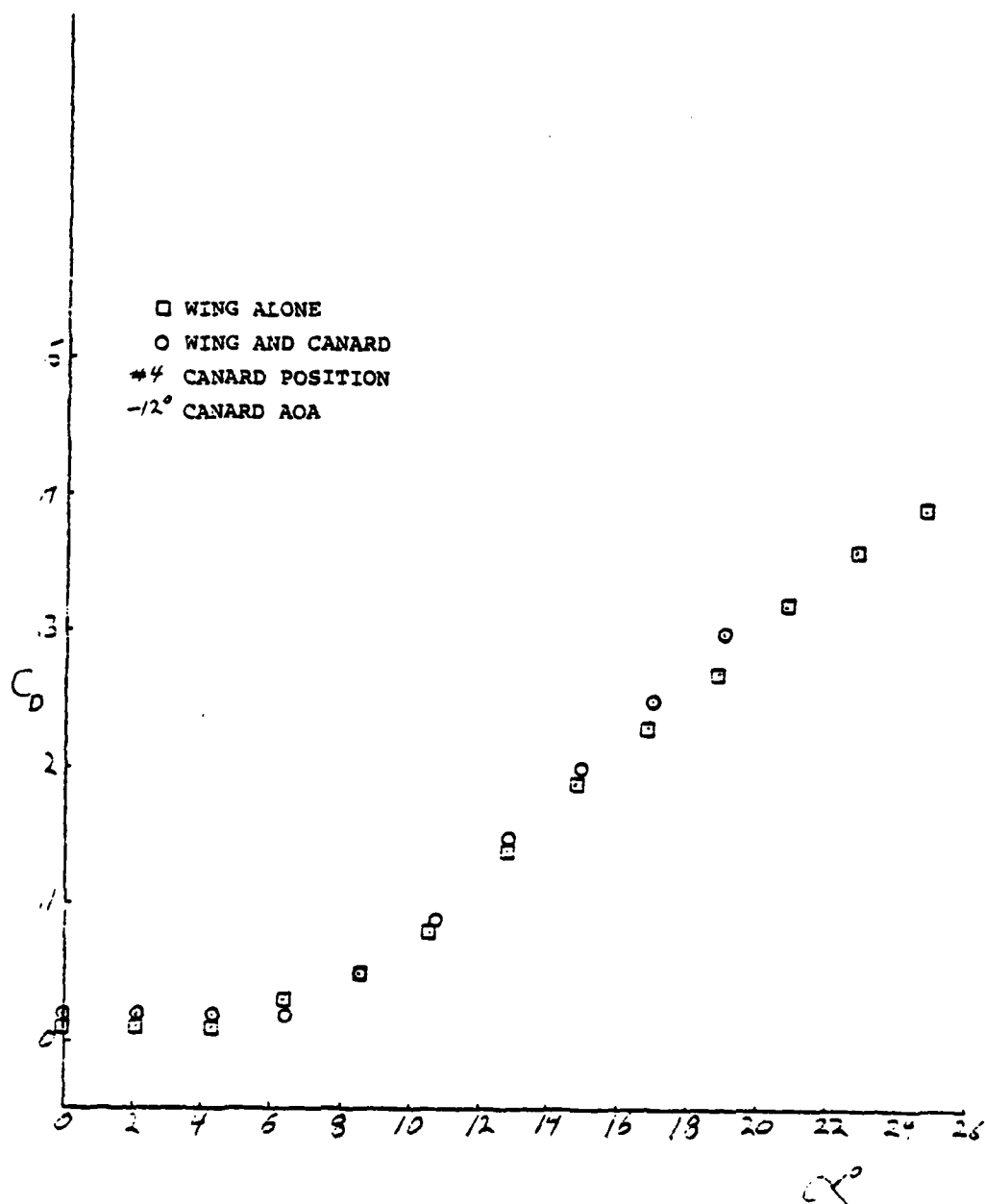


Figure 39A16D. Drag Coefficient vs Alpha

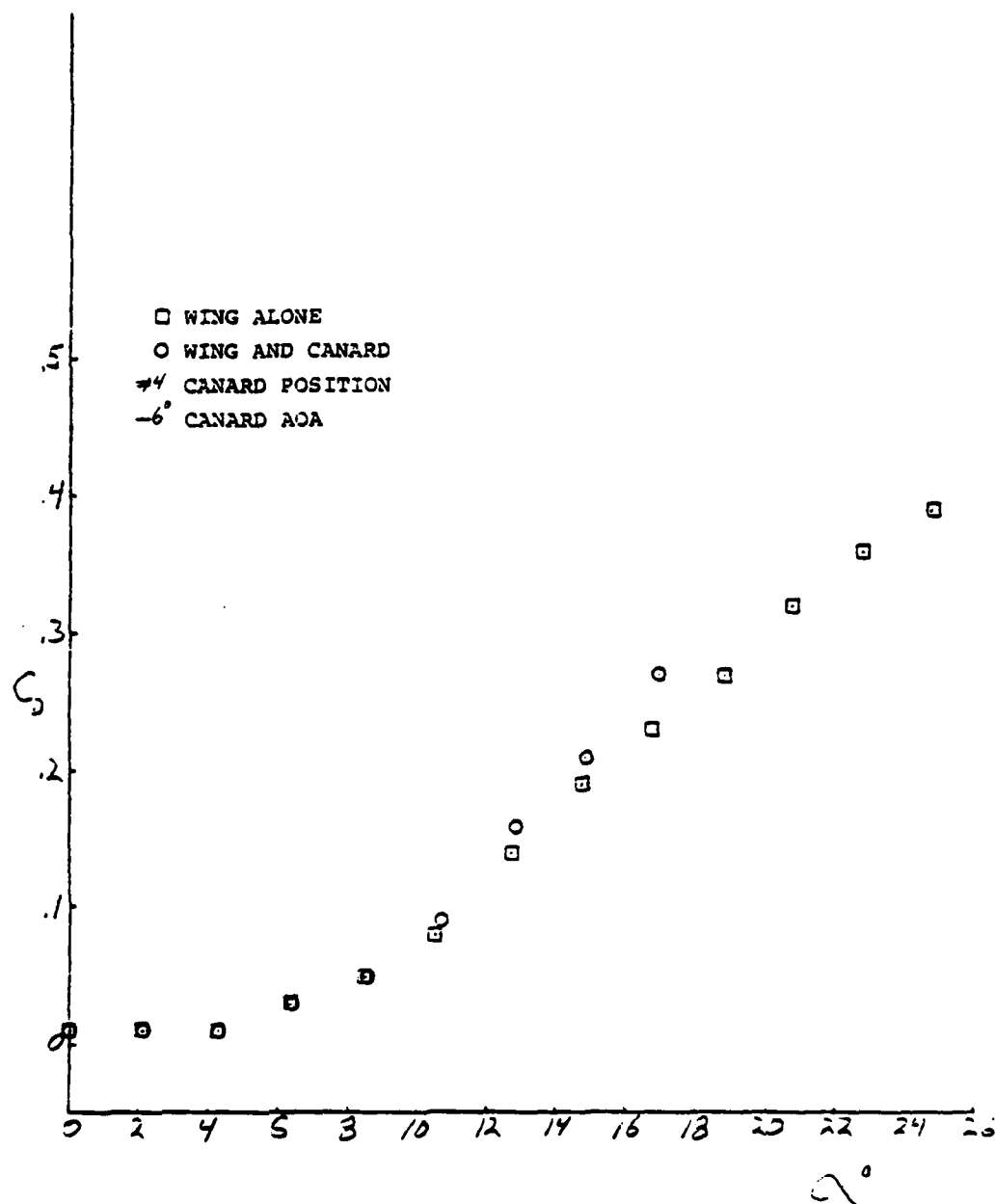


Figure 39A17D. Drag Coefficient vs Alpha

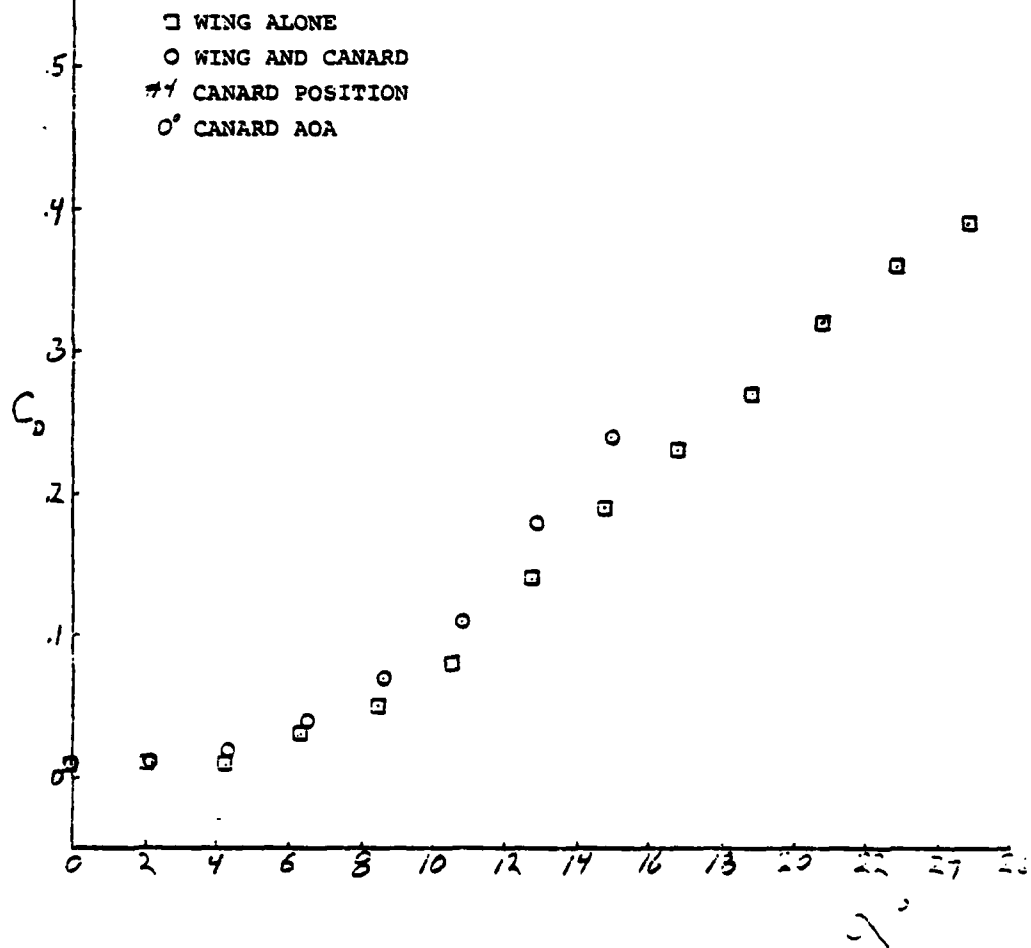


Figure 39A18D. Drag Coefficient vs Alpha

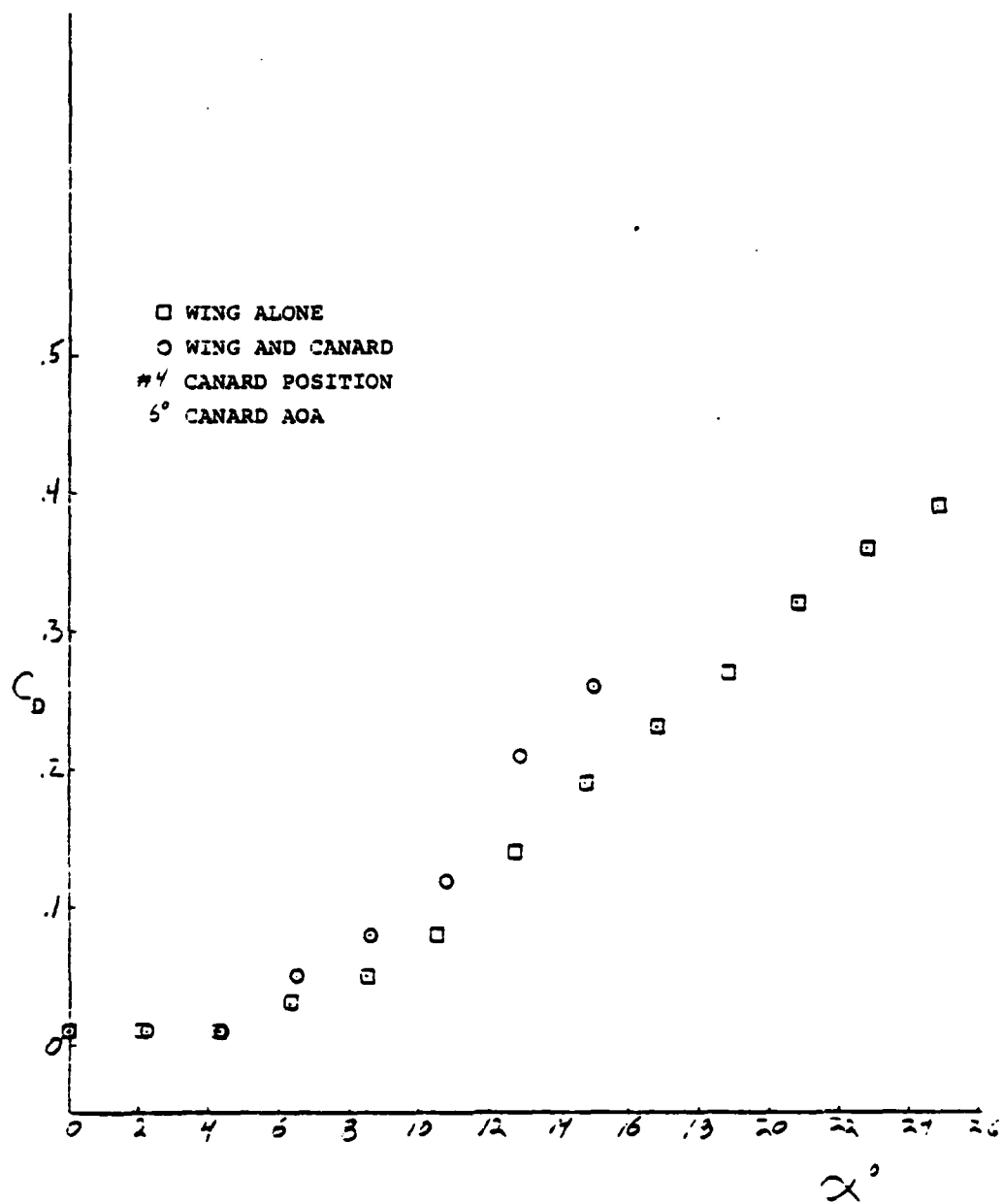


Figure 39A19D. Drag Coefficient vs Alpha

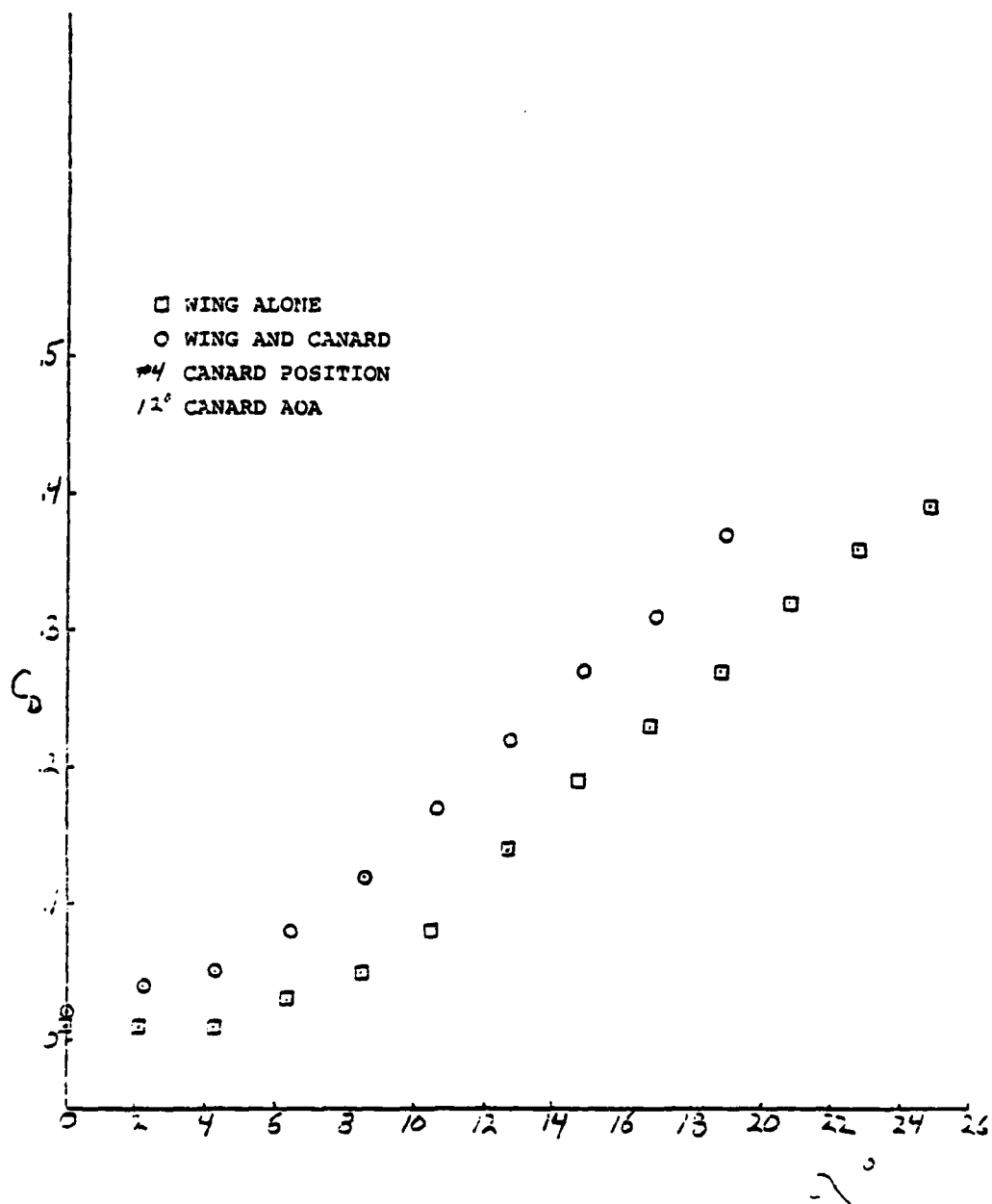


Figure 39A20D. Drag Coefficient vs Alpha

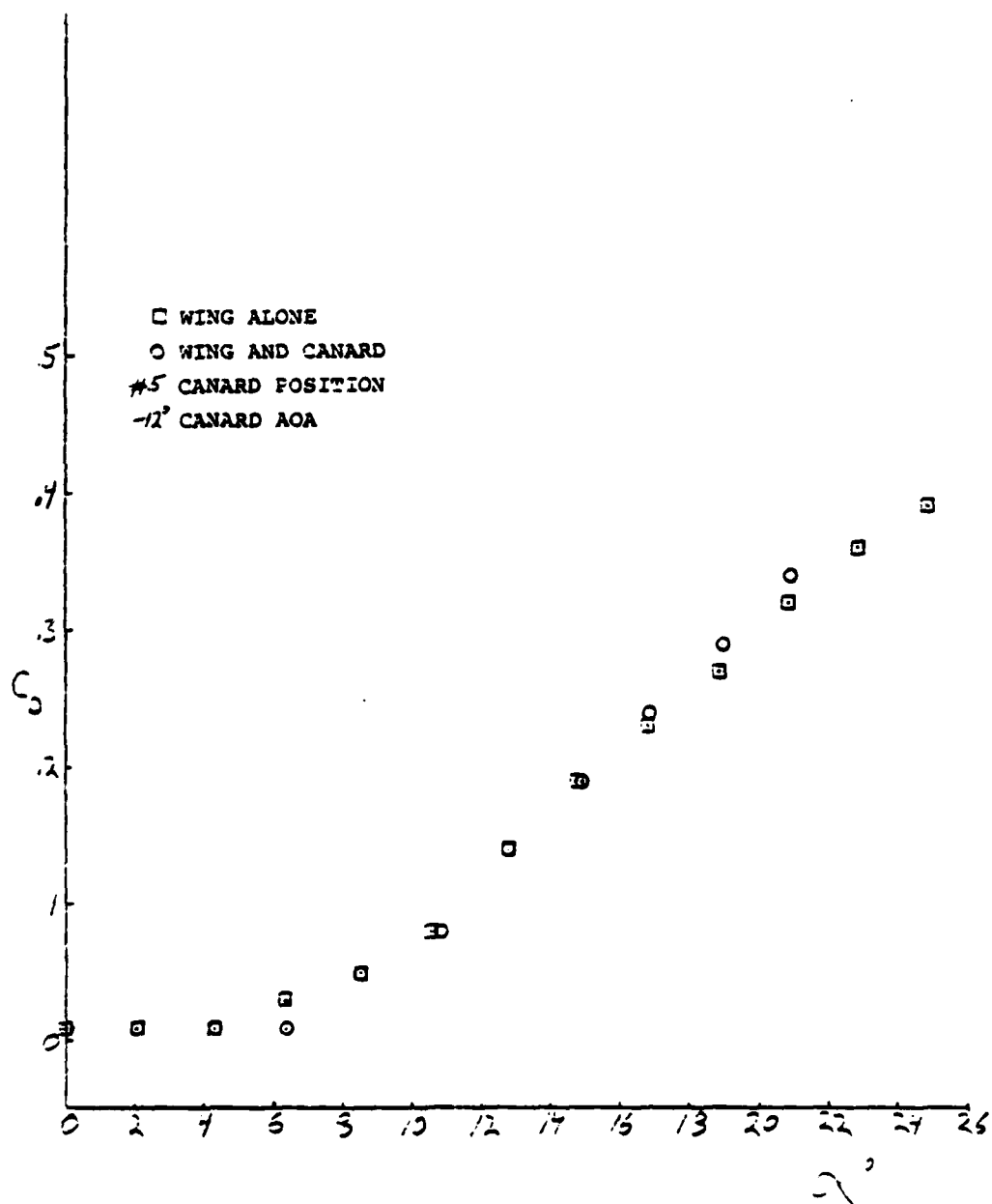


Figure 39A21D. Drag Coefficient vs Alpha

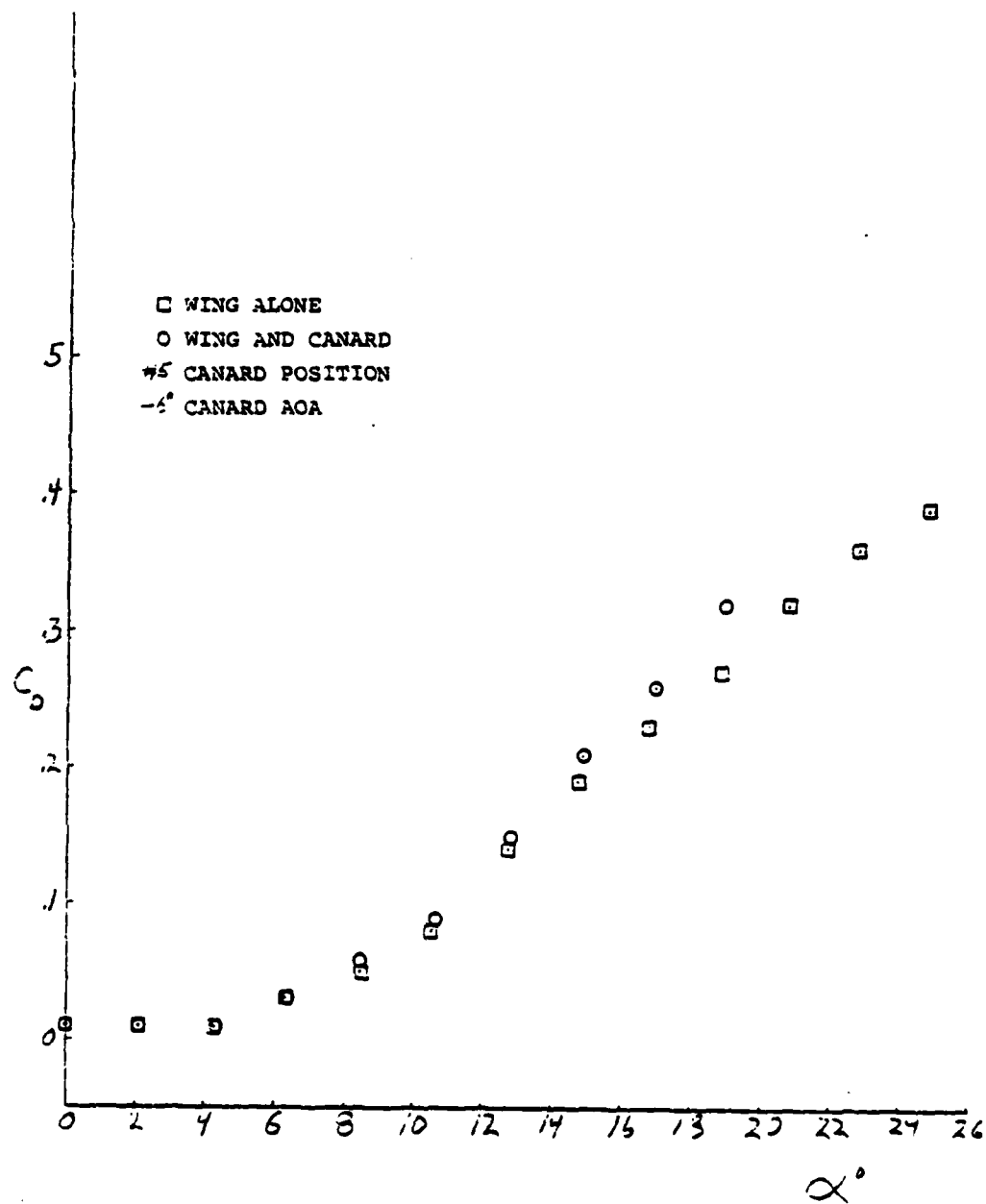


Figure 39A22D. Drag Coefficient vs Alpha

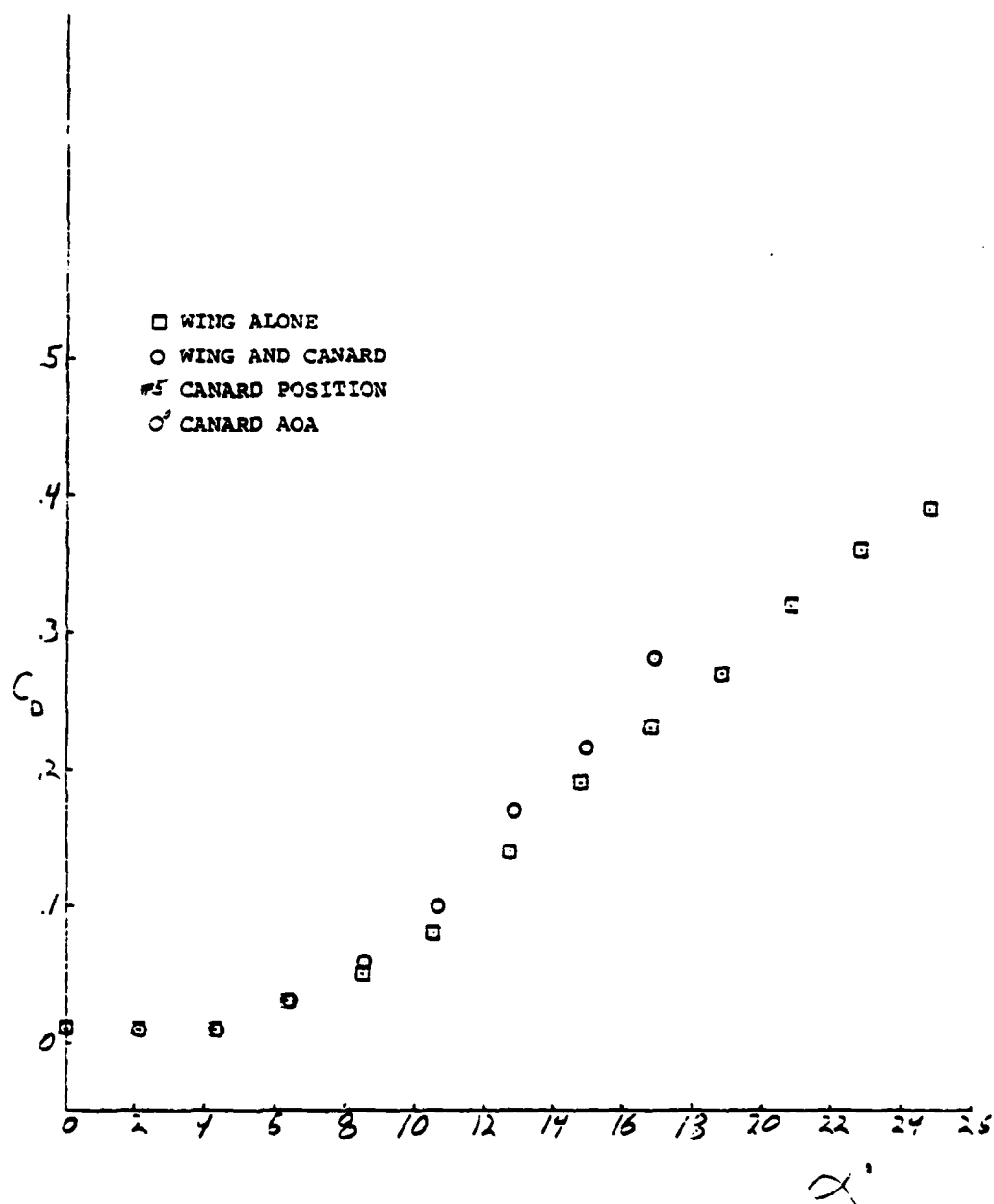


Figure 39A23D. Drag Coefficient vs Alpha

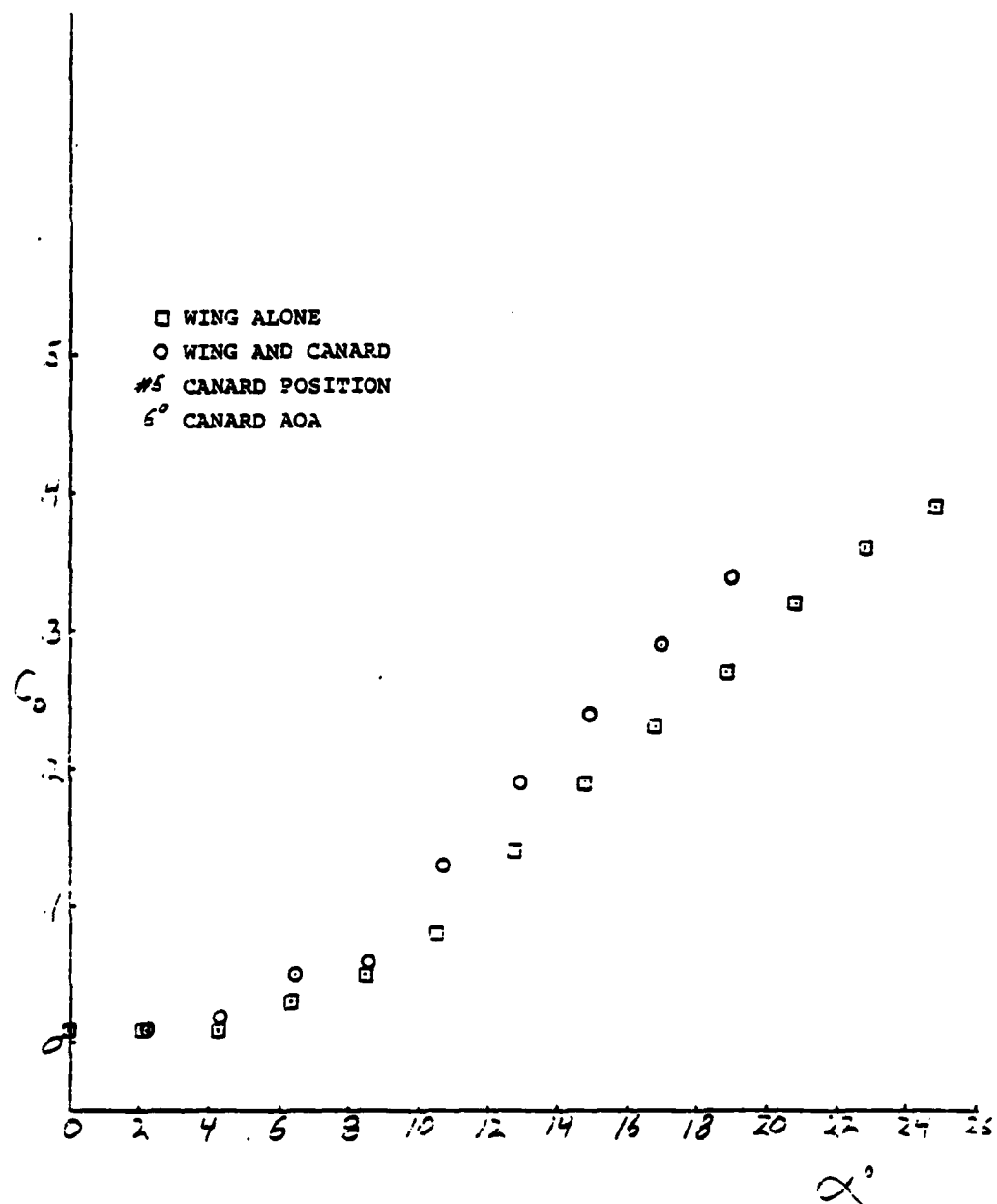


Figure 39A24D. Drag Coefficient vs Alpha

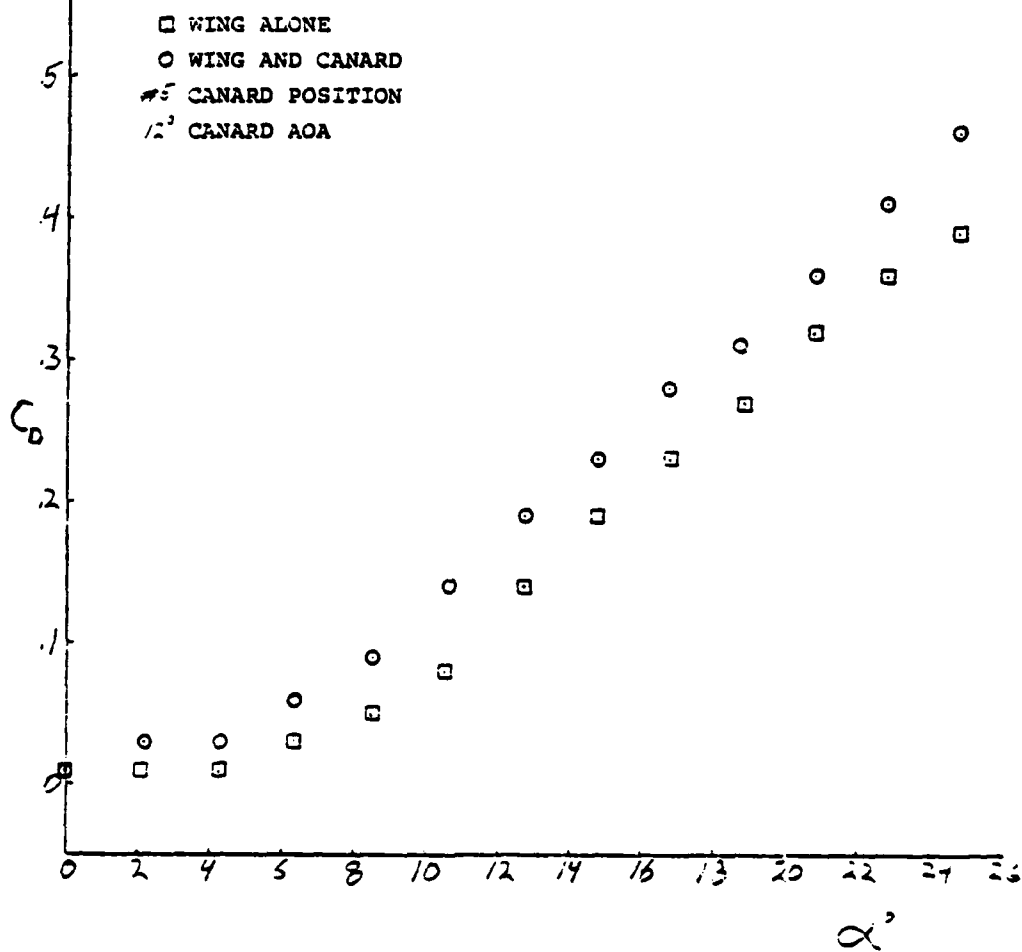


Figure 39A25D. Drag Coefficient vs Alpha

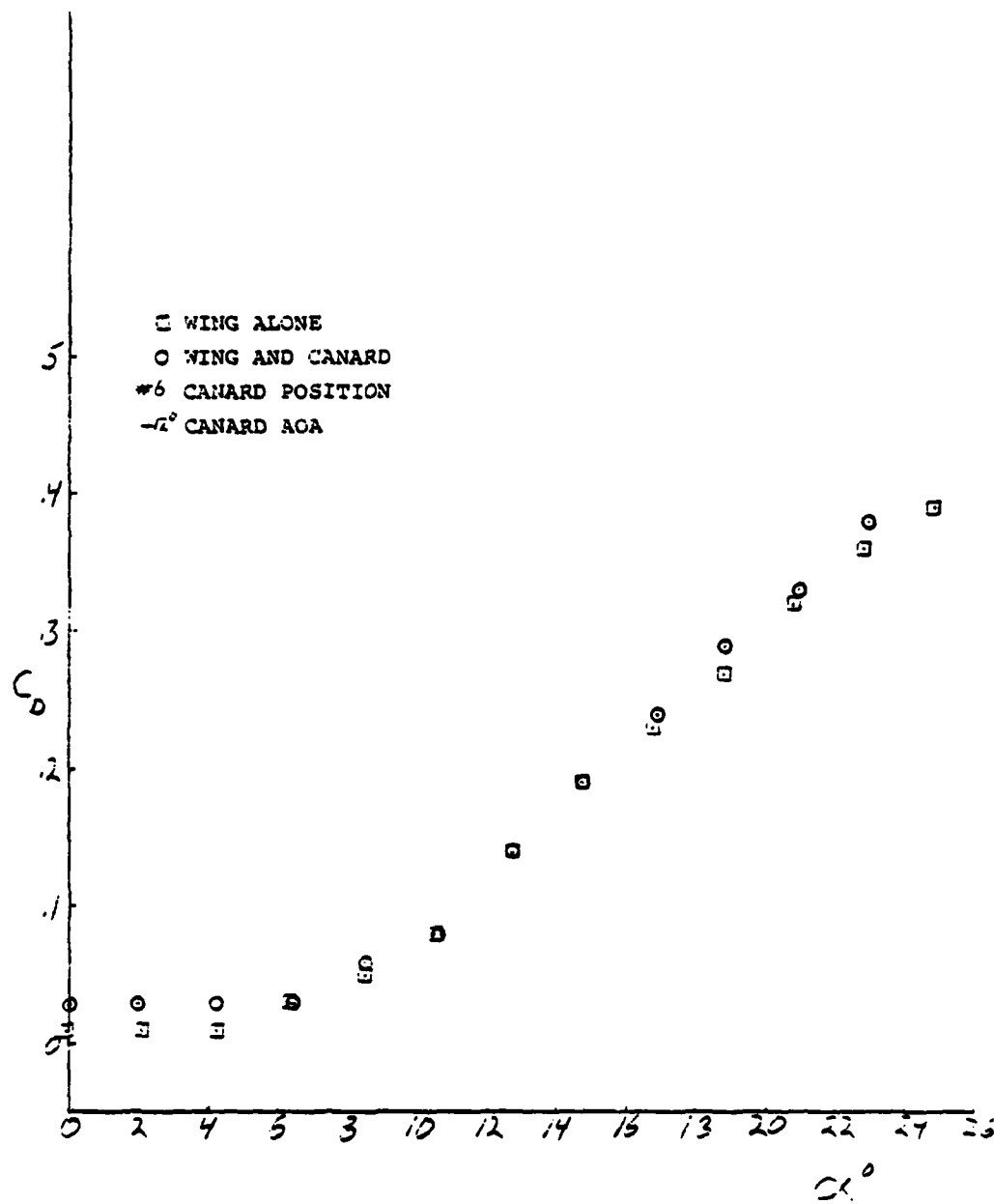


Figure 39A26D. Drag Coefficient vs Alpha

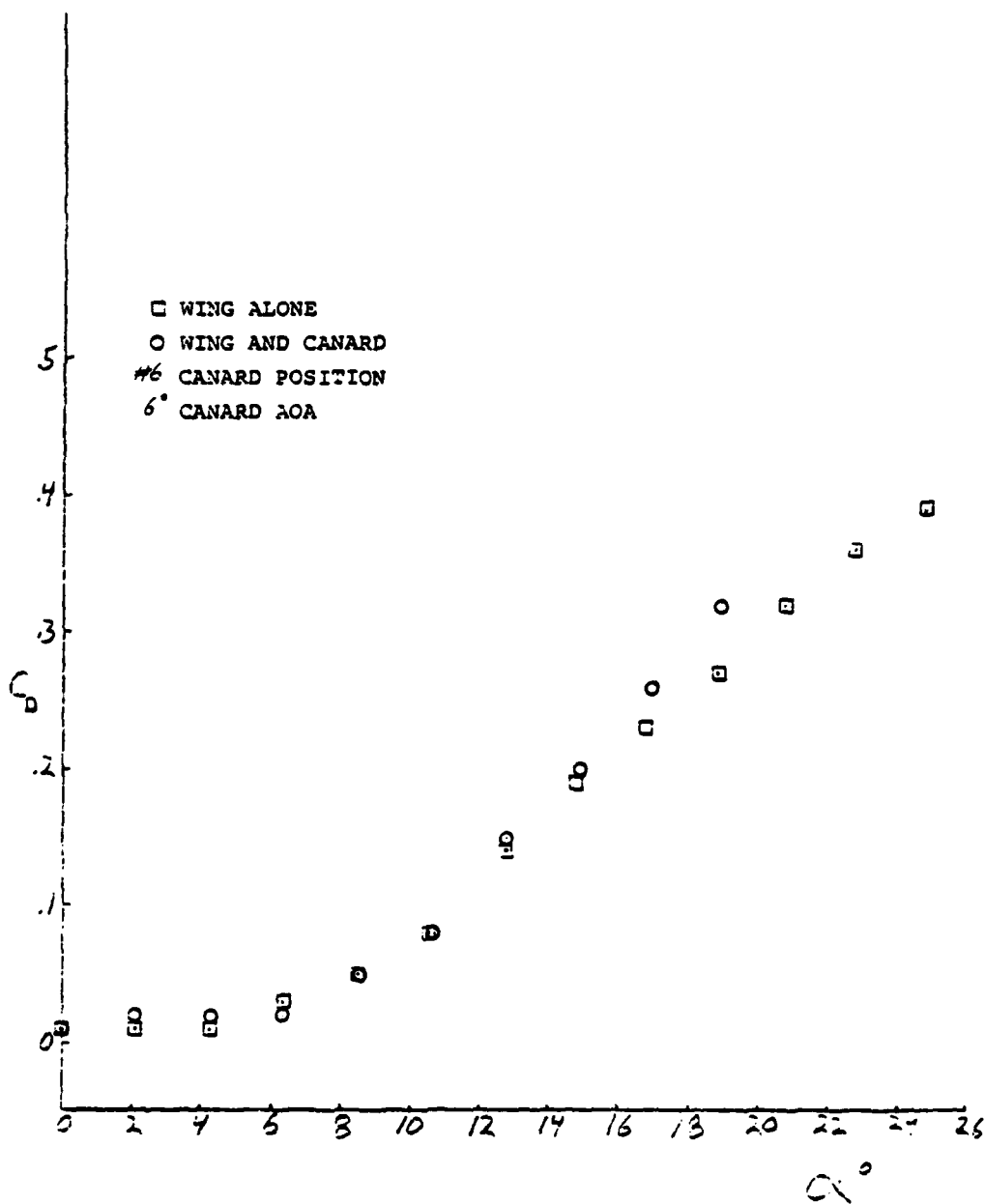


Figure 39A27D. Drag Coefficient vs Alpha

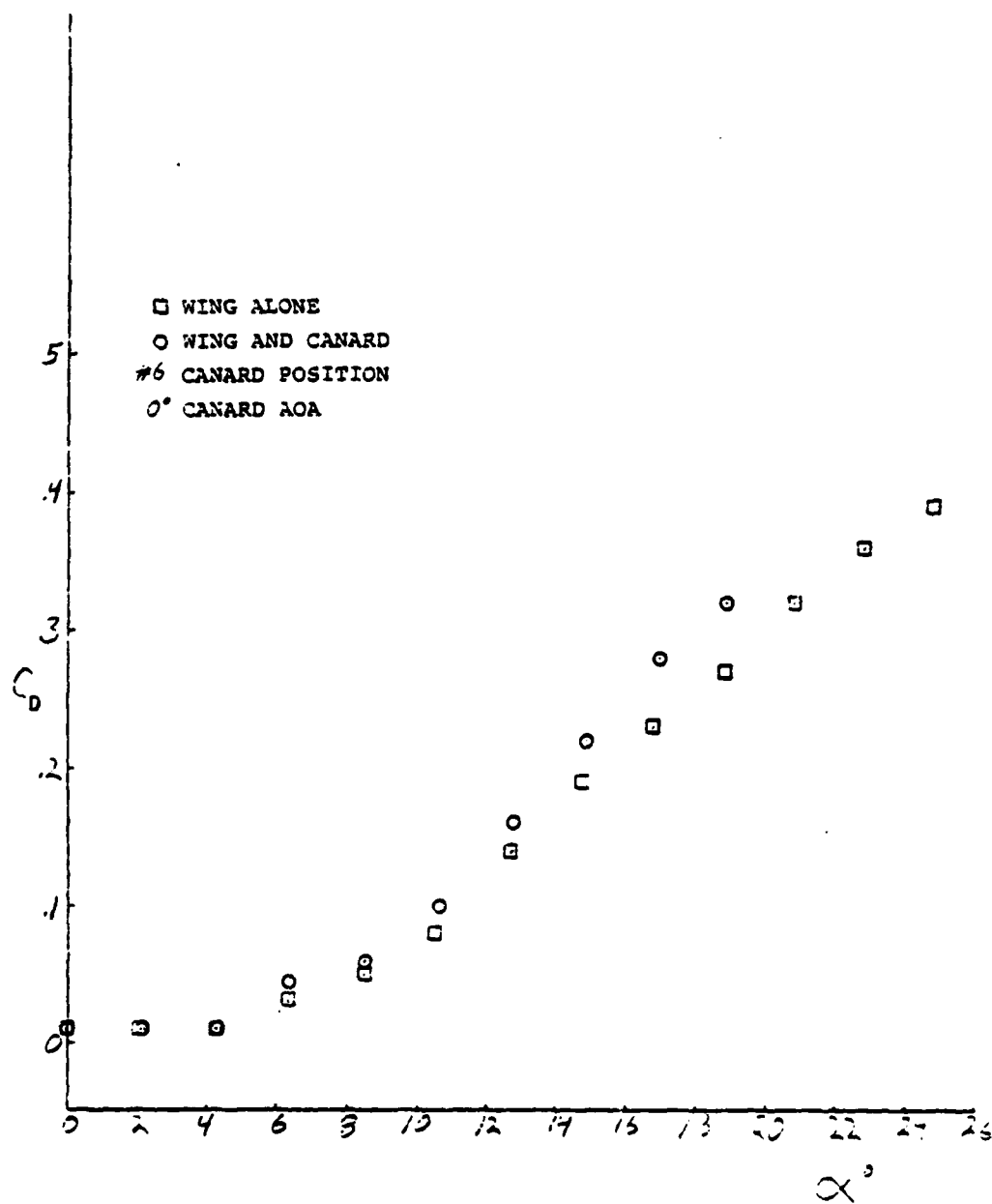


Figure 39A28D. Drag Coefficient vs Alpha

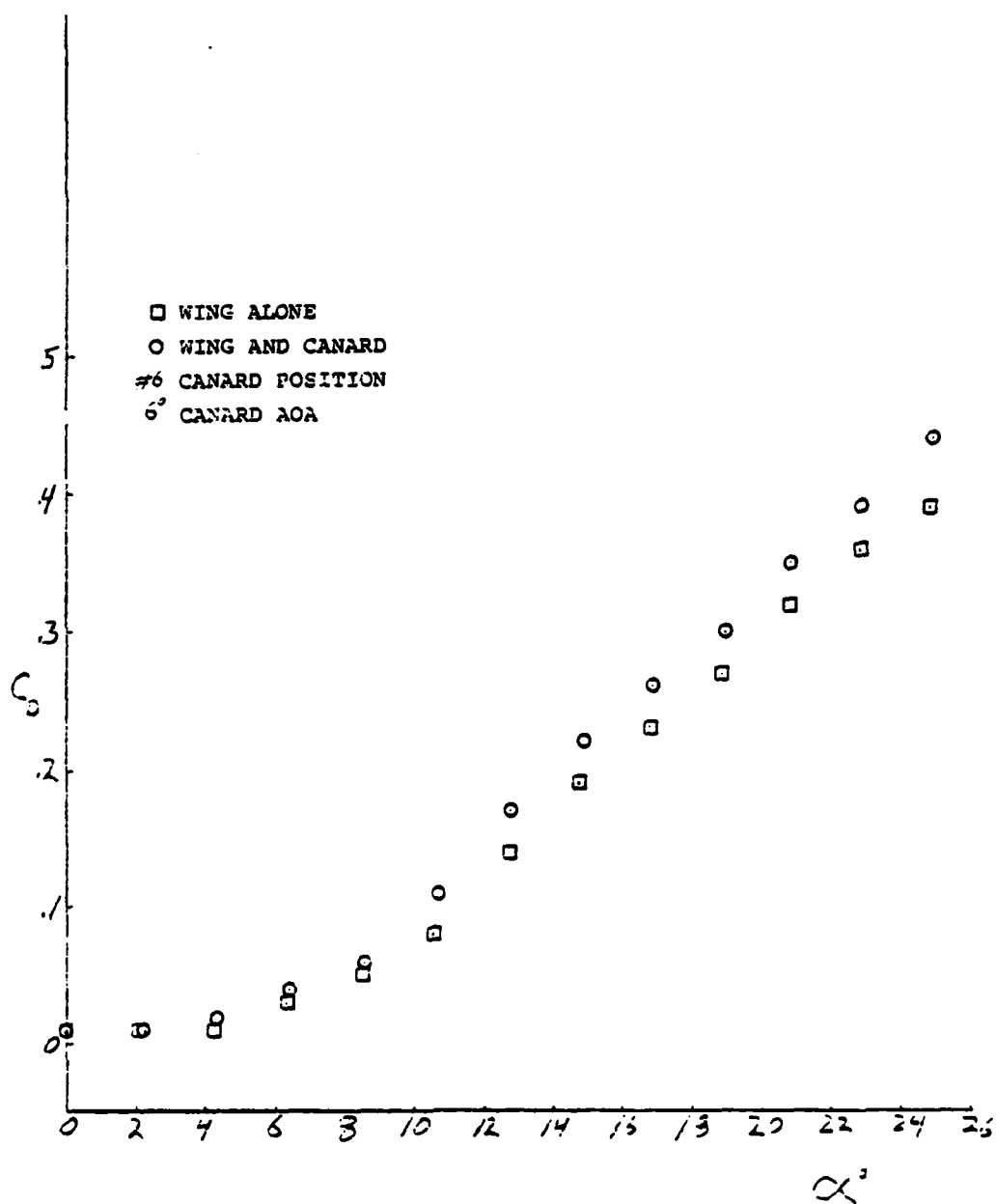


Figure 39A29D. Drag Coefficient vs Alpha

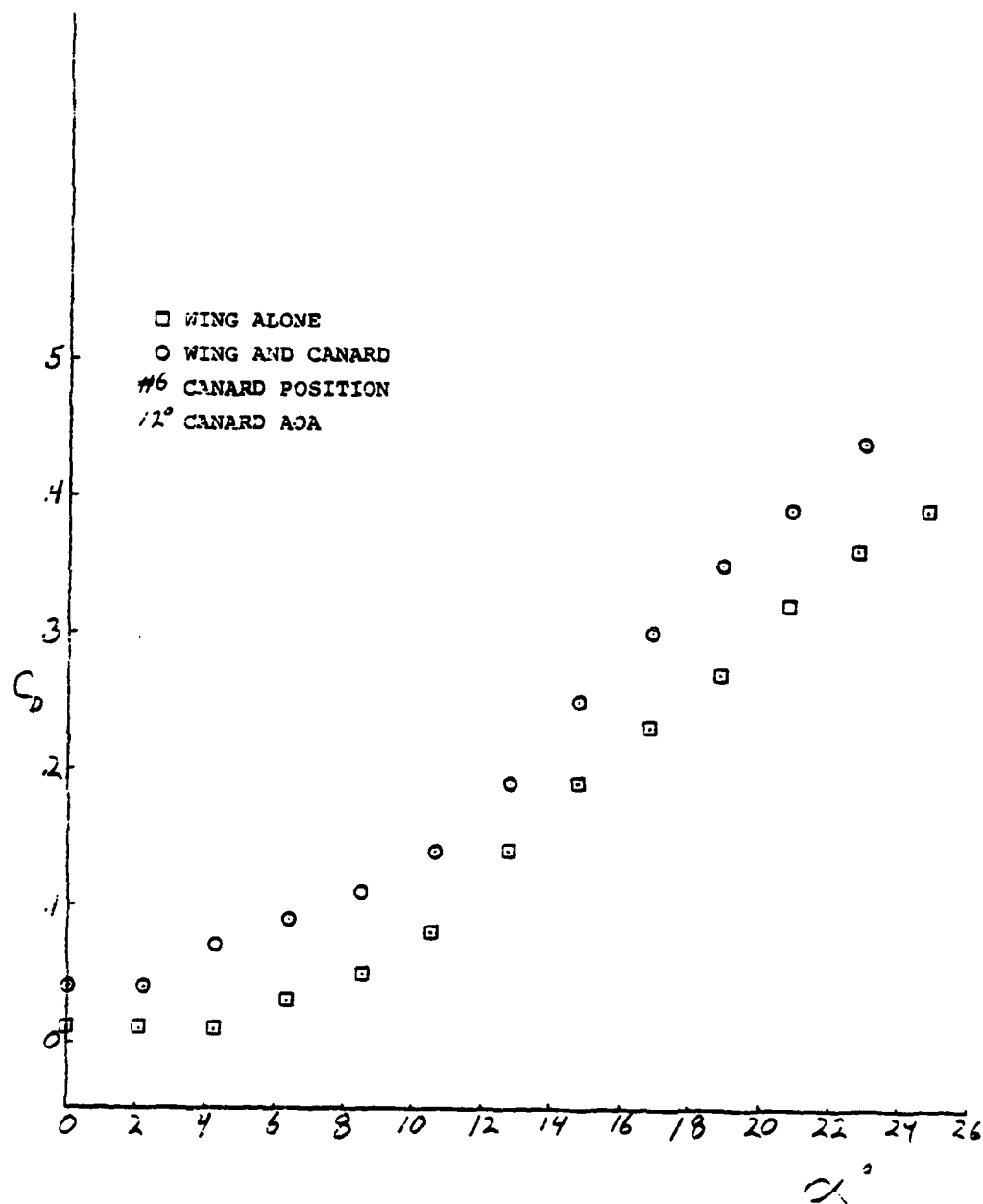


Figure 39A30D. Drag Coefficient vs Alpha

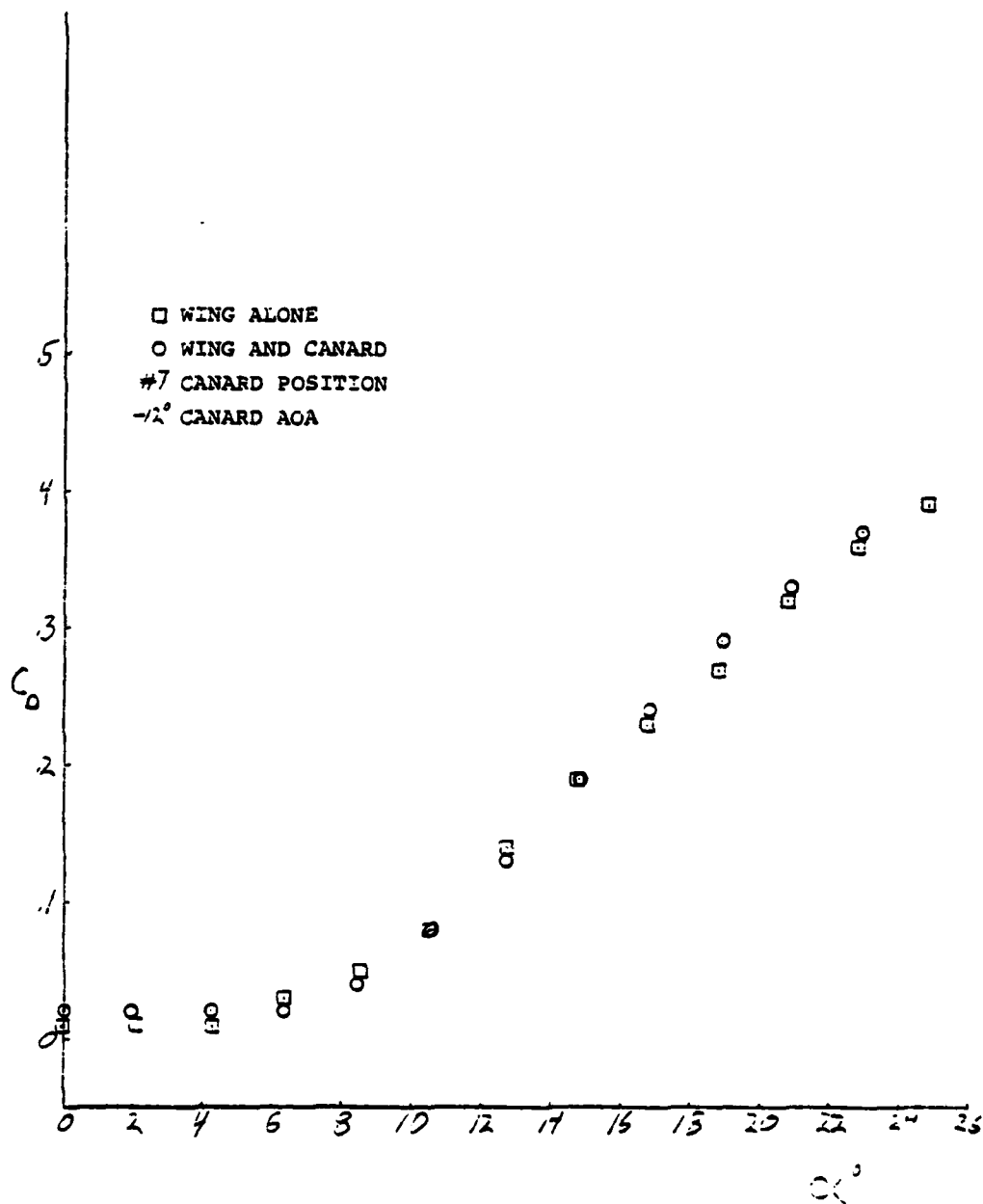


Figure 39A31D. Drag Coefficient vs Alpha

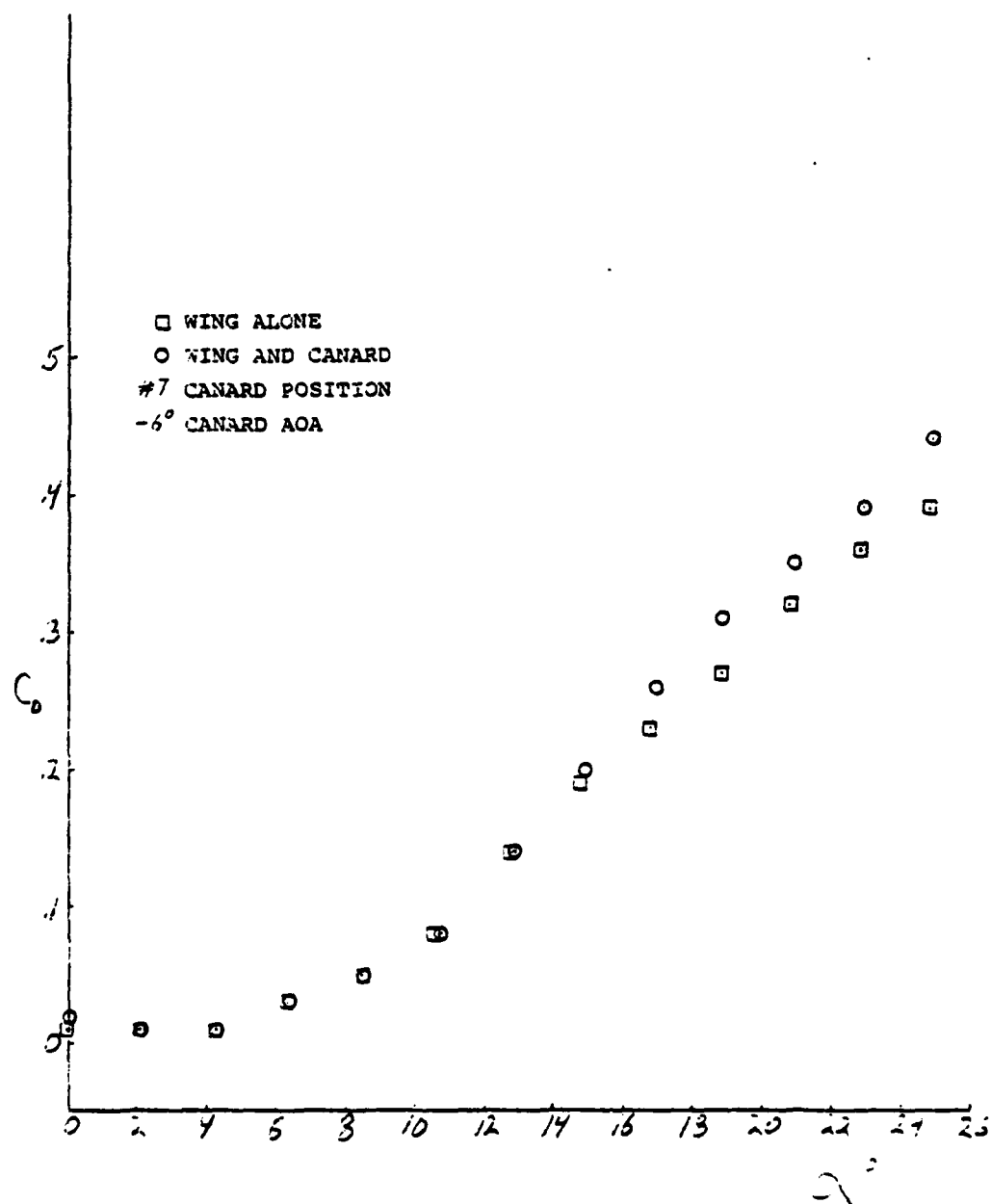


Figure 39A32D. Drag Coefficient vs Alpha

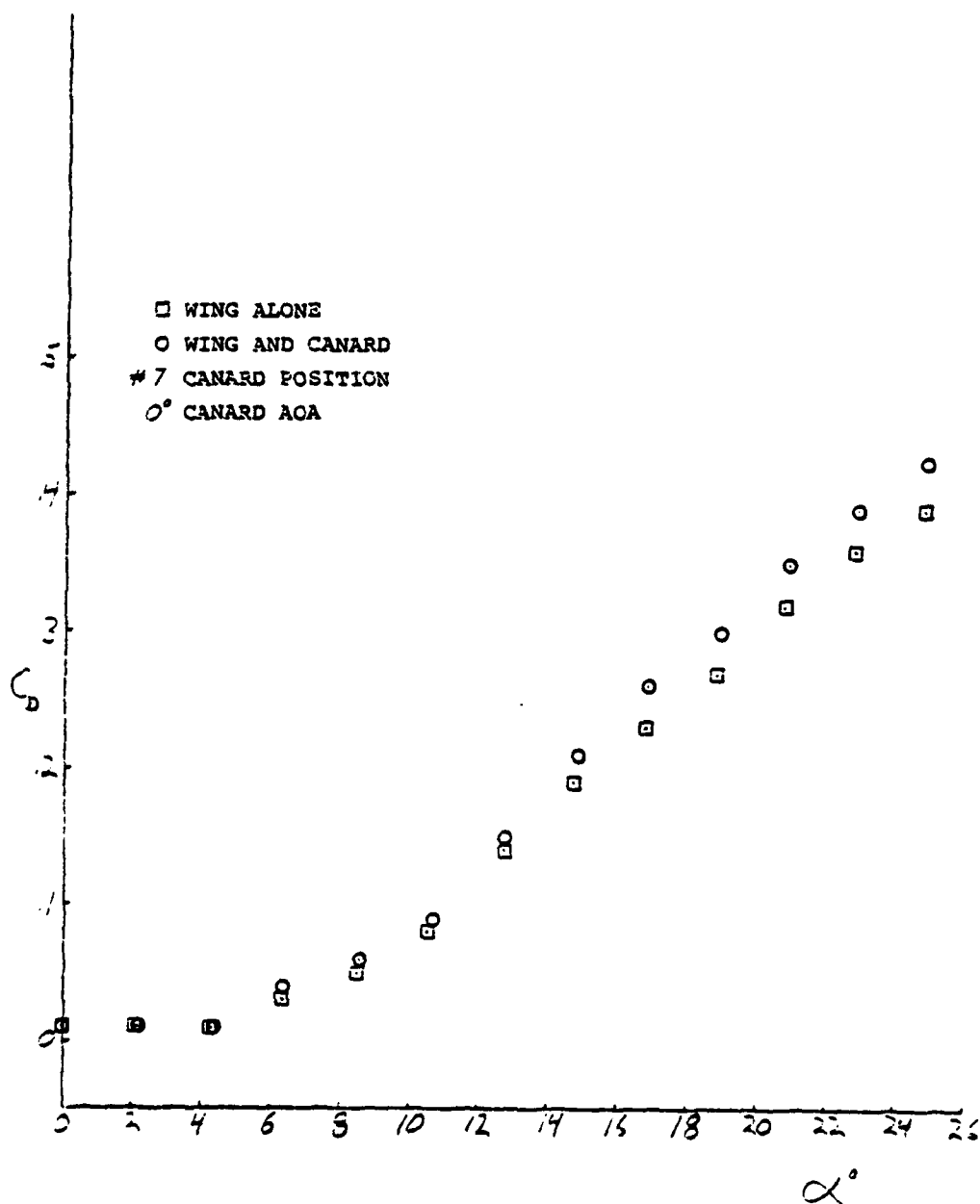


Figure 39A33D. Drag Coefficient vs Alpha

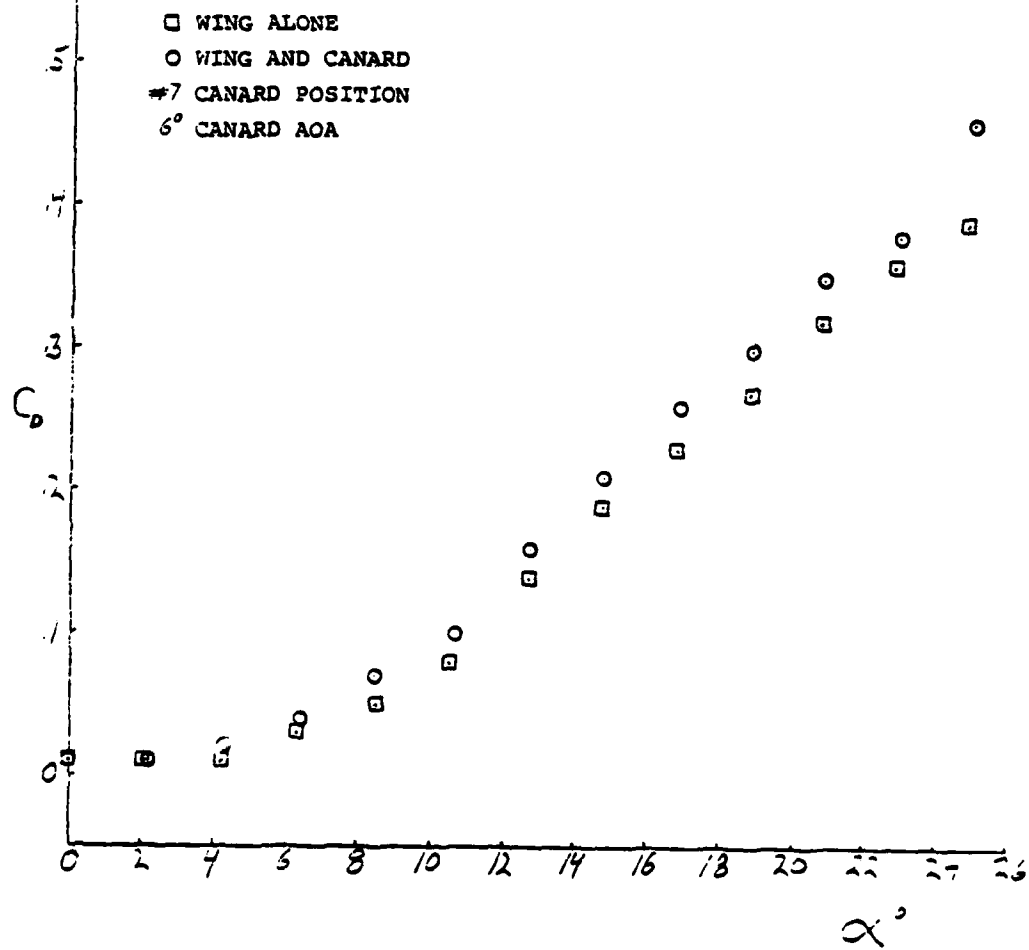


Figure 39A34D. Drag Coefficient vs Alpha

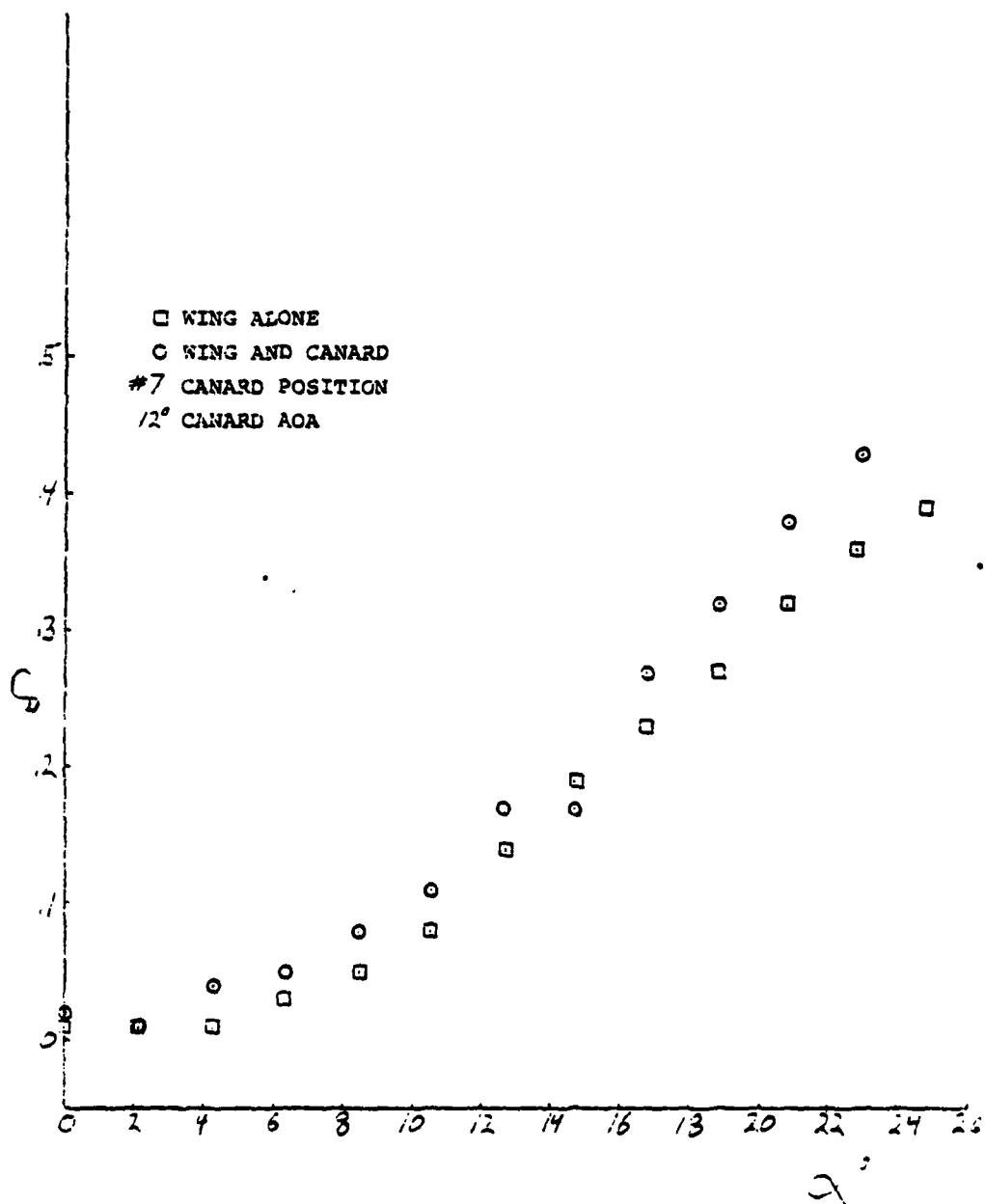


Figure 39A35D. Drag Coefficient vs Alpha

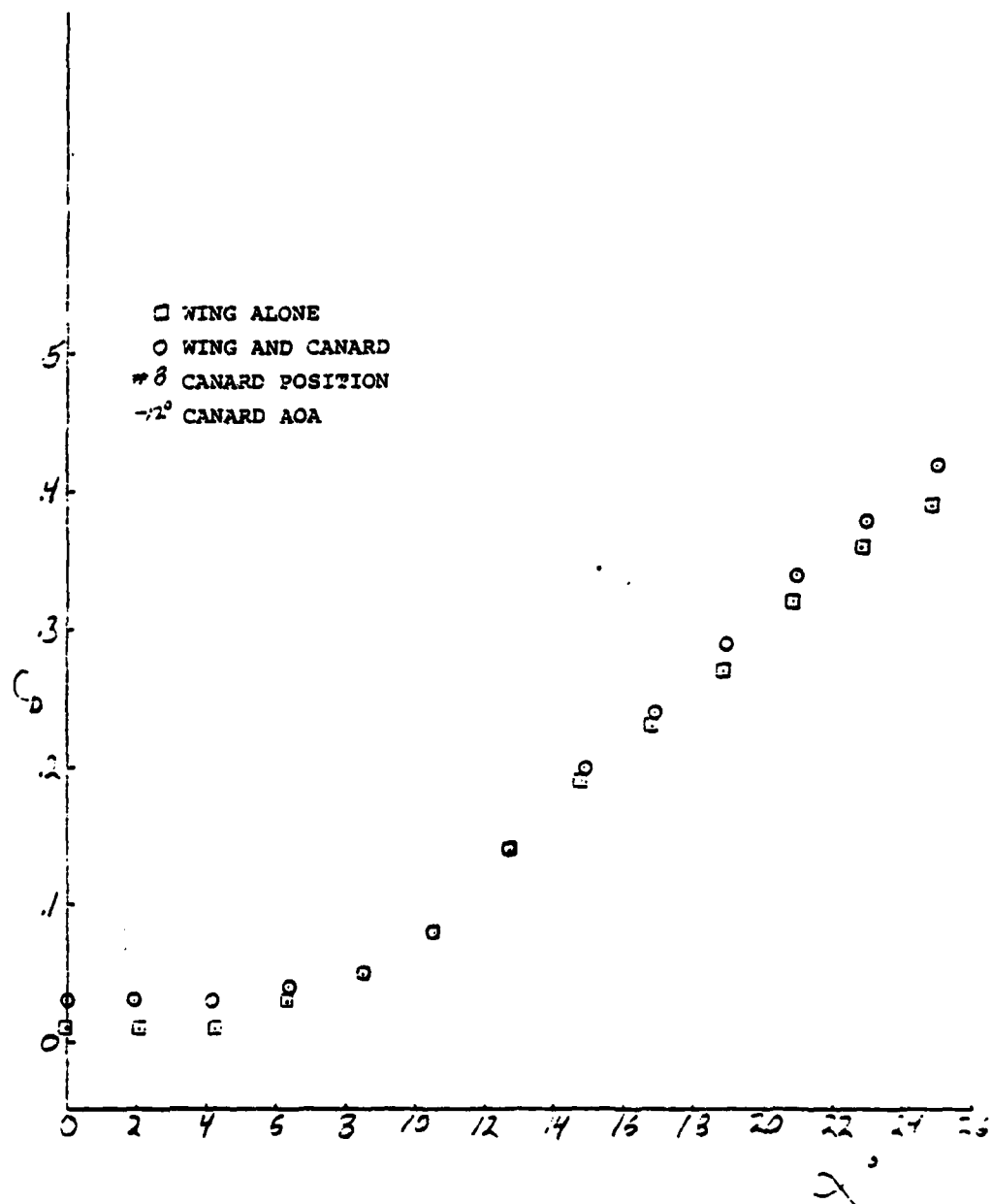


Figure 39A36D. Drag Coefficient vs Alpha

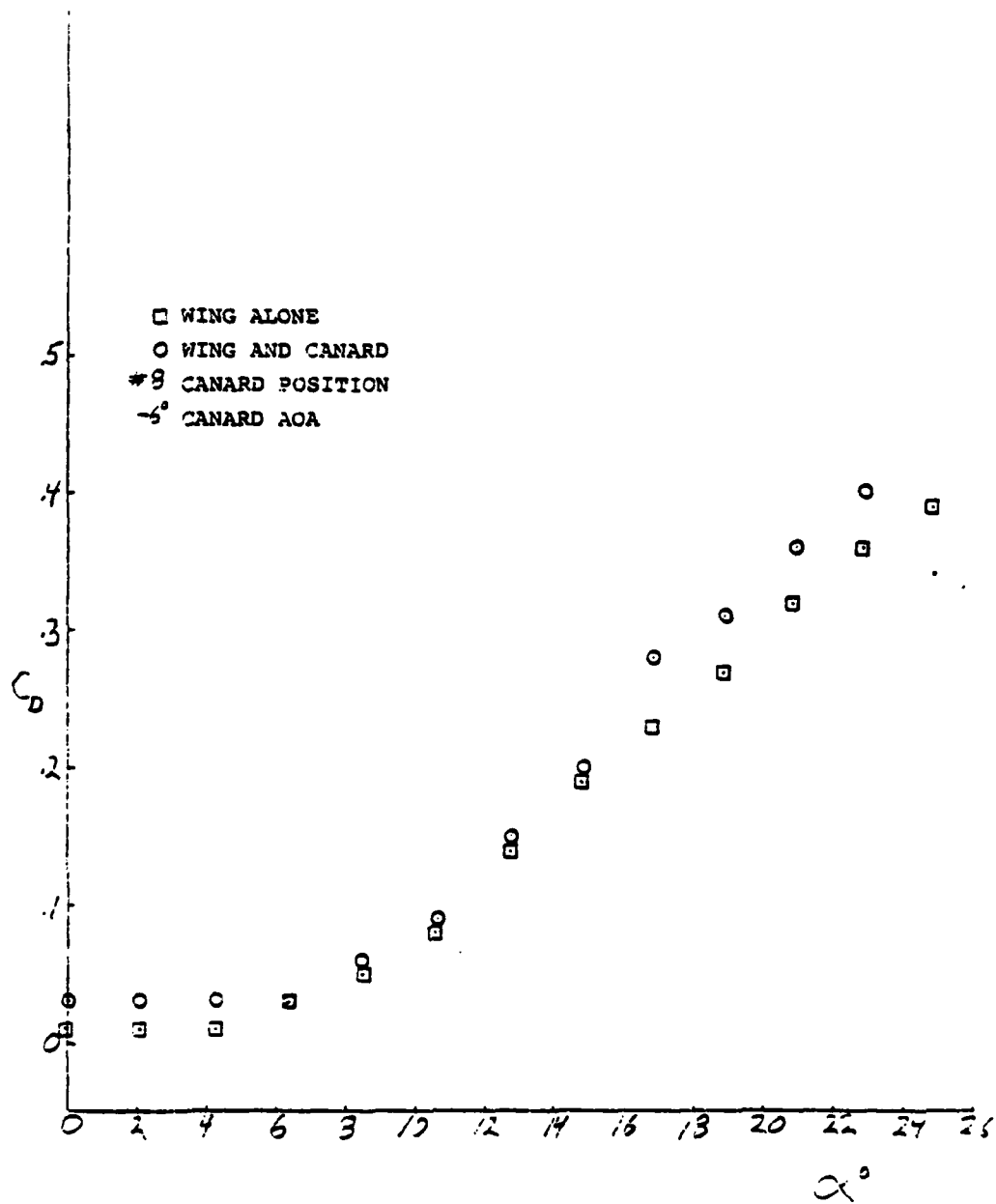


Figure 39A37D. Drag Coefficient vs Alpha

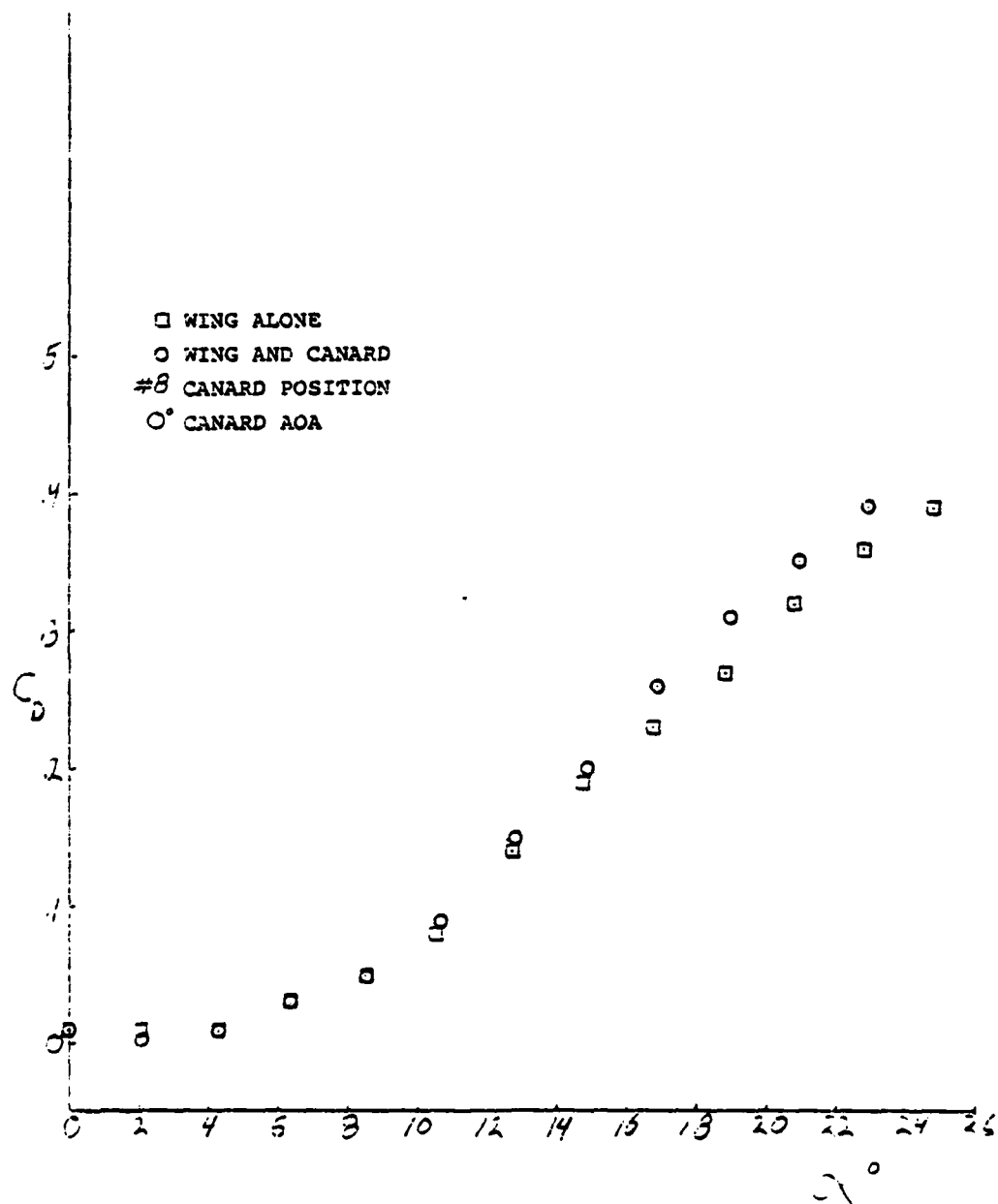


Figure 39A38D. Drag Coefficient vs Alpha

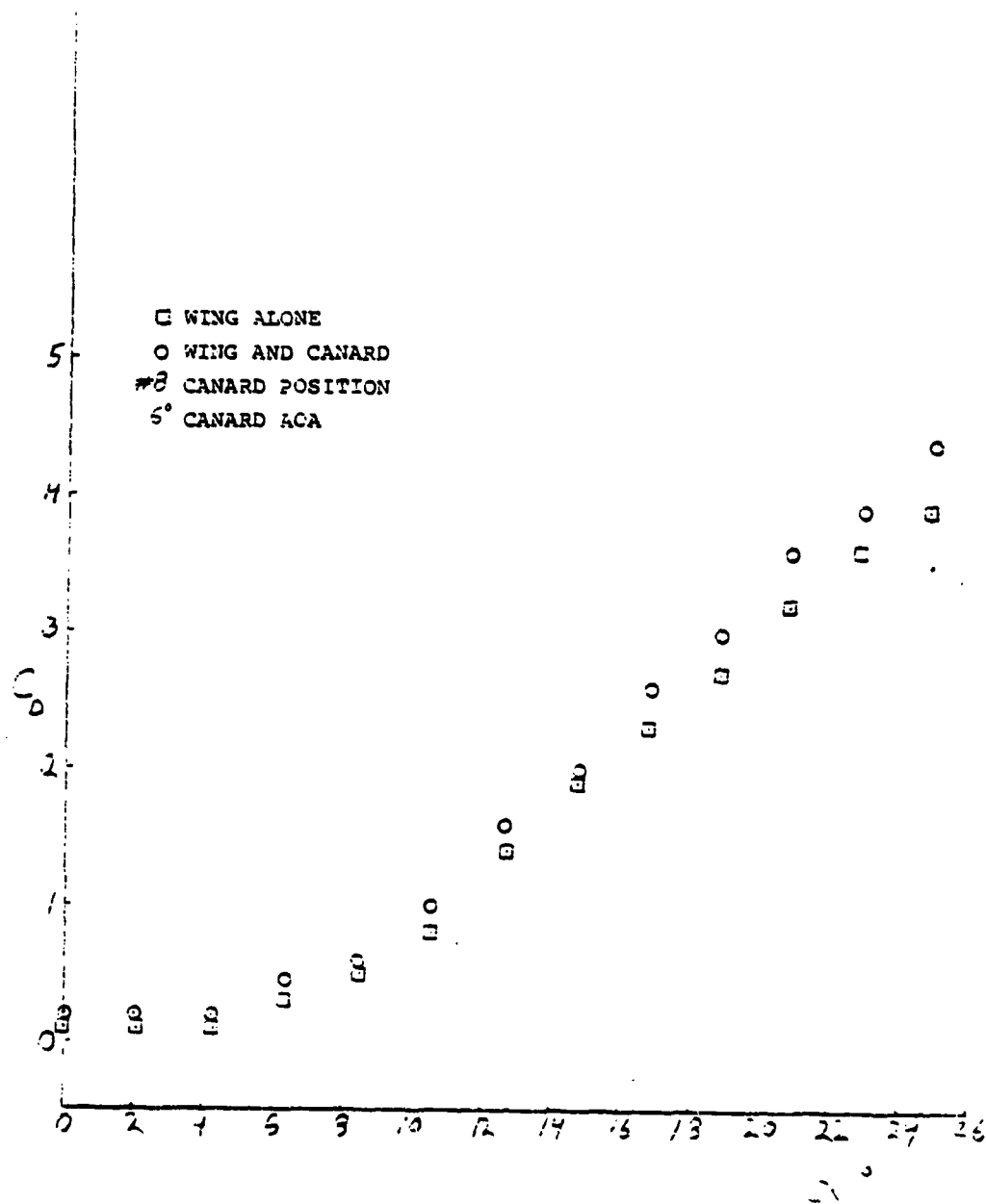


Figure 39A39D. Drag Coefficient vs Alpha

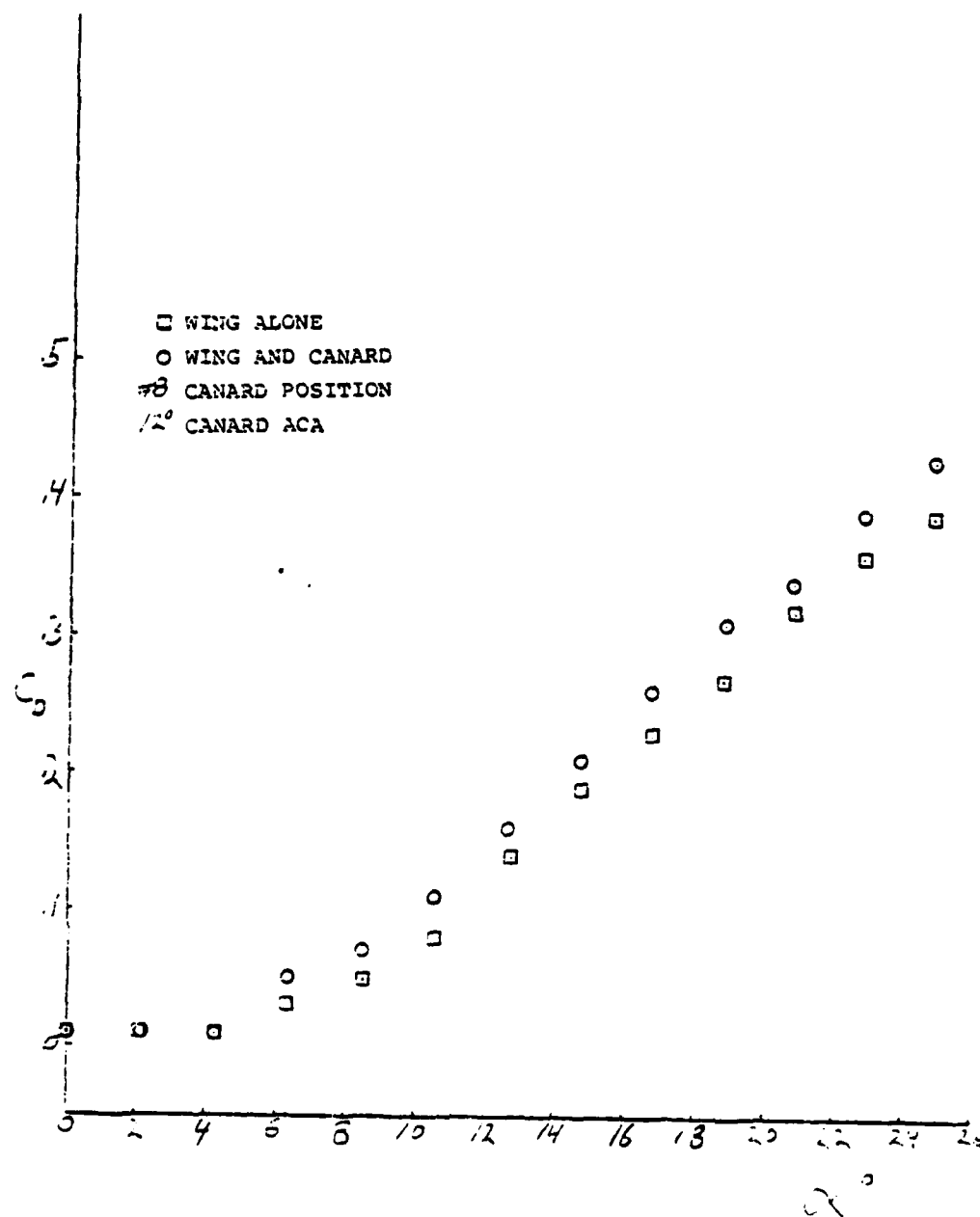


Figure 39A40D. Drag Coefficient vs Alpha

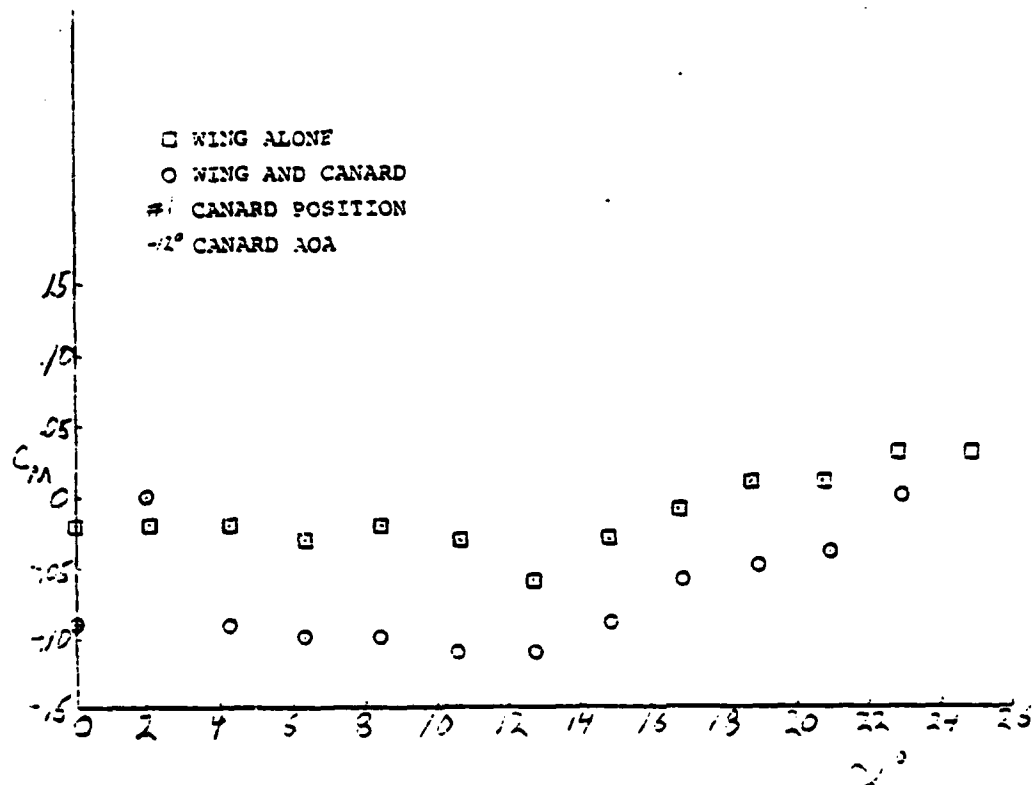


Figure 39A1M. Moment Coefficient vs Alpha

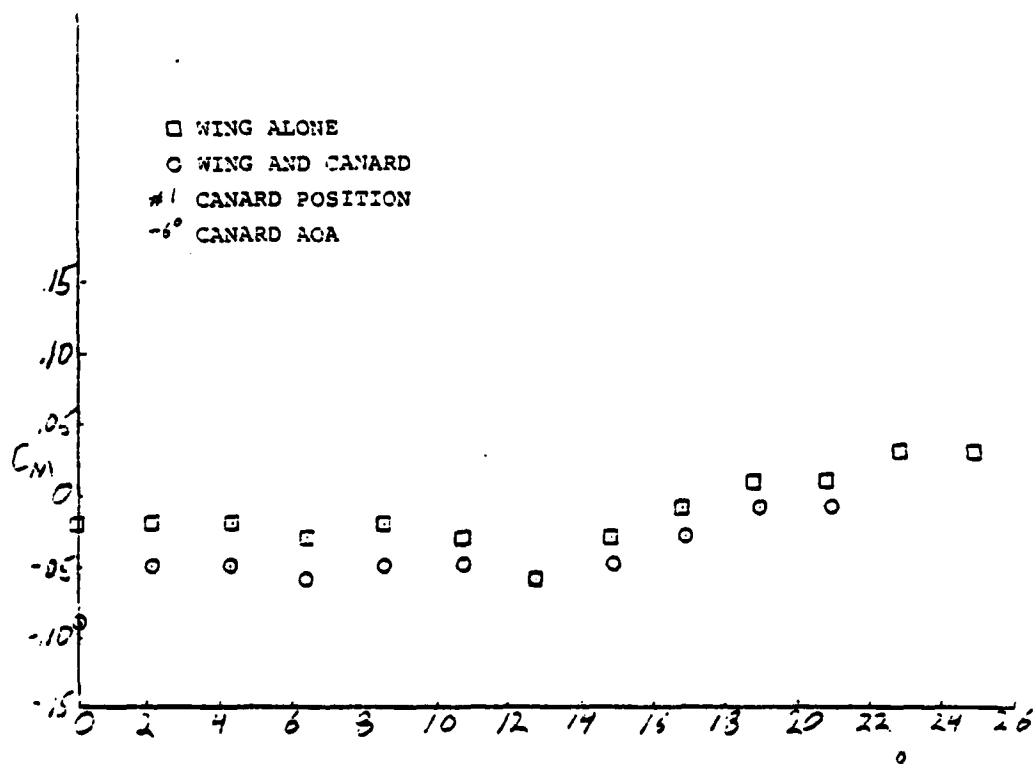


Figure 39A2M. Moment Coefficient vs Alpha

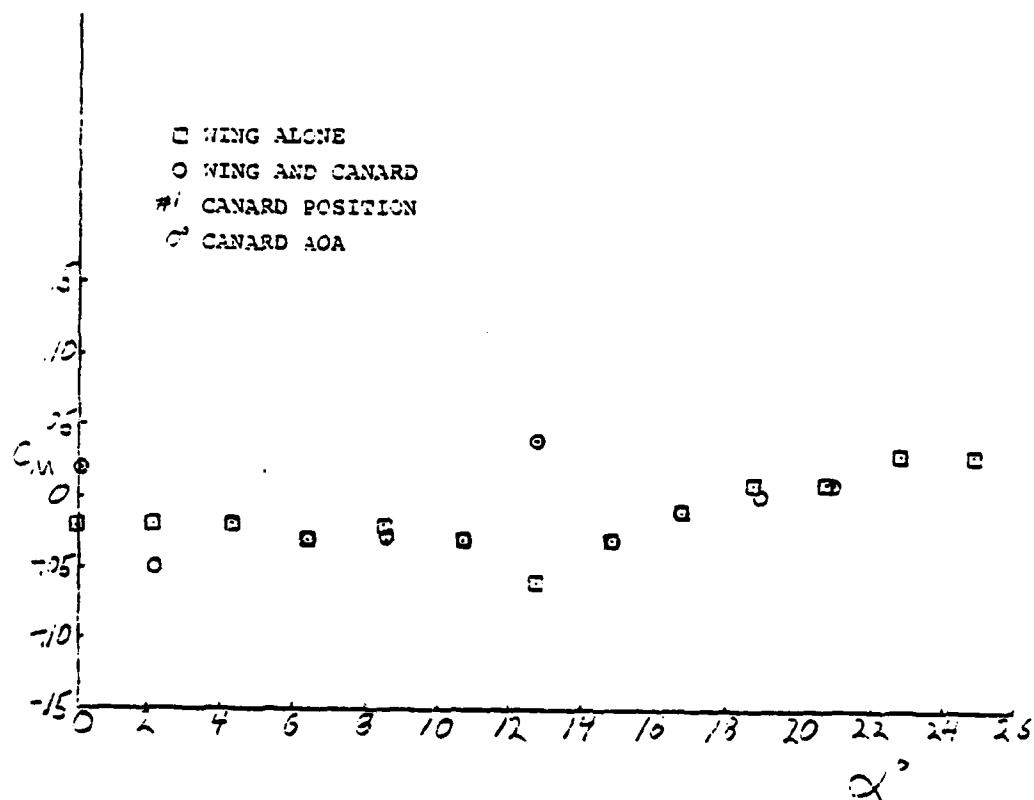


Figure 39A3M. Moment Coefficient vs Alpha

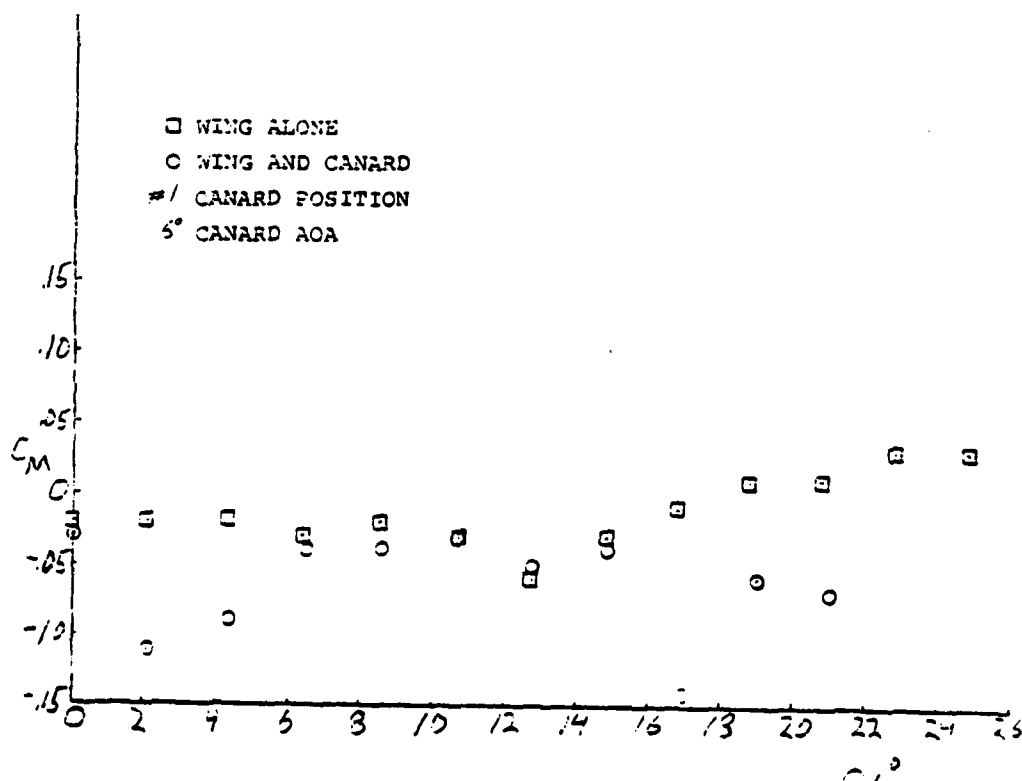


Figure 39A4M. Moment Coefficient vs Alpha

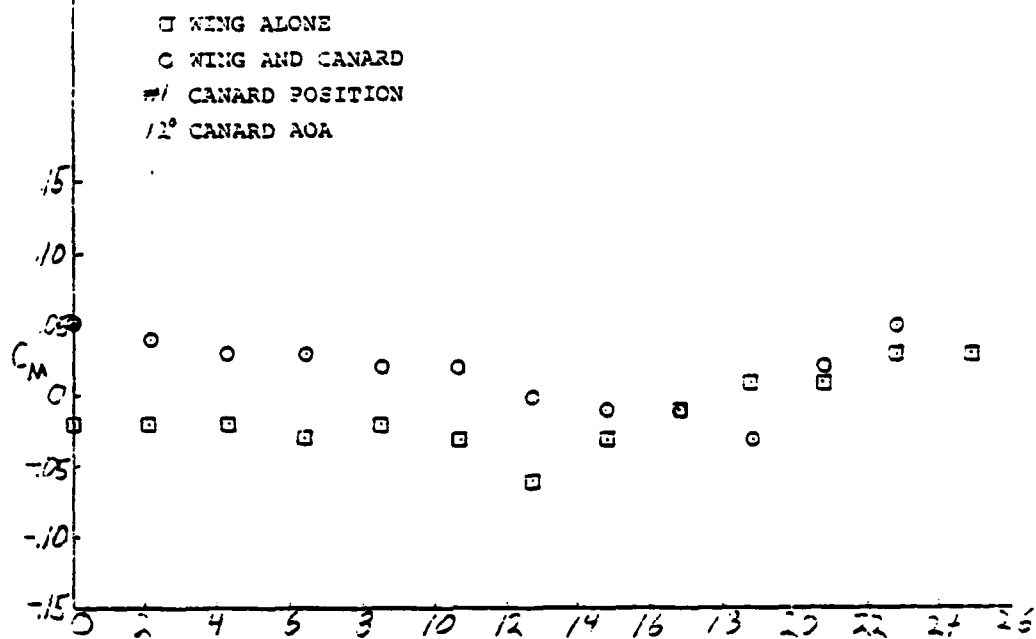


Figure 39A5M. Moment Coefficient vs α°

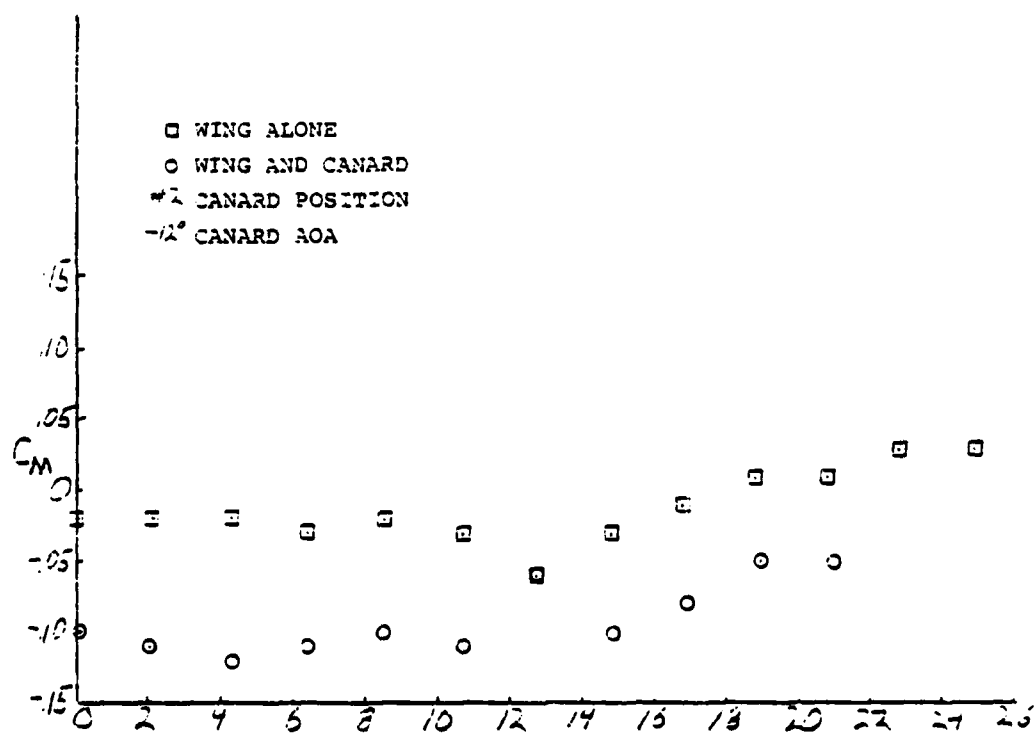


Figure 39A6M. Moment Coefficient vs α°

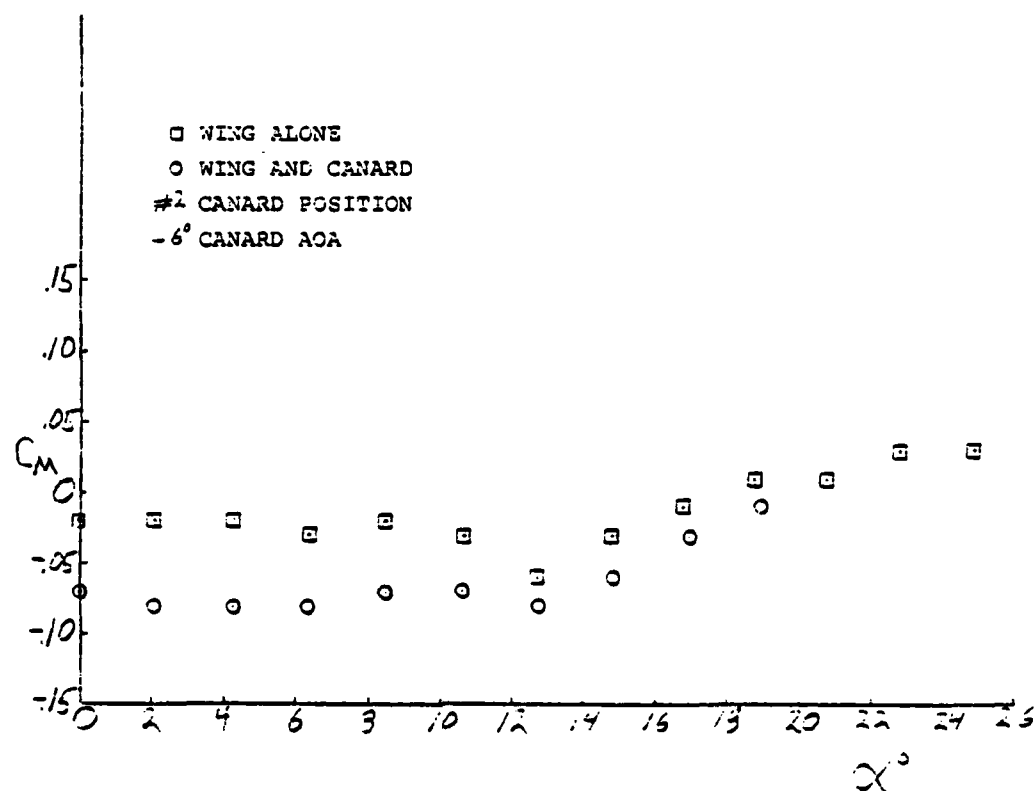


Figure 39A7M. Moment Coefficient vs Alpha

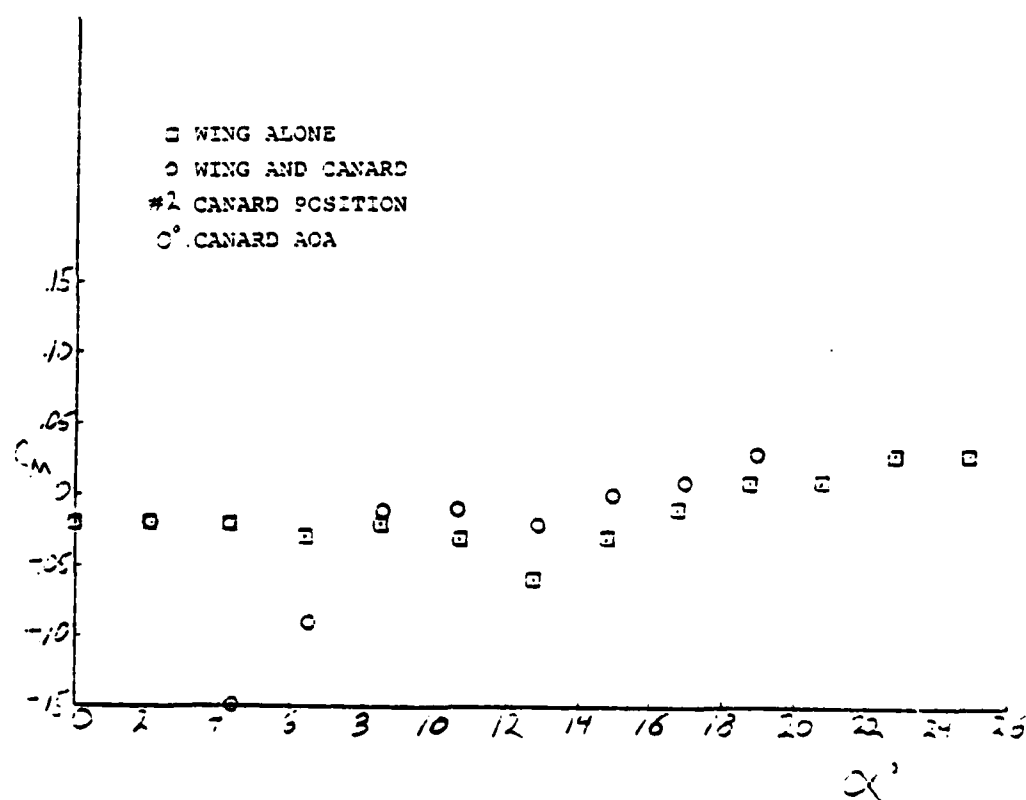


Figure 39A8M. Moment Coefficient vs Alpha

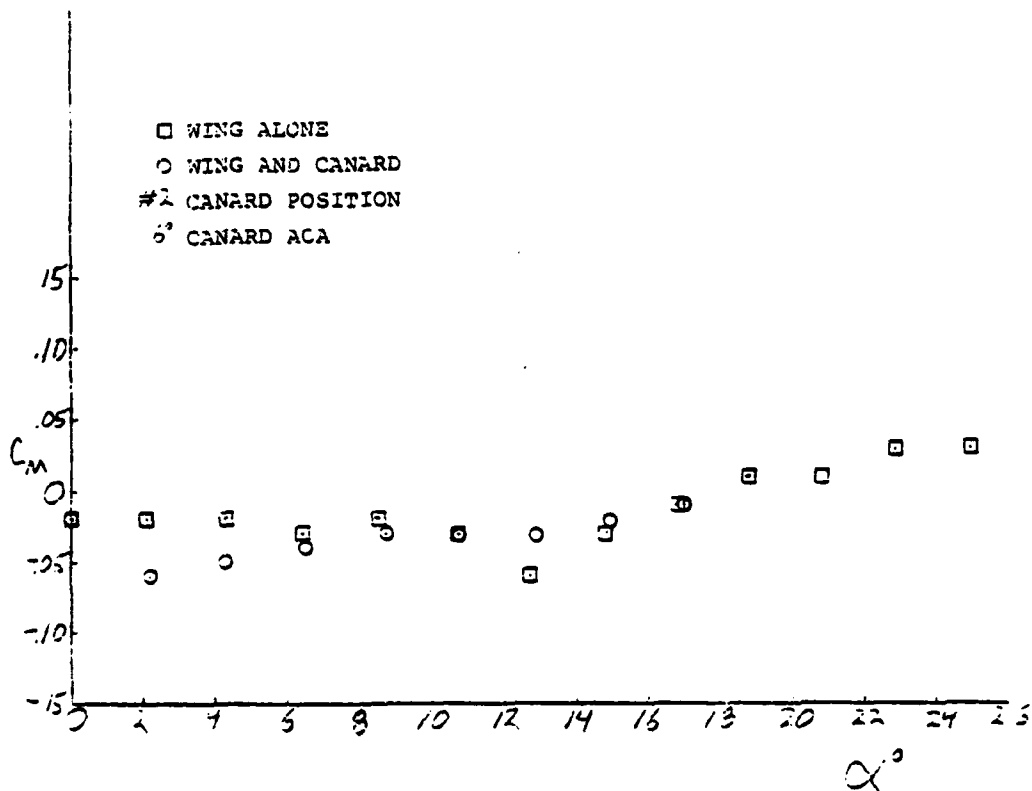


Figure 39A9M. Moment Coefficient vs α°

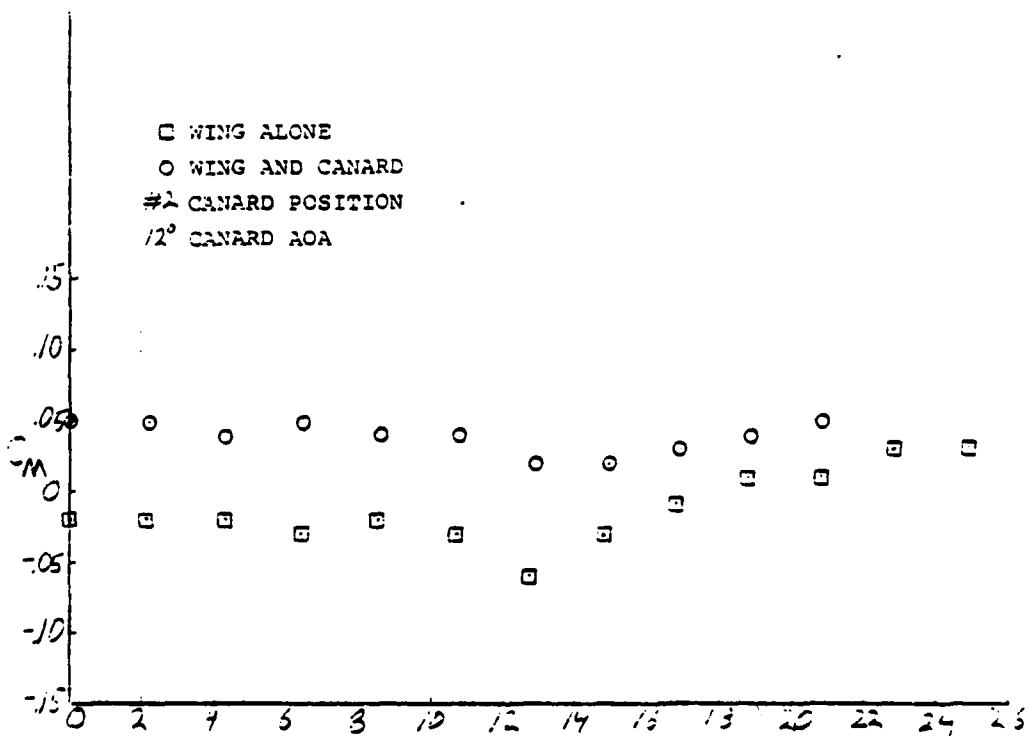
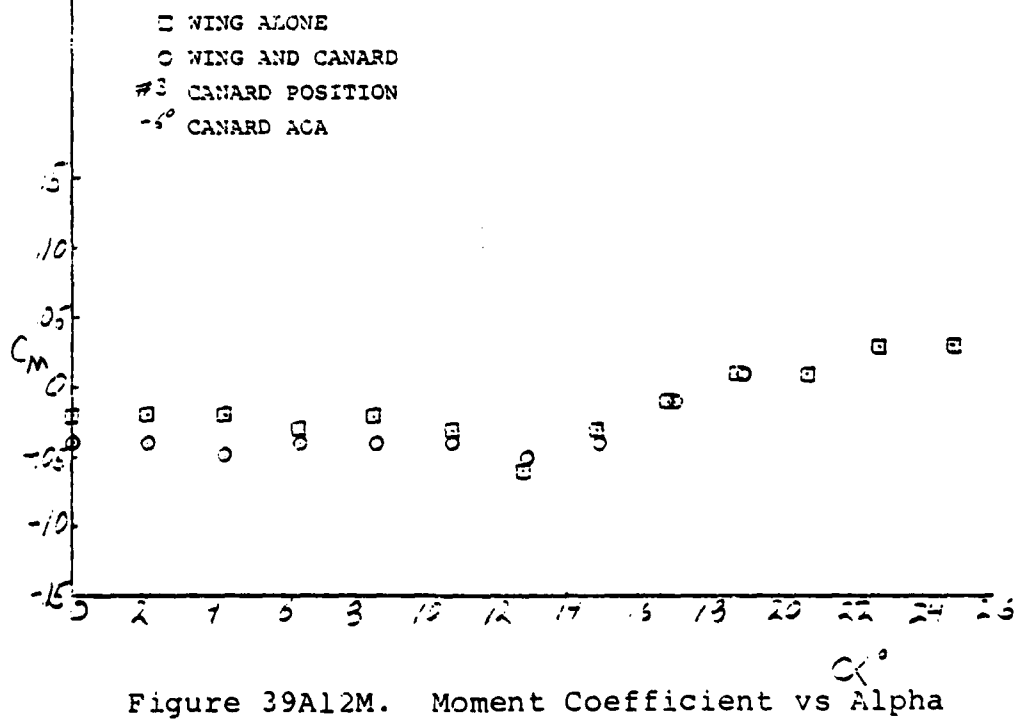
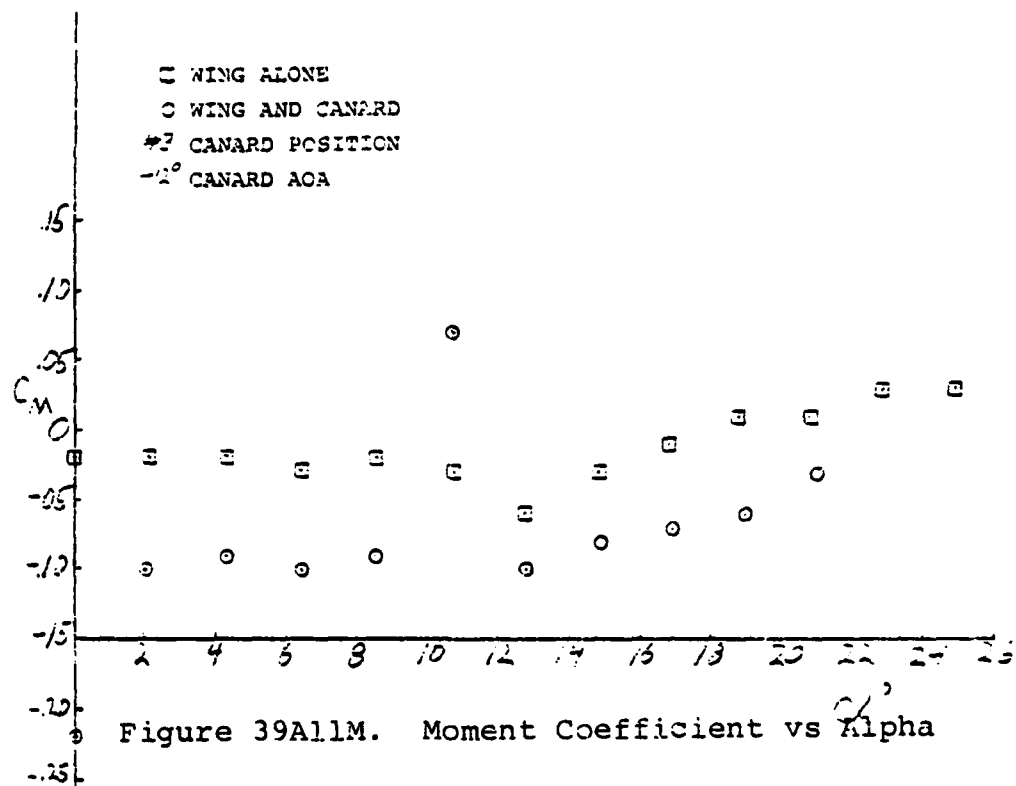


Figure 39A10M. Moment Coefficient vs α°



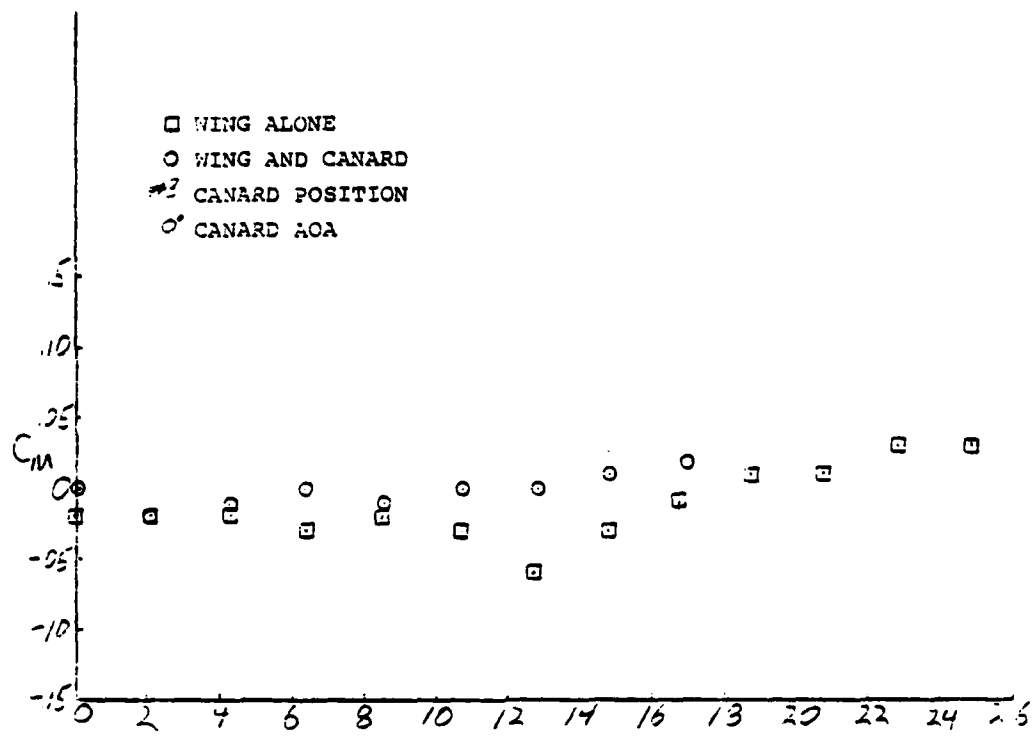


Figure 39A13M. Moment Coefficient vs Alpha

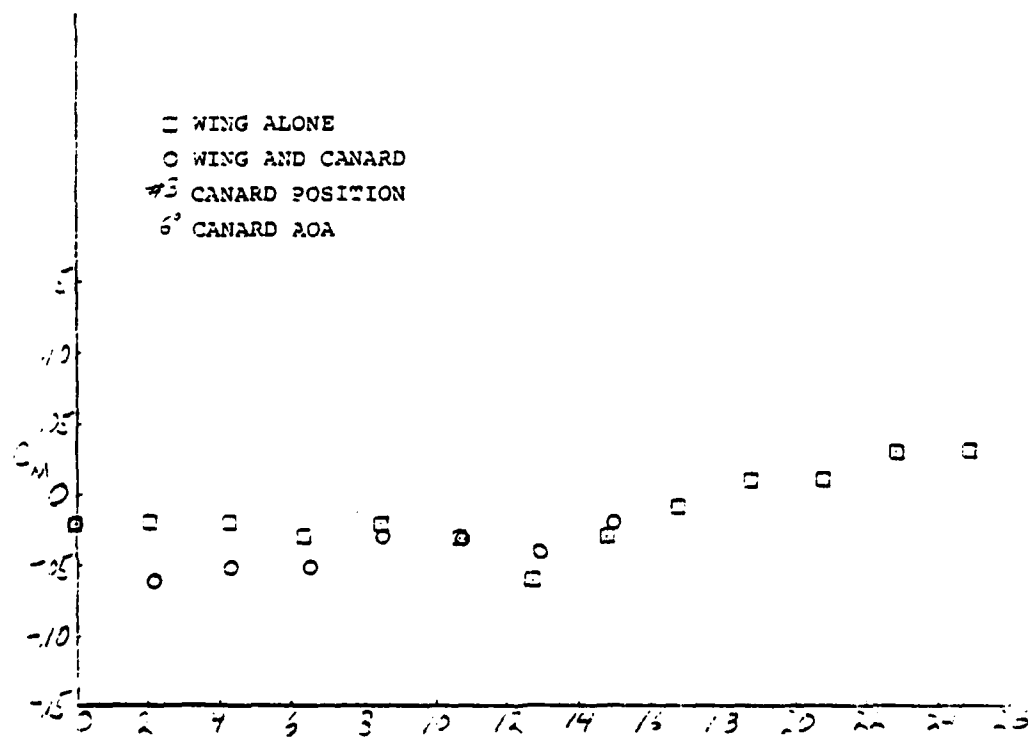


Figure 39A14M. Moment Coefficient vs Alpha

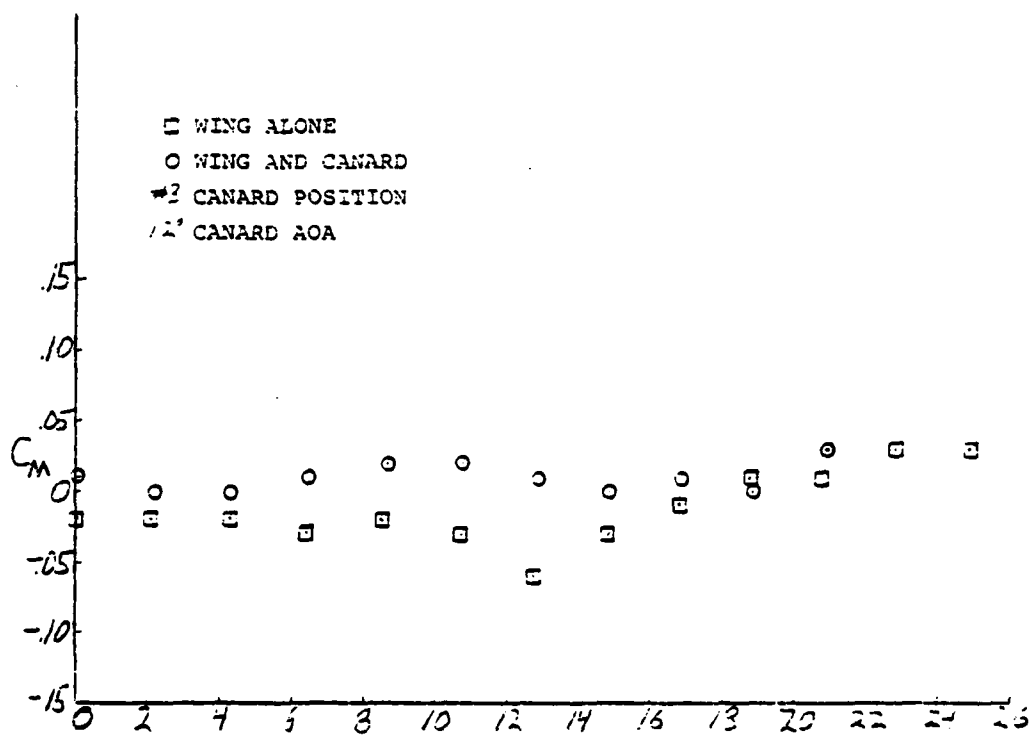


Figure 39A15M. Moment Coefficient vs α

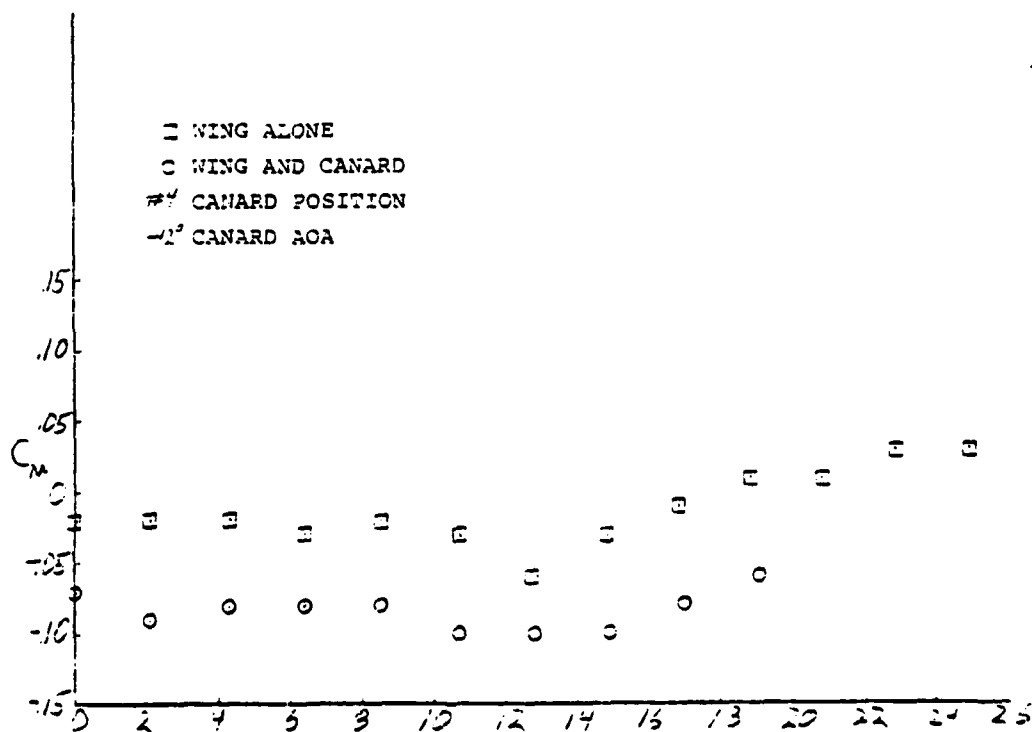


Figure 39A16M. Moment Coefficient vs α

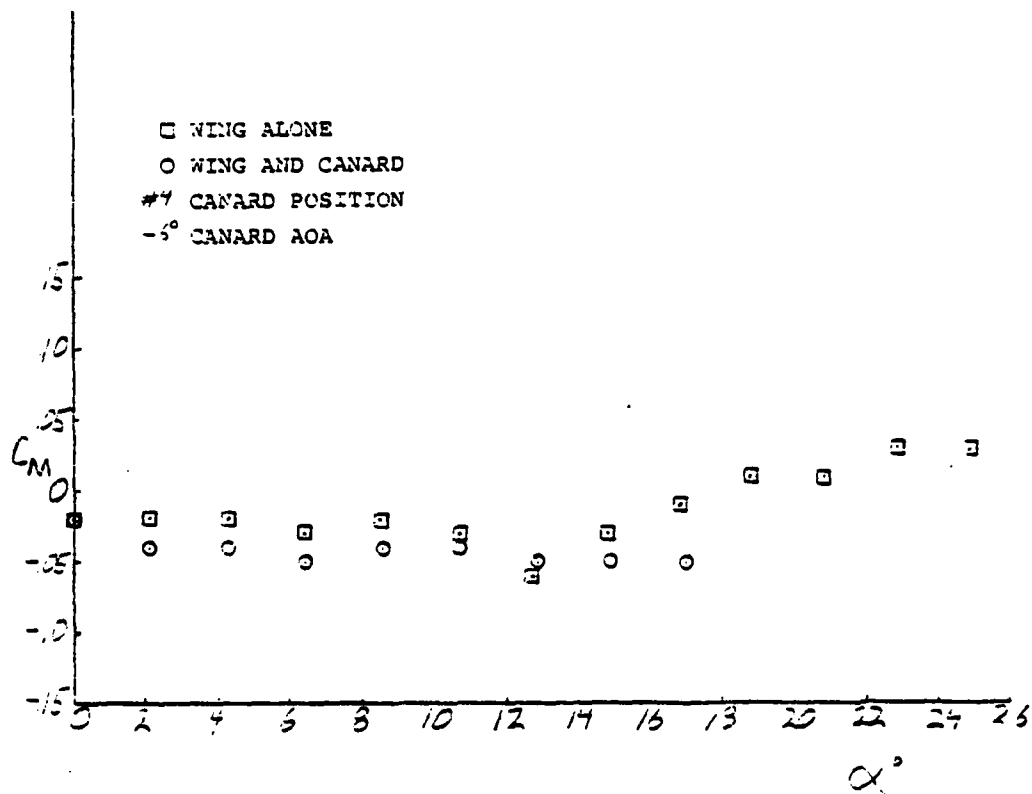


Figure 39A17M. Moment Coefficient vs Alpha

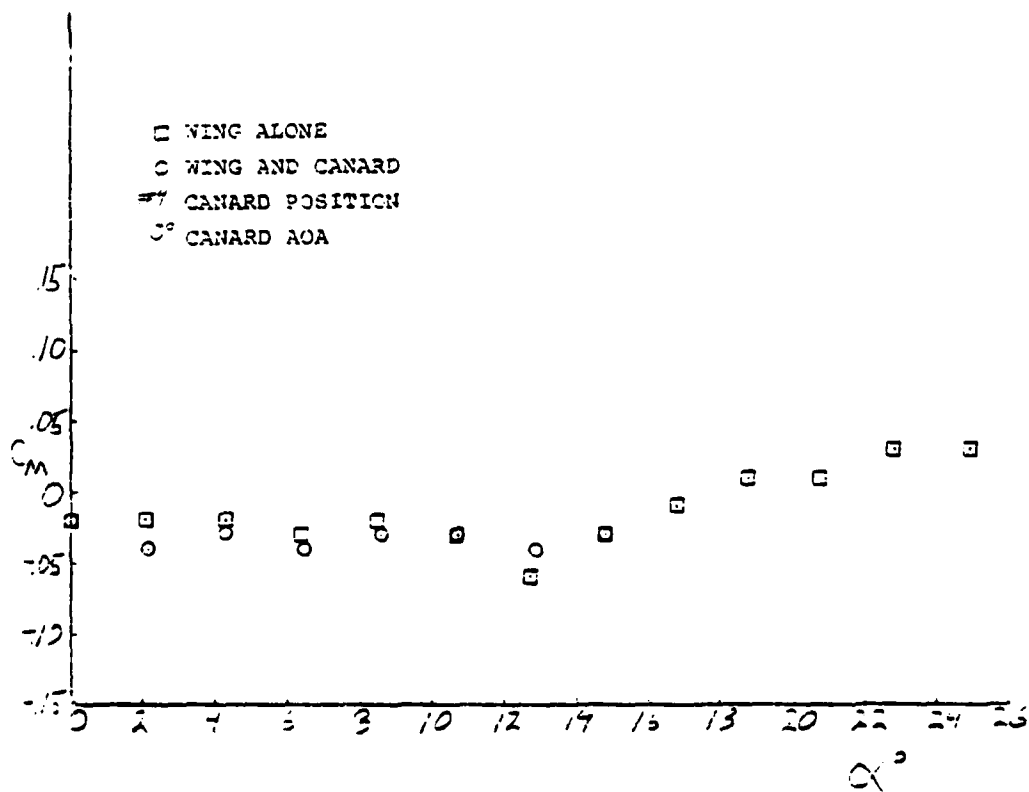


Figure 39A18M. Moment Coefficient vs Alpha

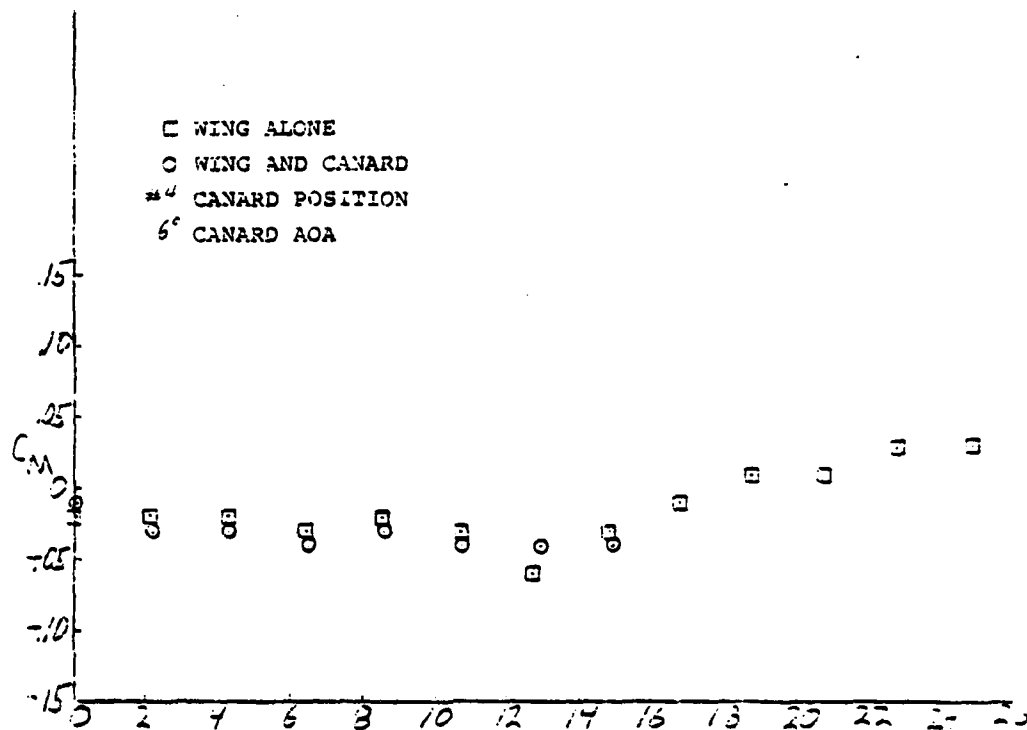


Figure 39A19M. Moment Coefficient vs α

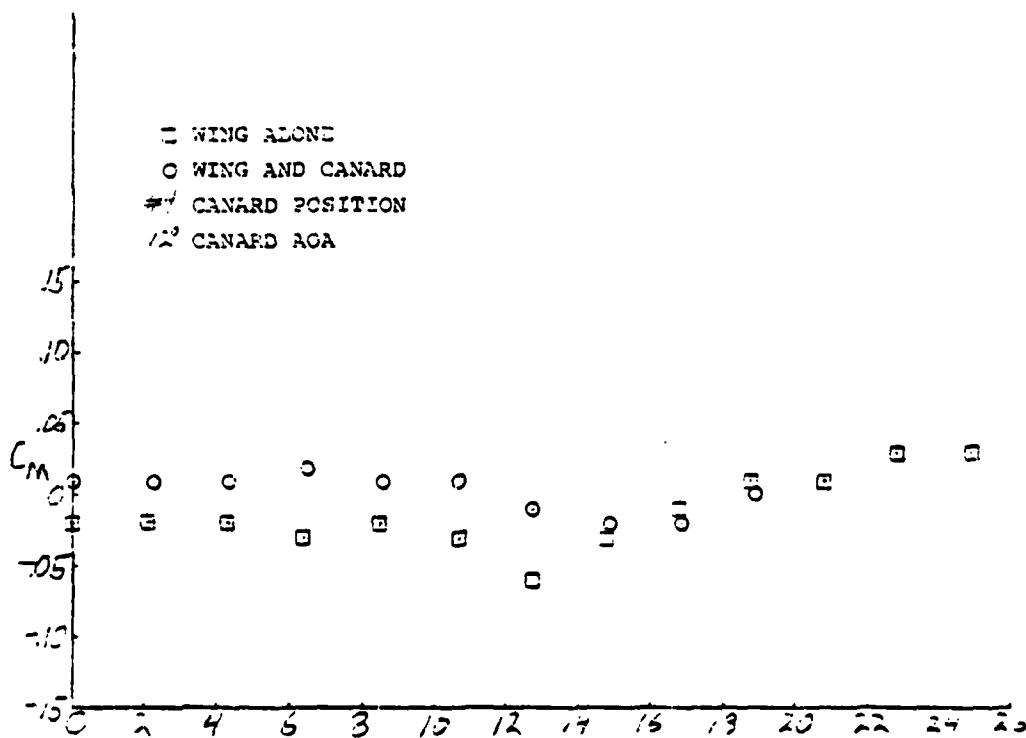


Figure 39A20M. Moment Coefficient vs α

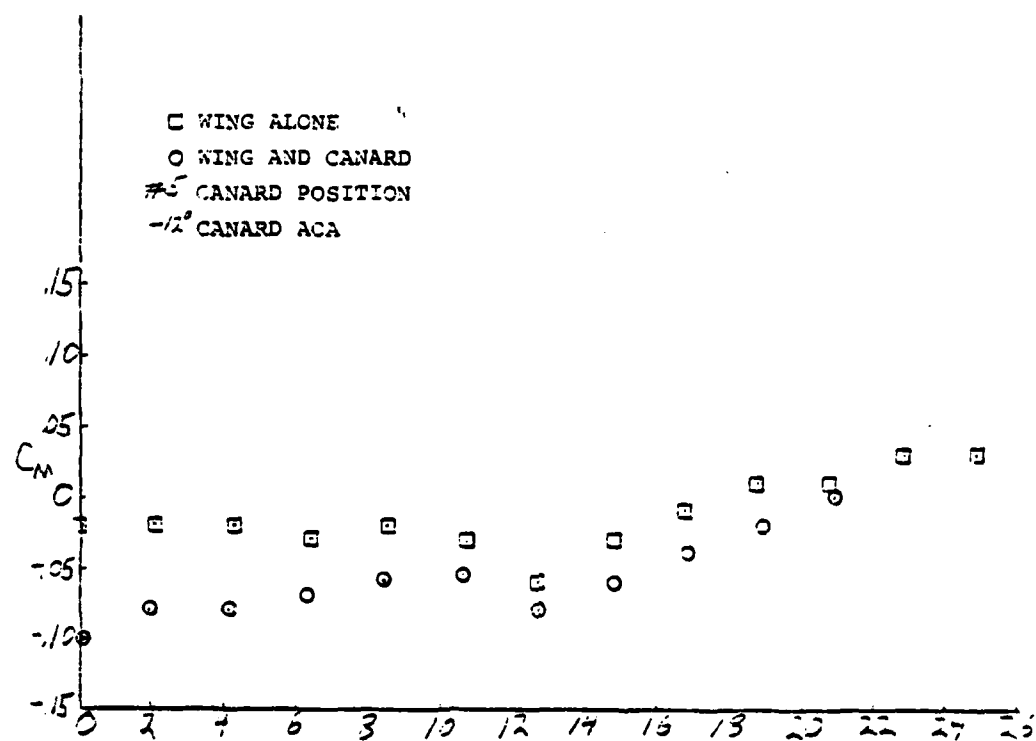


Figure 39A21M. Moment Coefficient vs Alpha

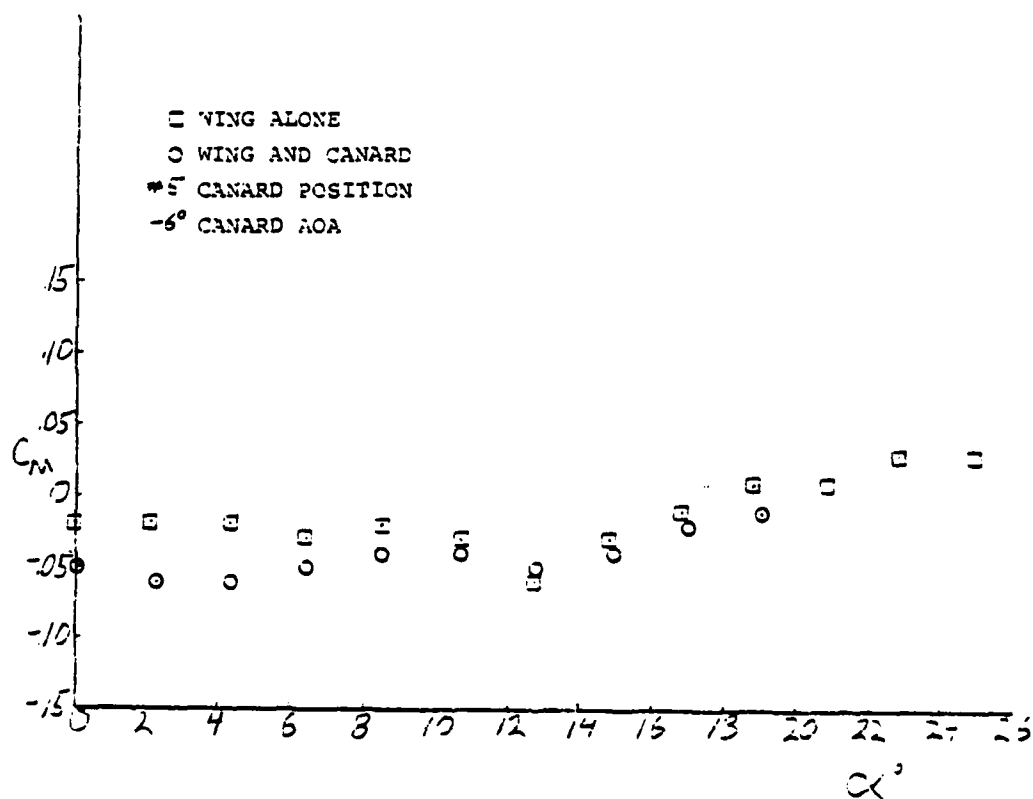


Figure 39A22M. Moment Coefficient vs Alpha

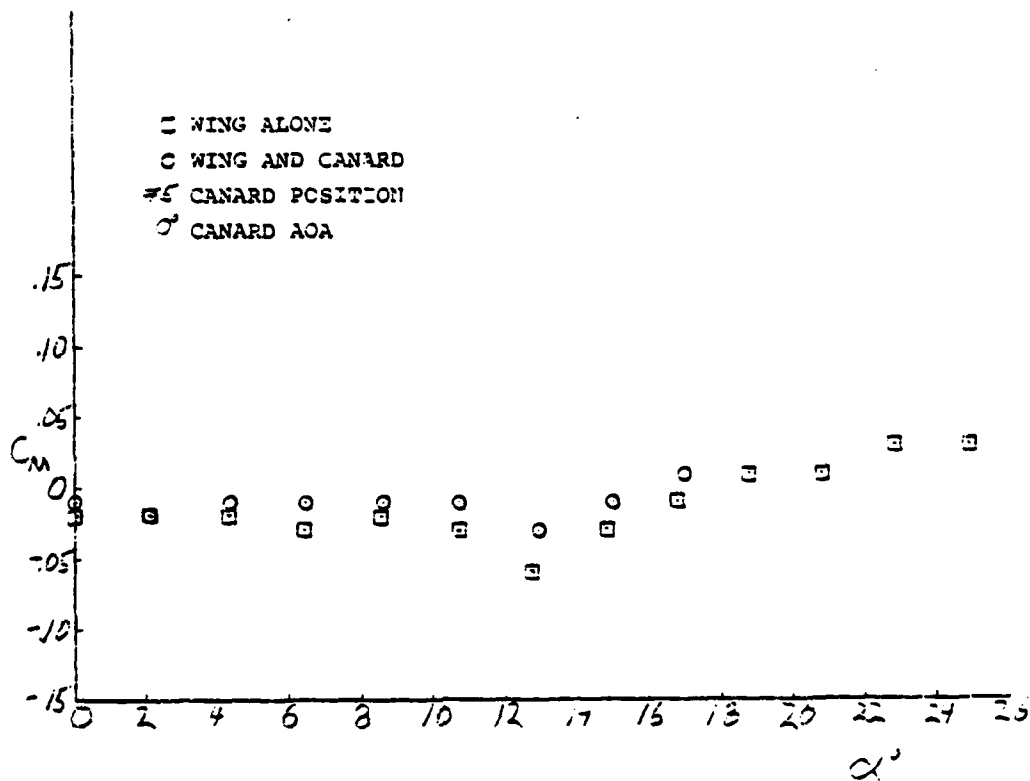


Figure 39A23M. Moment Coefficient vs Alpha

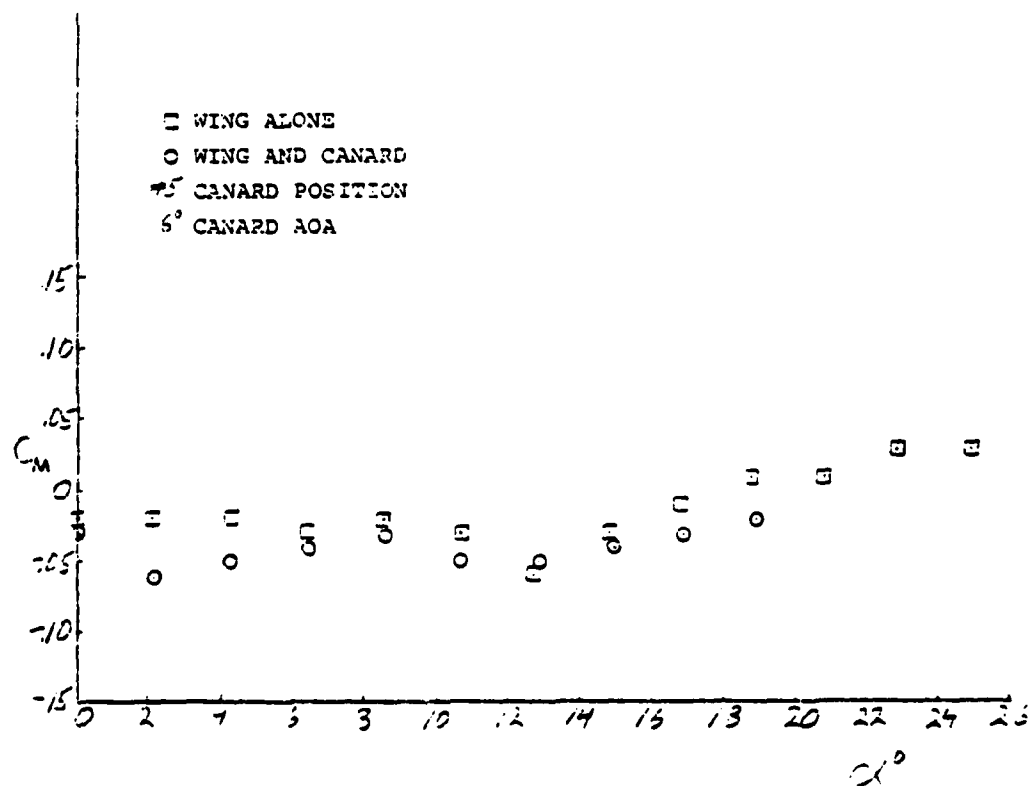


Figure 39A24M. Moment Coefficient vs Alpha

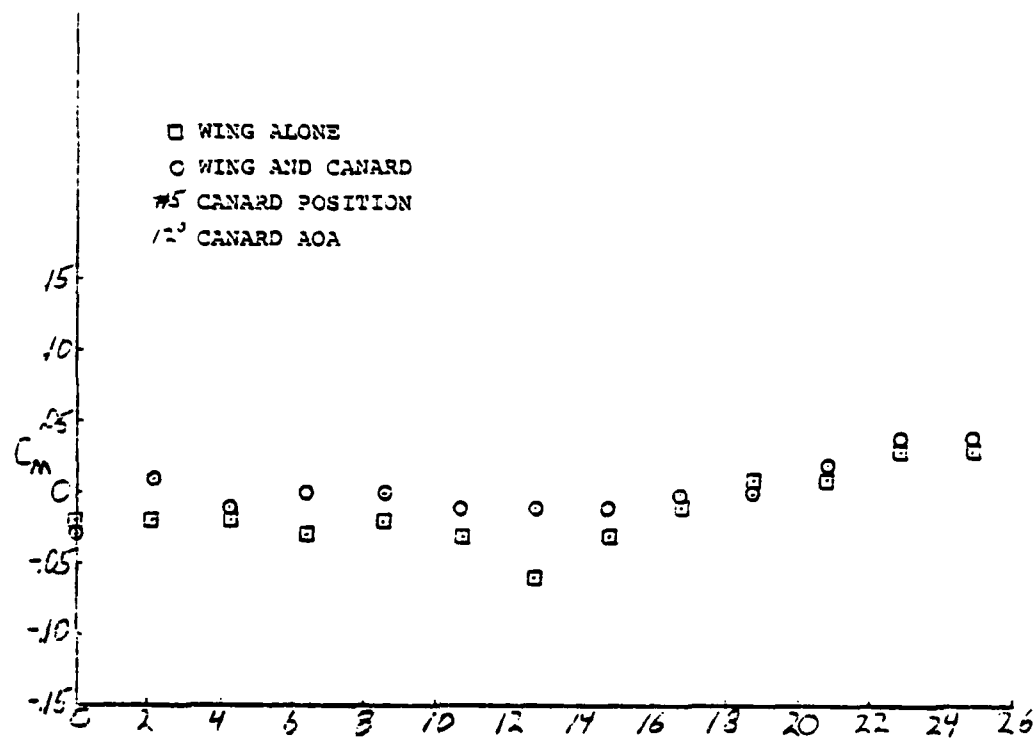


Figure 39A25M. Moment Coefficient vs α°

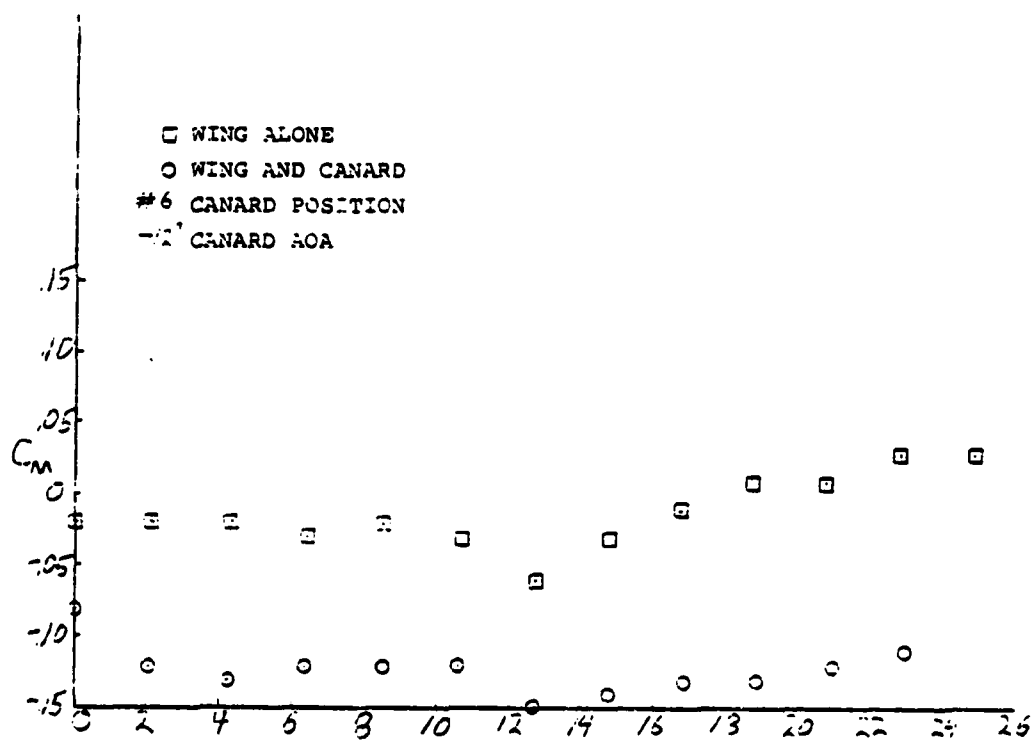
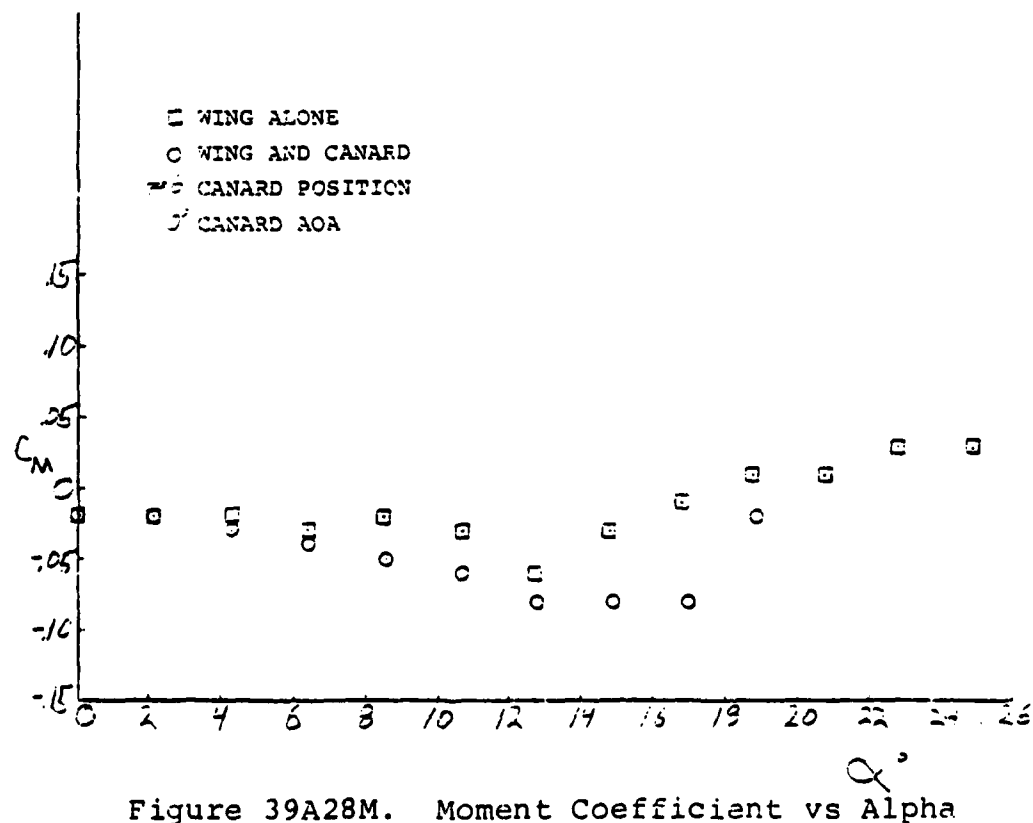
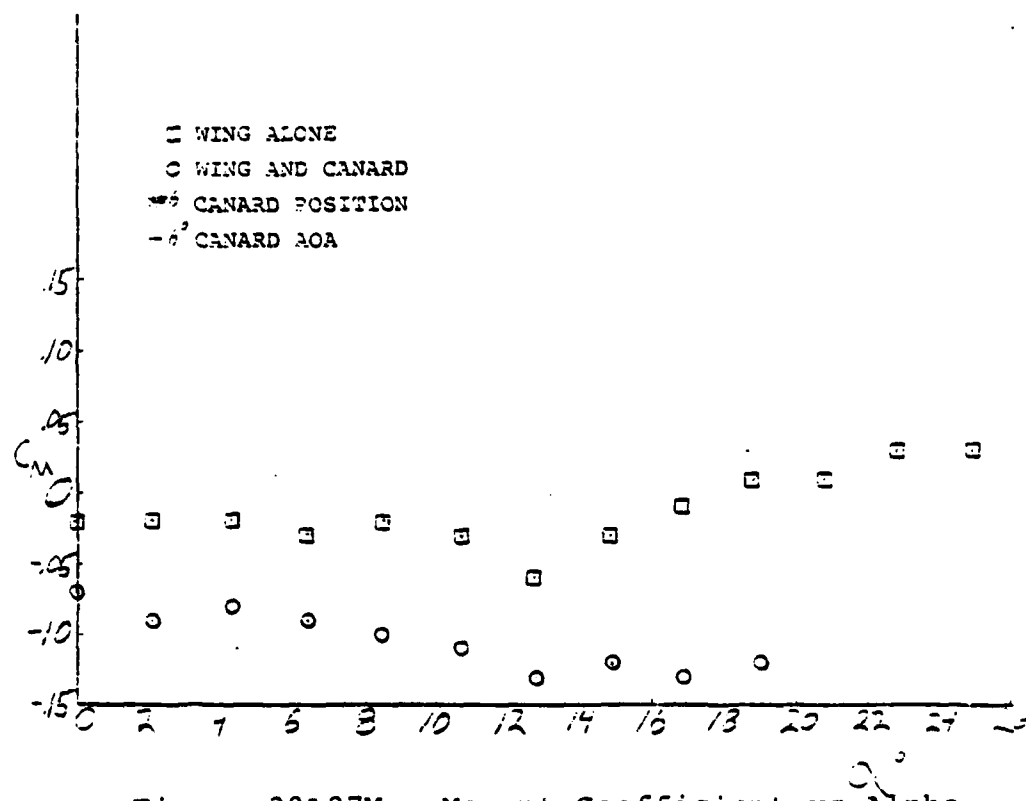


Figure 39A26M. Moment Coefficient vs α°



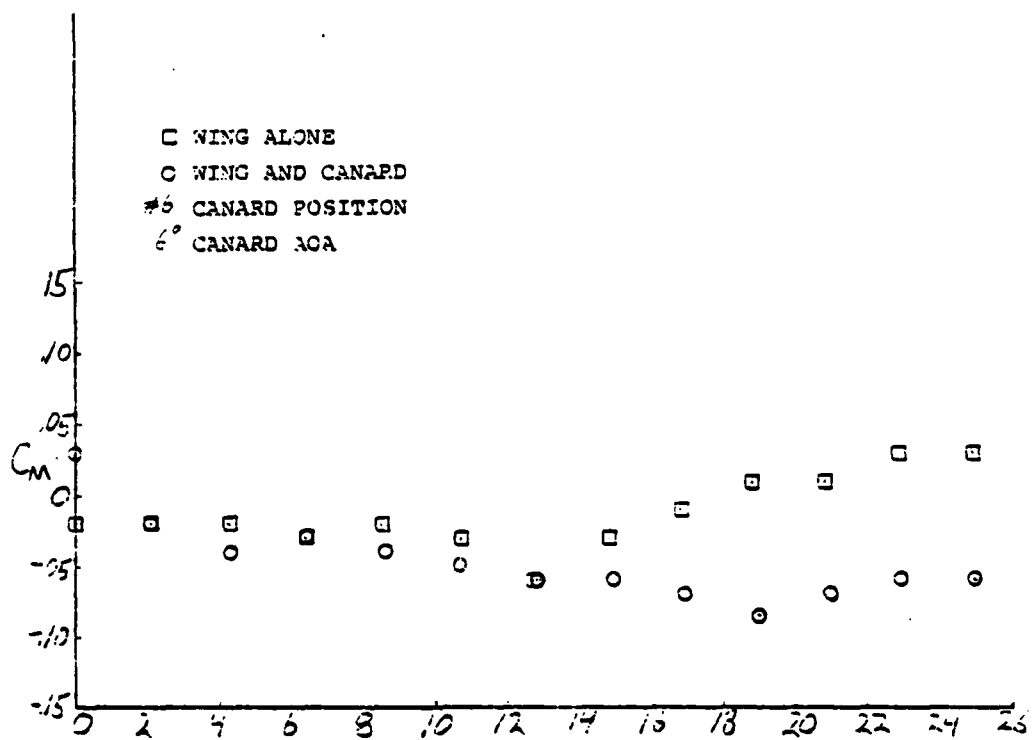


Figure 39A29M. Moment Coefficient vs α

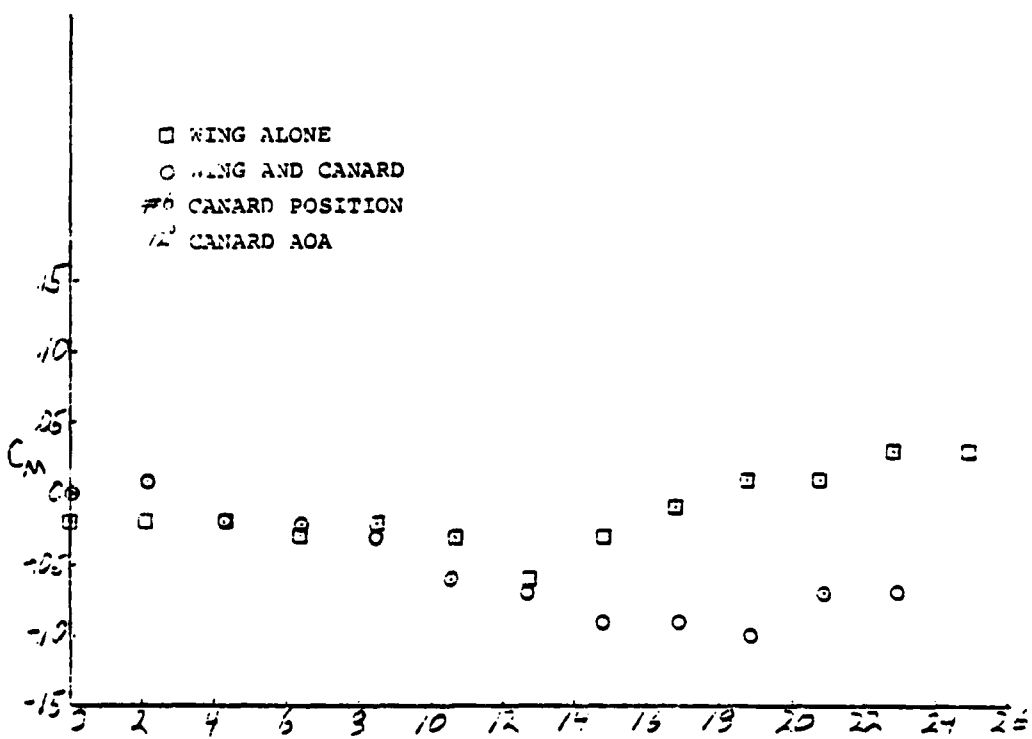


Figure 39A30M. Moment Coefficient vs α

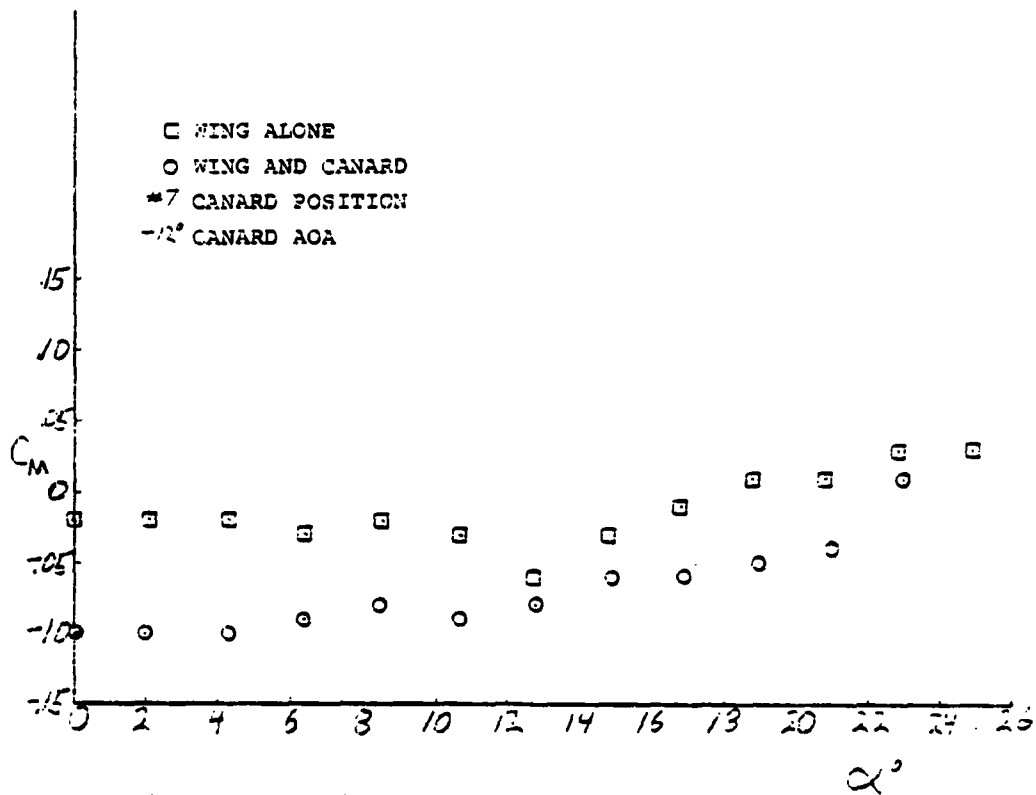


Figure 39A31M. Moment Coefficient vs α

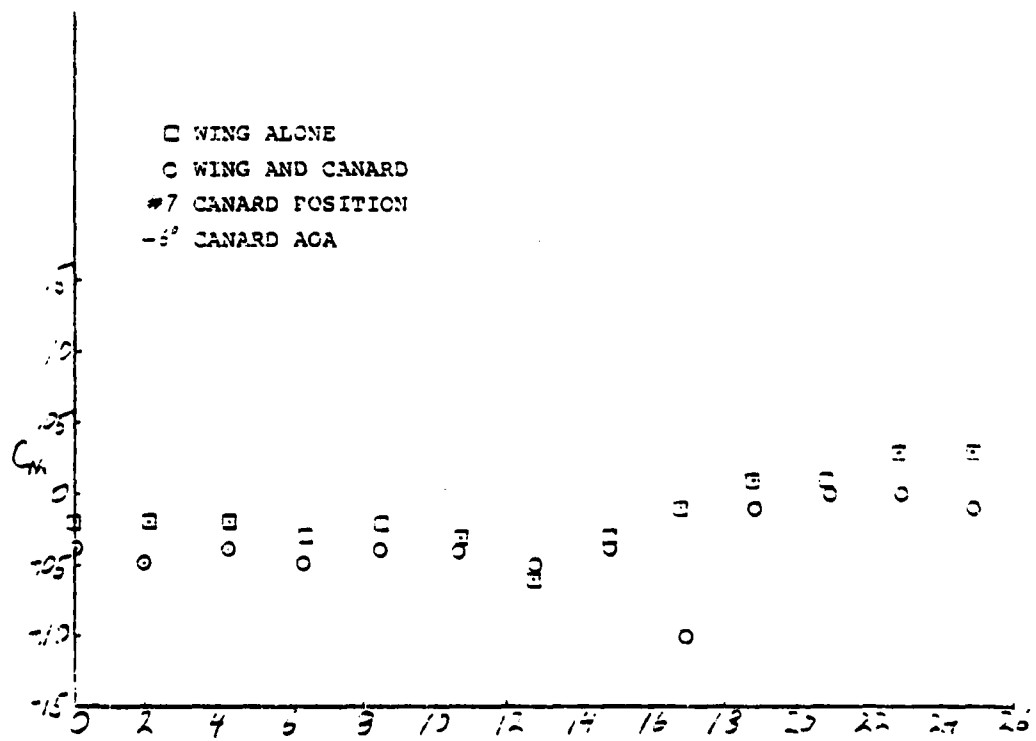


Figure 39A32M. Moment Coefficient vs α

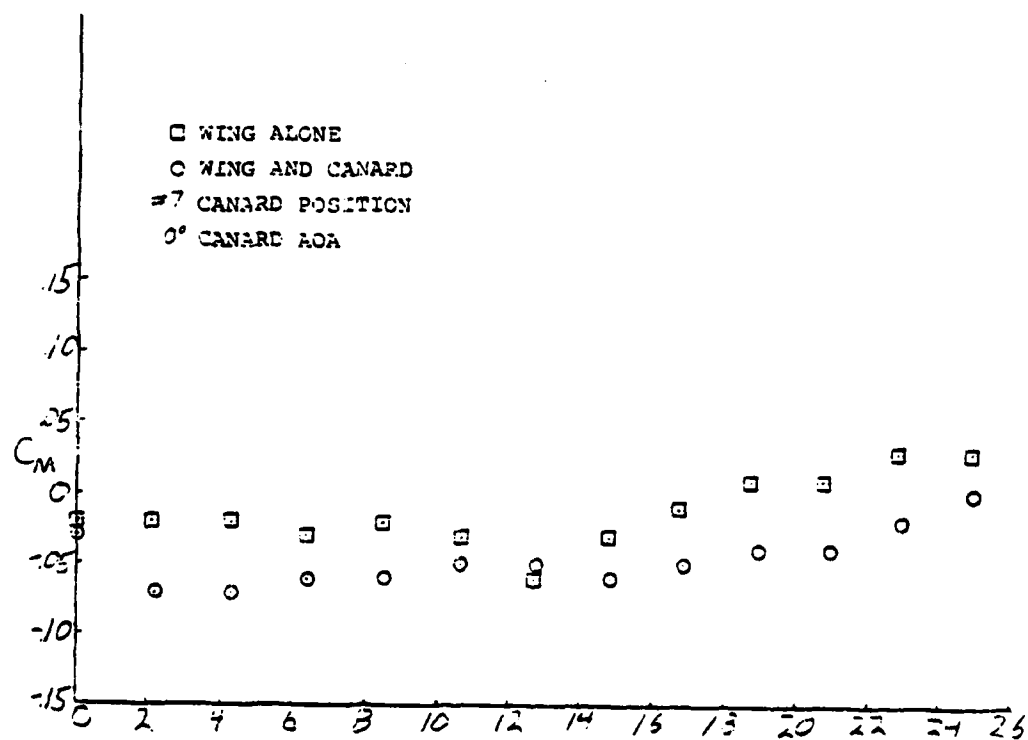


Figure 39A33M. Moment Coefficient vs α

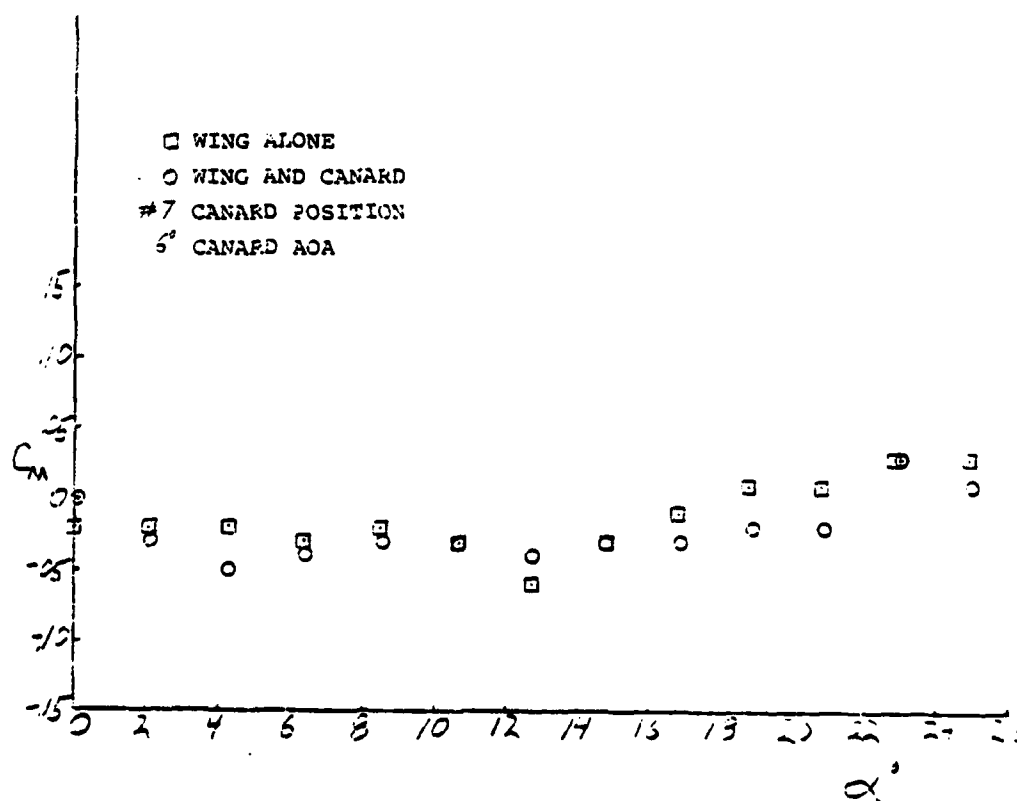


Figure 39A34M. Moment Coefficient vs α

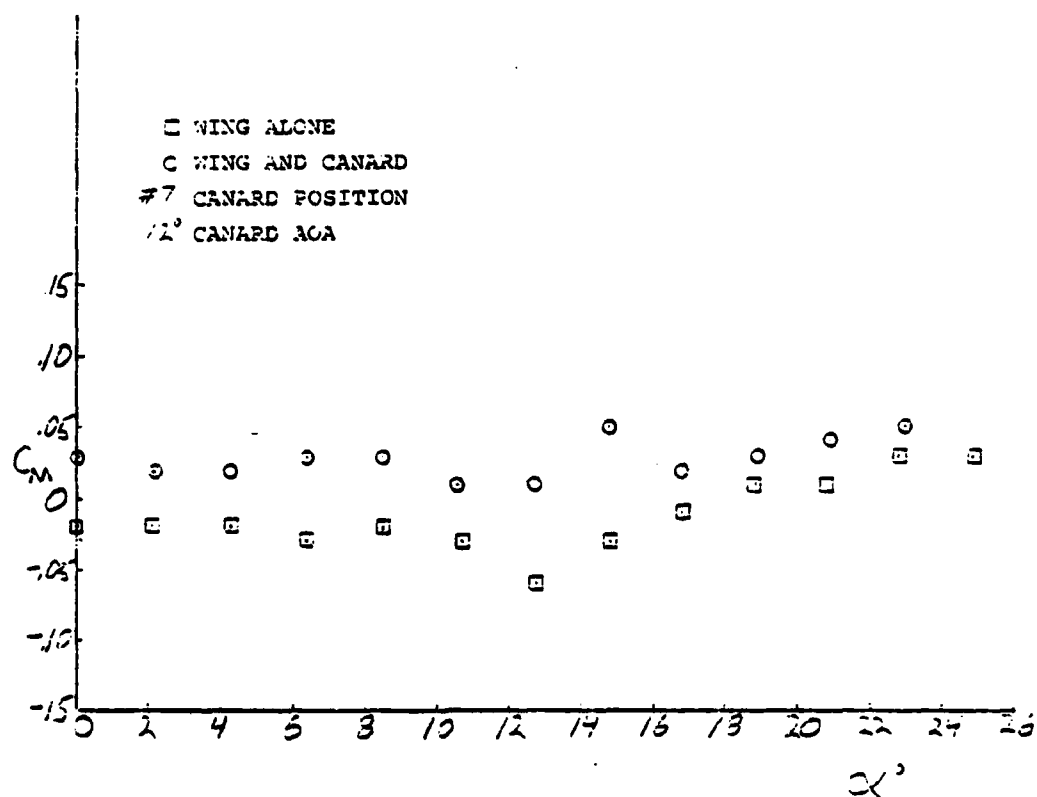


Figure 39A35M. Moment Coefficient vs Alpha

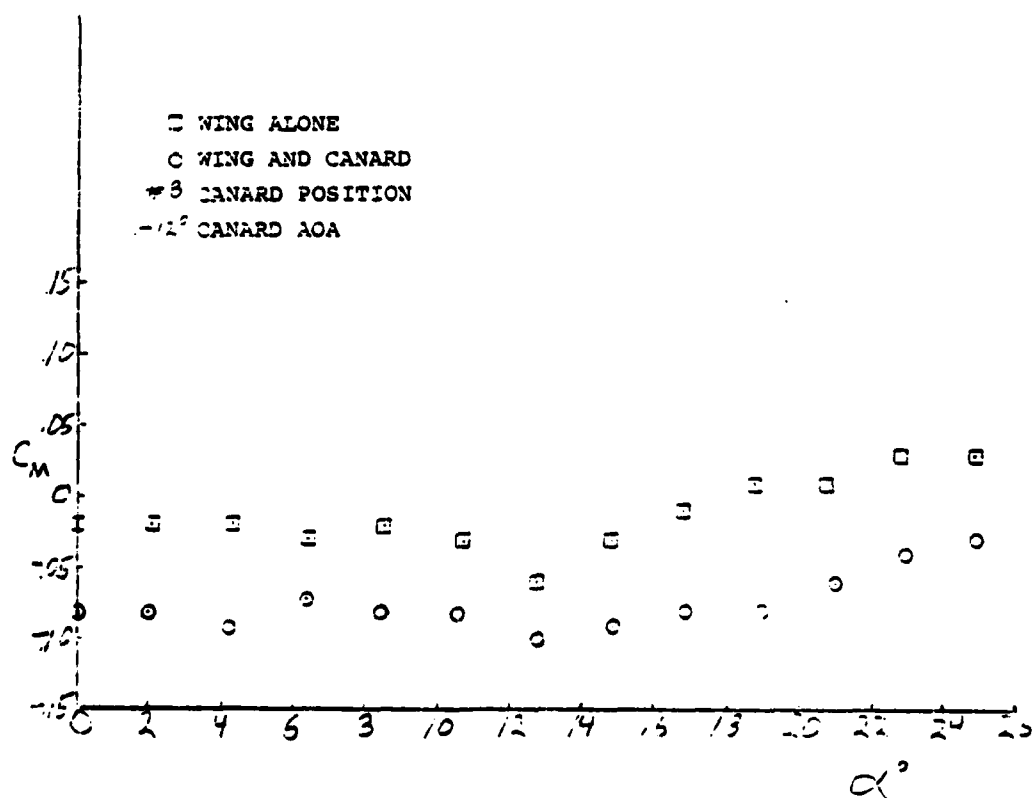


Figure 39A36M. Moment Coefficient vs Alpha

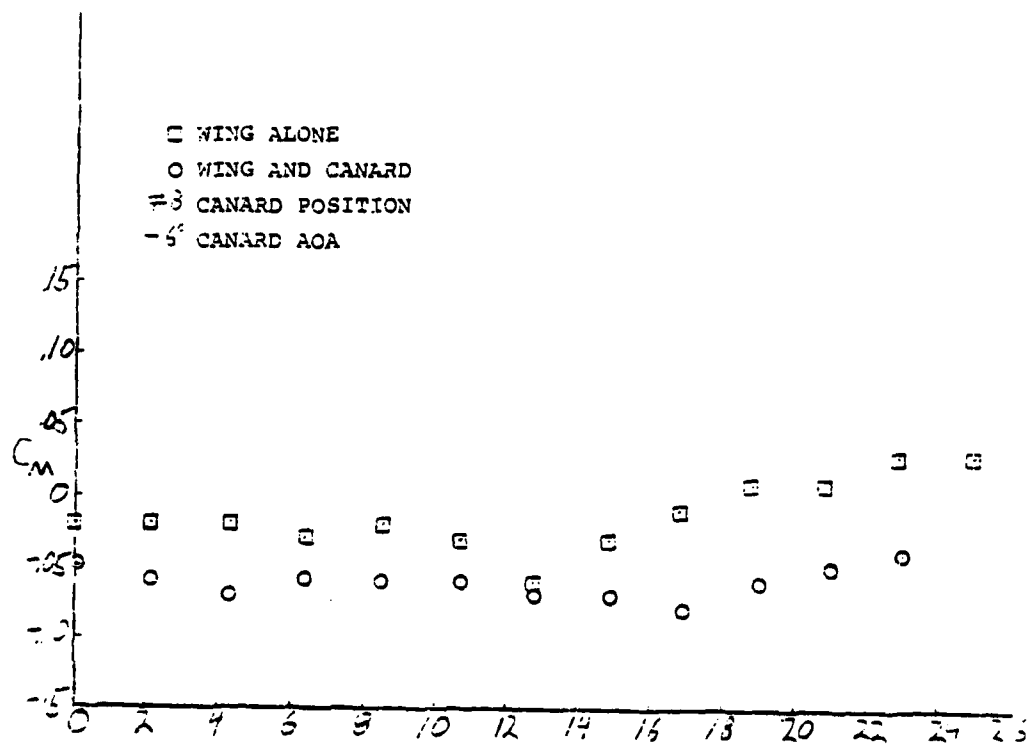


Figure 39A37M. Moment Coefficient vs α°

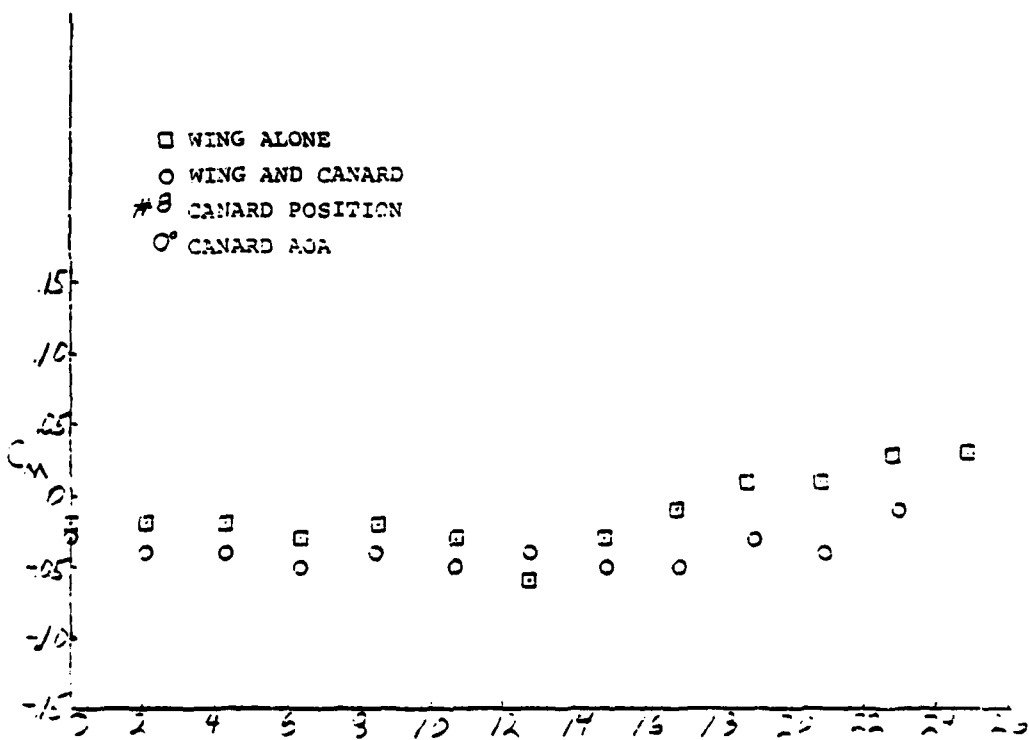


Figure 39A38M. Moment Coefficient vs α°

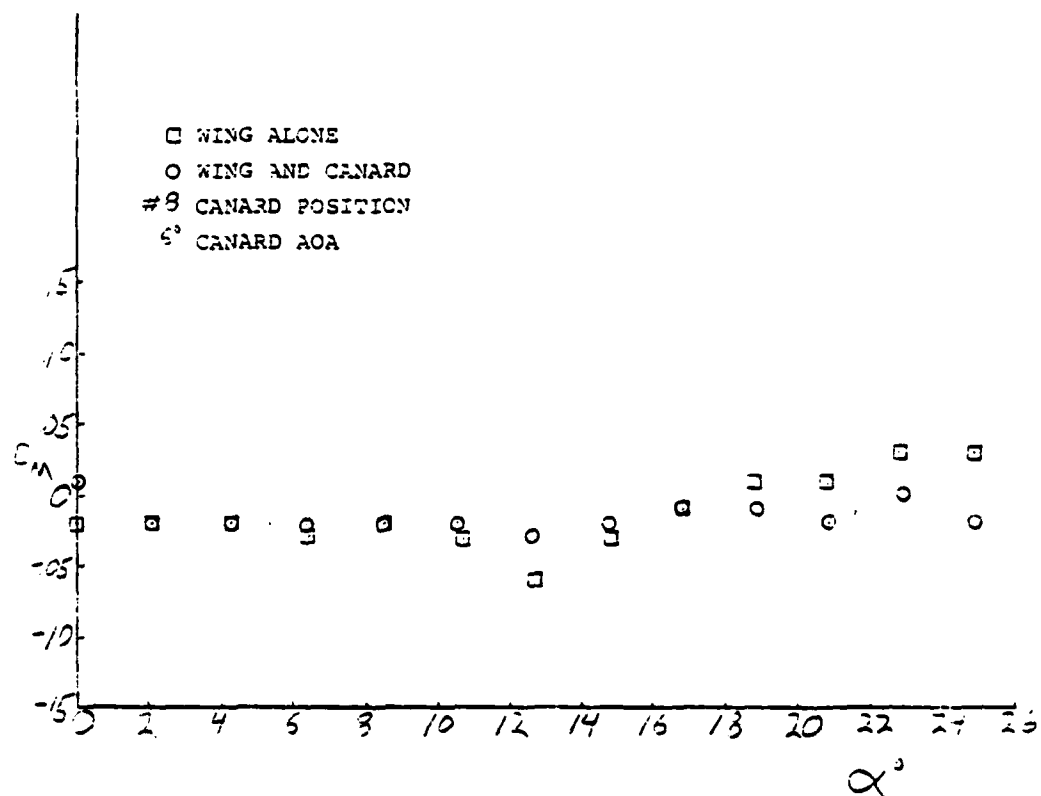


Figure 39A39M. Moment Coefficient vs α

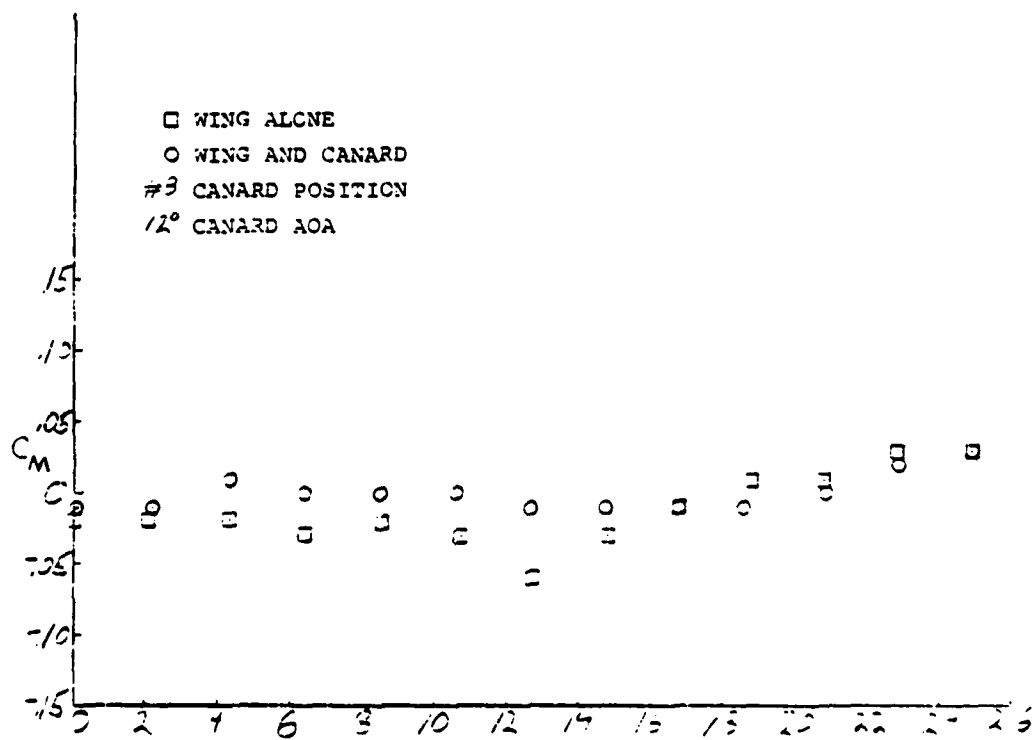


Figure 39A40M. Moment Coefficient vs α

AD-A124 722

A WIND TUNNEL STUDY OF THE EFFECTS OF A CLOSE-COUPLED

3/3

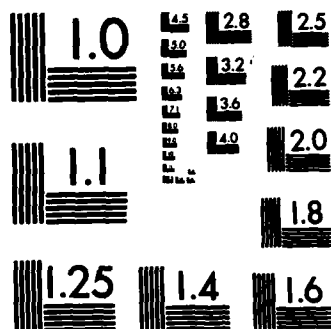
UNCLASSIFIED

DEC 82 AFIT/GAE/AA/82D-30

P N WEAVER
510-412

NL

--	--	--	--	--	--	--	--	--	--	--	--	--	--	--	--	--	--	--	--	--	--	--	--	--	--	--	--	--	--	--	--	--	--	--	--	--	--	--	--	--	--	--	--	--	--	--	--	--	--	--	--	--	--	--	--	--	--	--	--	--	--	--	--	--	--	--	--	--	--	--	--	--	--	--	--	--	--	--	--	--	--	--	--	--	--	--	--	--	--	--	--	--	--	--	--	--	--	--	--	--	--	--	--	--	--	--	--	--	--	--	--	--	--	--	--	--	--	--	--	--	--	--	--	--	--	--	--	--	--	--	--	--	--	--	--	--	--	--	--	--	--	--	--	--	--	--	--	--	--	--	--	--	--	--	--	--	--	--	--	--	--	--	--	--	--	--	--	--	--	--



MICROCOPY RESOLUTION TEST CHART
NATIONAL BUREAU OF STANDARDS-1963-A

Appendix E
Flow Visualization Data

This appendix contains the photographs obtained from the boundary layer flow visualization study done on model #3.

When studying the photographs, keep in mind that the tunnel airflow is from top to bottom and the black areas depicted are the airfoil surfaces. The white areas are the flow patterns created by the tunnel airflow moving the oil containing the white titanium dioxide particles.

The boundary layer patterns formed in this manner give an indication of the behavior of the airflow just above the wing surface. For example, lines that progress in an orderly manner from where the oil was brushed on the airfoil surface back to the trailing edge indicate attached flow and a flying airfoil (Fig 40A0a). On the other hand, lines that progress spanwise indicate boundary layer flow that is near separation (Fig 40A0b). Flow that is toward the leading edge indicates a stalled region on the wing (Fig 40A0b). Flow that is pooled or comes together at a point could indicate detached flow or a dripping of fluid from the canard to the wing (Fig 40A40b vs 40A20b).

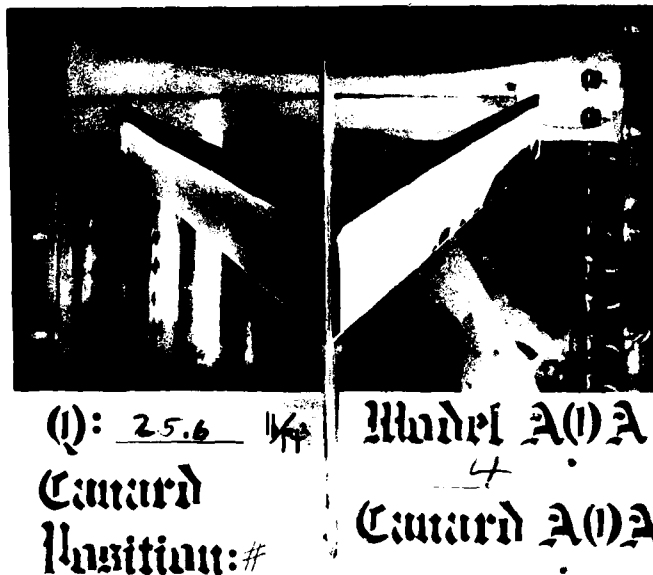


Figure 40A0a. Boundary Layer Flow Patterns



Figure 40A0b. Boundary Layer Flow Patterns

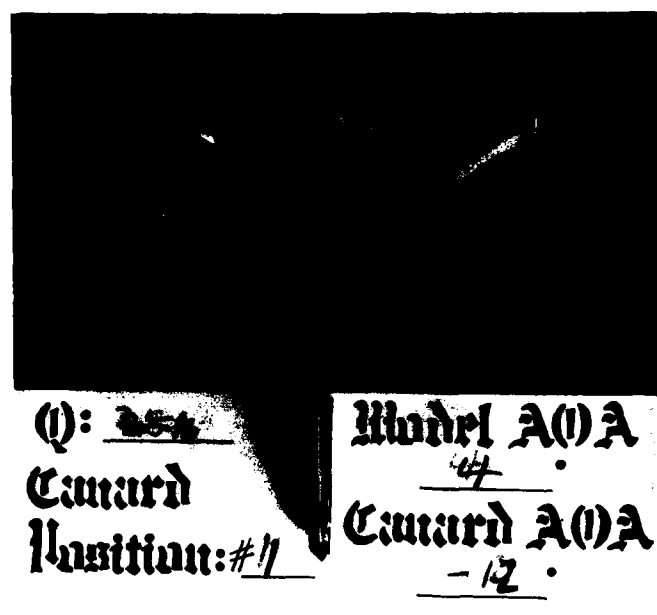


Figure 40A1a. Boundary Layer Flow Patterns

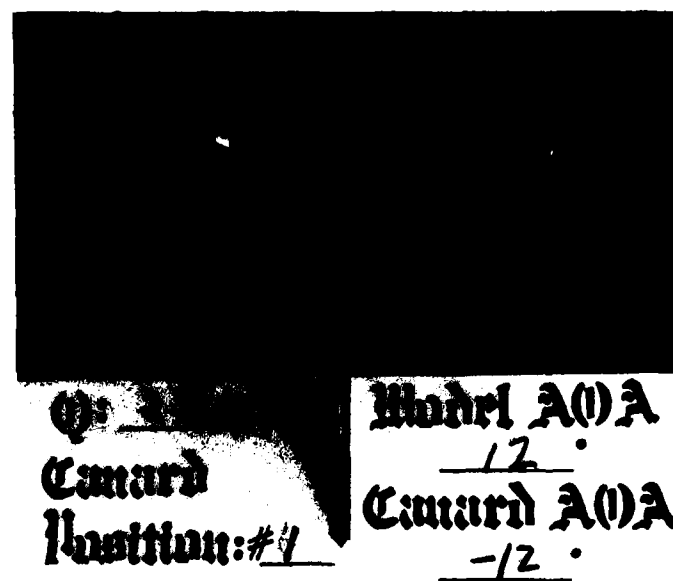
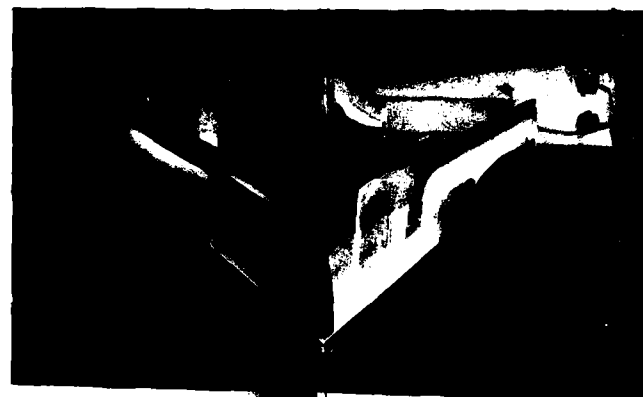
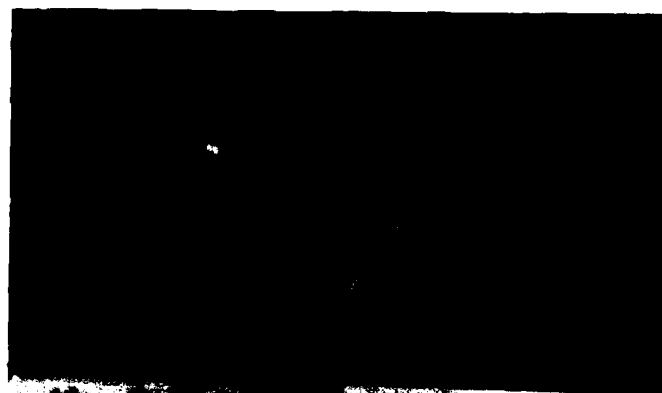


Figure 40A1b. Boundary Layer Flow Patterns



$Q: 25.6$
 Canard
 Position: #1
 Model A(0)A
 $\frac{4}{-6}$
 Canard A(0)A

Figure 40A2a. Boundary Layer Flow Patterns



$Q: 3.0$
 Canard
 Position: #4
 Model A(0)A
 $\frac{12}{-6}$
 Canard A(0)A

Figure 40A2b. Boundary Layer Flow Patterns

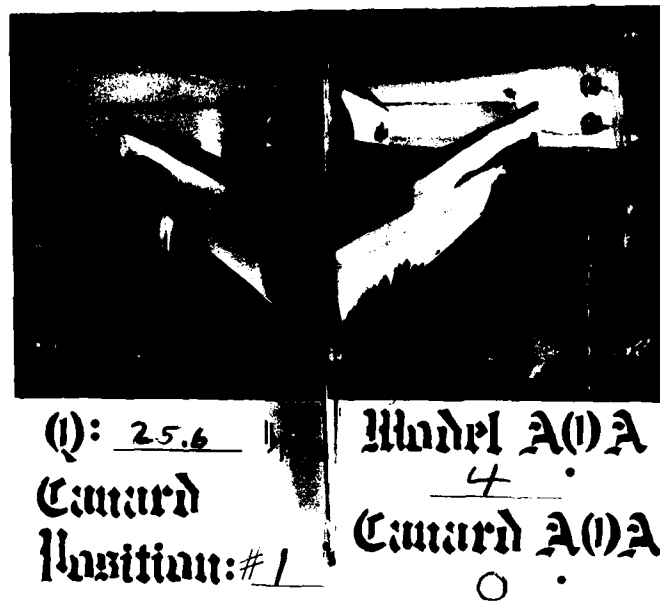


Figure 40A3a. Boundary Layer Flow Patterns

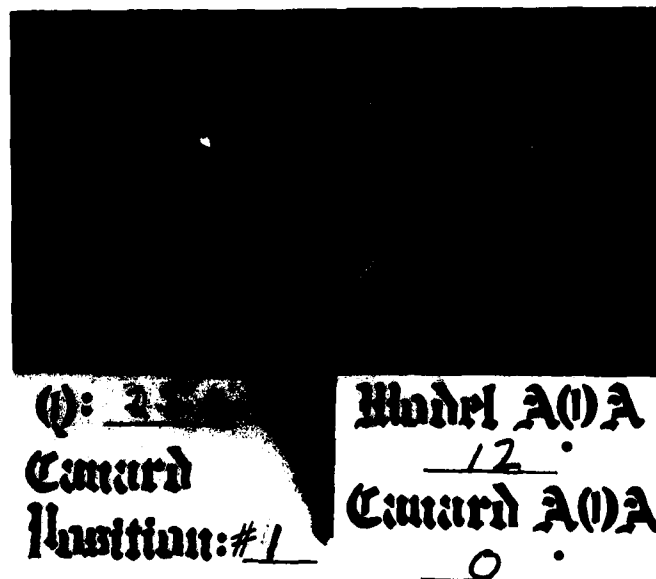


Figure 40A3b. Boundary Layer Flow Patterns

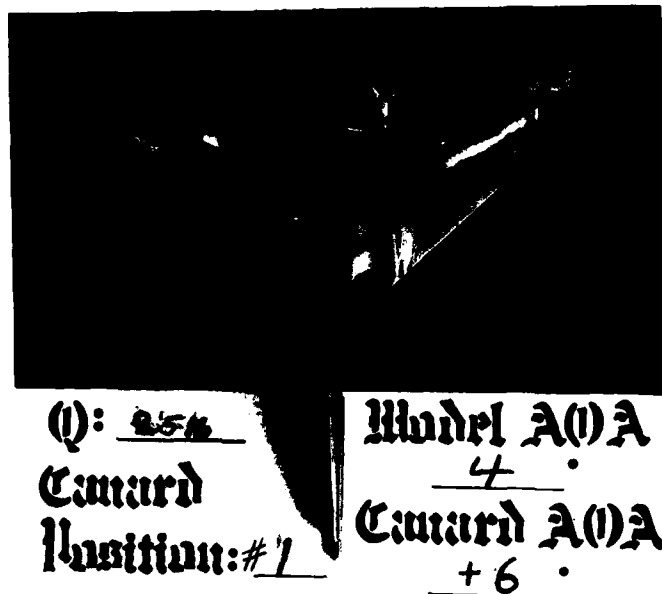


Figure 40A4a. Boundary Layer Flow Patterns

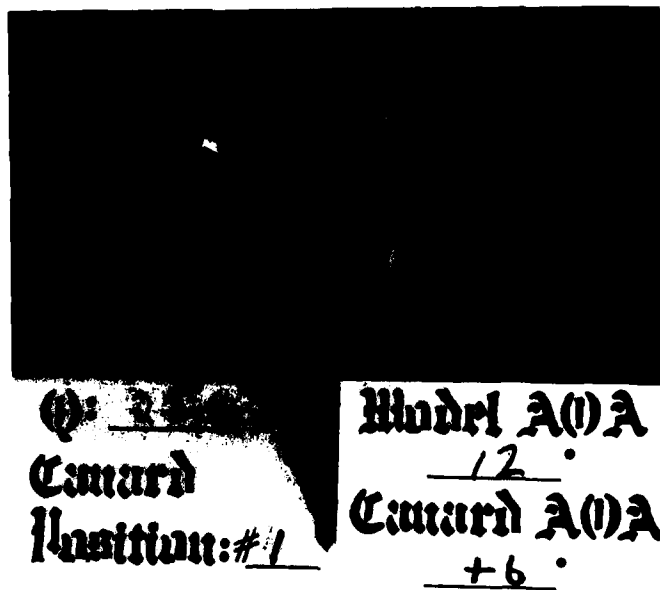


Figure 40A4b. Boundary Layer Flow Patterns

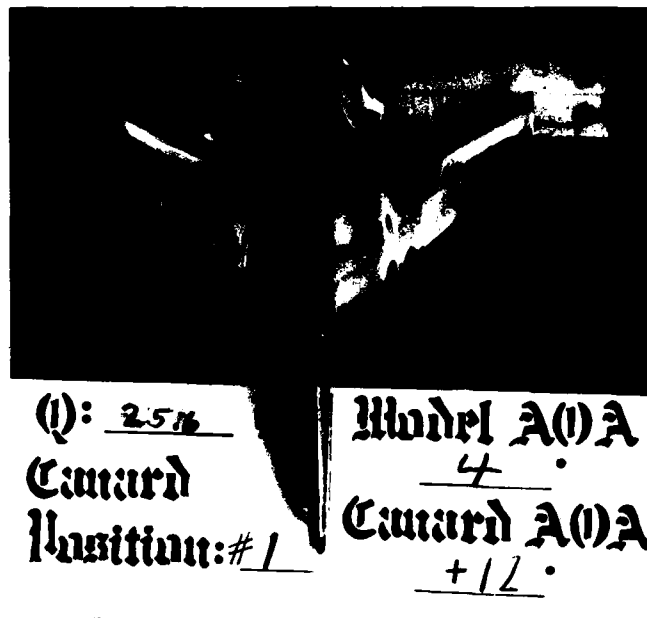


Figure 40A5a. Boundary Layer Flow Patterns

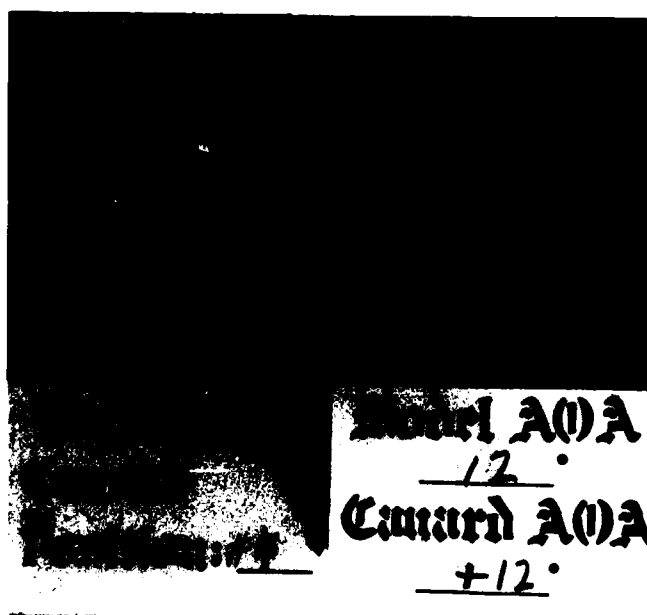


Figure 40A5b. Boundary Layer Flow Patterns

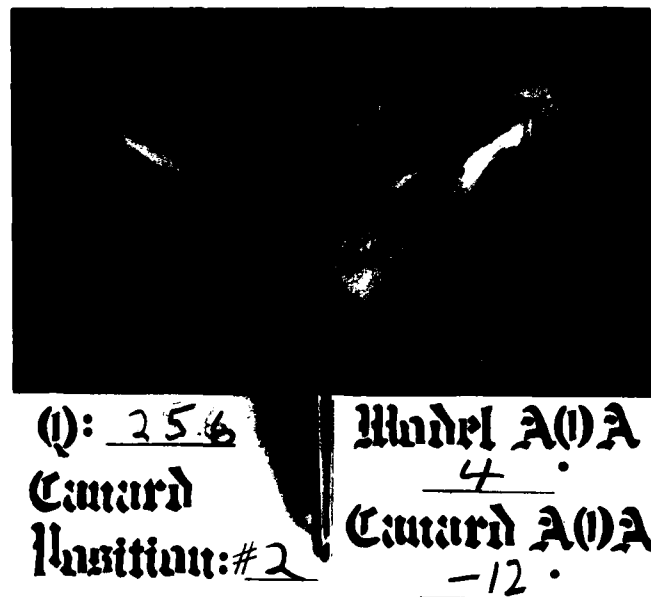


Figure 40A6a. Boundary Layer Flow Patterns

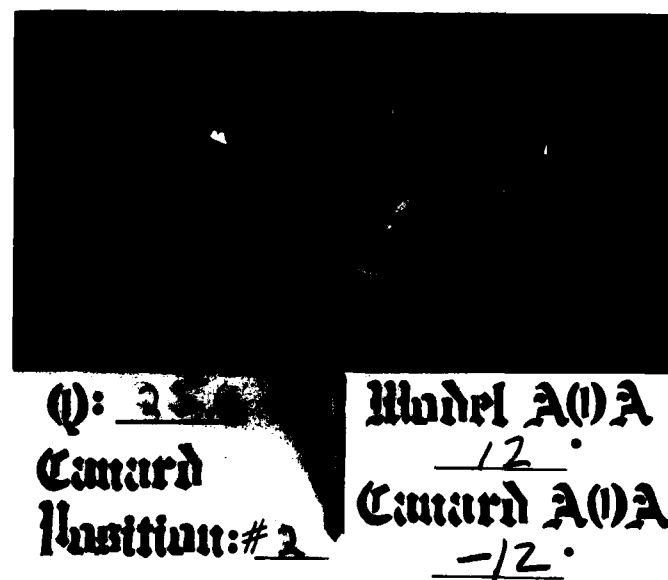


Figure 40A6b. Boundary Layer Flow Patterns

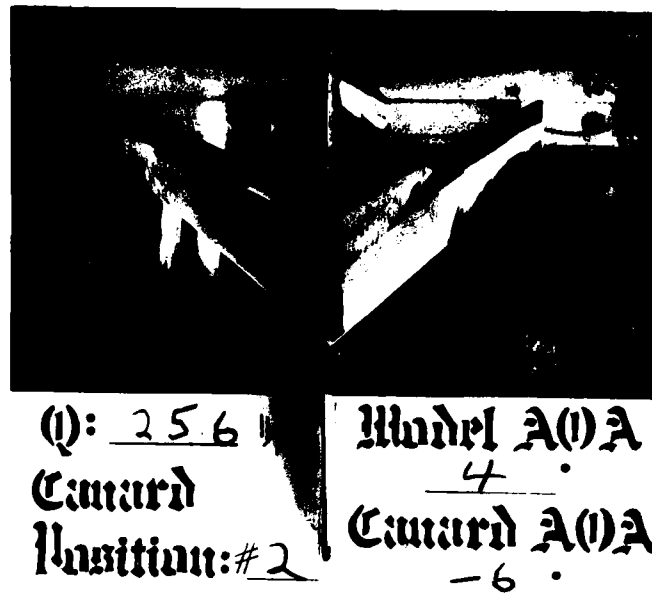


Figure 40A7a. Boundary Layer Flow Patterns

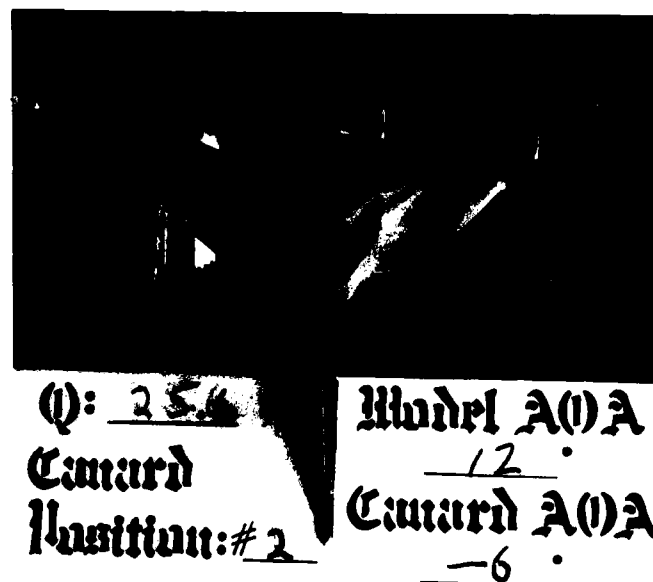


Figure 40A7b. Boundary Layer Flow Patterns

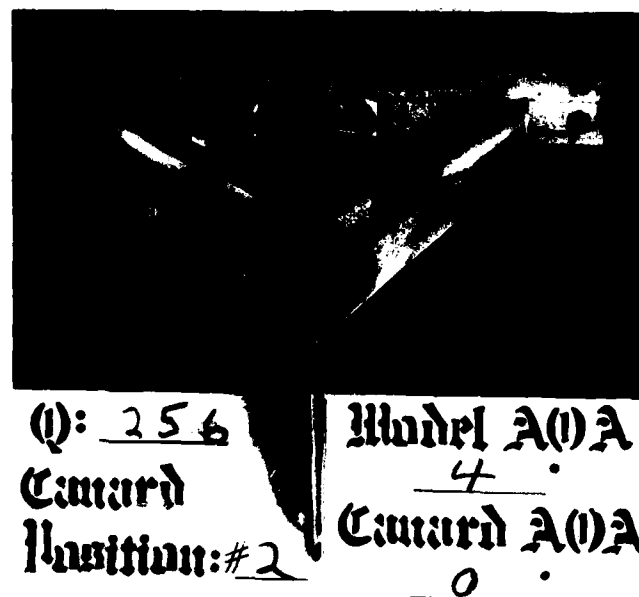


Figure 40A8a. Boundary Layer Flow Patterns

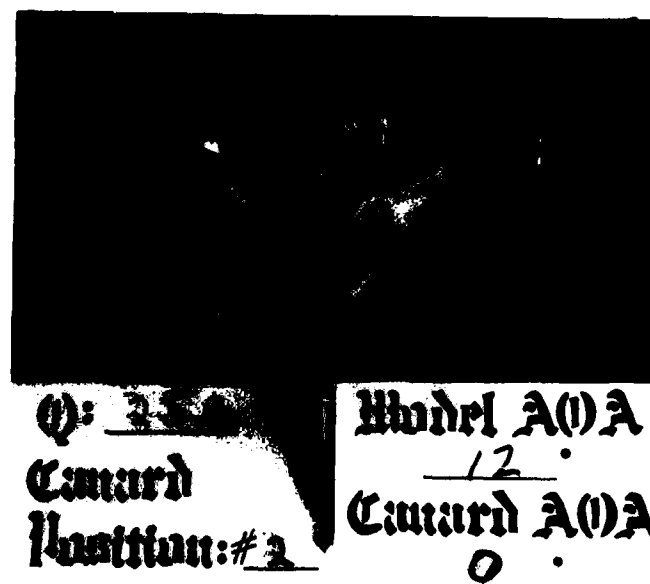


Figure 40A8b. Boundary Layer Flow Patterns

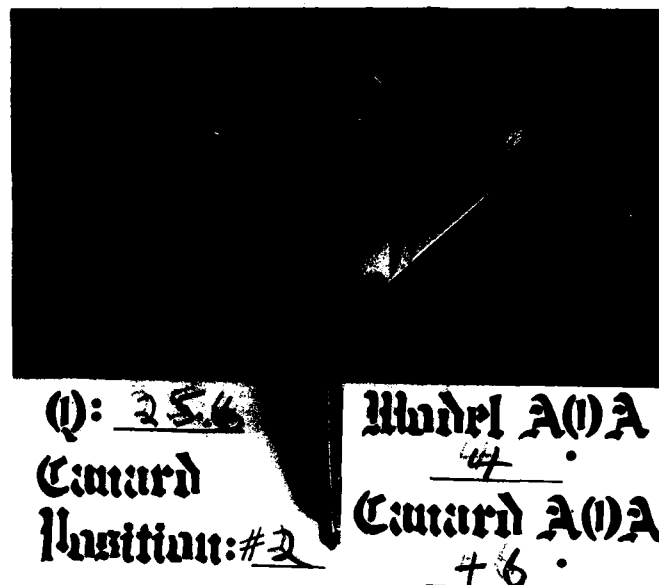


Figure 40A9a. Boundary Layer Flow Patterns

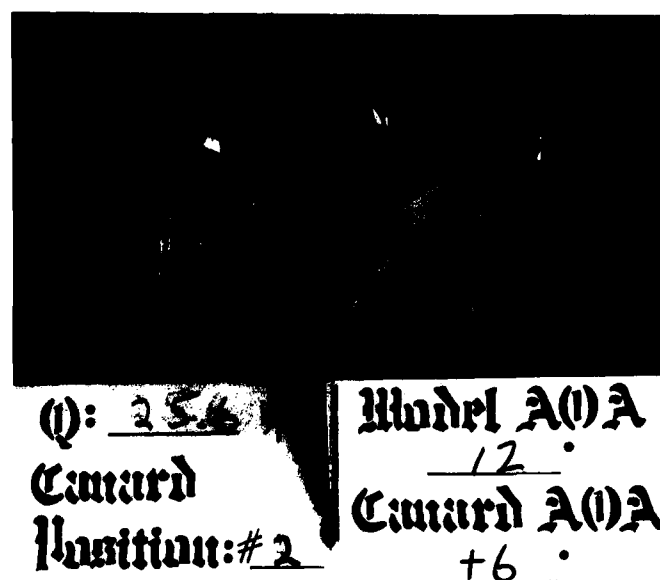


Figure 40A9b. Boundary Layer Flow Patterns

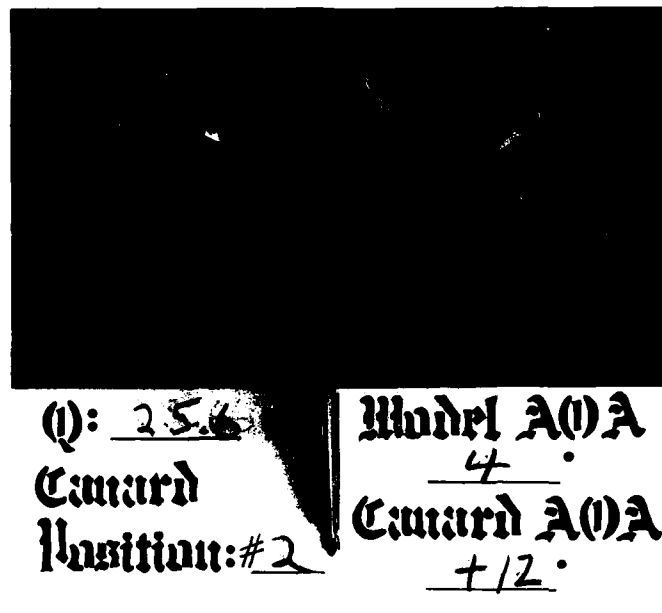


Figure 40A10a. Boundary Layer Flow Patterns

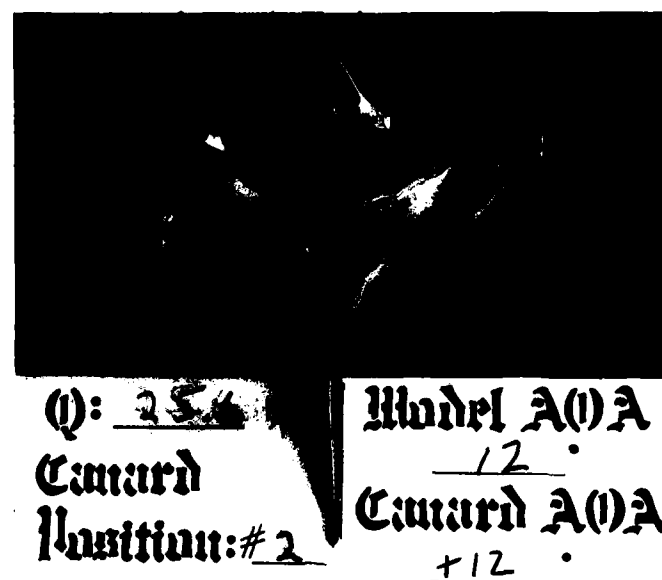


Figure 40A10b. Boundary Layer Flow Patterns

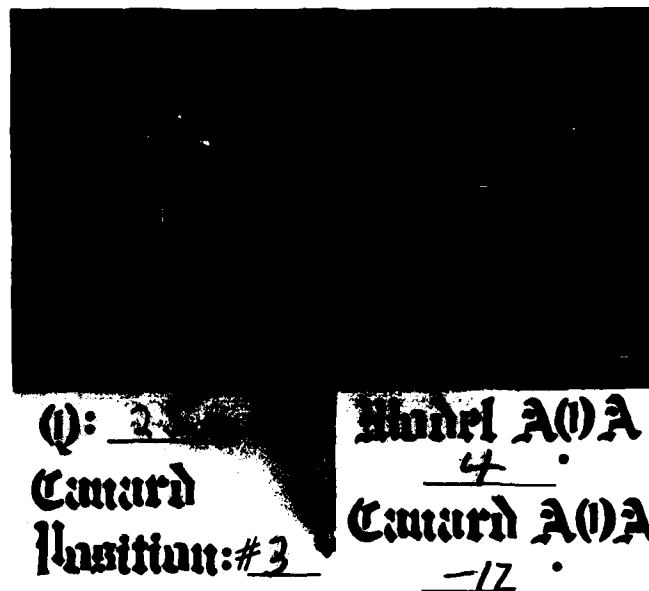


Figure 40A11a. Boundary Layer Flow Patterns

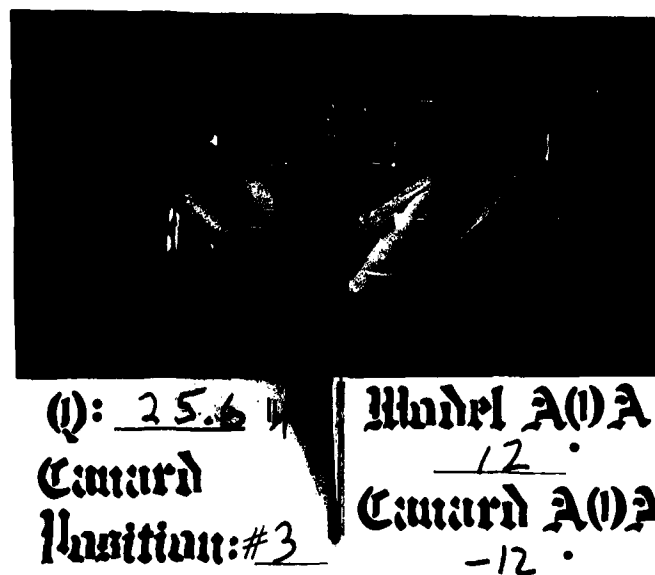


Figure 40A11b. Boundary Layer Flow Patterns

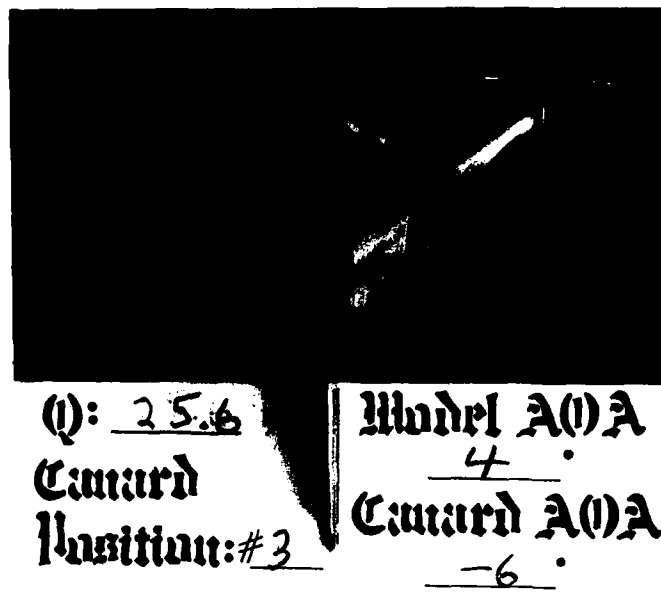


Figure 40A12a. Boundary Layer Flow Patterns

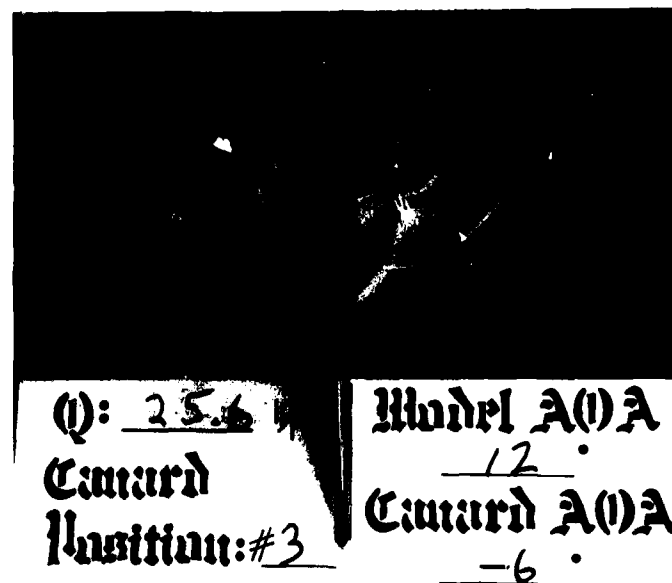


Figure 40A12b. Boundary Layer Flow Patterns

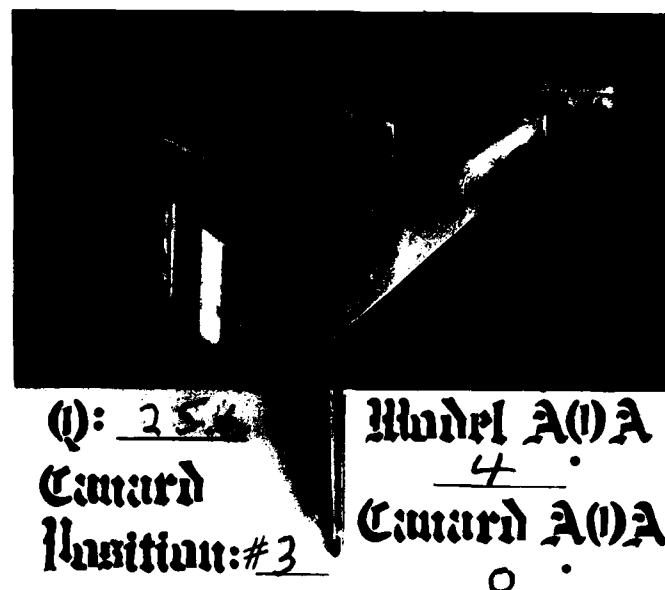


Figure 40A13a. Boundary Layer Flow Patterns

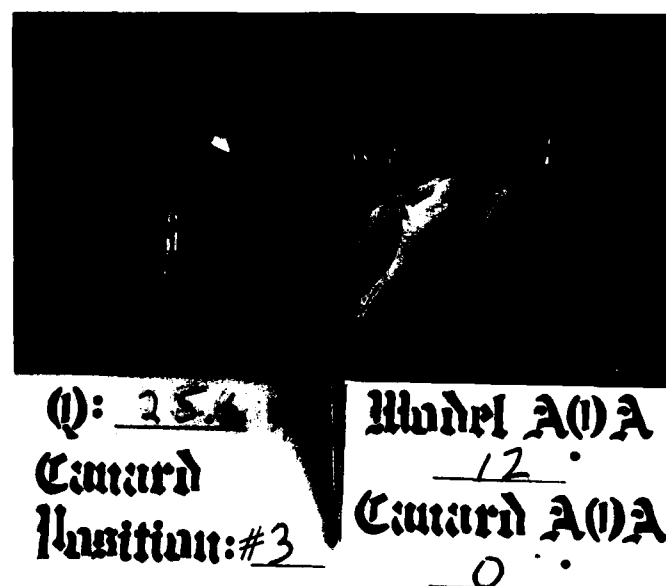


Figure 40A13b. Boundary Layer Flow Patterns



α : 25.6 Model AOA
 Camard 4
 Position: #3 Camard AOA
+6

Figure 40A14a. Boundary Layer Flow Patterns



α : 25.6 Model AOA
 Camard 12
 Position: #3 Camard AOA
+6

Figure 40A14b. Boundary Layer Flow Patterns



(Q): 25.6 $\frac{1}{4}$ Model A(0)A
 Camard 4 \cdot
 Position: #3 Camard A(0)A
+12 \cdot

Figure 40A15a. Boundary Layer Flow Patterns



(Q): 25.6 $\frac{1}{4}$ Model A(0)A
 Camard 12 \cdot
 Position: #3 Camard A(0)A
+12 \cdot

Figure 40A15b. Boundary Layer Flow Patterns

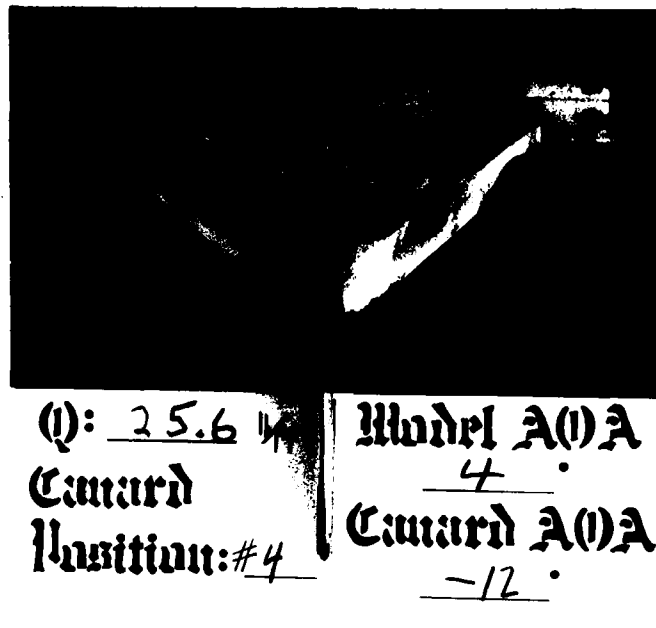


Figure 40A16a. Boundary Layer Flow Patterns

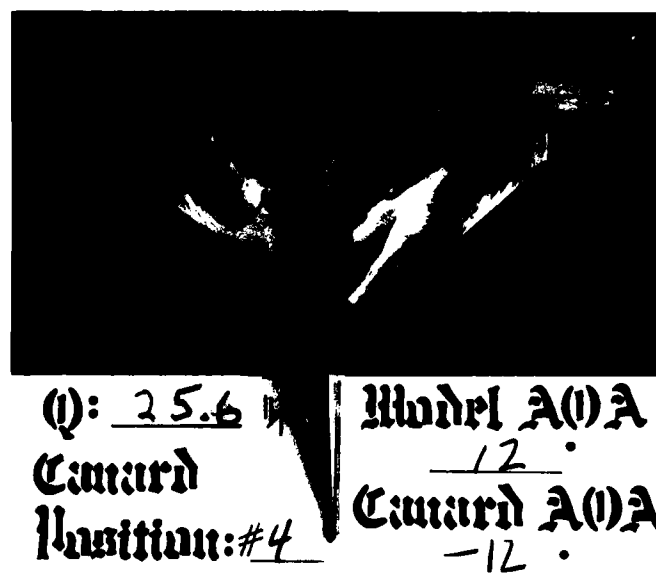


Figure 40A16b. Boundary Layer Flow Patterns

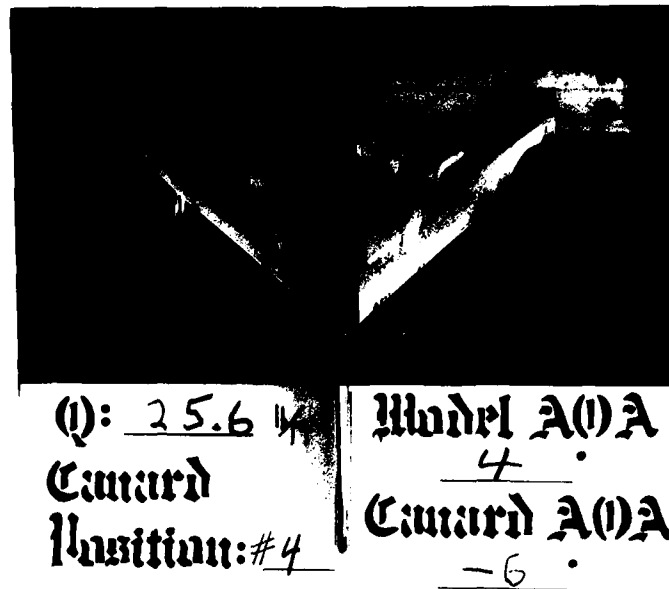


Figure 40A17a. Boundary Layer Flow Patterns

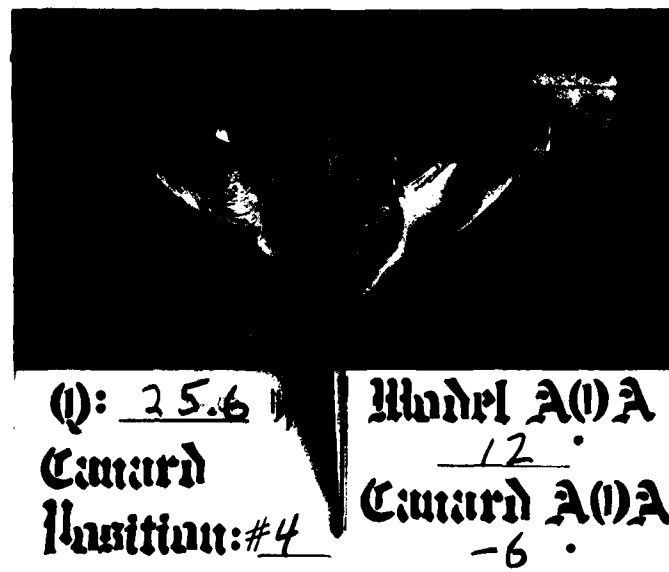


Figure 40A17b. Boundary Layer Flow Patterns



Q : 25.6 Model A(0)A
 Camard 4
 Position: #4 Camard A(0)A
0

Figure 40A18a. Boundary Layer Flow Patterns



Q : 25.6 Model A(0)A
 Camard 12
 Position: #4 Camard A(0)A
0

Figure 40A18b. Boundary Layer Flow Patterns



Q : 25.6 $\frac{1}{4}$ | Model A(0)A
 Camard 4 .
 Position: #4 | Camard A(0)A
 +6 .

Figure 40A19a. Boundary Layer Flow Patterns



Q : 25.6 $\frac{1}{4}$ | Model A(0)A
 Camard 12 .
 Position: #4 | Camard A(0)A
 +6 .

Figure 40A19b. Boundary Layer Flow Patterns

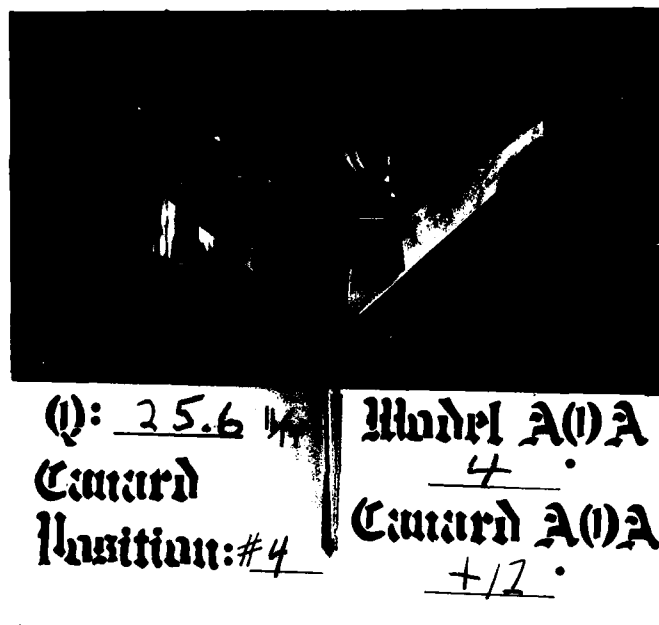


Figure 40A20a. Boundary Layer Flow Patterns

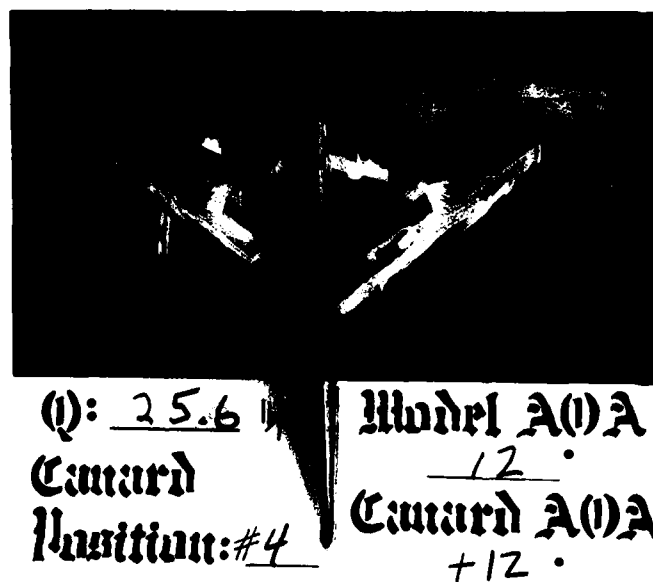


Figure 40A20b. Boundary Layer Flow Patterns



Q: 25.6 Model A0A
 Camard 4
 Position: # 5 Camard A0A
-12

Figure 40A21a. Boundary Layer Flow Patterns



Q: 25.6 Model A0A
 Camard 12
 Position: # 5 Camard A0A
-12

Figure 40A21b. Boundary Layer Flow Patterns



(Q): 25.6 1/4 Model A(0)A
 Camard 4
 Position: # 5 Camard A(0)A
-6

Figure 40A22a. Boundary Layer Flow Patterns



(Q): 25.6 1/4 Model A(0)A
 Camard 12
 Position: # 5 Camard A(0)A
-6

Figure 40A22b. Boundary Layer Flow Patterns



Q: 25.6 Model A(1)A
 Camard 4
 Position: # 5 Camard A(1)A
0

Figure 40A23a. Boundary Layer Flow Patterns



Q: 25.6 Model A(1)A
 Camard 12
 Position: # 5 Camard A(1)A
0

Figure 40A23b. Boundary Layer Flow Patterns



(Q): 25.6 $\frac{1}{4}$
 Canard
 Position: # 5

Model AOA
4
 Canard AOA
+6

Figure 40A24a. Boundary Layer Flow Patterns



(Q): 25.6 $\frac{1}{4}$
 Canard
 Position: # 5

Model AOA
12
 Canard AOA
+6

Figure 40A24b. Boundary Layer Flow Patterns



(1): 25.6 1/4 Model A(1)A
 Canard 4
 Position: # 5 Canard A(1)A
+12

Figure 40A25a. Boundary Layer Flow Patterns



(1): 25.6 1/4 Model A(1)A
 Canard 12
 Position: # 5 Canard A(1)A
+12

Figure 40A25b. Boundary Layer Flow Patterns



(Q): 25.6 $\frac{1}{4}$
 Camard
 Position: # 6

Model A(0)A
4°
 Camard A(0)A
-12°

Figure 40A26a. Boundary Layer Flow Patterns



(Q): 25.6 $\frac{1}{4}$
 Camard
 Position: # 6

Model A(0)A
12°
 Camard A(0)A
-12°

Figure 40A26b. Boundary Layer Flow Patterns



(1): 25.6 $\frac{1}{4}$
 Camard
 Position: #6

Model A(1)A
4
 Camard A(1)A
-6

Figure 40A27a. Boundary Layer Flow Patterns



(1): 25.6 $\frac{1}{4}$
 Camard
 Position: #6

Model A(1)A
12
 Camard A(1)A
-6

Figure 40A27b. Boundary Layer Flow Patterns



(Q): 25.6 Model A(0)A
 Camard 4
 Position: #6 Camard A(0)A
0

Figure 40A28a. Boundary Layer Flow Patterns



(Q): 25.6 Model A(0)A
 Camard 12
 Position: #6 Camard A(0)A
0

Figure 40A28b. Boundary Layer Flow Patterns



(1): 25.6 $\frac{1}{4}$
 Camard
 Position: #6

Model A(1)A
4
 Camard A(1)A
+6

Figure 40A29a. Boundary Layer Flow Patterns



(1): 25.6 $\frac{1}{4}$
 Camard
 Position: #6

Model A(1)A
12
 Camard A(1)A
+6

Figure 40A29b. Boundary Layer Flow Patterns



(1): 25.6 $\frac{1}{4}$ Model A(0)A
 Camard 4
 Position: #6 Camard A(0)A
+12

Figure 40A30a. Boundary Layer Flow Patterns



(1): 25.6 $\frac{1}{4}$ Model A(0)A
 Camard 12
 Position: #6 Camard A(0)A
+12

Figure 40A30b. Boundary Layer Flow Patterns



(Q): 25.6 Model A0A
 Camard 4
 Position: # 7 Camard A0A
 -12

Figure 40A31a. Boundary Layer Flow Patterns



(Q): 25.6 Model A0A
 Camard 12
 Position: # 7 Camard A0A
 -12

Figure 40A31b. Boundary Layer Flow Patterns



(Q): 25.6 $\frac{1}{4}$ Model A(0)A
 Camard 4
 Position: #7 Camard A(0)A
-6

Figure 40A32a. Boundary Layer Flow Patterns



(Q): 25.6 $\frac{1}{4}$ Model A(0)A
 Camard 12
 Position: #7 Camard A(0)A
-6

Figure 40A32b. Boundary Layer Flow Patterns



(1): 25.6 Model A(1)A
 Camard 4
 Position: # 7 Camard A(1)A
0

Figure 40A33a. Boundary Layer Flow Patterns



(1): 25.6 Model A(1)A
 Camard 12
 Position: # 7 Camard A(1)A
0

Figure 40A33b. Boundary Layer Flow Patterns



Q : 25.6 Model A(0)A
 Camard 4 ·
 Position: # 7 Camard A(0)A
 +6 ·

Figure 40A34a. Boundary Layer Flow Patterns



Q : 25.6 Model A(0)A
 Camard 12 ·
 Position: # 7 Camard A(0)A
 +6 ·

Figure 40A34b. Boundary Layer Flow Patterns



Q : 25.6 $\frac{1}{2}$ Model A(1)A
 Camard 4
 Position: # 7 Camard A(1)A
+12

Figure 40A35a. Boundary Layer Flow Patterns



Q : 25.6 $\frac{1}{2}$ Model A(1)A
 Camard 12
 Position: # 7 Camard A(1)A
+12

Figure 40A35b. Boundary Layer Flow Patterns



(1): 25.6 Model A(1)A
 Camard 4
 Position: # 8 Camard A(1)A
-12.

Figure 40A36a. Boundary Layer Flow Patterns



(1): 25.6 Model A(1)A
 Camard 12
 Position: # 8 Camard A(1)A
-12.

Figure 40A36b. Boundary Layer Flow Patterns



(Q): 25.6 $\frac{1}{4}$
 Camard
 Position: # 8

Model A(0)A
4
 Camard A(0)A
-6

Figure 40A37a. Boundary Layer Flow Patterns



(Q): 25.6 $\frac{1}{4}$
 Camard
 Position: # 8

Model A(0)A
12
 Camard A(0)A
-6

Figure 40A37b. Boundary Layer Flow Patterns



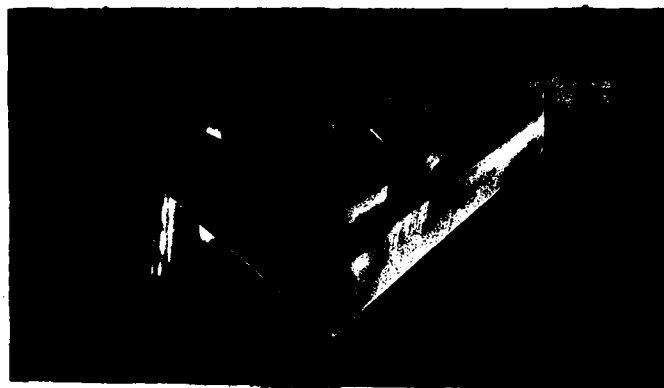
Q : 25.6 $\frac{1}{4}$ Model AOA
 Camard 4
 Position: # 8 Camard AOA
0

Figure 40A38a. Boundary Layer Flow Patterns



Q : 25.6 $\frac{1}{4}$ Model AOA
 Camard 12
 Position: # 8 Camard AOA
0

Figure 40A38b. Boundary Layer Flow Patterns



$Q: 25.6 \frac{1}{4}$ Model A(0)A
 Camard
 Position: # 8 $\frac{4}{+6}$

Figure 40A39a. Boundary Layer Flow Patterns



$Q: 25.6 \frac{1}{4}$ Model A(0)A
 Camard
 Position: # 8 $\frac{12}{+6}$

Figure 40A39b. Boundary Layer Flow Patterns



(Q): 25.6 $\frac{1}{4}$
 Camard
 Position: # 8

Model A(0)A
4
 Camard A(0)A
+12

Figure 40A40a. Boundary Layer Flow Patterns



(Q): 25.6 $\frac{1}{4}$
 Camard
 Position: # 8

Model A(0)A
12
 Camard A(0)A
+12

Figure 40A40b. Boundary Layer Flow Patterns

Vita

Paul M. Weaver was born on 3 January 1954 in Trenton, New Jersey. Upon graduation from the United States Air Force Academy in 1976 with a Bachelor of Science in Aeronautical Engineering, he attended Undergraduate Pilot Training at Vance AFB. Upon graduation in 1977, he was assigned to the C-141 at McGuire AFB. After two years, he was designated for T-38 instructor pilot duty at Vance AFB. After serving for one year in this capacity, he was assigned to the Air Force Institute of Technology in August, 1981.

UNCLASSIFIED

SECURITY CLASSIFICATION OF THIS PAGE (When Data Entered)

REPORT DOCUMENTATION PAGE		READ INSTRUCTIONS BEFORE COMPLETING FORM
1. REPORT NUMBER AFIT/GAE/AA/82D-30	2. GOVT ACCESSION NO. AD-A124722	3. RECIPIENT'S CATALOG NUMBER
4. TITLE (and Subtitle) A WIND TUNNEL STUDY OF THE EFFECTS OF A CLOSE-COUPLED CANARD ON THE AERODYNAMIC CHARACTERISTICS OF A FORWARD-SWEPT WING IN INCOMPRESSIBLE FLOW		5. TYPE OF REPORT & PERIOD COVERED MS Thesis
7. AUTHOR(s) Paul M. Weaver		6. PERFORMING ORG. REPORT NUMBER
9. PERFORMING ORGANIZATION NAME AND ADDRESS Air Force Institute of Technology Wright-Patterson AFB, Ohio 45433		8. CONTRACT OR GRANT NUMBER(s)
11. CONTROLLING OFFICE NAME AND ADDRESS		10. PROGRAM ELEMENT, PROJECT, TASK AREA & WORK UNIT NUMBERS
14. MONITORING AGENCY NAME & ADDRESS (if different from Controlling Office)		12. REPORT DATE December 1982
		13. NUMBER OF PAGES 223
		15. SECURITY CLASS. (of this report) UNCLASSIFIED
		15a. DECLASSIFICATION/DOWNGRADING SCHEDULE
16. DISTRIBUTION STATEMENT (of this Report) Approved for public release; distribution unlimited		
17. DISTRIBUTION STATEMENT (of the abstract entered in Block 20, if different from Report)		
18. SUPPLEMENTARY NOTES Approved for public release; LAW AFR 190-17. LYNN E. WOLAVER Dean for Research and Professional Development Air Force Institute of Technology (AIC) Wright-Patterson AFB OH 45433 19 JAN 1983		
19. KEY WORDS (Continue on reverse side if necessary and identify by block number) Forward-Swept Wings Swept Wings Canards		
20. ABSTRACT (Continue on reverse side if necessary and identify by block number) Low speed wind tunnel tests and a boundary layer flow visualization study were conducted in the Air Force Institute of Technology fourteen inch wind tunnel to determine the differences in the aerodynamic characteristics among a forward- swept wing and several forward-swept wing/canard configurations. Both the wing and canard were constructed with an NACA 0006 air- foil section and had quarter chord sweeps of -30 and +40 deg,		

DD FORM 1 JAN 73 1473

EDITION OF 1 NOV 65 IS OBSOLETE

UNCLASSIFIED

SECURITY CLASSIFICATION OF THIS PAGE (When Data Entered)

UNCLASSIFIED

SECURITY CLASSIFICATION OF THIS PAGE(When Data Entered)

39 17
100,000
respectively. All tests were conducted at a dynamic pressure of 25.6 lbf/ft² and a Reynolds number of 1.9×10^5 based on the wing mean aerodynamic chord.

The results show that the changes in the aerodynamic characteristics are dependent upon canard location relative to the wing, canard incidence, and model angle of attack. The largest increases in C_L were observed for the two canard positions above and closest to the wing. A decrease in C_M was noted as the canard location changed vertically from the upper to the lower test positions. An increase in C_D occurred as the canard location approached the wing horizontally.

Comparison of the force and moment data with the flow study photographs suggests that the canard wake/vortex system is responsible for the changes in the wing/canard aerodynamic characteristics.

UNCLASSIFIED

SECURITY CLASSIFICATION OF THIS PAGE(When Data Entered)

END

FILMED

3-83

DTIC